Thèse

insa

ueb

THESE INSA Rennes
sous le sceau de l'Université européenne de Bretagne
pour obtenir le titre de
DOCTEUR DE L'INSA DE RENNES
Spécialité : Génie Mécanique

présentée par
Chansopheak SEANG
ECOLE DOCTORALE : *SDLM*
LABORATOIRE : *LGCGM*

Evaluation numérique des contraintes résiduelles appliquée à l'acier DP600 soudé par laser de haute puissance Nd : YAG

Evaluation numérique des contraintes résiduelles appliquée à l'acier DP600 soudé par laser de haute puissance Nd : YAG

Chansopheak SEANG

Remerciements

Je tiens dans un premier temps à remercier M. Eric RAGNEAU, Professeur et directeur du département de Génie Mécanique et Automatique *(GMA)* à l'INSA de Rennes, pour m'avoir accepté dans son équipe et être le directeur de thèse. J'aimerais adresser un remerciement particulier à Mme Afia KOUADRI-DAVID, MCF à l'INSA de Rennes, qui a dirigé et encadré ce travail de thèse, pour sa sympathie, sa disponibilité, ses idées et ses conseils, ainsi que pour son aide précieuse pendant ces années de thèse.

Je tiens à remercier M. Laurent BARRALLIER, M. Pascal PAILLARD d' avoir accepté d' être rapporteur de mon travail de recherche ainsi que leurs commentaires portés sur mon travail. Je tiens à remercier également M. Hubert BOURY, M. Laurent CRETTEUR et M. Thierry GLORIANT d'avoir accepté d'être membre de jury.

Ce travail n'aurait pu aboutir sans l'aide de nombreuses personnes de l'équipe PSM en particulier Fabien Marco et Sylvain Rigaud qui m'ont aidés à la préparation des expérimentations.

J'ai pu travailler dans un cadre particulièrement agréable, grâce à l'ensemble des membres de l'équipe PSM et des collèges du bureau. Merci à tous pour votre bonne humeur et votre sympathie.

Je remercie le service de coopération et d'action culturelle de l'ambassade de France au Cambodge pour avoir financé ce travail de recherche.

Ces remerciements ne seraient pas complets sans une pensée à mes amis cambodgiens. Merci de m'avoir accueilli dans votre communauté, et pour tous les bons moments passés à Rennes pendant ma thèse.

Mes dernières pensées iront vers ma famille au Cambodge et en France, et surtout mes parents, qui m'auront encouragé à poursuivre mes études jusqu'aujourd'hui.

CONTENTS

Introduction Générale

Cette thèse a été réalisée à l'Institut National des Sciences Appliquées de Rennes *(INSA-Rennes)*, au sein de l'équipe PSM *(Procédés et Systèmes Mécaniques)* du laboratoire de génie civil et de génie mécanique *(LGCGM)* qui fait partie de l'Université Européenne de Bretagne *(UEB)*. Cette thèse a reçu le soutien financier du ministère des affaires étrangères par l'intermédiaire d'une bourse du gouvernement français à l'ambassade de France au Cambodge.

L'objectif de la thèse a été de développer une approche numérique et expérimentale permettant d'étudier les contraintes résiduelles générées par les modifications métallurgiques et mécaniques liées au procédé de soudage laser de type Nd:YAG. Cette étude a été menée sur des tôles en acier zingué de nuance DP600, d'épaisseur de 1.25mm. La configuration d'assemblage choisie est une configuration par recouvrement. Le choix du mode d'assemblage et du matériau est étroitement lié à leur utilisation dans le domaine automobile, Fig.1.1.

De façon générale, le soudage est une technique d'assemblage très répandue dans de nombreux secteurs industriels comme la marine, l'énergie, l'automobile, l'emballage ou encore dans les secteurs de l'aéronautique. Dans le cadre des structures soudées, la préoccupation majeure des industriels est le comportement en service des joints soudés. Les opérations d'assemblage comme le soudage conduisent à d'importantes déformations au niveau de la liaison ainsi qu'à l'apparition de contraintes résiduelles. La microstructure du matériau se trouve profondément modifiée par le cycle thermique appliqué localement à la structure; dans la zone fondue, on considère généralement qu'un nouveau matériau est élaboré. Cette zone est généralement constituée de gradients métallurgiques et mécaniques très localisés dans la structure au niveau du joint soudé qui conduisent généralement à l'apparition de champs de déformations et à la présence de contraintes résiduelles. C'est la

1

raison pour laquelle, les modifications et les conséquences induites par ce procédé se révèlent donc essentielles pour prédire le comportement en service des structures. En effet, la distribution des contraintes résiduelles joue un rôle important dans la tenue en service des structures en favorisant des ruptures par fatigue, des fissurations ou encore de la corrosion sous contraintes. Les distorsions associées peuvent causer des problèmes de tolérances dimensionnelles des structures. Ainsi, une meilleure compréhension et maitrise des contraintes résiduelles permettrait d'éviter l'utilisation de facteurs de sécurité plus élevés et, par conséquent de mieux optimiser la taille et la durée de vie des structures mécano-soudées.

A partir de ces constats, l'étude des procédés de soudage apparait actuellement comme un domaine de recherche qui est à la fois ouvert et complexe, car il nécessite de combiner des connaissances issues de différentes disciplines : l'étude des procédés, de la thermique, de la physique, de la métallurgie et de la mécanique.

Dans ce contexte, le développement des outils numériques pour simuler à la fois les procédés de soudage et les conséquences mécaniques sont devenues un outil indispensable pour la prédiction des contraintes résiduelles et des déformations d'une structure soudée car elles permettent de réduire le coût de l'investissement et le temps liés aux expériences.

Ainsi, à travers ce travail de recherche, nous nous sommes intéressés à la simulation des contraintes résiduelles par la prise en compte des caractéristiques du procédé utilisé, le laser de puissance, les propriétés du matériau en particulier les aspects métallurgiques et mécaniques.

Pour atteindre notre objectif, le manuscrit de thèse expose le travail réalisé en sept chapitres. Les deux premiers chapitres constituent l'état de l'art.

Le premier chapitre présente le procédé de soudage laser et ses conséquences mécaniques. Nous rappelons dans ce chapitre les mécanismes qui interagissent au cours du soudage ainsi que les conséquences de ce procédé sur les matériaux soudés, la genèse des contraintes et déformations résiduelles.

Le deuxième chapitre présente les différents modèles numériques utilisés et développés dans la littérature du soudage par fusion. Nous y présentons les différents modèles utilisés comme les modèles thermiques, métallurgiques et mécaniques.

Le troisième chapitre présente l'étude expérimentale de l'assemblage par faisceau laser Nd:YAG. Nous y présentons l'influence des paramètres du procédé laser sur certaines propriétés du joint soudé comme la microstructure, la micro-dureté, la résistance au cisaillement en traction dans le cas d'un assemblage par recouvrement, les propriétés géométriques du bain fondu en particulier la section transversale. Ces caractérisations ont été réalisées d'une part pour optimiser les paramètres du procédé laser mais également pour définir certains paramètres des modèles numériques développés dans ce travail de thèse comme la dimension de la source de chaleur, l'efficacité énergétique, la transformation microstructurale et la micro-dureté par exemple. A la fin de ce chapitre, nous exposons les différentes analyses métallurgique et mécanique réalisées sur différents cordons de soudure obtenus par les paramètres optimisés du procédé. Une étude comparative des résultats, obtenus aussi bien dans le métal de base que dans la soudure, a permis de déterminer les transformations microstructurales et les conséquences mécaniques dues au procédé de soudage par faisceau laser dans le cas de l'acier DP600 étudié.

L*e chapitre quatre* est consacré à la construction d'un modèle tridimensionnel, transitoire et non linéaire qui permet la simulation de l'histoire thermique au cours du soudage. L'analyse numérique, développée sur un code de calcul par élément finis ABAQUS, repose sur la modélisation des phénomènes de transfert de chaleur au cours du soudage. Dans ce cas, le chargement appliqué est une source de chaleur volumique associée à des conditions aux limites. Les résultats de l'analyse thermique sont présentés sous forme d'évolution spatio-temporelle de la température dans les différences régions des plaques soudées. Une comparaison des résultats numériques et expérimentaux permettra d'apprécier la pertinence du modèle thermique développé. La deuxième étape concerne la simulation de l'évolution de l'état mécanique des pièces au cours de l'assemblage en introduisant les résultats du modèle thermique comme chargement. A la fin de ce chapitre, nous présentons

une analyse permettant de prédire la distribution des contraintes résiduelles sous l'influence des paramètres numériques et des paramètres thermo-physiques.

Le cinquième chapitre décrit la simulation thermo-métallurgique qui a consisté à intégrer dans notre modèle les transformations métallurgiques associées au changement de phases ainsi que l'analyse de la dureté du joint de soudure. Le modèle thermo-métallurgique a été réalisé par couplage du modèle thermique *(décrit précédemment)* et par la réalisation d'un modèle numérique métallurgique. Dans ce dernier cas, l'étude numérique s'est appuyée sur l'intégration des modèles de Waeckel et de Koistinen-Marburger. Le modèle de Waeckel nous permis de simuler et de prendre en compte le phénomène d'austénitisation pendant la phase de chauffage. Le modèle de Koistinen-Marburger permet de tenir compte des fractions volumiques générées pendant le refroidissement et donc de prendre en compte les phénomènes de transformation de phase lors du soudage. Nous avons également implanté un modèle nous permettant d'obtenir les valeurs de micro-dureté basée sur une loi de combinaison linéaire de la dureté de chaque phase. Les propriétés mécaniques comme la limite élastique et la résistance maximale à la traction ont été également obtenues par l'introduction d'un modèle permettant de convertir la valeur de micro-dureté obtenue précédemment.

Le *sixième chapitre* intègre l'ensemble des modèles : thermique, métallurgique et mécanique. Les résultats obtenus dans la partie précédente, ont été implantés dans différents modèles mécaniques : le modèle mécanique classique et le modèle mécanique avec prise en compte de la dilatation liée aux effets des changements de volume au cours des transformations de phases. Cette effet a été intégré à travers le coefficient de dilatation thermique des phases ferritiques et martensitiques obtenues à partir du modèle thermo-métallurgique. Nous pourrons ainsi discuter et comparer l'évolution des contraintes résiduelles issues du modèle élastoplastique classique et du modèle élastoplastique avec prise en compte de la déformation thermo-métallurgique.

Le septième chapitre constitue une validation des paramètres d'optimisation qui ont été étudiés dans les chapitres précédents en abordant les résultats de la simulation et ceux issus de l'expérimentation. Nous pourrons donc comparer l'évolution expérimentale et numérique de la température au cours du soudage, la géométrie du bain de fusion, le déplacement hors plan et les contraintes résiduelles après soudage.

Enfin, nous terminons ce travail de recherche par une conclusion générale qui nous a permis de synthétiser les principaux résultats issus de ces travaux. Des perspectives sont également proposées afin d'améliorer la simulation numérique dans les travaux futurs.

6

General introduction

This thesis was conducted at the National Institute of Applied Sciences of Rennes (INSA-Rennes) in the PSM team *(Process and Mechanical System)* laboratory of civil engineering and engineering mechanical *(LGCGM)* which is part of the European University of Brittany *(UEB)*. This thesis has received financial support from the Ministry of Foreign Affairs through a grant from the French government at the France Embassy in Cambodia.

The aim of the thesis was to develop a numerical and experimental approach to study the residual stresses generated by the metallurgical and mechanical changes associated with laser welding process of Nd:YAG. This study was conducted on galvanized steel sheets DP600 grade, thickness 1.25mm. The assembly configuration is selected by overlapping configuration. The choice of assembly and the material is closely related to their use in the automotive field, Fig.1.1.

In general, welding is a joining technique widespread used in many industries such as marine, energy, automotive, packaging, or in aerospace. As part of welded structures, the major concern is the industrial service behavior of welded joints. The assembly operations such as welding lead to significant distortions in the connection as well as the appearance of residual stress. The microstructure of the material is greatly modified by the thermal cycle applied locally to the structure, the molten zone is generally considered a new material is developed. This is generally made of metal and mechanical gradients very localized in the structure at the welded joint which usually lead to the formation of deformation and the presence of residual stresses. This is why the changes and consequences induced by this process thus prove essential to predict the behavior of structures in service. Indeed, the distribution of residual stress plays an important role in the serviceability of structures promoting fatigue fractures, cracks or even stress corrosion. Distortions associated can cause problems of dimensional tolerances structures. Thus, a better understanding and mastery of

residual stress would prevent the use of higher safety factors and therefore better optimize the size and life of welded structures.

From these statements, the study of welding processes currently appears as an area of research that is both open and complex, as it requires a combination of knowledge from different disciplines: the study of thermal in heat transfer, physics, metallurgy and mechanics.

In this context, the development of numerical method to simulate both the welding and mechanical consequences have become an indispensable tool for the prediction of residual stresses and strains of a welded structure because they reduce the cost of investment and time-related experiences.

Thus, through this research, we are interested in the simulation of residual stresses by taking into account the characteristics of the method used, the laser power, material properties, in particular metallurgical and mechanical aspects.

To achieve our goal, the PhD thesis presents the work are described in seven chapters. The first two chapters are state of the art.

The *first chapter* introduces the laser welding process and its mechanical consequences. We review in this section the mechanisms that interact during welding and the consequences of this process on the welded materials, the genesis of residual stresses and deformations.

The *second chapter* presents the different numerical models developed and used in the literature of fusion welding. We present the various models used as thermal, metallurgical and mechanical models.

The *third chapter* presents the experimental study of the assembly by laser Nd:YAG. We present the influence of the laser process parameters on certain properties of the weld such as the microstructure, the micro-hardness, the tensile shear strength, the geometric properties of the melt in particular the cross section. These characterizations were carried out not only to optimize the parameters of the laser process, but also to set some parameters developed in this thesis as the size of the heat source of numerical models, energy efficiency,

microstructure and micro-hardness transformation example. At the end of this chapter, we discuss the different metallurgical and mechanical tests performed on different welding conditions obtained by the optimized parameters of the welding process. A comparative study of the results obtained as well as the base metal in the weld has identified the microstructural changes and the mechanical effects due to the laser welding in the studied case of steel DP600.

The *fourth chapter* is devoted to the construction of a three-dimensional, transient and non-linear model that allows simulating the thermal history during welding. The numerical analysis, developed a code of finite element of ABAQUS, based on the modeling of heat transfer phenomena during welding. In this case, the applied load is a source of heat density associated with boundary conditions. The results of thermal analysis are presented in the spatio-temporal evolution form of the temperature in different parts of the welded plates. A comparison of numerical and experimental results will assess the relevance of the thermal model developed. The second step involves the simulation of the evolution of the mechanical state of the assembled model by introducing the results of the thermal model as a load. At the end of this chapter, we present an analysis to predict the residual stress distribution under the influence of numerical parameters and thermo-physical parameters.

The *fifth chapter* describes the thermo-metallurgical simulation integrated in our model. The metallurgical transformations associated with the phase change and the analysis of the hardness of the weld joint. The thermo-metallurgical model was made by coupling the thermal model *(described above)* and by carrying out a metallurgical numerical model. In the latter case, the numerical study is based on the integration of models Waeckel and Koistinen-Marburger. Waeckel model allowed us to simulate and to take into account the phenomenon of austenitization during the heating phase. Koistinen-Marburger model takes into account volume fractions generated during cooling and thus to take into account the phenomenon of phase transformation during welding. We also implemented a model that allows us to obtain the values of micro-hardness based on a law of linear combination of the hardness of each phase. Mechanical properties such as yield strength and maximum tensile strength was also

obtained by the introduction of a model to convert from the value of micro-hardness obtained above.

The *sixth chapter* includes all types: thermal, metallurgical and mechanical. The results obtained in the previous section have been implemented in two mechanical models: the classical mechanical model and the mechanical model taking into account the transformations induced volume strain. This effect has been built through the coefficient of thermal expansion of ferritic and martensitic phases obtained from the thermo-metallurgical model. This will allow us to discuss and compare the evolution of residual stresses from the classical elastoplastic model and elastoplastic model taking into account the thermo-metallurgical deformation .

The final chapter, *seventh chapter*, consists of an validation of the optimization parameters that had been studied in the previous chapters by approaching the simulation results to that of experiment such as the approaching of temperature, the cross section dimension, the out of plane displacement and the residual stresses. The general conclusion is also given at the end of this chapter. The reader can also find the suggestion or recommendation to improve the numerical simulation in future work at the end of this dissertation.
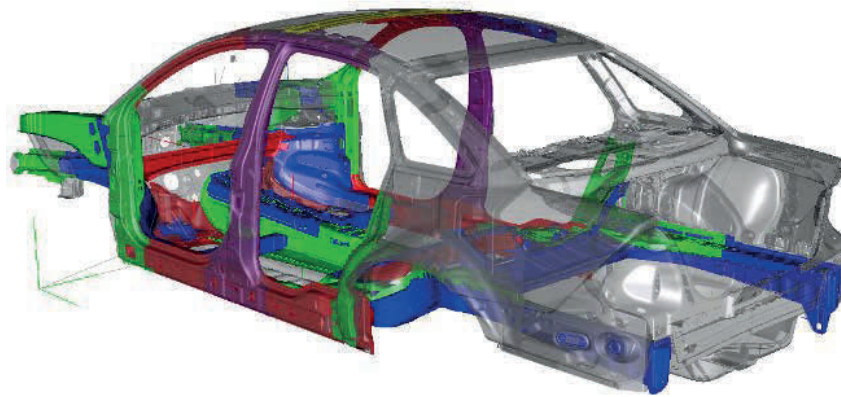
Green: HSLA 250

Blue: HSLA 350

Yellow: HSLA 550

Red: DP 600

Purple: Inner: Top DP600 / Bottom HSLA 250

Outer: Top DP600 / Bottom Mild Steel

Fig.1. 1   Body structure of Ford 500 [1]

12

Contents

Figures

14

<div align="right">

Chapter **1**

</div>

Laser welding processes

1.1. INTRODUCTION TO LASER WELDING

The use of lasers in materials processing has become widespread in recent years, so that an understanding of the nature of heat and mass transfer in this branch of modern technology is of increasing importance [4]. The laser welding is used for many different standard processes, such as resistance (spot or seam), submerged arc, RF induction, high-frequency resistance, ultrasonic, electron beam and others processes include cutting, drilling, scribing, sealing. The lasers generate light energy that can be absorbed into materials and converted to heat energy. By employing a light beam in the visible or infrared portion of the electromagnetic spectrum, we can transmit this energy from its source to the material using delivery optics which can focus and direct the energy to a very small, precise point.

Generally, there are two types of lasers that are being used for welding operation: CO_2 and Nd:YAG. Both CO_2 and Nd:YAG lasers operate in the infrared region of the electromagnetic radiation spectrum, invisible to the human eye [14].

- The Nd:YAG provides its primary light output at a 1.06 microns wavelength. This wavelength is absorbed quite well by conductive materials, with a typical reflectance of about 20 to 30 percent for most metals. The near-infrared radiation permits the use of standard optics to achieve focused spot sizes as small as 0.001inch in diameter.

- On the other hand, the CO_2 laser with 10.6 micron wavelength has an initial reflectance of about 80 percent to 90 percent for most metals.

In this research program we are interested in laser welding precisely the Nd:YAG laser in continuous mode to join the sheet metal.

1.2. LASER Nd:YAG

The solid state lasers, Nd:YAG, composes of Yttrium-Aluminum Garnet ($Y_3Al_5O_{12}$) doped with trivalent Neodymium ions 10^{20}($Nd3^+$) that is a crystalline in nature. The first demonstration was carried out by Geusic et al [21] in Bell laboratory in1964.

The laser beam wavelengths are 940nm, 1064nm, 1120nm and 1320nm. Its short wavelength can transfer high power with good coupling of the weld metal and laser beam and does not cause the formation of plasma when the density is greater than $10^{12}W/m^2$. The principle of laser welding presents in Fig.1.2.
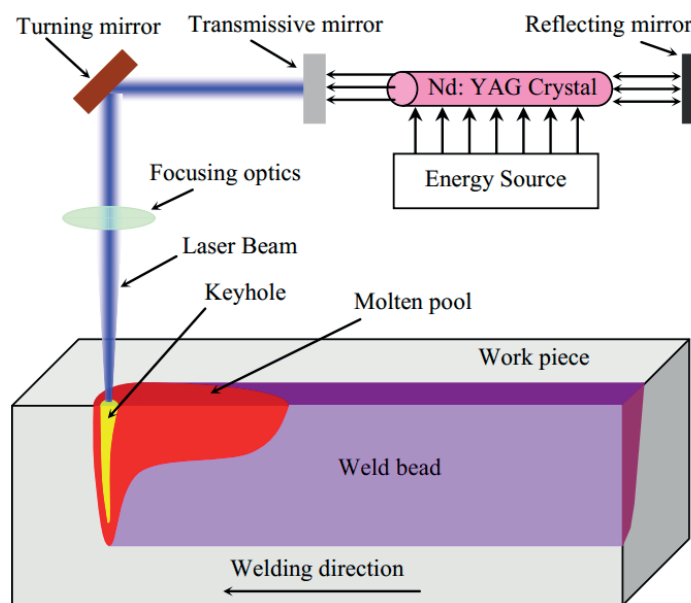
Fig.1. 2   Principle of laser Nd:YAG welding [20]

1.3. WELDING PARAMETER

The main parameters to be considered in laser welding are, laser spot diameter, laser velocity, laser power and focal point position. Its effects on the welding operation are describing here. Other effects from preparation and environment of welding such as plasma

formation, role of shielding gas, clamping force and preheating are also discussing in this chapter.

1.3.1. Laser power

For a defined diameter of the laser beam the penetration depth is increasing linearly with the power density. This density depends on the power of the laser beam transmits from laser generator to the welded joint. So it depends on the efficiency of laser.

The efficiency of the laser welding beam is the proportion of energy received by the metal which is radically affected by the absorbency of the material called absorption coefficient. Addition of active gas, 0_2 for example, to the shielding gas can increase the absorptivity. The range of energies absorbed by a material is also a function of decreasing the wavelength, for the steels of the absorptivity of the laser beam radiation Nd:YAG laser is about 3 times more than that of CO_2 laser process.

The efficiency of Nd:YAG Laser Beam spot welding is in considered in range of 38%-67% [6].

1.3.2. Focal characteristic

According to Laser Institute of America, the focus is characterized by the minimum diameter of the focal point *(d_{min})* and the focal depth *(Z)*, normally the diameter of the focal spot is larger due to the imperfection lens and it describe in equation 1.1 [8] and shown in Fig.1.3.

$$d_{min}=1{,}27.f.\frac{\lambda}{D} \tag{1.1}$$

The focus depth *(Z)* is the distance in which the radius of the focal point is increasing by 5%. It can express by the equation 1.2, where F is the number of focusing optics, equation 1.3.

$$Z=1{,}488.F^2.\lambda \tag{1.2}$$

$$\text{with } F=f.\lambda \tag{1.3}$$

f: focal length

λ: wavelength

D: beam diameter in front of optical lens

The focus position has a great influence on the quality of the joint. If it is above the surface of the metal, the form of weld seam appears as is the nail head and little deep. Instead the V shape appears when it is below the metal but it needs more precise adjustment. The optimum position is below the sheet surface and the distance is dependent on the thickness of the sheet to be assembled [8].
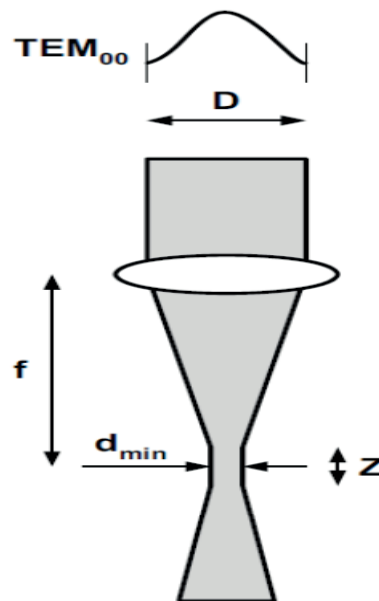

Fig.1. 3   Characteristic parameter of focal system [8]

1.3.3. Welding speed

The increase of the welding speed is the cause of linear decrease of the penetration depth and the width of the weld pool. However when the speed drops suddenly, we see a small increase of the depth but the width of the FZ increase importantly. The depth and the width of the Fusion Zone *(FZ)* depend on the laser power [13]. Because the power input per unit length decreases, the high speed is the main cause of less melt. On the contrary during welding with slower speed causes an excessive melt, thus vaporizing and plasma formation.

1.3.4. Welding mode

In welding operation two modes are used base on the power density, keyhole mode and conductive mode as indicated in Fig.1.4.

- Keyhole mode

By heating the spot of laser focus above the boiling point, a vaporized hole is formed in the metal. This is filled with ionized metallic gas and becomes an effective absorber, trapping about 95% of the laser energy into a cylindrical volume, known as a keyhole. Temperatures within this keyhole can reach as high as 25.000°C, making the keyholing technique very efficient [5]. With this technique, a higher power lasers, more than 10^{12} W/m², can make deeper penetration [24]. The keyhole can reach 50mm depth inside the metal.

- Conductive mode

The mode of heat by conduction, which results in 90% loss of energy by reflection, causes a wide melt shallow and unable to evaporate the metal. This mode is used in the case of small components in the medical field and the surface treatment.
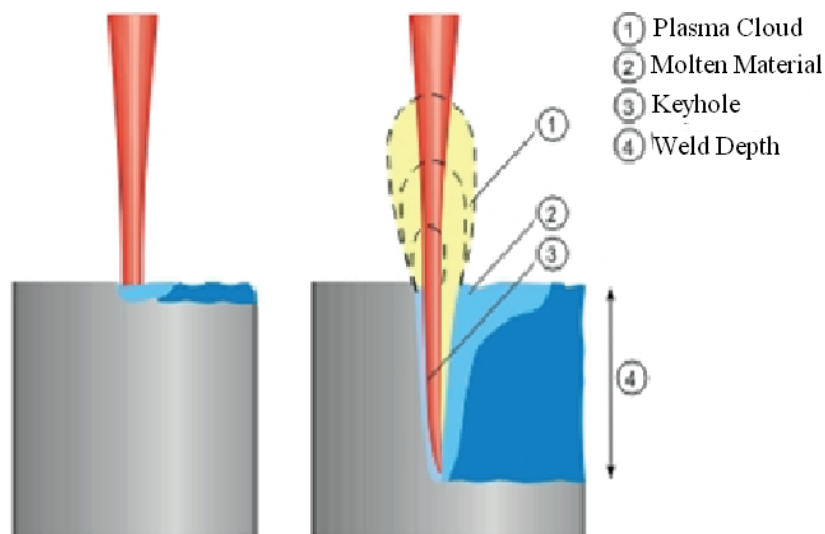

Fig.1. 4   Laser welding mode

1.3.5. Plasma formation

Plasma is presented in form of cloud around the laser beam as indicated in Fig.1.4. It appears when the power density is greater than 10^{12} Wm^{-2}. In the weld Nd:YAG laser. The laser beam assists with metal vapor and the inert gas creates a cloud of plasma above the welded surface. At the beginning of the formation of keyhole plasma attends the energy transfer to the metal. But later, the plasma can limit or reduce heat transfer to the metal [9].

In general the plasma can be removed from the area adjacent to the laser beam by injecting of shielding gas, helium or argon, to 1mm in front the laser beam in inclined position about 20 degrees with the surface of the sheet [15].

1.3.6. Shielding gas

The formation of Zn in the case of galvanized steel, presents in the welded joint may be reduced by the combination of the position of the shielding gas and inclined and coaxial mode. The hardness of the weld metal varies depending on the nature of the protective gas, for example N_2 gas seal gives hardness harder than that of argon, and more, N_2 is the cause of porosity and nitride in the welding [13].

The number of pores is reduced if and only if the laser power decreases. But increasing laser power is to increase the penetration of the laser beam and the size of the melt [13]. Increasing the welding speed reduces the penetration depth for any protective gases argon or helium because the power input per unit length decreases, the high speed is the main cause of less melt [13]. So the shielding gas has no influence on the fusion zone dimension.

1.3.7. Clamping force

The clamping of sheet metal during the welding increases the amplitude of the residual stresses but some will relax after relaxing the mounting force. The clamping system cannot completely eliminate residual stresses. To eliminate the residual stresses, the weld area would have to be deformed more, can be achieved by superimposing a supplement tensile [18].

By experiment method, in case of butt weld, the clamping force preset certainly influences the strength of the weld and it is a force that would enhance optimal rupture load of welding joint. The measurement of the optimum clamping force during the welding Nd:YAG laser shows that the force is varied during operation due to local extension of material at seam weld. The ultimate clamping force drops down to zero at the end of welding operations regardless of initial preset clamping forces. He also found that there is a linear relationship between the maximum clamping force induced during welding and the initial preset clamping force exists, which can be used in the design of a clamping system.

The temperature measurement indicated that the maximum welding temperature remains constant with the variation of clamping force [10].

The coefficient of friction influent the final welding distortion is less than 3%. Schenk [18] simulates the application of clamping force depending on the position welding mode with the lap joint clamping force until the end of the cooling phase reduces distortion up to 60%. It seems that the buckling occurs only in the lower plate and not on the top plate which corresponds to the curve of reduced compressive stress on the top plate. Relax de clamping force at the end of the heating step gives more residual stresses in compression.

1.3.8. Preheating

The preheating of base metal before welding depends on the welding process and also the chemical composition of base metal. Preheating affects the properties of welded joint such as deformation and residual stresses. The distortion is reduced from 15% to 30% depending on the condition of the clamp with preheating up to 200°C. This is the result of two effects:

- The temperature gradient in the material is reduced, which allows having more homogeneous contraction part in the longitudinal direction during the cooling and thus less of residual longitudinal stresses.

- Preheating also reduces the cooling rate and, consequently, the martensite fraction is reduced and the fraction of bainite is increased. Since the volume of bainite is greater than the volume of martensite, it also reduces the tensile stresses and thus results in a less magnitude of buckling.

The stresses are reduced by a long period of clamping *(500 seconds after welding cycle)*, preheating and transient clamping *(the clamps become active as soon as the welding torch reaches its position)* respectively [18].

1.4. SHEET METAL ASSEMBLY

Assembly of thin galvanized steel by laser welding is often in transparent or lap mode. The depth of the melt in the second metal is about 50% of its thickness. The process is the same as that of ordinary steel. An excellence gap of 0.1 to 0.2mm is recommended by experimental methods of World Auto Steel for lap joint of advance high strength steel

(AHSS) galvanized in low weight automotive research program [23] where Zinc is the main cause of porosity inside the FZ without using gap between the two plates [22].

The study on resistance welding (resistance spot weld) steel DP 420/800 differential mode galvanizing Hot-Dipped Galvanealed (HDGA) or Hot Dipped Galvanize (HDGI) shows that the mechanical properties (tensile shear, hardness, transverse section) of these joints are identical [19]. So the galvanized technique has no influence on the resistance of the welded joint. Another research done by Lu [11] showed that the dual laser is able to weld galvanized steel without gap in lap joint by two laser head. The first laser used to heat and to evaporate the zinc layer and the second laser used to weld. The dual laser beam is combined with 2 heads focused.

1.5. RESIDUAL STRESSES AND DEFORMATIONS

1.5.1. Residual stresses

The magnitude of residual stresses presents after welding is important in the prediction of the resistance to fracture. In this case the transverse or hoop stresses are of particular interest because they will influence the growth of axial flaws or axial default [7].

During the thermal welding process the weld region is heated up and fused locally. The material expands as a result of being heated. The thermal expansion is restrained by the colder surrounding region, thus leading to thermal stresses. The thermal stress partly exceeds the yield limit which is lowered at elevated temperatures. Consequently, the weld region is upset plastically and, after cooling-down. It thus displays tensile residual stresses while the surrounding region exhibits compressive residual stresses [17]. Existing residual stresses can be reduced at high temperature by the reduction of yield limit and elastic modulus as well as by stress relaxation.

Fig.1.5 shows the residual stress distribution expected for a butt-welded mild steel plate. The longitudinal stresses are tensile at the weld seam and in compression in the base material. The transverse stresses are tensile at the weld seam and decline towards the edges of the plate. At the beginning and the end of the weld, the transverse stresses are in compression.
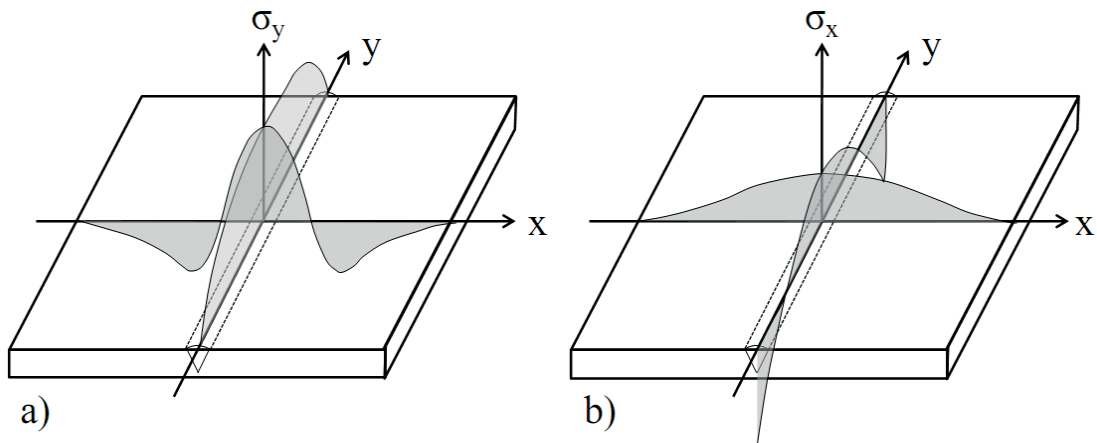
Fig.1. 5   Longitudinal (a) and transversal (b) residual stresses in but-welded [3].

The higher amplitude of welding residual stress fields are the longitudinal and transversal residual stresses [17]:

Weld-longitudinal residual stresses result from longitudinal contraction of the cooling weld in accordance with the "too short weld length" mechanism. The tensile stresses are limited to the weld region, their maximum value being at or above the uniaxial yield limit. Lower compressive stresses exist in the surrounding region, dropping off rapidly the more distant they are from the weld as shown in Fig.1.5 (a).

Weld-transverse residual stresses in the plane of the plate are generated as a result of the transverse contraction of the cooling weld in accordance with the " too narrow weld width" mechanism, especially in the case of rigidly restrained plate edges. They are not restricted to a narrow region close to the weld but also comprise the more distant surrounding region as shown in Fig.1.5 (b). They are supported in a similar way as external loads and provided that the support has sufficient elasticity, remain below the yield limit.
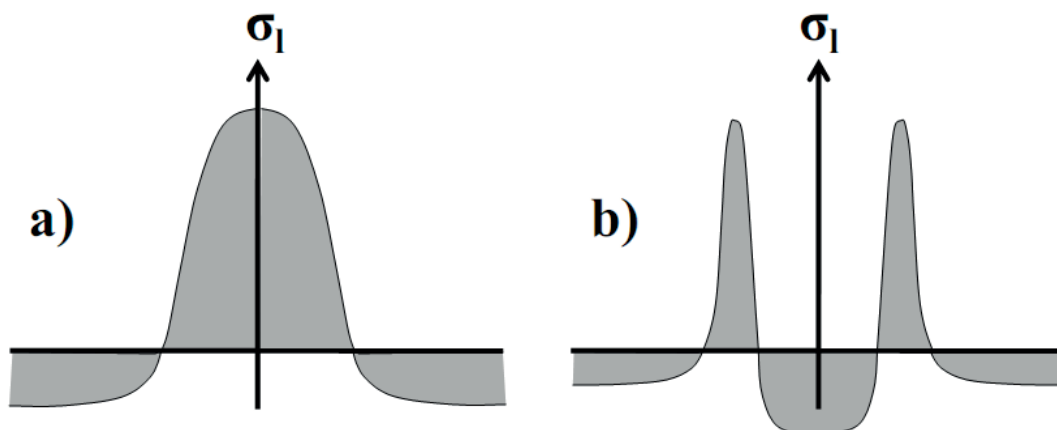

Fig.1. 6   Longitudinal residual stresses for mild steel (a) and for high-alloy steel with martensite filler material (b) [16]

23

The metallurgical transformations inside the HAZ and FZ also affect on the residual stress. Under influence of martensite in the weld seam, the gradual thermal contraction changes to a quick volumetric phase expansion which turns the tensile stresses into compression. In the HAZ, the material cools downs slower and exhibits no phase transformation to martensite and hence, tensile stresses are still present, Fig.1.6 (b) and there is a tensile longitudinal stresses inside the HAZ and the FZ of the mild steel as presented in Fig.1.6 (a). Martensite formation is less influent on the residual stresses for low carbon steel (0.05% -0.15%) but a significant effect for mild steel (0.16% -0.29% C) so the phase change can be neglected for low carbon steel [2].
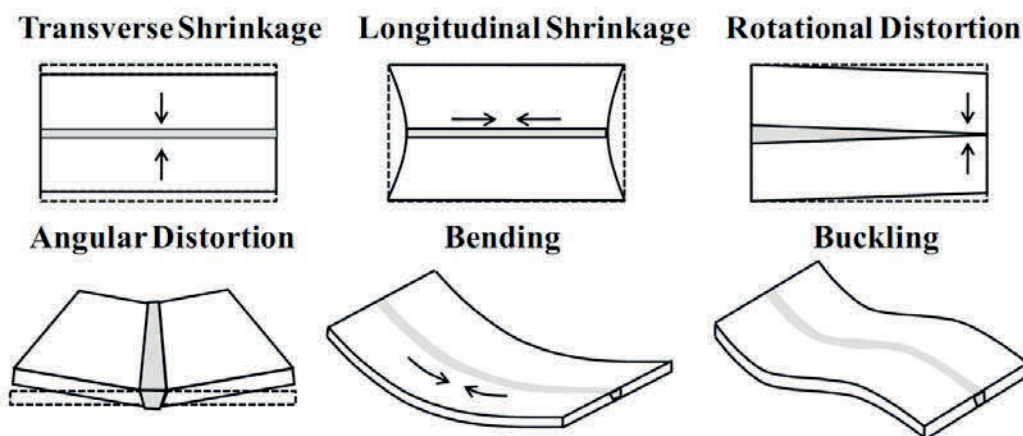
1.5.2. Deformation

Fig.1. 7   Types of welding distortions [12]

Together with the welding residual stresses there also occur welding deformations such as displacements and rotation. The statement frequently encountered that distortion is the result of residual stresses is not generally true. Residual stresses and distortion are largely opposed. High stresses occur where the deformation is restrained, low stresses where the deformation is unrestrained [17]. All these kinds of distortions, Fig.1.7, are related to the shrinkage of the weld metal during cooling. They can be subdivided into [12]:

- Transverse shrinkage: shrinkage perpendicular to the weld seam
- Longitudinal shrinkage: shrinkage in direction of the weld seam

- Angular distortion: transverse uplift caused by a non-uniform temperature distribution in the through-thickness direction. For instance in case of butt-joints with a V-groove.

- Rotational distortion: in-plane angular distortion due to the localized thermal expansion and contractions. Very relevant for overlap joints, for instance.

- Bending distortion: longitudinal uplift. The same causes as angular distortion.

- Buckling distortion: caused by compressive stresses inducing instabilities in the plates.

1.6. CONCLUSION

The laser Nd:YAG welding process has been described include some others mechanisms that interact during this process such as the physical properties of material, the shielding gas, the clamping conditions and also the proper property of welding process which affect on the final results of the joining material . So the understanding of laser process and its preparation in an important part in this research without the basic knowledge of laser welding the selection of numerical method is unreachable. The numerical model of welding simulation such as the thermal model, the metallurgical model, the mechanical model and the influence of numerical models and the physical properties of material on the numerical analysis will be discuss on the second chapter.

REFERENCE

[1] Dave Anderson. Application and repairability of ahss. Technical report, 2008.

[2] Dean Deng. Fem prediction of welding residual stress and distortion in carbon steel considering phase transformation effects. *Materials & Design*, 30(2):359 – 366, 2009.

[3] U. Dilthey. *Schweisstechnische Fertigungsverfahren, Bd. 2 – Verhalten der Werkstoffe beim Schweißen*. VDI-Verlag, ISBN: 3184013995, 1995.

[4] John Dowden. *The theory of Laser Materials Processing*. Sringer, 2008.

[5] R. F. Duhamel and C. M. Banas. Laser welding of steel and nickel alloys. *Lasers in Material Processing, American Society of Metals*, 1983.

[6] P. W. Fuerschbach and G. R. Eisler. Effect of laser spot weldenergy and duration on melting and absorption. *Science and Technology of Welding and Joining*, 7:241–246, 2002.

[7] John A. Goldak. *Computational Welding Mechanics*. Springer, 2005.

[8] Altino Loureiro J. Norberto Pires and Gunnar Bölmsjo. *Welding Robots: Technology, System Issues and Applications*. Springer, 2006.

[9] Mizutani M. Matsunawa A. Katayama S., Seto N. Interaction between plasma and laser beam, and its effect on keyhole dynamics in high power c02 laser welding. Technical report, IIW Docs IV-765-00, SG-212-976-00, 2000.

[10] Quan Sheng Liu, S.M. Mahdavian, Davy Aswin, and Songlin Ding. Experimental study of temperature and clamping force during nd:yag laser butt welding. *Optics & Laser Technology*, 41(6):794 – 799, 2009.

[11] F. Lu and M. Forrester. Proceeding of 23rd international congress on application of laser and electro optics. 2002.

[12] K. Masubuchi. *Analysis of Welded Structures*. Pergamon Press Ltd, ISBN: 0080227147, 1980.

[13] Lifang Mei, Genyu Chen, Xiangzhong Jin, Yi Zhang, and Qiang Wu. Research on laser welding of high-strength galvanized automobile steel sheets. *Optics and Lasers in Engineering*, 47(11):1117 – 1124, 2009.

[14] Carl B. Miller. Laser welding article. Technical report, U.S. Laser Corporation, 10/26/2011.

[15] J Norrish. Advanced welding processes. *Institute of Physics Publishing*, 1992.

[16] Artem Pilipenko. *Computer Simulation of Residual Stress and Distortion of Thick Plates in Multielectrode Submerged Arc Welding: Their Mitigation Techniques.* PhD thesis, Norwegian University of Science and Technology, Faculty of Engineering Science and Technology, 2001.

[17] Dieter Radaj. *Welding residual stresses and distorsion : calculation and measurement*, volume 2. DVS, 2003.

[18] Tobias Schenk. *Modeling welding Distortion Influence of Clamping and Sequencing.* PhD thesis, Material Innovation Institute, www.m2i.nl, 2011.

[19] M. Tumuluru. The effect of coating on the resistance spot welding behavior of 780 mpa dual phase steel. *Welding Journal*, 86, June 2007.

[20] Muhammad Zain ul abdein. *Experimental investigation and numerical simulation of laser beam welding induced residual stresses and distortion in AA6056-T4 Sheets for Aeronautic application.* PhD thesis, 2009.

[21] Wikipedia. Nd:yag laser. Technical report, Online Encyclopedia, http://en.wikipedia.org/wiki/Nd:YAG_laser, 22 September at 14:19. 2012.

[22] WordAutoSteel. Ahss weld performance study fot autobody structural component. Technical report.

[23] WordAutoSteel. Advance high strength steel : Application guidelines. Technical report, June 2009.

[24] Michael Yessik and Duane J. Schmatz. Laser processing and ford metal progress. May 1975.

28

Résumé

Chapitre 2: Méthodes numériques pour la simulation du soudage laser

Ce chapitre décrit l'état de l'art sur les différents modèles numériques développés et utilisés pour simuler et analyser les procédés de soudage. Les modèles numériques utilisés sont regroupés généralement sous la forme de trois modèles:

- Le modèle thermique

Ce modèle permet de décrire et de choisir la nature de la source de chaleur en adéquation avec le procédé de soudage utilisé. Dans notre cas, nous nous sommes focalisés sur les sources appropriées pour le procédé de soudage laser. Il permet d'intégrer l'équation de transfert de chaleur pour résoudre le problème thermique.

- Le modèle métallurgique

Il décrit les transformations de phase permettant le passage de l'état solide-liquide puis liquide-solide pendant le chauffage et le refroidissement du métal. Les modèles étudiés et utilisés sont le modèle de John Mehl Avrami (JMA), le model Inoue, le modèle INPL, le modèle Leblond et enfin le modèle Waeckel.

- Le modèle mécanique

Ce modèle décrit le comportement élastoplastique généré par le soudage laser.

D'un point de vue analyse numérique, nous avons traité dans ce chapitre également sous forme de discussion l'influence des paramètres du modèle numérique sur la robustesse des résultats finaux.

Abstract

Chapter 2: Numerical methods for welding simulation

This chapter consists of the state of art of numerical model used in the analysis of welding process. The numerical models constitute of three models:

- *Thermal model*

    It describes the thermal model appropriate to the welding process such as the model of heat source. In this case we are focused on the appropriate model for laser welding and the equation of heat transfer to solve the thermal problem.

- *Metallurgical model*

    It describes the solid-solid state phase transformation under heating and cooling of the metal. Those models include the John Mehl Avrami *(JMA)* model, Inoue model, INPL model, Leblond model and finally Waeckel model.

- *Mechanical model*

    It describes the elastoplastic model applied for numerical analysis of laser welding

At the end, we have discussed in this chapter the influence parameters of the numerical model on the robustness of the final results.

Contents

Figures

Chapter **2**

Numerical methods for welding simulation

2.1. INTRODUCTION TO NUMERICAL METHODS FOR WELDING SIMULATION

The strategy for analyzing welds and numerical methods such as finite difference analysis and finite element analysis begin in the 1960s [25] with a pioneering work of Habbit [26] and Marcal [37], Friedman [24], Westby [3], Masubuchi [30] and Andersson [5]. The use of finite difference methods is more a transition between analysis and finite element methods. The main advantage of the finite difference method is that is rather simple and easily understandable physically [9, 39]. But finite element analysis *(FEA)* methods, where the structure is represented as an assembly of finite elements, gained a wide acceptance only over the last decades because of it is capable of solving the nonlinear problem, the complex geometry and practicable in many analysis software ABAQUS, ANSYS, CASTEM, Code-Aster, SYSWELD.

To solve the welding problem by the numerical methods, the welding phenomena have to be representable by mathematical formula. There're mathematical model for thermal model, mechanical model and metallurgical model, which will be shown in the subsequent chapters. Goldak [25] considered that the mechanical behavior of welds is sensitive to the close coupling between heat transfer, microstructure evolution and thermal stress analysis. Fig.2. 1 describes the coupling between the different fields in the modeling of welding. *The dominant couplings in welding are shown with bold lines, the secondary couplings are shown with dotted lines.*
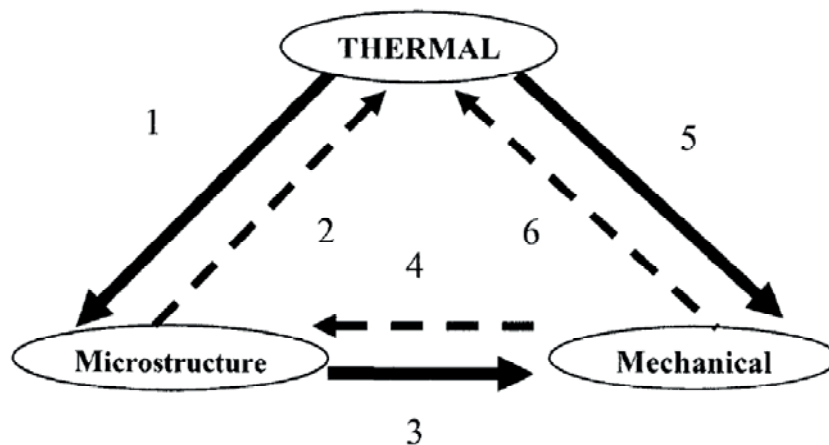
Fig.2. 1 Coupling between different fields in welding analysis [25]

Coupling Explanation of physical phenomena in welding [25]

1- Transformation Rates: The microstructure evolution depends on variation of temperature during heating and cooling cycle.

2- Latent heats: (each phase transformation can have an associated latent heat). They act as a heat sink on heating and as a heat source on cooling.

3- Phase Transformations: The volume changes and transformation induced plasticity due to phase changes affect the plastic and elastic material behavior.

4- Transformation Rates: The microstructure evolution, martensitic and bainitic transformations depend on mechanical deformation.

5- Thermal Expansion: The mechanical deformations depend on temperature variation.

6- Plastic Work: The mechanical deformation generates heat in the material and changes the thermal boundary conditions. In most welding processes this effect is very small.

Thermal model, the metallurgical model and the mechanical model will described as follows in this chapter.

2.2. THERMAL MODELS

For thermal simulation Goldak classifies the heat source model into five generations by increasing order of difficulty and accuracy [25].

1st Generation

The shape of the heat source is represented by point, line and plane which are developed by Rosenthal [16] and Rykalin [43]. It is more useful for shadow weld pools on thick plates, for full penetration laser beam or electron beam welding on the sheets. But those models ignore the distribution of energy in the real weld heat source. So the weld pool is not an essential part of these models.

2nd Generation

It is the first distribution of heat flux model developed by Pavelic [38], Rykalin [43] and finally by Goldak and Radaj [15, 14]. The most recognized model is Goldak boundary conditions are:

- Distributed heat source models such as double ellipsoid model and conical model will presented in section 2.2.3.1 and section 2.2.3.2.

- Prescribed temperature heat source models. These models treat the weld heat source as a sub-domain in which the temperature or specific enthalpy in known as a function of space and time (x,y,z,t). Even if it does not know the physical parameters of melt, in these models, but still gives a good accuracy of temperature distribution outside the melt.

The shape of the heat source most commonly use are double ellipsoidal, cylindrical, conical, linear combination of ellipsoidal, conical or other must be used according to the form observed by experiment.

3th Generation:

The third generation model was initiated by Ohji et al [36] then Sudnik [52] and Weiss [57]. Which predicted the liquid weld pool shape. This method is more accurate than the second generation by solving Stefan problem (Liquid-solid free boundary). However it requires a lot of computation time and ignores the Lorenz forces (it is a force caused by the electromagnetic field on a material point).

While the data required by the first and second generation models was the distribution of power density, flux or temperature, the data required by these third generation models usually include a pressure distribution from the arc, a mass flow rate into the weld pool and surface tension on liquid surface of the weld pool. Now the geometry of the weld pool is not input data but output data.

4th Generation:

In this model the fluid dynamic equation has been added to the equation of the weld heat source. Equation of fluid dynamics, Navier-strokes, with influence of Buoyancy and Lorentz force acting on the interior of the liquid phase are include in the model.

5th Generation:

The magneto-hydrodynamics equation is added to the previous equation in 4th generation, but much more difficult than the 4th generation.

For Goldak, [25], the 4th and 5th generations are not yet applicable in predicting the melt due to its high difficulty of the equation and instability in some welding parameter variations and capacity calculation does not allowed.

2.2.1. Heat transfer

Equation of heat transfer in a solid phase occupying by domain Ω is governed by the following expression:

$$\rho \frac{dH}{dt} - div(\lambda \, grad T) - Q = 0 \tag{2.1}$$

The enthalpy H can be express as a function of temperature:

$$H(T) = \int_{T_0}^{T} \rho C_p(u). \, du \tag{2.2}$$

So the expression 2.1 can write as:

$$\rho. C_p \frac{dT}{dt} - div(\lambda \, grad T) - Q = 0 \tag{2.3}$$

with ρ density (Kg.m^3)

H   enthalpy (J.kg^{-1}.C^{-1})

C_p specific heat capacity (J. kg^{-1}.$^{\circ}$C^{-1})

T   temperature (C)

λ thermal conductivity (W.m^{-1}.C^{-1})
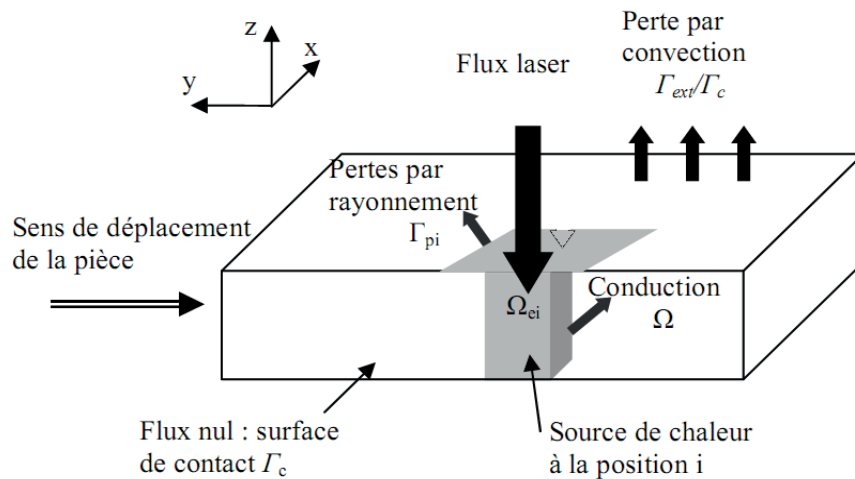
Q   heat source density (W.m^{-3})

Fig.2. 2 Energy balance during laser welding Nd: YAG [11]

The heat source generator *(Q)* heats the metal to fusion by conduction during welding process and formed a melting pool as expressed in equation 2.1. The heat transfer forming around the melting pool loss to the surrounding environment by convection, radiation as express in the expression 2.4 and 2.5. Another important of heat loss is the heat transfer between the melting pools to the base metal by conduction mode.

Natural convection with the outer surface is:

$$\lambda(T)gradT(x_i,t)_{surface} + h(T(x_i,t) - T_0) = 0 \quad on\ \Gamma_{ext}/\Gamma_c \tag{2.4}$$

Radiation around the laser beam is:

$$\lambda(T)gradT(x_i,t)_{surface} + \varepsilon\sigma[((T(x_i,t) - T_{abs})^4 - (T_0 - T_{abs})^4] = 0\ on\ \Gamma_{p,i} \tag{2.5}$$

With the boundary condition adiabatic surface (in case of modeling the symmetric surface of the weld model) given by:

$$\lambda(T)grad T(x_i,t) = 0 \quad on \; \Gamma_c \tag{2.6}$$

The equation 2.6 is used in condition of simulation of ½ symmetric models as presented in Fig.2. 2.

Another boundary condition caused by heat transfer between the work piece and the welded body by contact model [33] is:

$$\lambda(T)grad T(x_i,t)_{surface} + h_{cont}(T(x_i,t) - T_0) = 0 \tag{2.7}$$

The initial condition before welding, the model is considered to be equal to ambient temperature:

$$T(x_i,t) = T_0 \quad at \; t = 0 \; second \tag{2.8}$$

with: λ thermal conductivity (W.m^{-1}.C^{-1})

       h   convection coefficient in function of temperature (W.m^{-2}.C^{-1})

       T_0 temperature ambient (^{o}C)

       σ Stefan Boltzmann constant (WC^{-4}m^{-1})

       e   emissivity of the radiating surface

      T_{abs} absolute zero,

       T   temperature of work piece (^{o}C).

      h_{cont} coefficient of heat transfer by contact of two metals (W.m^{-2}.C^{-1}).

2.2.2. Time step

The transient thermal analyses determine temperatures and other thermal quantities that vary over time. It is corresponded to the case of welding in which the temperature varies on time and also on the welding speed.

Suppose that a heat source is moving at a constant speed, V, in X direction so the eulerian (moving) frame with an origin at center of heat source (ζ,y,z) transformed from the fixed frame (x,y,z) of the Lagrangian frame is given by :

$$\zeta = x\text{-}V.t \tag{2.9}$$

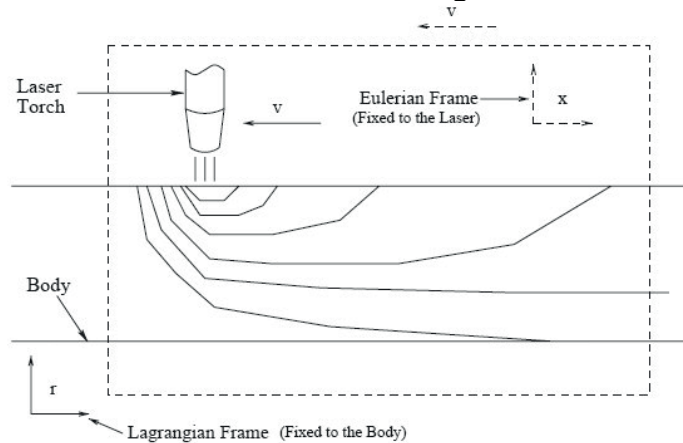where: t is time in second as showed in Fig.2. 3 bellow:

Fig.2. 3 Lagrangian and Eulerian Frame [34]

The temperature *T(x, y, z)* in Lagrangian frame will change to *T(x-V.t, y, z)* in Eulerian frame for resolving the moving heat source model in the case of welding phase as indicated in Fig.2. 3.

These relations allow us to set the relation of moving heat source in the welding step:

$$t = \frac{L}{V} \tag{2.10}$$

The time increment Δt can be defined as:

$$\Delta t = \frac{\Delta L}{V} \tag{2.11}$$

where: L   is element length or length of the model in welding direction (m).

ΔL is length of the mesh in welding direction (m).

V   is the welding speed (m/s).

2.2.3.   Heat source model

The thermal solution is a very important source for solving mechanical problems in welding. The shape of the heat source is very important for thermal model [33]. So the precision of thermal model is depended on the choice of heat source model. The selection of model is also based on the type of welding processes and welding mode.

In the simplest case, the heat source distribution is assumed to be constant over a circular area [36, 47] or over a defined volume applied in the thesis of AIT ALI [4]. More

realistic technique with regard to physics was the heat source distribution according to the Gauss normal distribution *(Bell curve)* that was introduced by Rykalin [35].

The radial normal distribution of the heat flow density over a circular base area is described by the exponential function below:

$$q_{ar}(r) = q_{ar}(0)e^{(-kr^2)} \tag{2.12}$$

The maximum value $q_{ar}(0)$ results from the effective heat power q of the heat source according to the relation :

$$q_{ar}(0) = \frac{k}{\pi}q \tag{2.13}$$

With the radial distance r and the concentration coefficient k, the concentrate coefficient *k* characterizes the width of the bell curve. It is in relationship to the inflection point σ of the bell curve by relation.

$$k = \frac{1}{2\sigma^2} \tag{2.14}$$

For $r \geq 3\sigma$, the bell curve exhibits very low values but reaches the zero value only at infinity. According to Rykalin [35], the heat flux on the edge of the volume or the surface ($r_{0.05}$) is 5% of the maximum flux in the center of this volume ($q(r_0)$) or surface as shown in Fig.2. 4 (b and c).

$$r_{0.05} = \sqrt{\frac{3}{k}} \tag{2.15}$$

Value which heat flux density *[$q_{ar} = 0.05\ q_{ar}(0)$]* where r is a radial distance from the heat source central.

The laser beam exhibits high intensity within a small diameter. The circular normal distribution is described by the focus radius $r_f = 2\sigma$ which includes 86.5% of the heat power [41] as shown in Fig.2. 4 (a).
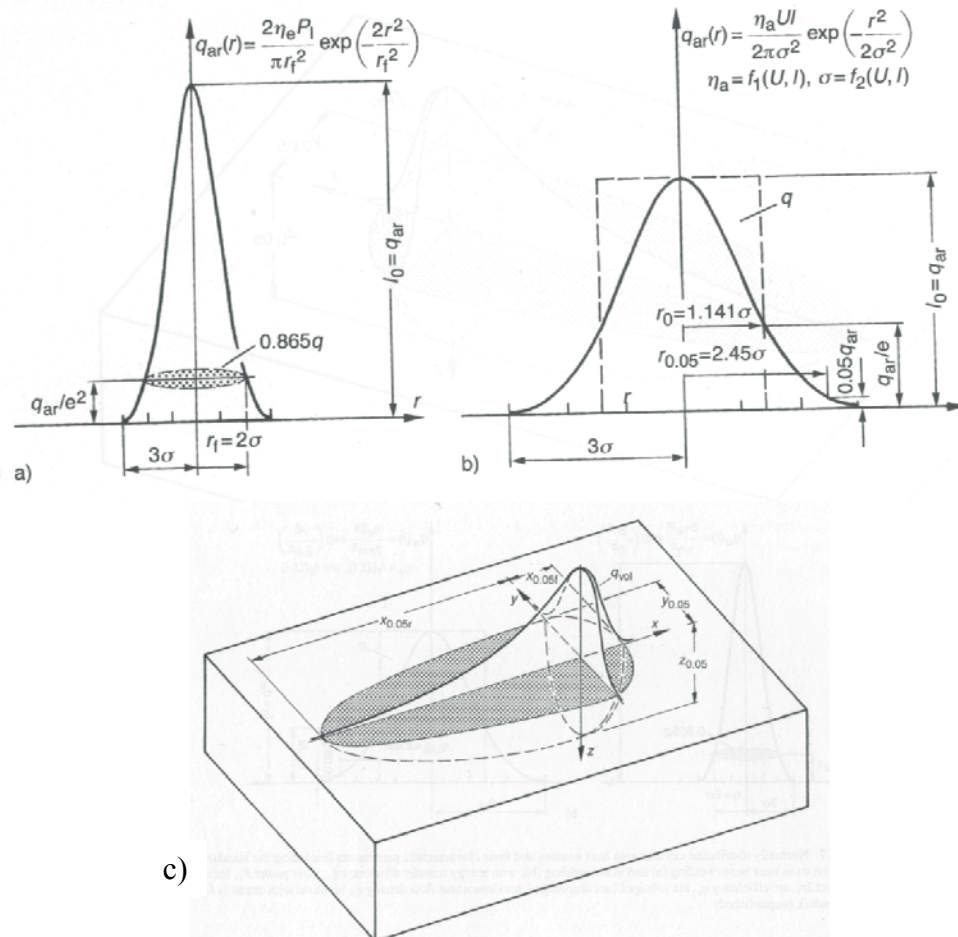

Fig.2. 4 Normally distributed heat source and their characteristic parameters in laser welding (a) and in arc welding (b) double ellipsoidal volume heat source (c) [41]

In this section, two heat sources models are presented: Double-ellipsoidal heat source model and conical heat source model by using Gaussian distribution of heat source over a volume.

2.2.3.1. *Double-ellipsoidal heat source model*

In double-ellipsoidal heat source model, the heat flux is distributed on front part and on rear part of the ellipse as indicated in Fig.2. 5.

- Front part of heat source (Y>0):

$$q(x, y, z, t) = \frac{6\sqrt{3}f_f Q}{ab_1 c\pi\sqrt{\pi}} \exp\left(-3\left(\frac{x}{a}\right)^2 - 3\left(\frac{y}{b_1}\right)^2 - 3\left(\frac{(z+v(\tau-t))}{c}\right)^2\right) \tag{2.16}$$

- Rear part of heat source (Y<0) :

$$q(x, y, z, t) = \frac{6\sqrt{3}f_r Q}{ab_2 c\pi\sqrt{\pi}} \exp\left(-3\left(\frac{x}{a}\right)^2 - 3\left(\frac{y}{b_2}\right)^2 - 3\left(\frac{(z+v(\tau-t))}{c}\right)^2\right) \tag{2.17}$$

With the fraction $f_f + f_r = 2$

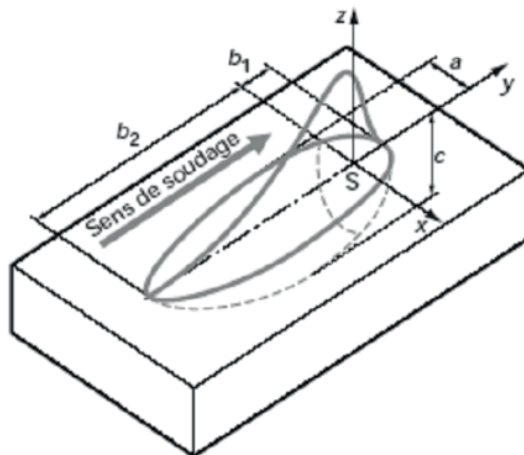q : rate of energy input (W).

Q : density of heat power (W/m^3)

Fig.2. 5   Form doubles ellipsoidal [25]

2.2.3.2. *Conical heat source model*

The conical heat source model, presented in Fig.2. **6**, has the advantage compared to the previous form (ellipsoid, disc...etc) for laser welding because of the deep of the FZ and concentrated heat source. So the heat intensity distribution can be written as follows [18]:

$$Q(r, z) = Q_c exp\left[-3\left(\frac{r^2}{r_c(z)^2}\right)\right] \tag{2.18}$$

which

$$Q(r,z) = \frac{9\eta P exp(3)}{\pi (exp(3)-1)} \cdot \frac{1}{(z_e - z_e)(r_e^2 + r_e r_i + r_i^2)} \cdot exp\left[-3r^2/r_c^2\right] \tag{2.19}$$

and

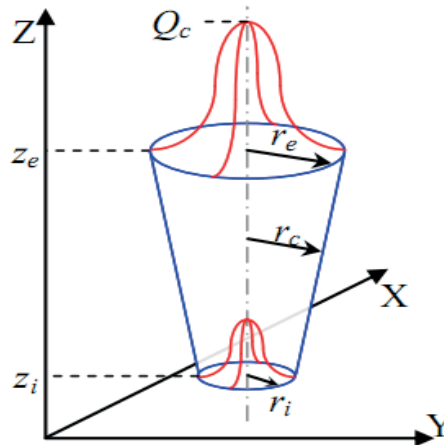$$r_c = r_i + \frac{(r_e - r_i)(z - z_i)}{z_e - z_i} \tag{2.20}$$

Fig.2. 6   Conical heat source [51]

2.3. METALLURGICAL MODELS

The metallurgical structure of welded joint consists of all aspects physical metallurgy [27]. Generally the welded joint composes of Fusion Zone (FZ), Heat Affected Zone (HAZ) and the parent metal or Base Metal (BM) where no influence of temperature on metal structure.

- The formation and solidification of FZ: The size of FZ is depended on the welding parameters such as speed, focal point, power and also the thermo-physical properties of welded metal. The solidification of FZ is also depended on the welding process that cause different cooling speed, different composition of inclusion and also the shielding gaz. Cochrane [42] indicated that the acid shielding gas promotes the growth of acicular structures and basic shielding gas promotes the growth of lamellar structures.

- The formation of HAZ: The HAZ is dependent on the welding process that causes different heating and cooling speed. The HAZ is located between the

BM and the FZ so different maximum heating temperature is appeared and causes a total austenitization, closed the FZ, and non-complete austenitization closed to the BM presented in Fig.2. 7.
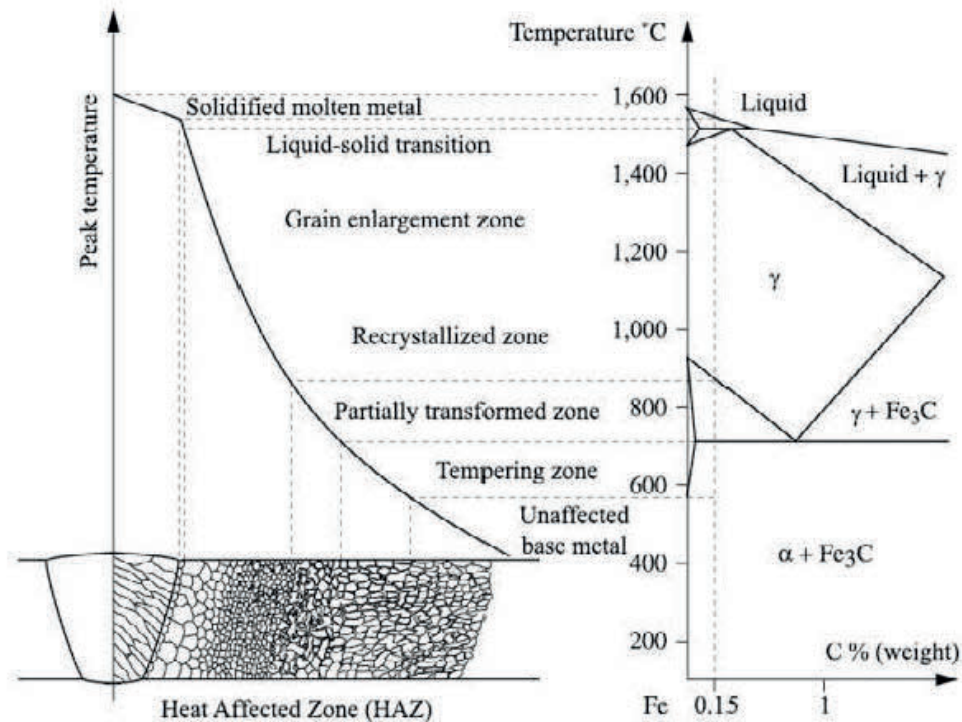

Fig.2. 7   Structure metallurgies of laser welded joint [20]

2.3.1.   Metallurgical structure of steel

The pure iron structure can exists in two solid-state phases, which are characterized by the spatial configuration of the atoms. The smallest repetitive building block which uniquely describes this atomic configuration is called a unit cell. The body centered cubic BCC constitutes of atoms at each corner of the cubic unit cell and one centered on the middle. The face centered cubic FCC configuration has atoms at the corner of each unit cell, but also centered in each of six faces of the cube as indicated in Fig.2. 8.

At room temperature, iron is stable as the ferrite phase, which has a BCC configuration. At Ac3 temperature, iron transforms into austenite phase and the atoms are reorganized into the FCC configuration. During cooling cycle the austenite phase

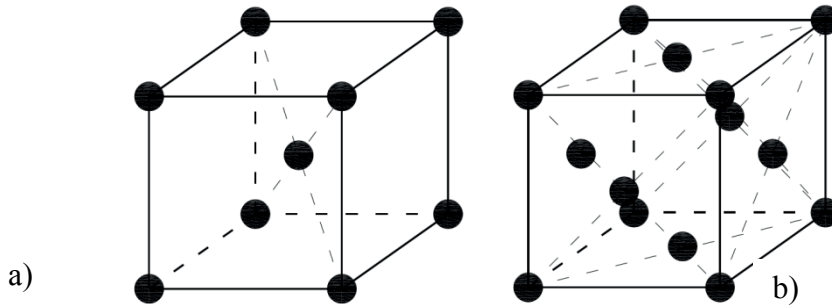transformed to BCC such as ferrite, pearlite, bainite and body centred tetragonal crystal structure for martensite.

Fig.2. 8   body-centered cubic BCC (a) and face-centered cubic FCC (b)
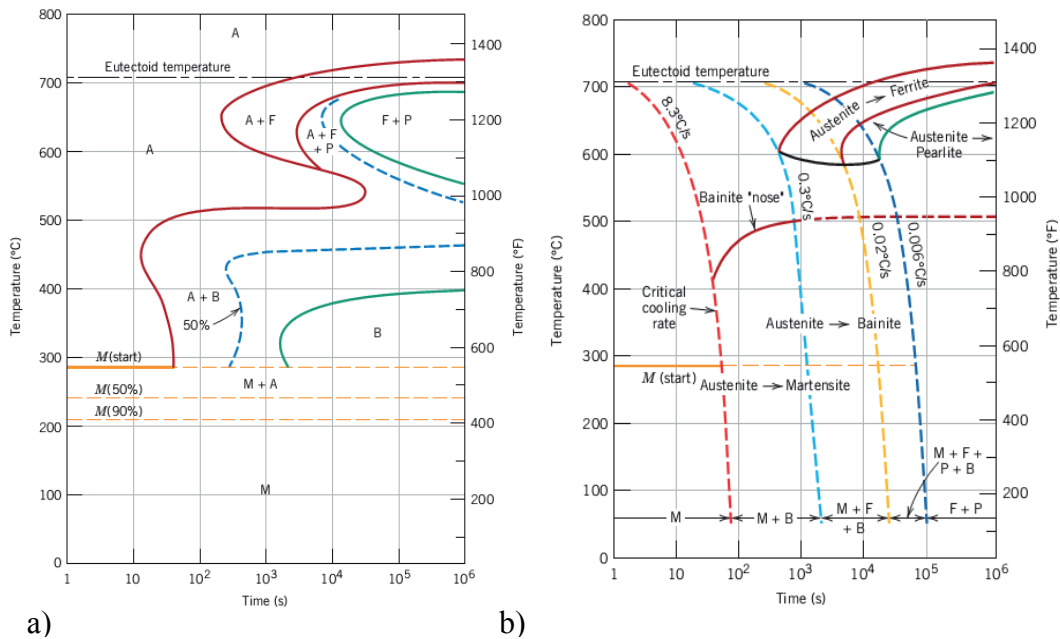
2.3.2.   Transformation diagram

Fig.2. 9   TTT Diagram (a) [2] and CCT Diagram of an alloy steel 4340(b) [1]

In general, thermal cycles of welding or heat treatment simply consist of heating and cooling. So one can use charts to predict preset temperature ranges of phase transformation and the final metallurgical state obtained from an initial austenitic state transformation to others phase such as ferrite, pearlite, bainite and martensite.

For isothermal transformations, it consists of TTT diagrams (Time-Temperature-Transformation), Fig.2. 9 (a), describe the transformation of austenite as a function of time at a given temperature. Isothermal heat treatments are not the most practical to conduct because alloy must be rapidly cooled and maintained at an elevated temperature from a higher temperature above the eutectoid. Most heat treatments for steels involve the continuous cooling of a specimen to room temperature. So the continuous cooling transformation diagram (CCT), Fig.2. 9 (b), is more applicable.

2.3.3.   Phase transformation model

The progress of a phase transformation may be broken down into two distinct stages: nucleation and growth. Nucleation involves the appearance of very small particles, or nuclei of the new phase *(often consisting of only a few hundred atoms)*, which are capable of growing. During the growth stage these nuclei increase in size, which results in the disappearance of some (or all) of the parent phase. The transformation reaches completion if the growth of these new phase particles is allowed to proceed until the equilibrium fraction is attained [13].

In order to study the evolutions of metallurgical structure one has to approach the metallurgical models using in heat treatment process. The solid-solid phase transformation is in trend in present research. During cooling process, two diagrams are used; Time-Temperature Transformation (TTT) is for isothermal transformation and Continuous Cooling Transformation (CCT) for anisothermes transformation as shown in Fig.2.9.

Isothermal transformation or JMA model

The first model of kinetics of phase change in isothermal transformation is developed by Avrami [6, 7, 8], which is described in the form:

$$z = 1 - e^{(-b.t^n)} \tag{2.21}$$

Where z is the volume fraction of new phase

        b, n experimental parameters depended on temperature

        t is time in second

This model is used to describe the isothermal transformation during the phase transformation from austenite to pearlite. It has been generally used to translate the diffusion transformation (ferrite, bainite) during cooling process by modifying the coefficient b and n. Afterward it has been modified by including the anisothermes effects by Inoue and also by the research at Institut National Polytechnique de Loraine *(INPL)*[17, 22, 44].

Anisothermes transformation

The transformation during cooling process is mostly in anisothermes transformation especially in the industrial application. It can be classified as diffusion transformation *(Transformation from austenite to pearlite, ferrite, bainite)* and diffusionless phase transformation *(martensite transformation)*.

Diffusion transformation

The diffusion transformation is a mechanism of displacement of atom *(order of several inter-atomic distances)*. Atomic diffusion is easier at high temperature. This transformation does not occur until the change rate of temperature variation is low enough that the diffusion has time to fulfill.

In thermo-metallurgical model of welding one can classify the diffusion transformation into three groups as follows:

- The Inoue models (Group 1)

- The Fernandes models or INPL models (Group 2)

- The Leblond-Devaux and Giusti models (Group 3)

- The Waeckel models (Group 3)

The first model is developed from on the JMA models. The mechanical effects such as stresses and carbon content on the metallurgical behaviors are considered in the Inoue models.

In models developed by Fernandes [22], the kinetics of transformation anisothermes is based on an add-on incremental concept and fictive time. The last two models are based on differential equation to describe the evolution of phase transformation.

47

Martensite transformation

The transformation from austenite phase to martensite is independent of time by cooperative small displacements of all atoms in structure. The kinetic of phase transformation developed by Koistinen- Marburger Model [31] gives results in good agreement with the experimental measurements. The formation of martensite volume fraction is described by the following expression:

$$z_m = z_0[1 - \exp[-\beta\langle M_s - T\rangle]] \tag{2.22}$$

Where $\langle x\rangle = 0 \ \forall x < 0 \ et \ \langle x\rangle = x \ \forall x \geq 0,$

z_m is the proportion of martensite formed,

z_0 is the proportion initial of austenite,

Ms   is the martensite start temperature,

β   is a material parameter and

T   is the temperature in degree Celsius.

2.3.4. Inoue model

Inoue [28, 29] considers there are three types of transformations in solid state: the austenite transformation during heating cycle, the diffusion transformation and the martensite transformation during cooling cycle.

During heating case, the austenite transformation is depended only on the temperature and its evolution is increased linearly from Ac_1 to Ac_3.

The diffusion transformation is considered to be the pearlite transformation. Where the formation of pearlite is defined by:

$$z = 1 - \exp[\int_0^t f(T, \sigma, c)(t - \tau)^3 . d\tau] \tag{2.23}$$

Where $f(T, \sigma, \tau)$ is a function describe the effect of stresses and the carbon content on the transformation kinetic. All parameters are identified from the TTT or CCT diagram. But the identification operation is not well presented by the auteur [21].

The martensite transformation is developed from the Koistinen-Marburger Models [31]. The stresses effect and the carbon content have been implemented as present by the follow equation:

$$z_m = z_0[1 - \exp[-\alpha(M_s - T) - g(\sigma, c)]] \tag{2.24}$$

Where Zm   is the martensite volume fraction formed

Zo   is the initial volume fraction of austenite

g(σ,c) is the function described the stresses and carbon content

2.3.5.   INPL model

This model is based on the working research of Fernandes at the Institute National Polytechnic of Loraine (France) [22]. Based on the fictive time (incubation time) and the addictively principal developed by Pumphrey and Jone [40].

The formation of new phase is developed based on the model John-Mehl-Avrami *(JMA)*:

$$z_{i+1} = z_{ad} z_{max,i+1}[1 - \exp[-b_{i+1}(t_{i+1}^* + \Delta t_{i+1})^{n_{i+1}}]]$$

$$t_{i+1}^* = [\frac{1}{b_{i+1}} \ln(\frac{1}{1 - z_i})]^{\frac{1}{n_{i+1}}} \tag{2.25}$$

Where z_{i+1} volume fraction formed at the end of increment i+1

z_{ad} volume fraction of austenite at the start of increment

$z_{max, i+1}$ maximum of volume fraction at increment i+1

T_{i+1} temperature at i+1 increment

t_{i+1}^* fictive time corresponding to the time which the volume fraction (z_i) is formed at temperature T_{i+1}

Δt_{i+1} increment time at the instance t_{i+1}

b_{i+1} and n_{i+1} coefficient of model JMA at instant i+1

This relation can be used to describe the transformation of austenite during heating and also the diffusion transformation during cooling cycle. Where the transformations begin after an incubation time calculated by the Scheil's method [45].

49

This model gives correct results for transformations ferrite, pearlite or bainite alone. However difficult it simulates the sequence of transformations ferrite/pearlite and bainite despite correction terms. The fact that the model is identified from TTT diagrams, where this type of transformation never occurs, also explains the difficulties [49]. The martensite transformation is modeling by the Koistinen-Marburger model [31].

Effect of applied Stresses

The diffusion transformation is defined by the new relation of coefficient in the model JMA:

$$b_\sigma = \frac{b}{[1-D(\sigma)]^n} \tag{2.26}$$

Where D (σ) is a function set by the experimental temperature described on the variation of transformation start time (t_d) under the effect of stress:

$$t_{ds} = (1 - D(\sigma))t_d \tag{2.27}$$

The martensite transformation is defined as:

$$M_{s\sigma} = M_s + A.\sigma_H + B.J_2(\sigma) \tag{2.28}$$

Where M_s is martensite start temperature

σ_H and $J_2(\sigma)$ are the hydrostatic stresses and equivalence Von Mises Stresses.

A and B are the coefficients to be defined

2.3.6. Leblond model

Leblond et al [32] propose a model of phase transformation in form of differential first order.

$$\overset{\bullet}{z} = \frac{z_{eq}(T) - z}{\tau(T)} \tag{2.29}$$

Where z is the new phase formed

50

$z_{eq}(T)$ is the equilibrium phase

The model describes the formation of austenite during heating and ferrite and pearlite during cooling with good results but for the bainite transformation a factor λ is needed. So the new model for bainite transformation is:

$$\dot{z} = \lambda(\dot{T}_{700°C}) \frac{z_{eq}(T) - z}{\tau(T)}$$

(2.30)

Where $\lambda(\dot{T}_{700°C})$ is depended on the cooling rate at 700°C

The martensite formation is based on the Koistinen-Marburger model.

The austenitization present in Fig.2.10 bellow showed the different formation of austenite in function of heating rate.
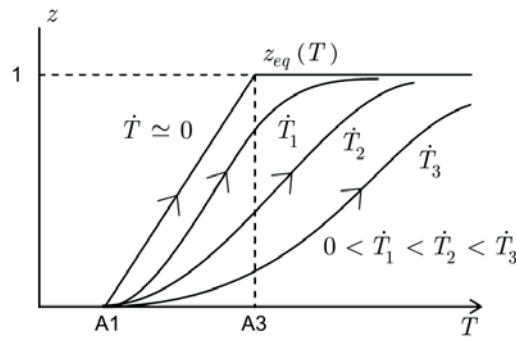
Fig.2. 10   Heating curve [32]

2.3.7.   Waeckel model

This model has the characteristics to describe the metallurgical behavior anisothermes provided by a differential equation, Model Waeckel [21, 55, 56] derived from Model Leblond, based on the CCT diagram data, which is particularly suitable to describe the industrial applications such as welding, it is able to simulate all thermo-metallurgical histories, and has been inserted in the thermo-mechanics finite element code, Code Aster, and give more simplicity for identification of the model.

<u>During heating</u> the only one transformation is the transformation into austenite which is not strongly depends to the heating rate:

$$\dot{Z}_\gamma = \frac{Z_{eq} - z_\gamma}{\tau(T)} \tag{2.31}$$

Where z_γ denotes the austenite proportion and Z_{eq} and τ are two temperatures depending functions.

Which

$$Z_{eq}(T) = \begin{cases} 0 & \text{if } T \leq Ac1 \\ \frac{T - Ac1}{Ac3 - Ac1} & \text{if } Ac1 < T < Ac3 \\ 1 & \text{if } T \geq Ac3 \end{cases} \tag{2.32}$$

and

$$\tau(T) = \begin{cases} \tau_1 & \text{if } T \leq Ac1 \\ \tau_1 + \frac{T - Ac1}{Ac3 - Ac1}(\tau_3 - \tau_1) & \text{if } Ac1 < T < Ac3 \\ \tau_3 & \text{if } T \geq Ac3 \end{cases} \tag{2.33}$$

The value of τ_1 and τ_3 determined by experiment of thermal expansion corresponded to the time for quasi static temperatures of start (Ac_1) and end (Ac_3) of austenite transformation.

<u>During cooling process</u>

The model Waeckel [21, 55] is based primarily on the fact that the metallurgical behavior of steels in continuous cooling is completely characterized by the diagrams CCT and supplemented by empirical kinetic Koistinen-Marburger. So the kinetics of diffusion transformations can be written:

$$\dot{z} = f(T, \dot{T}, z, Ms, d), z = \{z_1, z_2, z_3\}$$

$$Ms(z, d) = Ms_0(d) + A(d)\left[\sum_{i=1}^{3} Z_i - Z^s(d)\right]^+ \tag{2.34}$$

Where Z1, Z2, Z3 are the volume fraction of ferrite, pearlite and bainite.

2.4. MECHANICAL MODELS

2.4.1. Introduction

Mechanical modeling predicts the state of deformation and residual stress necessary to study the fatigue behavior of parts in service. In order to predict the residual stresses, the distortion, the deformation in the welding, it is necessary to know how the

materials respond to a given constraint or deformation. Increasing of temperature create not only the phenomenon of dilatation but also the phenomenon of viscosity materials created by the diffusion of dislocation.

Depending on the temperature, three models are classified for studying the mechanism of welding residual stresses and deformation [25].

- The model of linear viscous-for $T> 0.8T_{fusion}$ (K).

- The model of rate-dependent plasticity is characterized by the elastic tensor, viscosity and deformation, as $0.5T_{fusion}<T <0.8T_{fusion}$ is considered elasto-viscoplastic model.

- The model of rate independent plasticity or elastoplastic model, not viscous, characterized by the elastic tensor, the elastic limit, the isotropic hardening modulus for $T<0.5T_{fusion}$.

2.4.2. Setting equation

The resolution of the mechanical equation based on the equation of static equilibrium [25].

$$\text{div}\sigma(x_i, t) - f_{volume} = 0 \tag{2.35}$$

> σ stress tensor
>
> f_{volume} force density

Boundary conditions: based on the imposition of a zero transverse displacement on the contact surface of the work pieces by:

$U_x(x_i,t)= 0$ on the face of the joint process (edge to edge) $\tag{2.36}$

Initial condition: is considered as the zero stress before the welding process:

$$\sigma(x_i,0)=0 \quad \text{at instant t=0} \tag{2.37}$$

The relationship of deformation is described in the following case

2.4.3. Strain decomposition

The relationship of the total strain tensor consideration of phase transformation [25] presents in equation 2.38 below:

$$\varepsilon_{ij}^{tol} = \varepsilon_{ij}^{e} + \varepsilon_{ij}^{th} + \varepsilon_{ij}^{p} + \varepsilon_{ij}^{vp} + \varepsilon_{ij}^{Trv} + \varepsilon_{ij}^{Trp} \tag{2.38}$$

Or in form of strain rate or strain increment as follow:

$$\dot{\varepsilon}_{ij}^{tol} = \dot{\varepsilon}_{ij}^{e} + \dot{\varepsilon}_{ij}^{th} + \dot{\varepsilon}_{ij}^{p} + \dot{\varepsilon}_{ij}^{vp} + \dot{\varepsilon}_{ij}^{Trv} + \dot{\varepsilon}_{ij}^{Trp} \tag{2.39}$$

For the first expression, equation 2.38, from left to right represents the total strain, the elastic strain, the thermal strain, the plastic strain, the (creep) or viscoplastic strain, the volume changed strain and transformation induced plasticity strain (TRIP).

Equation 2.39 shows plastic strain rate and viscoplastic strain rate in the total strain rate. In general, these two strain rate do not intervene simultaneously in the numerical implementation. The plastic deformation mechanism, being dependent upon temperature, is often chosen as purely viscoplastic behavior at high temperature and purely plastic at low temperatures [51].

The separation of the volume changed strain from thermal strain by changing the coefficient of thermal expansion allows us to have the flexibility to describe the behavior of the material [25].The phase transformation plays an important role in modeling the residual stress [33]. To count these changes in volume, just replace the thermal deformation by a thermo-metallurgical strain [12].

$$\varepsilon^{th}(T) = \sum_{Phases} P_K \cdot \varepsilon_K^{th}(T) \tag{2.40}$$

with ε_K^{th} thermal deformation of the phases

pk volume fraction of formed phase

In the case of a macroscopically isotropic material containing two phases with different crystal structures, the classical thermal expansion can be replaced by a thermo-metallurgical strain which is expressed by Leblond et al [32]:

$$\epsilon^{thm} = (1 - z_\gamma)\varepsilon_\alpha^{th} + z_\gamma\left(\varepsilon_\gamma^{th} + \Delta\varepsilon_{\alpha\gamma}^{Tref}\right)$$

$$= \left[(1 - z_\gamma)\alpha_\alpha + z_\gamma.\,\alpha_\gamma\right](T - T_{ref}) + z_\gamma\Delta\varepsilon_{\alpha\gamma}^{Tref} \tag{2.41}$$

Where: z_γ is the proportion of γ phase.

ε_α^{th}, ε_γ^{th} are respectively the thermal expansion of the phase α and γ.

T_{ref} is the reference temperature

$\Delta\varepsilon_{\alpha\gamma}^{Tref}$ is transformation strain due to the difference in compactness between the

two phases at room temperature T_{ref}.

2.4.4. Constitutive behavior laws

The plastic behavior of material is defined by the criterion for plasticity, the flow rule and the hardening law.

Criterion for plasticity, suppose to be a function, *f*, which defines the elastic domain. It is independent of the orientation of the system coordinates and it is defined with the help of three invariant of stress tensor.

For the plasticity independent of time, the model that is mostly used for numerical simulation of welding is the Von Mises criterion. Criterion of Tresca is also amongst others famous models. Drucker-Prager criterion and Mohr-Coulomb criterion, are the rarely used for numerical simulation of welding [51].

Flow rule, or plastic flow relates the incremental plastic deformation to the incremental stress. This rule allows defining the plastic or viscoplastic deformation rate when the material behavior is no more elastic. It is suppose to be a vector normal to yield surface or loading surface.

Hardening law specifies the evolution of plasticity criterion during the plastic flow resulting because of the rearrangement of the internal structure of material. The hardening laws are actually the rules that characterize the evolution of hardening variables during the inelastic deformation.

2.4.4.1. Perfect elastoplastic model

The yield   criterion of Von   Mises is   often chosen to   model   themo-mechanical behavior of the weld and it is programmed into the commercial FEA software code ABAQUS *(Rate Independent Model).*

In this case the elastic range is defined by the yield function *f:*

$$f(\sigma_{ij}) = \sigma_{VM} - \sigma_y < 0 \tag{2.42}$$

With σ_{VM} is the Equivalent Von Mises stresses and σ_y is the yield strength of the material.

$$\sigma_{VM} = \sqrt{3J_2} = \sqrt{\frac{3}{2}S:S} = \sqrt{\frac{1}{2}[(\sigma_1 - \sigma_2)^2 + (\sigma_2 - \sigma_3)^2 + (\sigma_3 - \sigma_1)^2]} \tag{2.43}$$

with   S   deviatoric stress tensor $(S = \sigma - \frac{tr(\sigma)}{3}I)$

J2   second deviatoric stress tensor

$\sigma1, \sigma2, \sigma3$ principal stresses

There   are   a   plastic   flow when $f(\sigma_{ij}) = 0$,   the plastic   multiplier *($\dot{\lambda}$)*   can   be determined by the law of plastic behavior and the consistency condition *($f = \dot{f} = 0$).*

$n: \dot{\sigma} = 0$ with $n = \frac{\partial f}{\partial \sigma}$, n: represents the normal to the surface

For a particular case of isotropic elasticity and Von Mises criterion, it leads to

$$\dot{\lambda} = \frac{2}{3}n:\dot{\varepsilon} \tag{2.44}$$

The perfect elastoplastic behavior is defined by the expression 2.45 and 2.46:

$$\textit{Elastic behavior: } \sigma = \Lambda:(\varepsilon - \epsilon^p - \epsilon^{th}) \tag{2.45}$$

$$\textit{Flow rule: } \dot{\varepsilon}^p = \frac{\dot{\lambda}df(\sigma_{ij})}{d\sigma_{ij}} = \frac{3\dot{\lambda}S_{ij}}{2\sigma_{VM}} \tag{2.46}$$

Λ, the 4th order stiffness tensor is defined by the elastic modulus E and Poisson's ratio ν.
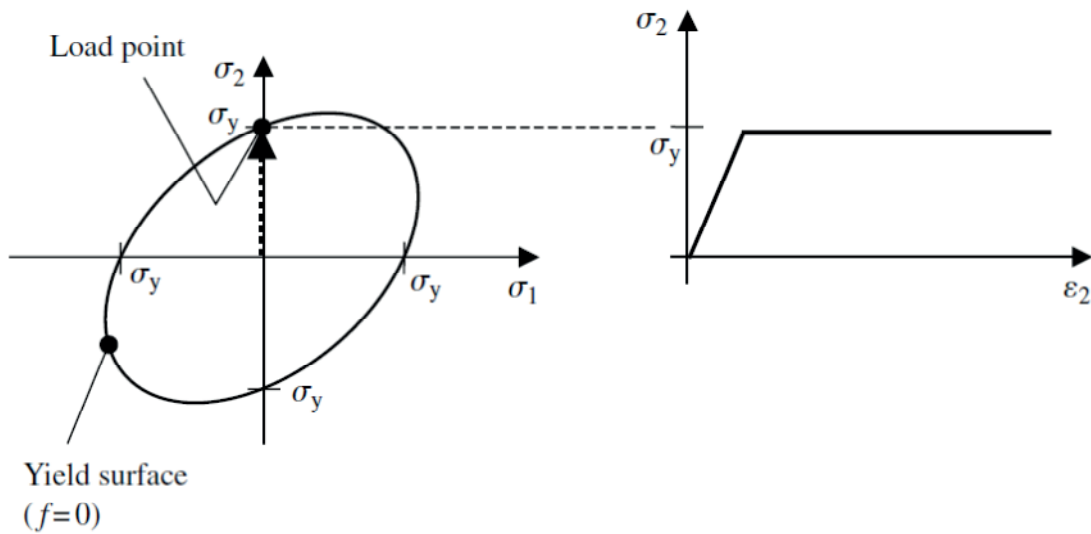
Fig.2. 11   The von Mises yield surface for plane stress and the corresponding stress–strain curve obtained for uniaxial straining in the 2-direction [23].

Note: Important parameters in the simulation of this model are: Young's modulus E, Poison coefficient ν, thermal expansion coefficient α and the yield strengthσ_y.

2.4.4.2.   *Elastoplastic model with isotropic hardening*

In this model the elastic domain transforms without the translation of the origin as shown in Fig.2.12.The hardening parameter dependent on a scalar variable called isotropic hardening (R). The relation obtained using Von Mises criterion and isotropic hardening behavior leads to a particular law of plasticity known as Prandtl-Reuss law. The yield function f is defined by the expression below:

$$f(\sigma, R) = \sqrt{3J_2(\sigma)} - \sigma_e - R(p) \qquad (2.47)$$

The isotropic hardening is defined by R (p), which is expressed as a linear

$$R(p) = H\varepsilon^p \ and \ \dot{p} = \sqrt{\left(\frac{2}{3}\right)\dot{\varepsilon}^p : \dot{\varepsilon}^p} \qquad (2.48)$$

Where p is the accumulated plastic strain, H is the hardening modulus. Independent of chosen form for R, the coherence condition allows finding the plastic multiplier in equation 2.49:

$$\dot{\lambda} = \frac{(n:\dot{\sigma})}{H} = \dot{p} \tag{2.49}$$

Elastoplastic behavior with linear isotropic hardening is defined by:

Elastic behavior $\sigma = \Lambda:(\varepsilon - \epsilon^p - \epsilon^{th})$ (2.50)

Flow rule: $\dot{\varepsilon}^p = \frac{\dot{\lambda}df}{d\sigma_{ij}}$ with $\dot{\lambda} = \frac{(n:\dot{\sigma})}{H}$ (2.51)
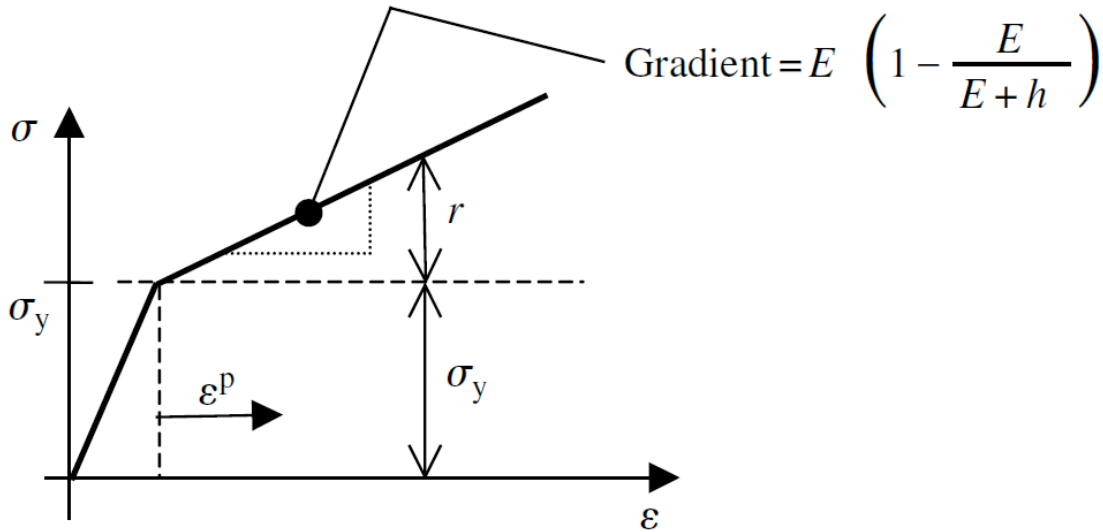
Fig.2. 12 Isotropic hardening, in which the yield surface expands with plastic deformation, and the corresponding uniaxial stress–strain curve [23].

Note: Important parameters in the simulation are: Young's modulus E, Poison's coefficient ν, thermal expansion coefficient α, the yield strength σ_y and hardening modulus H.

2.5. INFLUENCE OF MATERIAL PROPERTIES

2.5.1. Temperature dependent material properties

The temperature dependent material properties are often not available or are difficult to obtain especially at high temperature. Another problem is a divergent of calculation by peak point on material dependent temperature such as at the start of phase transformation

temperature Ac1. Based on this difficulty, the simplification has been studied by Zhu and Chao [59] and has concluded as follow:

(1) The thermal conductivity has some effect on the distribution of transient temperature field during welding. The material density and specific heat have negligible effect on the temperature field. Although using the average values over the temperature history is better, adopting room temperature values of all thermal properties in the welding simulation can predict reasonable results for the transient temperature distribution.

(2) The yield stress is the key mechanical property in welding simulation. Its value has significant effect on the residual stress and distortion. If the room temperature value of the yield stress is taken, the FEA computation predicts zero residual stress and no permanent distortion because only elastic strain, and no plastic strain, occurs under this circumstance. The temperature dependency of the yield stress must be considered in a welding process simulation to obtain correct results.

(3) The Young's modulus and the thermal expansion coefficient have small effects on the residual stress and distortion, respectively, in welding deformation simulation. It is found that the numerical results obtained by using the room temperature value of Young's modulus are much better than those using its average value over temperature history.

A cut-off temperature above which unchanged in mechanical material properties is considered. It serves as an upper limit of the temperature in the mechanical analysis [33]. Ueda et al [50] assumed that the material did not have any stiffness above $700^{o}C$. Tekriwal and Mazumder [48] varied the cut-off temperature from $600^{o}C$ up to the melting temperature. They found out that the residual stresses were overestimated by 2-15% when the cut-off temperature was lowered.

The conductivity and the specific heat in function of phase metallurgy have no influence on the thermal model and are classified from 1 to 2 of 5 in order of precision of the thermal model [33].

Sensitivity analyses in the thesis of Schwenk [46] for laser welding of a dual phase steel grade DP600 indicated that the most important quantities in order to obtain accurate

results are the thermal expansion coefficient, the phase transformation and the temperature dependent yield stress. Here, the yield stress appears to be particularly important for homologous temperature less than 0.7 fusion temperature (Tm). The hardening mechanism plays a less important role.

2.5.2. Model dependency

In the nineties and before, ideal-plastic hardening has been employed very often due to its simple numerical integration and hence, enormous gain of computational time [33].

During welding simulation ZF and HAZ areas undergo plastic deformation during the cooling phase, using the elastoplastic model (EP) with the isotropic hardening law, kinematic, or combined viscoplasticity (EVP) will affect these areas. These models do not affect other regions [10].

Devaux et al [19] found a small difference in the simulation of residual stresses by comparing the EP model with isotropic hardening and combined. Vincent et al [54] shows that the EP model with combined hardening gives a result close to the experiment by the method Satoh.

The Viscous effect of EVP model gives a better result for the prediction of the distortion (deformation out of plane), but indifference to the EP model for predicting the residual stresses [53]. The rate-dependent plasticity or viscoplasticity can be neglected even at very high homologous temperatures due to the relatively short time of the weld thermal cycle bas on the work of Hibbitt and Marcal [26].

It should be noted that the biggest problem is not the lack of the model but the lack of parameters for these models [54].

2.6. CONCLUSION

The numerical model of welding simulation had been presented. The variation of thermal models, metallurgical models and the mechanical models had been described based on the literature studied of the previous research work. The choice of numerical model to be

implemented in this thesis is based on many constraints such as the welding process, material properties, and also the facility of implement of this numerical model and finally the precision getting from each selected model.

In this context, one can summery that the section of those models is based on the criteria as follow:

- The conical volumetric heat source with Gaussian distribution is suitable for laser welding Nd: YAG because of it sharps is suited to the cross section of laser sheet welding joint. The high intensity with a small diameter of laser beam is also a factor important that approach the conical volumetric heat source to the laser beam than the hemispherical volume source.

- For phase transformation in the metallurgical model, this problem remains a debatable issue because of many mechanisms involved and completely different from one transformation to another. The phenomenological models are often used in the simulation of industrial processes such as welding. In the case of the martensitic transformation kinetics Koistinen-Marburger empirical is often used in the numerical simulation of welding and heat treatment. In contrast, the diffusion transformation is poorly documented. Models Inoue and INPL based on the kinetic isothermal Johnson-Mehl-Avrami which is originally proposed for pearlitic transformation and it seems difficult to adapt to other transformations. Model Leblond is quite simple and gives acceptable results but the parameter identification is complicated. The same type phenomenological model Waeckel gives good results with simple and quick identifications.

- Finally the determination of residual stresses and strains of welding numerical simulation requires thermomechanical behavior laws. The elastoplastic model gives a fear result of residual stresses and residual strain caused by laser welding. The consideration of microstructural transformations is an advantage because it can well describe the mechanism during welding process.

In this work, we focus on the modelisation of laser welding Nd: YAG with keyhole mode by using the conical volumetric heat source for thermal model, the Waeckel phase transformation to describe the metallurgical phase transformation during and after welding and finally the elastoplastic model with transformation induced volume strain to predict the residual stresses and strain.

REFERENCE

[1] *The Making, Shaping and Treating of Steel*. United States Steel Corporation, 9th edition, 1971.

[2] *Atlas of isothermal Transformation and Cooling Transformation Diagrams*. American Society for Metals, 1977.

[3] Westby 0. Temperature distribution in the workpiece by welding. Department of Metallurgy and Metals Working, The Technical University, Trondheim, Norway, 1968.

[4] Mohamed Elamine AIT ALI. *Etude numéerique et experimentale d'un procédé de mise en forme de structure raidies dédiées à des applications aéronautiques*. PhD thesis, Université européenne de bretagne, 2009.

[5] BAB Andersson. Thermal stresses in a submerged-arc welded joint considering phase transformations. *Eng. & Tech. Trans. ASME*, 100:356–362, 1978.

[6] M Avrami. Kinetics of phase change. i: General theory. *The Journal of Chemical Physics*, 7, Issue 12:1103–1112, 1939.

[7] M Avrami. Kinetics of phase change. ii: Transformation-time relations for random distribution of nucleo. *The Journal of Chemical Physics*, 8:212–224, 1939.

[8] M Avrami. Kinetics of phase change. iii: Granulation, phase change, and microstructure. *The Journal of Chemical Physics*, 9:177–184, 1940.

[9] Pilipenko A.Yu. Analysis of the temperature distribution during gta welding of thick-walled pipes. Master's thesis, St.-Petersburg Technical University, 1997.

[10] D.J.and A.R. Ortega Bammann. The influence of the bauschinger effect and yield definition on the modeling of welding processes in modeling of casting, welding and advanced solidification processes. *The Minerals, Metals & Materials Society*, VI, 1993.

[11] Asma BELHADJ. *Contribution à l'étude expérimentale et numerique du soudage laser : Application aux alliage de magnésium*. PhD thesis, 2009.

[12] Jean-Michel BERGHEAU. Modelisation numerique de soudage. *Technique de l'ingénieur*, 2004.

[13] William D. Callister. *Materials Science and Engineering : An introduction*. John Wiley & Sons, 2007.

[14] Radaj D. Schweissprozesssimulation. *DVS-Verlag, Duesseldorf*, 1999.

[15] Radaj D. Eigenspannungen und verzug beim schweissen, rechen- und messverfahren, fachbuchreihe schweisstechnik,. *DVS-Verlag GmbH, Duesseldorf*, 2000.

[16] Rosenthal D. The theory of moving sources of heat and its application to metal treatments. *Trans ASME*, 68:849–865, 1946.

[17] Simon A Denis S, SJÖSTRÖM S. Coupled temperature, stress, phase transformation calculation model, numerical illustration of the internal stresses evolution during cooling of a eutectoïde carbon steel cylinder. *Metallurgical Transactions A*, 18:1203–1212, 1987.

[18] Depradeux.L. *Simulation Numérique du Soudage en vue de la Prédiction des Distortions et Contraintes Résiduelles- Validation Expérimentale sur Cas Tests de Référence-Acier 316L*. PhD thesis, Institut National des Science Appliquées de Lyon, 2004.

[19] Leblond Deveaux, D.Pont. Numerical simulation of the repair of a defect containing zone by a manual welding procedure. In *ASME 10th Conference on Offshore and Artic Engineering. Starvanger, Norway.*, 1991.

[20] K. Easterling. *Introduction to the Physical Metallurgy of Welding*. Butterworths, 1983.

[21] Waeckel F. Modélisation du comportement thermo-métallurgique des aciers. volume 4. EDP Sciences, févier 1994.

[22] SIMON A. FERNANDES F. M. B., DENIS S. Mathematical model coupling phase transformation and temperature evolution during quenching of steels. *Material Science and Technology*, 1:838–844, 1985.

[23] Nik Petrinic Fionn Dunne. *Introduction to computational plasticity*. Oxford, 2005.

[24] E Friedman. Analysis of weld puddle distortion. *Welding J Research Suppl*, pages 161–166, 1978.

[25] John A. Goldak. *Computational Welding Mechanics*. Springer, 2005.

[26] Marcal P.V Hibbitt H.D. A numerical thermo-mechanical model for the welding and subsequent loading of a fabricated structure. *Comp. & Struct*, 3:1145–1174, 1973.

[27] Bhadeshia H.K.D.H. Modelling of stee welds. *Material Science and Technology*, 8:123–133, 1992.

[28] et Wang Z. Inoue, T. Coupling between stress, temperature and metallic structures during processes involving phases transformations. *Mater.sci. and Tech*, 1:845–850, 1985.

[29] Yamaguchi et Wang Z Inoue, T. Stresses and phase trandformations occuring in quenching of carburized steel gear wheel. *Mater.sci. and Tech*, 1:872–876, 1985.

[30] Masubuchi. K. *Analysis of welded structures*. Pergamon Press, 1980.

[31] D.P. Koistinen and R.E. Marburger. A general equation prescribing the extent of the austenite-martensite transformation in pure iron-carbon alloys and plain carbon steels. *Acta Metallurgica*, 7(1):59 – 60, 1959.

[32] J.B. Leblond and J. Devaux. A new kinetic model for anisothermal metallurgical transformations in steels including effect of austenite grain size. *Acta Metallurgica*, 32(1):137 – 146, 1984.

[33] Lars-Erik Lingren. *Computational Welding Mechanics: Thermomechanical and microstructural simulations*. Woodhead Publishing in Materials, 2007.

[34] P. Michaleris. *Modeling the effects of welding*. Woodhead Publishing Limited and CRC Press, 2005.

[35] Rykalin NN. Berechnung der warmevorgange beim schweiben. In *VEB Verlag Technik*, 1957.

[36] Ohkubo A.and Nishiguchi K Ohji T. Mathematical modeling of molten pool in arc welding, mechanical effects of welding. *Publ. Springer,Berlin*, pages 207–214, 1992.

[37] Marcal P. Weld problems, structural mechanics programs. pages 191–206. Charlottesville, University Press, 1974.

[38] Uyehara 0. A. Pavelic V., Tanbakuchi R. and Myers. Experimental and computed temperature histories in gas tungsten arc welding of thin plates. *Welding Journal Research Supplement*, 48:295s–305s, 1969.

[39] Artem Pilipenko. *Computer Simulation of Residual Stress and Distortion of Thick Plates in Multielectrode Submerged Arc Welding: Their Mitigation Techniques*. PhD thesis, Norwegian University of Science and Technology, Faculty of Engineering Science and Technology, 2001.

[40] Jones F.W Pumphrey W. I. Inter-relation of hardenability and isothermal transformation data. *J.I.S.I*, 159:137–144, 1948.

[41] Dieter Radaj. *Welding residual stresses and distorsion : calculation and measurement*, volume 2. DVS, 2003.

[42] Cochrane R.C. Microstructure du métal fondu. etat actuel des connaissances. soudage et techniques connexes. Technical report, pp334-340, September-Octobre 1983.

[43] Rykalin R.R. Energy sources for welding. *Welding in the World*, 12, No. 9/10:227–248, 1974.

[44] SJÖSTRÖM S. Interactions and constitutive models for calculating quench stresses in steel. *Material Science and Technology*, 1:823–829, 1985.

[45] Scheil.E. Analaufzeit der austenitumwanlung. *Arch. Eisenhuttenw.*, 8:565–567, 1935.

[46] Christopher Schwenk. *FE-Simulation des Schweißverzugs laserstrahlgeschweißter dünner Bleche :Sensitivitätsanalyse durch Variation der Werkstoffkennwerte*. PhD thesis, Bundesanstalt für Materialforschung und prüfung, 2007.

[47] Ohji T. Heat conduction theory and its application to welding. *Japan Welding Soc*, 64(4):32–36, 1994.

[48] P. Tekriwal and J. Mazumder. Transient and residual thermal strain-stress analysis of gmaw. *ASME Journal of Engineering Materials and Technology*, 113:336–343, 1991.

[49] Ngoc Thuy TRINH. *Modelisation du comportement thermomecanique et metallurgique des aciers*. PhD thesis, 2008.

[50] et al. Ueda, Y. Mathematical treatment of phase transformation and analytical calculation of restraint stress-strain. *Transactions of Japan Welding Institute*, 14(1):153–162., 1985.

[51] Muhammad Zain ul abdein. *Experimental investigation and numerical simulation of laser beam welding induced residual stresses and distortion in AA6056-T4 Sheets for Aeronautic application*. PhD thesis, 2009.

[52] Sudnik V.A. and Erofeew W.A. Computerberechnungen von schweissprozessen. In *Tech. Hochschule Tula, Schweden*, 1986.

[53] Yannick Vincent, Jean-Michel Bergheau, and Jean-Baptiste Leblond. Viscoplastic behaviour of steels during phase transformations. *Comptes Rendus Mecanique*, 331(9):587 – 594, 2003.

[54] Yannick Vincent, Jean-François Jullien, and Philippe Gilles. Thermo-mechanical consequences of phase transformations in the heat-affected zone using a cyclic uniaxial test. *International Journal of Solids and Structures*, 42(14):4077 – 4098, 2005.

[55] Anrieux S. Waeckel F. Thermo-metallurgical modelling of steel cooling behaviour during quenching or welding. In *14th Internatiinal Conference on Structural Mechanics in Reactor Technology (SMiRT), Lyon, France*, August 17-22, 1997.

[56] P. Dupas Waeckel F. and Andrieux. A thermo-metallurgical model for steel cooling behaviour: Proposition, validation and comparison with the sysweld's model. In *Journal de physique IV*, volume 6. EDP Sciences, Janvier 1996.

[57] Schmidt J. Weiss D. and Franz U. *A model of temperature distribution and weld pool deformation during arc welding, Mathematical Modeling of Weld Phenomena 2*. The Institute of Materials, 1995.

[58] L. Zhang, E. W. Reutzel, and P. Michaleris. Finite element modeling discretization requirements for the laser forming process. *International Journal of Mechanical Sciences*, 46(4):623 – 637, 2004.

[59] X. K. Zhu and Y. J. Chao. Effects of temperature-dependent material properties on welding simulation. *Computers & Structures*, 80(11):967 – 976, 2002.

Résumé

Chapitre 3: Approche expérimentale du soudage laser Nd:YAG

Cette partie présente l'influence des paramètres du procédé laser sur les propriétés géométriques du cordon de soudure, microstructurales et métallurgiques ainsi que mécaniques. Les paramètres du procédé laser ont été sélectionnés suivant leur degré d'influence sur la qualité finale du cordon de soudure. Il s'agit du point focal, de la vitesse et de la puissance de soudage.

Le matériau étudié est un acier zingué, dual phase de nuance DP600, utilisé dans le domaine de l'automobile. La configuration de soudage est une configuration par recouvrement de deux tôles minces d'épaisseurs 1,25 mm. Après optimisation du jeu inter-tôle, un jeu de 0,1 mm a été utilisé pour éviter les problèmes de dégazage et permettre au zinc de s'évaporer. Le laser utilisé est un laser de puissance Nd: YAG laser composé d'un générateur 4kW avec un bras robot de type Fanuc R2000iB.

Une étude de l'interaction entre la puissance du laser, la position du point focal et la vitesse du soudage a été réalisée. Les résultats ont montré que la vitesse du soudage et la distance focale sont les facteurs qui influencent principalement la largeur de la zone soudée (FZ). La puissance du laser présente une contribution moindre sur largeur FZ. Par contre, la profondeur et la largeur de la FZ peuvent être obtenues par l'optimisation de la puissance du laser et de la position du point focal. L'étude de l'ensemble des paramètres du laser sur la dureté et la microstructure à l'intérieur de la FZ, la ZAT et la zone de revenue a montré très peu d'influence. La résistance à la traction maximale de cisaillement semble dépendre fortement de la puissance du laser.

Abstract
Chapter 3: Experiment of ND: YAG Laser Welding

This section presents the influence of the laser process parameters on the geometric properties of the weld bead, and metallurgical microstructure and mechanical properties. The laser process parameters were selected according to their degree of influence on the final quality of the weld bead. It is the focal point, and the speed of the welding power.

The material studied is a galvanized steel, dual phase DP600 grade, used in the automotive field. The welding configuration is a configuration of two overlapping thin sheets 1.25 mm in thickness. After optimization of the inter-plate gap, a clearance of 0.1 mm was used to avoid problems with degassing and allow zinc to evaporate. The laser used is a laser power Nd: YAG laser consisting of a generator with a 4kW type arm robot R2000iB Fanuc.

An interaction between the laser power, the focal point position and welding speed are observed. The welding speed and focused position are the most important factors affecting the welded zone width. The laser power contributes secondary effect in the FZ width dimensions. The main factor influencing the width of HAZ is the welding speed and the focused position. So the relation between the depth and width of FZ can be obtained by optimizing laser power and focal point position. In contrary the laser parameters have less influent on the hardness and the microstructure inside the FZ, the HAZ and the Softening Zone. The maximum shear load is depended strongly on the laser power. Finally a compromise between the shape of FZ, its hardness, its microstructure and also the maximum shear load are reached to ensure the strength of lap joint during service.

Contents

Figures

Tables

Chapter **3**

Experimental of Nd: YAG laser welding

3.1 INTRODUCTION

In laser welding without filler metal, one observe some kind of geometric shape imperfections types under influence of welding parameters such as speed, power and focal point. The effects of welding process parameters have been studied for laser CO_2 by Reisgen et all [17]. He focused on the influence of laser on the weld penetration and welded zone width under effect of laser power, the welding speed, and the welding efficiency. Benyounis et al [6] shown that increasing CO_2 laser power with decreasing the welding speed leads to increase of heat input. Interaction between laser parameters such as laser power, speed, focal point position and the dimension of welded zone such as penetration, FZ width and HAZ width are studied. But none of them had shown the relation between the laser parameters and the imperfections of welded joint. Those common imperfections include the excess penetration, the lack of penetration, the root concavity and the top concavity, etc.

The HAZ hardness in excess of 350HV occur readily requiring high pre-heat temperatures, slow cooling and hydrogen controlled welding procedures [20]. The non-isothermal tempering in the HAZ starts from the temperature of 650°C for DP600 [5] and become maximum softening at the Ac_1 temperature [21]. So the softening zone situated at the interface of base metal (BM) and the HAZ of welded joints. The weld cooling rates that

are too high through the result of insufficient pre-heat or low welding heat inputs can result in HAZ hardening [20]. Conversely the high heat-input welding processes can lead to softening of the HAZ with associated loss of strength.

A full penetration lap joint of laser welding under influence of laser incident angle, joint gap and sheet metal thickness was studied by Chen et all [9]. The interaction between those parameter was found out to get better shear strength of lap joint. So to observe more effect the different lap joint, full penetration and non penetration welded joint, the shear test of welded joint, *from non penetrated welded joint to full penetration welded joint*, are observed.

The strength of a material under tension has long been regarded as one of the most important characteristics required for design, production quality control and life prediction of industrial plant [14]. Many authors had used different testing parameter to adapt to their application. In welding strength test, the force loading rate of 1mm/min has been used in the experiment of Chen et all [9] for shear testing of automotive steel sheets. The loading rate of 20mm/min has been used in the shear test of lap joint of DP600 [7].

So the studied of the geometric, the microstructure and the hardness of Nd: YAG laser welding lap joint under influence of laser welding parameter is necessary.

The welding process were prepared to study the influence of welding parameters such as power, focal point position and welding speed on the lap joint of DP600 steel 1.25mm of thickness and galvanized and 0.1mm- gap lap joint . The gap was controlled by pre-positioned standard plug gauge between the two sheets.

This part is included the cross section of lap joint, its hardness, its micrographic and its shear load.

3.2 MATERIALS AND EXPERIMENTAL PROCEDURE

3.2.1 Material

Based on trend of high strength steel in car manufacturing [19], the high strength steel is considered in the selection of material for this research. Depending on the chemical composition and metallurgical structure, there may be two classes of high strength steel:

- The UHSS steels *(Ultra High Strength Steel)* are boron steels and martensite.

- The AHSS steels *(Advanced High Strength Steel)* are DP *(Dual Phase)*, CP *(Complex Phase)*, TRIP *(Transformation Induced Plasticity)* and HSLA *(High Strength Low Alloy)* steels.

The mechanical properties of high strength steel are presented in Tab.3.1 and Fig.3.1.

Class	Limit Elastic (YS) (MPa)	Ultimate shear strength UTS (MPa)	Total Elongation (%)
HSLA 350/450	350	450	23-27
DP 300/500	300	500	30-34
DP 350/600	*350*	*600*	*24-30*
TRIP 450/800	450	800	26-32
DP 500/800	500	800	12-20
CP 700/100	700	1000	12-15
DP 700/1000	700	1000	12-17
MS 1250/1520	1250	1520	4-6

Notice: YS and UTS are the minimum values

Tab.3. 1 Mechanical properties of high strength steel [19]
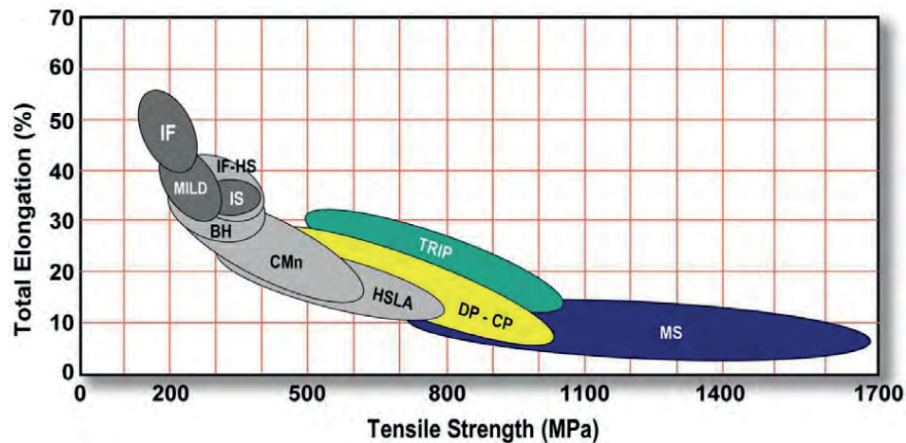
Fig.3. 1   Shear and total elongation of high strength steel [19]

What is the DP steel ?

DP steels consist of a ferritic matrix containing a hard martensitic second phase in form of islands as shown in Fig.3.2. Increasing the volume fraction of martensite generally increases the strength. DP steels are produced by controlled cooling from the austenite phase

(in hot-rolled products) or from the two-phase ferrite plus austenite phase *(for continuously annealed cold-rolled and hot-dip coated products)* to transform some austenite to ferrite before a rapid cooling transforms the remaining austenite to martensite [19].

The soft ferrite phase is generally continuous, giving these steels excellent ductility. When these steels deform, strain is concentrated in the lower-strength ferrite phase surrounding the islands of martensite, creating the unique high work-hardening rate exhibited by these steels. Its ultimate shear strength reach 400 MPa to 1000 MPa, with a maximum elongation of 30% [19] as presented in Fig.3.1.
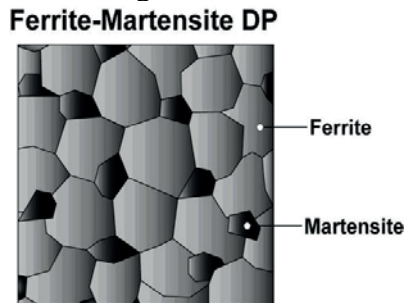
Fig.3. 2   Microstructure of dual phase steel [19]

How about DP600 ?

DP600 is a family of DP steel with the volume fraction of martensite is approximately 22% for DP600 steel [13]. And between 22.8% 27.4% base on the chemical composition of DP600 [11]. The microstructure of DP00 from Arcelor Mittal is shown in Fig.3.3. In which the martensite is represented by the white color. The brown color belongs to the grain of ferrite.
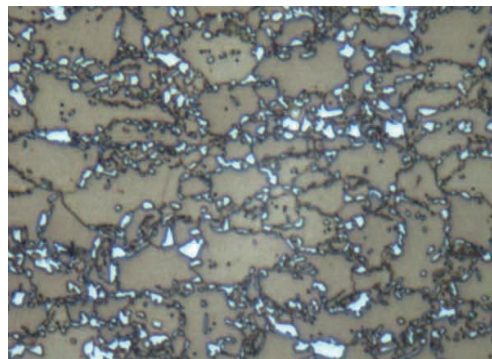
Fig.3. 3 Microstructure DP600 [3]

The chemical composition of DP600 is presented in Tab.3.2 and Tab.3.3. The relation of stress strain compared to others high strength steel showed in Fig.3.4.
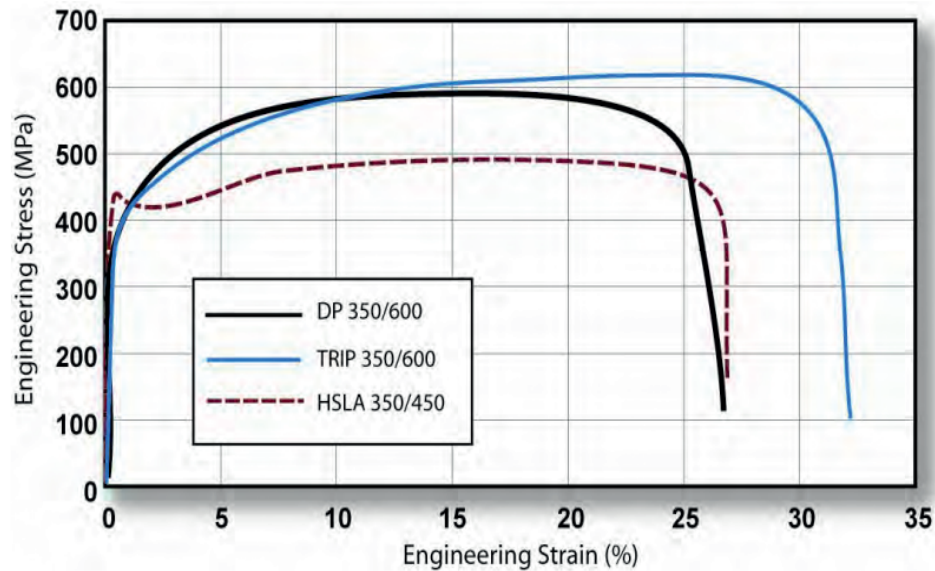

Fig.3. 4   The relation of Engineering strain versus Engineering stress of high strength steels [19]

	C (Max)	Mn(Max)	Si(Max)
DP600	0.14	2.1	0.4

Tab.3. 2 Chemical composition of DP600 fom ArcelorMittal [3]

	C	Mn	P	Si	Al	Cr	Mo	B
	0.0086	1.573	0.017	<0.001	1.16	0.452	0.009	0.0003
Ni	Ti	Nb	Zr	V	W	Co	Cu	Ca
0.02	0.009	0.005	0.005	0.006	0.042	0.008	0.019	0.0012
N	Pb	Sn	As	Sb	Te	Zn	Mg	Si
0.006	0.01	0.004	0.00	0.01	0.002	0.014	0.003	0.104

Tab.3. 3   Chemical composition of DP600 [18]

The chemical composition in Tab.3.3 is more precise and more describe than the chemical composition in Tab. 3.2. But the main chemical composition, C, Mn and Si are in a limit defined in Tab.3.2.

Why DP600 in this research?

The dual phase steel DP600 is chosen to use in this research because of continuity from the previous research work in PSM team, the reachable steel supplied by Accelor Mittal France and not forgetting the trend of applying new high strength steel in the car manufacturing.

3.2.2   Laser welding

The Nd: YAG laser welding machine, Fig.3.5 and Tab.3.4, compose of a 4kW generator with an arm robot type Fanuc R2000iB for welding operation. The laser beam is transmitted by optical wire of 200µm diameter with focus spot diameter of laser 560µm and the focal length of 583.5mm corresponds to reference of focal point position on the upper surface of sheet metal.

Laser Nd:YAG   Test table
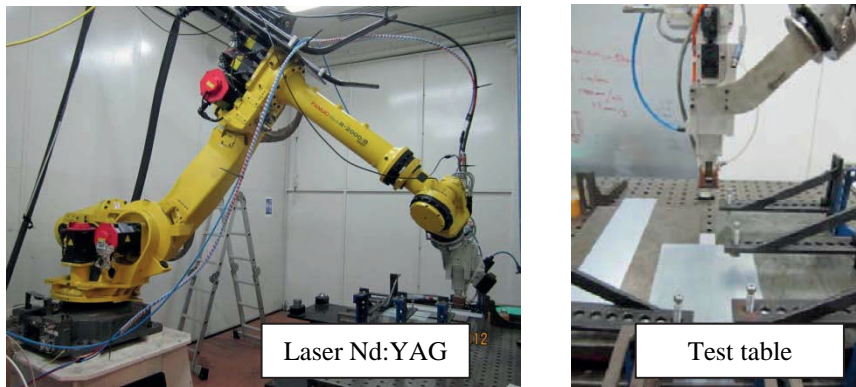
Fig.3. 5 Laser Nd: YAG and table

Specification	Substances
Laser type	Nd:YAG 4Kw
Focal length	583.5mm
Optical wire	200µm
Laser spot diameter	560µM
Gap	0.1mm
Size of welding cell	120mmx250mmx 1.25mm

Tab.3. 4 The specification of laser welding

The galvanized sheet metal, DP600, assembled by lap joint presents in Fig.3.5. and prepared specimen for observing in Fig.3.6. The gap of 0.1mm is used and it was controlled by pre-positioned standard plug gauge between the two sheets.
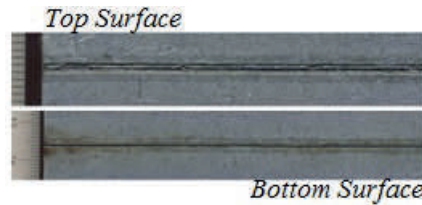

Fig.3. 6 Welding specimen prepared for cross section observation

3.2.3   Specimen preparation

There are two kind of specimen:

- Specimen for microstructure and micro-hardness observation
- Specimen for shear test

The transverse cross sections of welding sample are cut and mounted in an hot mounting machine at 200°C during 5 minutes, for better manipulation the specimen on the optical microscopy support, afterward its pass though a grinding papers *(P120-P4000 Grade)* with water-cooling. Each grinding stage removes the scratches from the previous coarser paper by orienting the specimen perpendicular to the previous scratches. The operation is done manually until no scratches on the surface.

The samples are washed with ethanol and are dried with hot air to avoid the oxidation on the metal surface and are polished with a pH solution *(MasterMet 2: 0.02 micron non-crystallizing colloidal silica, pH.10.5)* during 20 minutes on the rotate machine. The samples are cleaned with ethanol and an ultrasonic bath of ethanol during 5 minutes for removing the pH on the interface of the metal and the resin.

Etching is used to reveal the microstructure of the metal; it also removes the thin, highly deformed layer introduced during grinding and polishing. The Nittal 4% is used for these specimens during 10 to 15 seconds then the samples were immediately washed with water follow by ethanol, and then were blown dry in hot air.

The shear strength of work piece was measured by Instron-4204 testing machine. The experiment was done at room temperature. Two samples per test are used to evaluate the shear strength of the lap joint. The loading rate of 5mm/min is used in the shear test of lap joint in this case.

3.3 RESULTS

3.3.1 Microstructure

Optical metallographic of welded joint was carried out at the materials science and engineering department *(MNT of INSA-Rennes)* to observe the variation of microstructure content in Base Metal *(BM)*, Heat Affected Zone *(HAZ)* and Fusion Zone *(FZ)*. From these micrographs it is evident that the distribution of metallurgical phase and its grain is different inside the BM, HAZ and FZ. The grain nature and grain arrangement depend on the location where it heat at a given specific time and temperature and also the nature of cooling curve as shown in Fig.3.7.
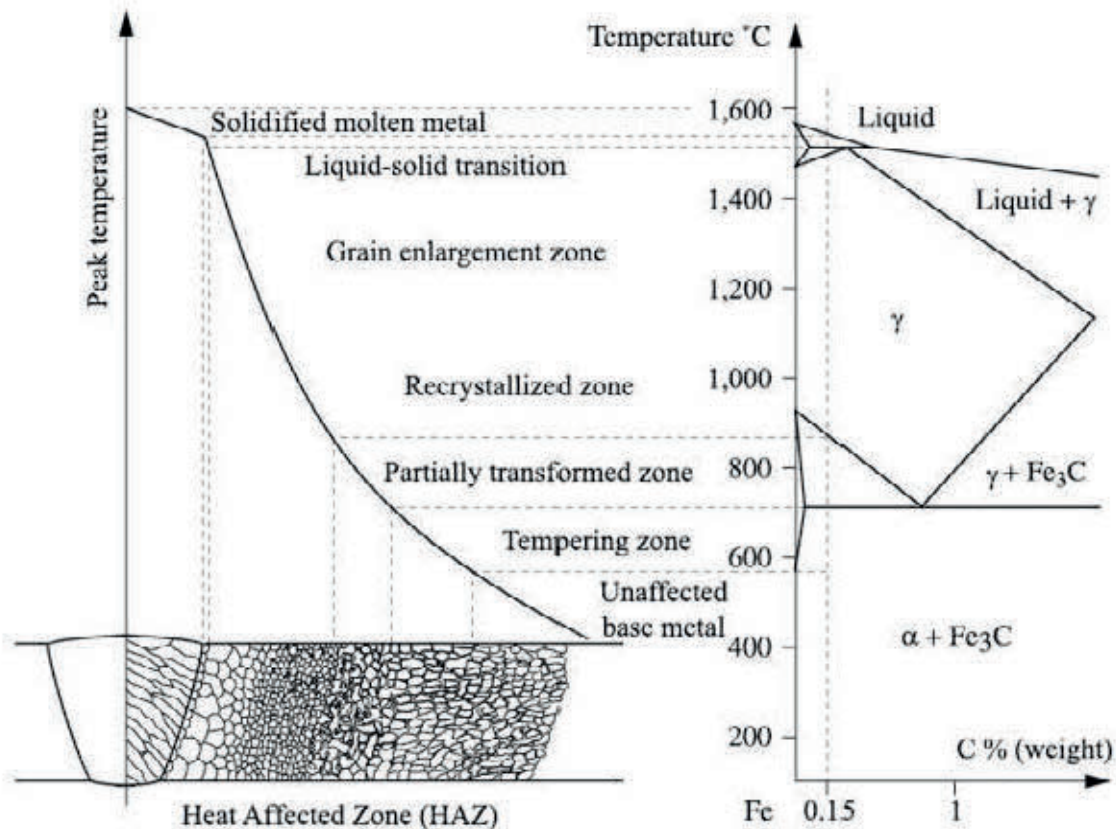
Fig.3. 7 Microstructure of welded joint [8]

82

The scanning electron microscopy (SEM) is also used to observe the microstructure of weld joint. The SEM model JOL JSM-6301F at the CMEB *(Centre de Microscopie Electronique à Balayage et micro-analyse)* of Rennes-1 University.

3.3.1.1   Parent Metal or Base Metal *(BM)*

Fig.3.8 presents the microstructure of dual phase steel DP600 constitutes of ferrite grains show in white color with a matrix containing islands of martensite presented by the grain in brown/dark color. Its chemical and metallurgical property had been studied in many research works [7, 4, 15, 12, 5].
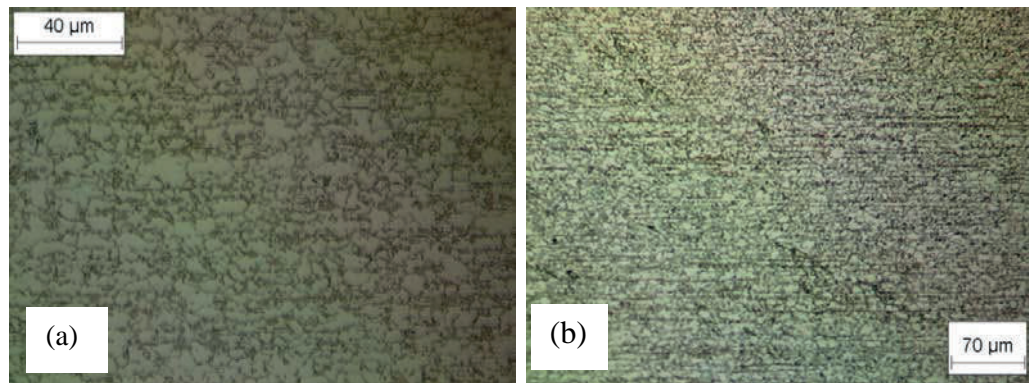
Fig.3. 8 Optical microstructure of BM
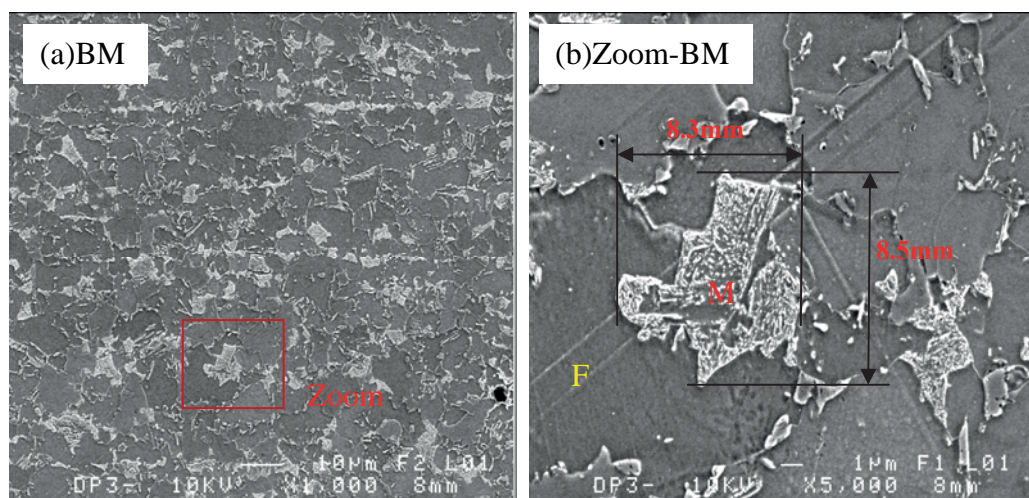
Fig.3. 9 SEM micrographs of BM

83

The image of microstructure of DP600, Fig.3.9, from scanning electron microscopy (SEM) technique seems to be clear and identifiable compared to the image from Optical microscopy technique (OM). The lamellar structure, anisotropy of martensite in the matrix of ferrite, appears in the base metal (BM) by the distribution of martensite grain in white color aligned horizontally which is parallel to the lamellar direction as indicated in Fig.3.9 (a). The size of martensite islands was varied from 2µm to 8.3µm as shown in Fig.3.9 (a) and Fig.3.9 (b).

3.3.1.2   Heat Affected Zone *(HAZ)*

The optical microscopic image shows that the white colors of ferrite grains were disappeared progressively inside the HAZ from BM's front to FZ's front, where its width is about 300 micrometers as presented in Fig.3.10 (a). At the interface between the BM and the HAZ the number of ferrite grain reduces sharply to zero inside the HAZ within only a distance of around 70 micrometers from the BM to the HAZ, Fig.3.10 (b), it is consider to be the tempered zone and the partial transformed zone where the aging of the ferrite phase by carbon segregation on the dislocation introduced by the welding process in the zone where temperature less than Ac_1. The fast cooling of the partial transformed zone causes an increase of martensite volume fraction. The formation of ageing ferrite [10] and martensite causes sudden increase in the microhardness as presenting in the section 3.5.

The austenitization complete inside the HAZ, where temperature increase from Ac_3 *(830^oC)* to the fusion temperature, causes the re-crystallization and grain enlargement close to the FZ *(1440°C)*. During the rapid cooling cycle austenite grain transform to coarse grain of martensite as indicated in Fig.3.10 (d-e).

The present of distribution of martensite is the same and gives a stabilize value of microhardness inside the HAZ and the FZ about 400VHN described by the indented shape of Vickers hardness measurement in Fig.3.10 (f) and Fig.3.10 (g). The microhardness measurement in section 3.5 and the cooling time from 800^oC to 500^oC, $t_{8/5}$ in thermal simulation, *chapter 5*, and also in literature [2] are also confirmed this statement.
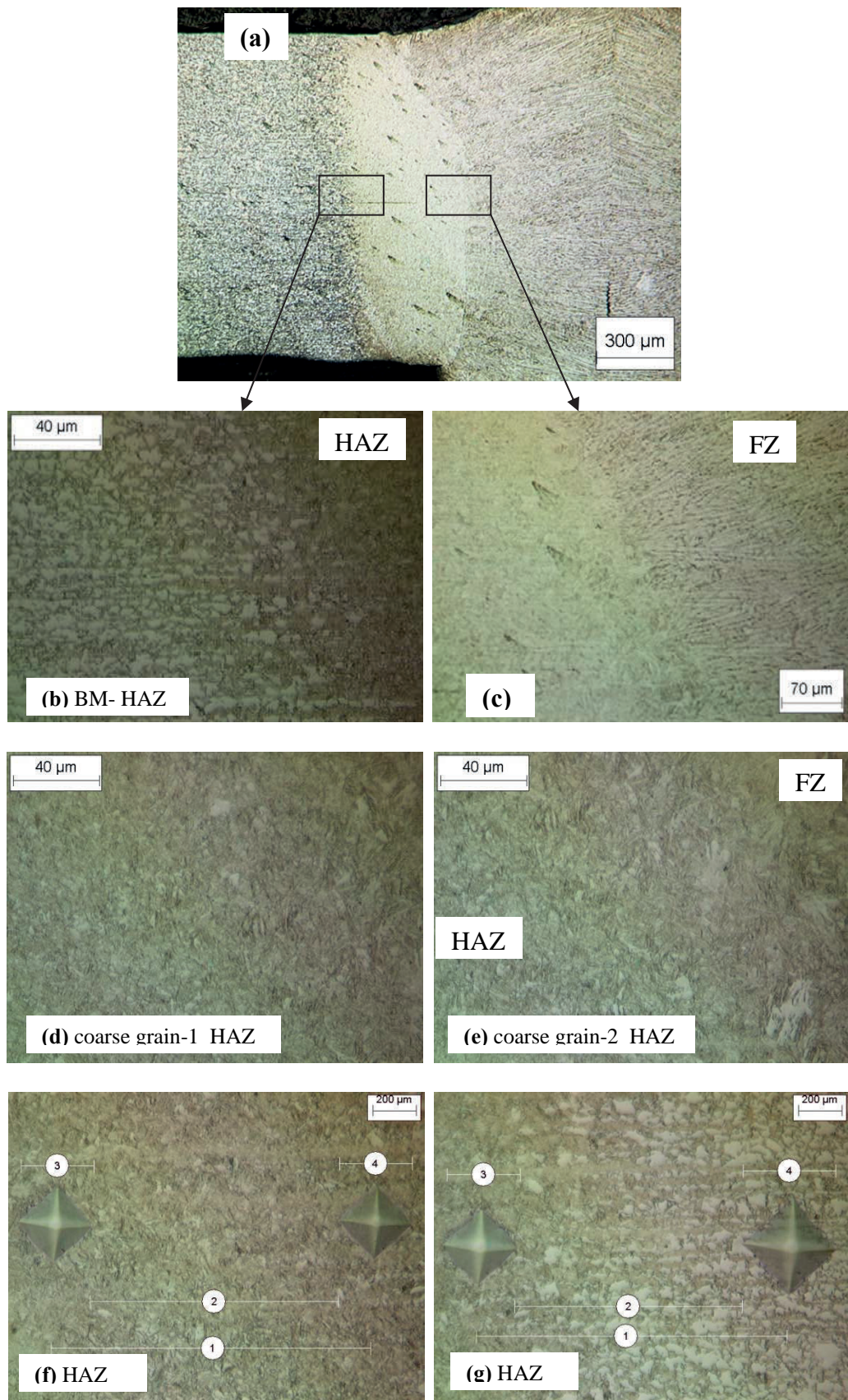
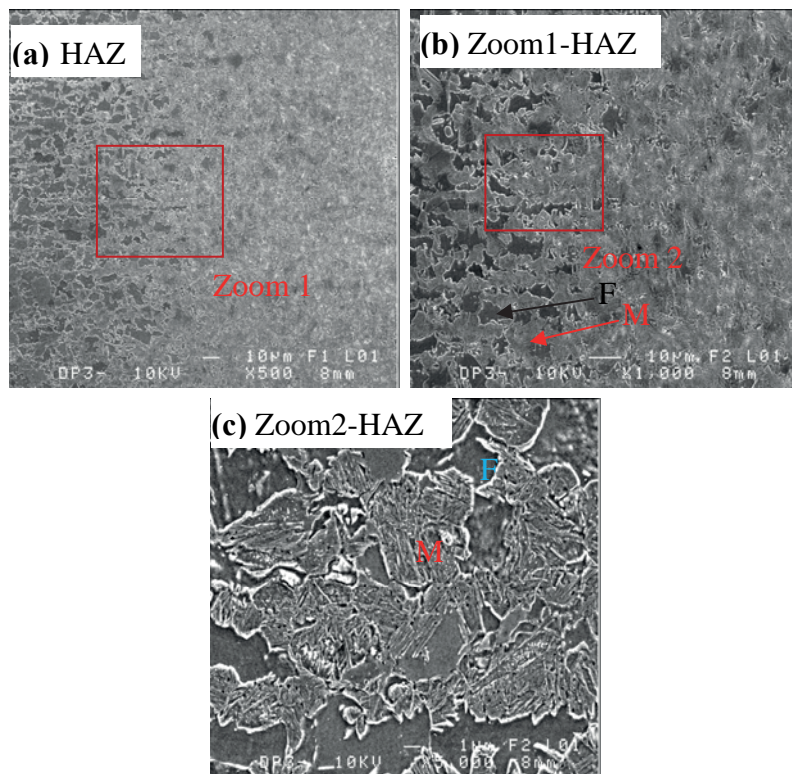Fig.3. 10 Optical microstructure of HAZ

Fig.3. 11   SEM micrographs of HAZ

The SEM technique used to observe the variation of volume fraction of martensite inside the HAZ. The martensite volume fraction increase from the BM to the FZ in a short distance of 50-70µm *(BM-HAZ)* as showed in Fig.3.11(a) and a large view in Fig.3.11(b) and Fig.3.11(c). At a distance of 70µm from BM the ferrite grain is eliminated. Only the martensite volume fraction is appeared inside the HAZ closed to the FZ.

3.3.1.3   Fusion Zone *(FZ)*

The martensite experience coarsening in the FZ as shown in Fig.3.12(a), Fig.3.10(k), Fig.3.12 (a-b-c-d) this coarsening is observed high in the FZ compared to the HAZ, Fig.3.10 (i-j), because the degree of coarsening increase with an higher degree of austenitizing temperature during the cooling phase after passed by laser heat source.

86
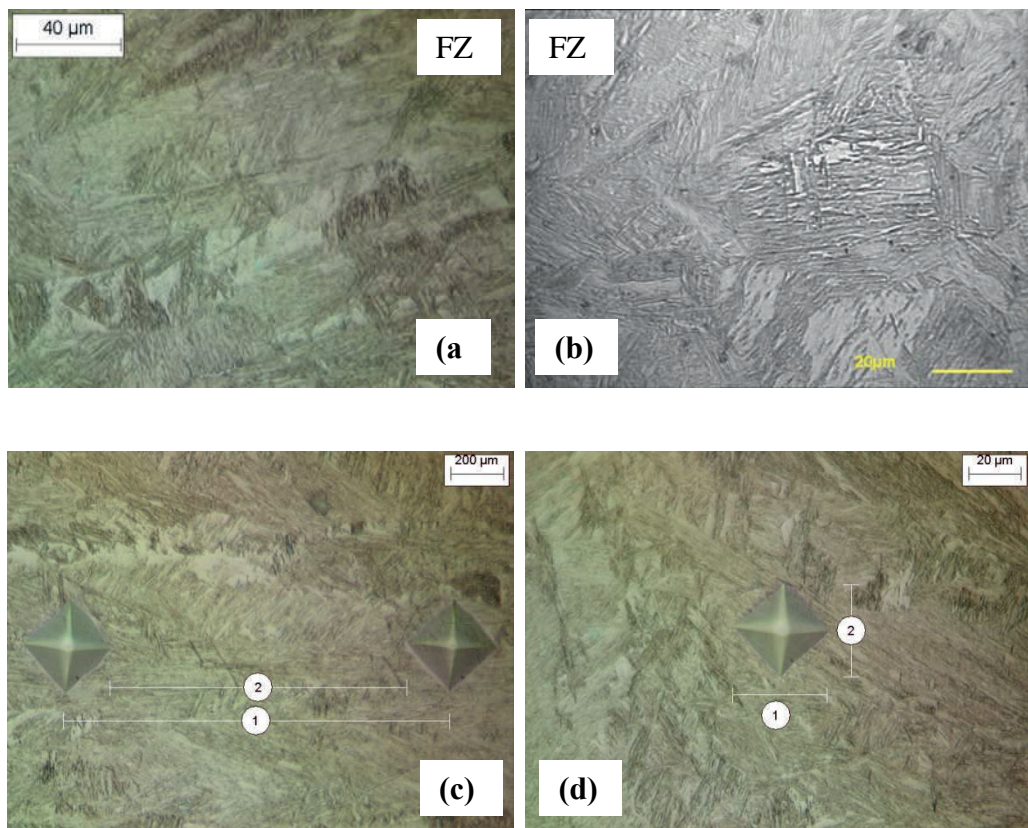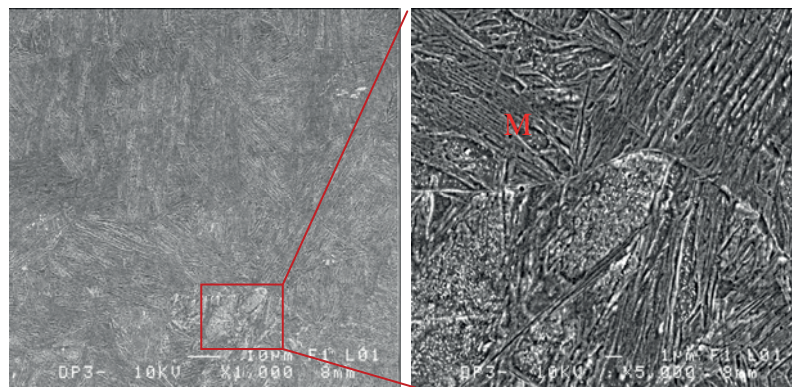
Fig.3. 12 Optical microstructure FZ

Fig.3. 13 SEM micrographs of FZ

The SEM technique of FZ, Fig.3.13, presents also the dominated martensite volume fraction inside the FZ. No ferrite grain has been observed inside this zone.

3.3.2 Lap joint dimension

3.3.2.1 Preparation

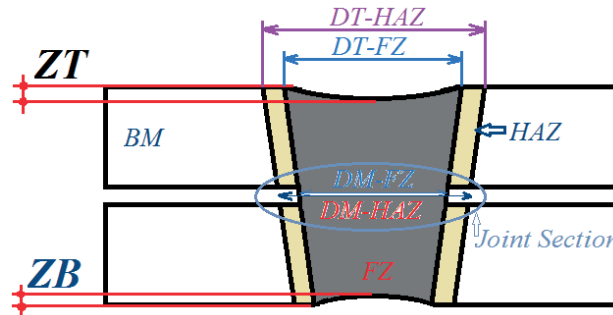The parameters of the joint cross section under effect of welding parameters, as shown in Fig.3.14, to be studied are:

Fig.3. 14 Weld bead cross section

- The Dimension of Fusion Zone on Top surface *(DT-FZ)*, on the inter-metal joint *(DM-FZ)*.
- The Dimension of Heat Affected Zone on Top surface *(DT-HAZ)*, on the inter-metal joint *(DM-HAZ)*.
- The Metal lost in FZ on Top surface *(ZT)*, on Bottom surface *(ZB)*.

The *DM-FZ* is an important parameter of the lap joint assembly, because the strength of lap joint is depended on this dimension.

3.3.2.2 Influence of welding speed

Fives welding speeds are chosen for this study at 4kW at reference focal point position, the welding speeds are listed in Tab.3.5, the observation on the welded joint assume that all lap joints are open or penetrated welded joint.

Speed (m/min)	2.4	3.4	4	4.3	4.5
Sample Index	V1	V2	V3	V4	V5

Tab.3. 5 Speed variation

The influence of laser welding speed is illustrated in Fig.3.15 and Fig.3.16. Fig.3.17 shows a decrease of FZ and HAZ dimension when the speed increases from 2.4m/min to 4.5m/min. But the variation of FZ and HAZ on top and middle of the keyhole is not proportional. The FZ width on the middle of keyhole varies from 1.3mm to 1.1mm, are less sensitive to the variation of speed compared to the dimension on the top of the keyhole. So the speed variation has less influence on the dimension of the middle bead width *(DM)*.

At welding speed 4.5m/min, the FZ and HAZ widths at the interface of the top and the bottom sheet are increasing *(DM-FZ and DM-HAZ)* as illustrated in Fig.3.15 and Fig.3.17(b), this is maybe come from the results of multiple reflection were highly concentrated at the middle part of the keyhole. This increase in multiple reflections caused an increase in plasma absorption in that region, resulting in the widening of the weld width as proofs in [1].
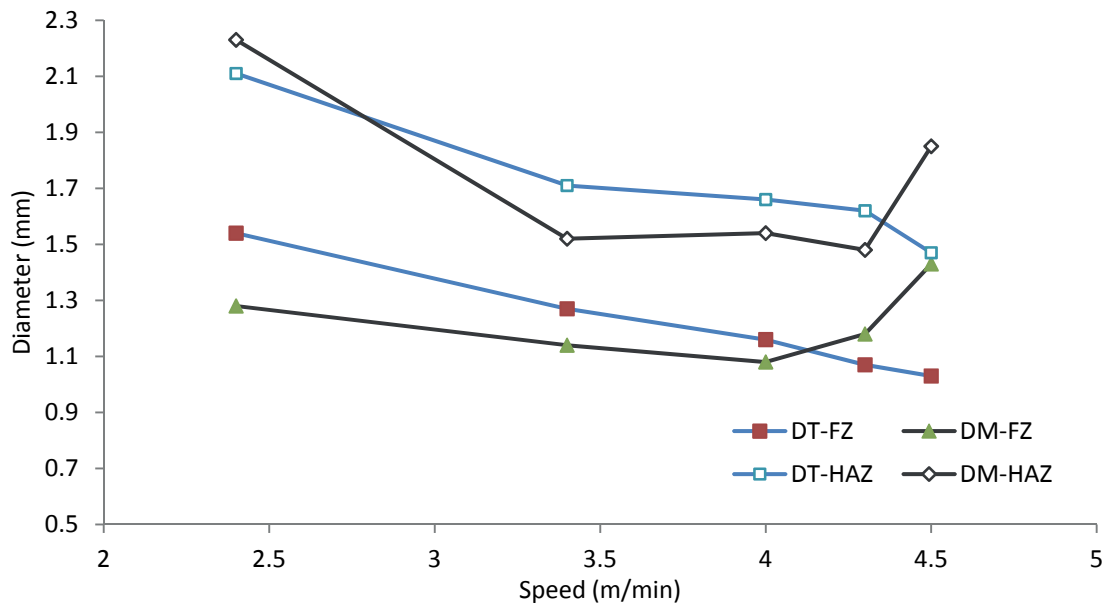

Fig.3. 15 Dimension of lap joint under effect of speed variation

The FZ height lost on top surface, indicated in Fig.3.16, become very important compared to the FZ height lost on the bottom surface because the higher welding speed creates thinner FZ width on top surface and enlarges FZ width at the middle of the FZ height,

The external concavity on the top sheet become important when the welding speed increases from 4m/min to 4.5m/min.
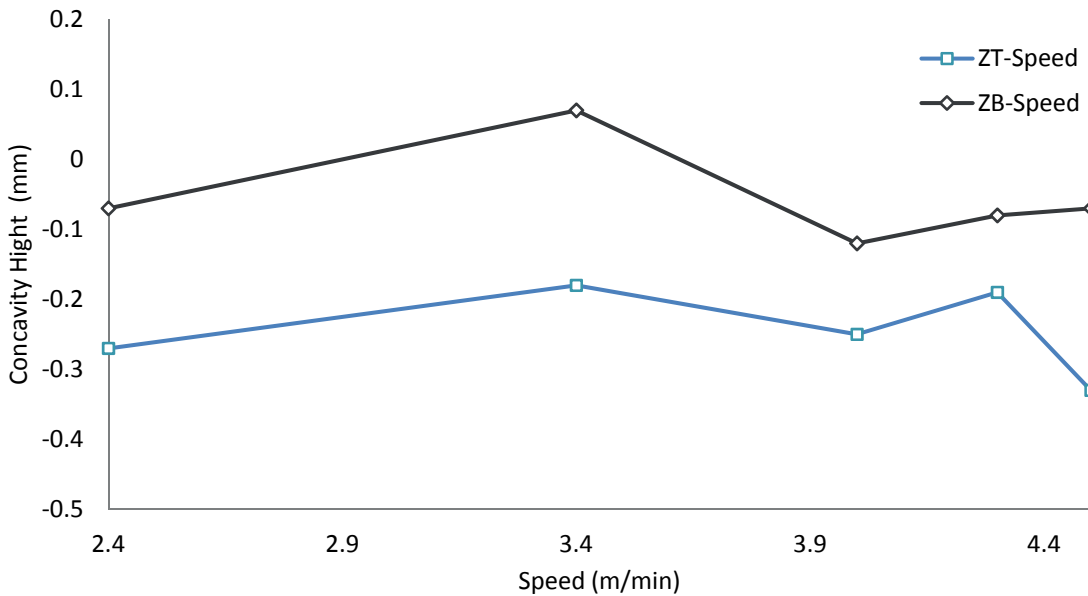

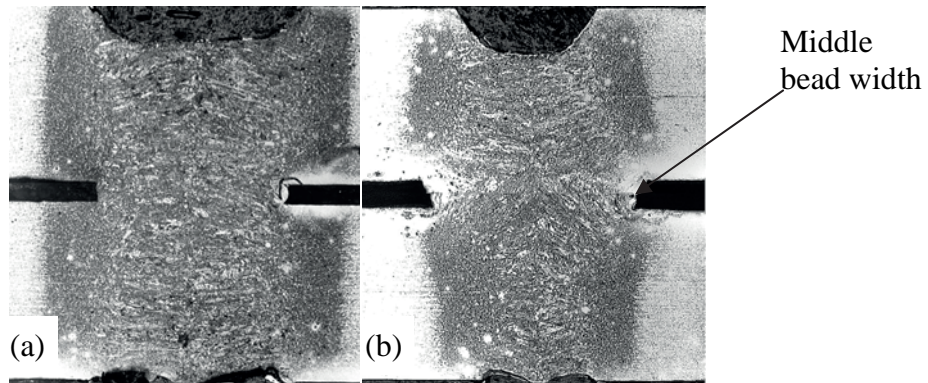Fig.3. 16 Concavity under influence of speed variation

Fig.3. 17 weld cross section corresponds to the welding speed 2.4m/min (a) and 4.5m/min (b)

So the higher welding speed cannot reduce the imperfection caused by the higher laser power used because the higher speed cannot reduce the power density inside the keyhole, but rather it create a higher concavity on top and root of the weld bead by reducing the bead width as presented in Fig.3.17 (a) and Fig.3.17 (b). Otherwise, the higher welding speed increasing the middle bead width as indicated in Fig.3.15.

3.3.2.3   Influence of focal point position

Three focal points positions of laser power situate at 0mm, 4mm and 8mm from top surface of sheet metal which was defined in the previous research in laboratory [7] are used in this study, as indicated in Fig.3.18, which are welded with laser power of 4kW at welding speeds, shown in Tab.3.6.

Power 4kW	Focal Point		
Speed	*0mm*	*4mm*	*8mm*
2.4m/min	A0	A4	A8
3.4m/min	B0	B4	B8
4.3m/min	C0	C4	C8
4.5m/min	D0	D4	D8

Tab.3. 6 Focal point variation
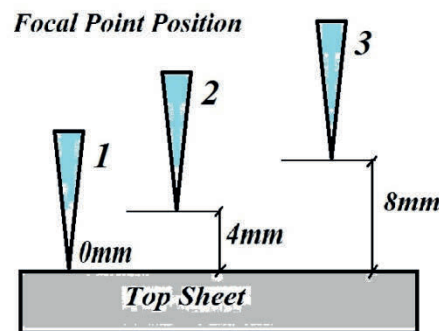
Fig.3. 18   Laser focal point position

The results of top weld bead widths include the FZ *(DT-FZ)* and HAZ *(DT-HAZ)* under the influence of welding speeds are shown in Fig.3.19, where each curve represents the bead widths at a fixed focal point position *(0mm, 4mm and 8mm)*.

The width of FZ and HAZ are decreased during increasing the welding speed at reference focal point *0mm* and focal point at *4mm* but it become less sensitive to the welding speed variation when the focal point situated at *8mm* from top sheet as indicated in Fig.3.19. Anyways at higher speed, 4.5m/min, with focal point 8mm, the width of HAZ increase but

91

the FZ width decrease instantly, because the laser density is less than the power density at lower focal point position and it is sufficiency to increase the HAZ width.
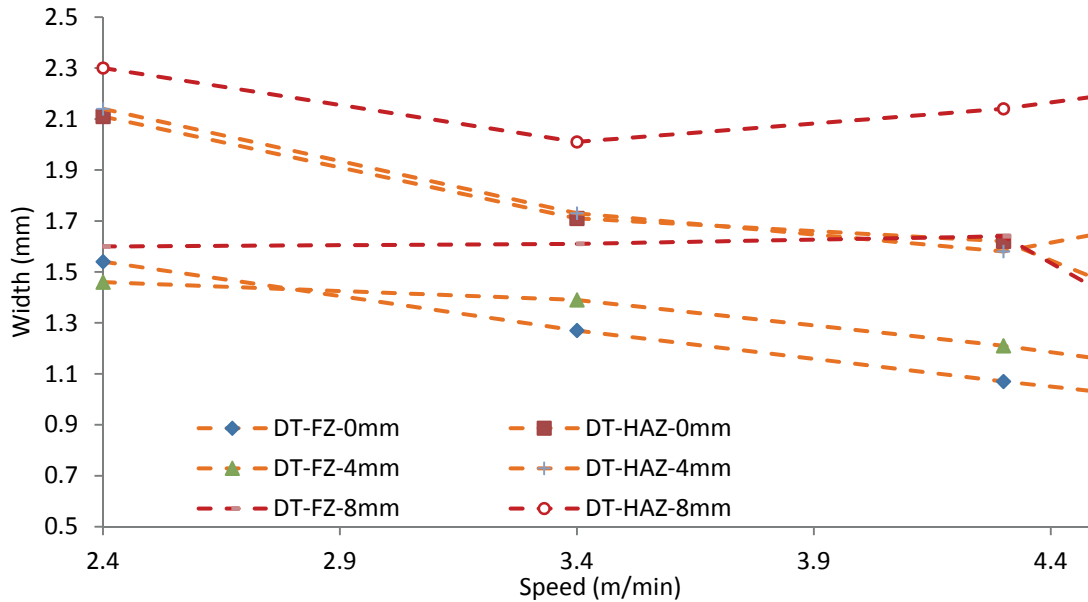

Fig.3. 19 Dimension on top of the upper sheet

Fig.3.20 represents the variation of FZ and HAZ width at the joint section *(DM)* under influence of welding speed with different focal points positions *(0mm, 4mm and 8mm)*.

The observation on curves represent the width of FZ and HAZ at three focal point positions under speed variation indicate that the 4mm focal point position, represented by the curve DM-FZ-4mm and DM-HAZ-4mm in Fig.3.20, seems to be more advantage than 8mm focal point position. Not only the widths variations of FZ in the jointed area *(DM)* are more stable than the others focal points position but also it is larger than that of others values of focal point position *(0mm and 8mm)*.

At higher welding speed *(more than 4mm/min),* the FZ and HAZ width are increased, this is maybe come from the reflection of laser beam inside the weld pool for welding with focal point 0mm and 4mm and non penetrated joint for 8mm focal point position as illustrated in Fig.3.22.

Fig.3.21 shown the variation of metal lost inside FZ represented by the curve ZT for the concavity height on top surface and ZB for the concavity height on bottom surface as represented in Fig.3.14.
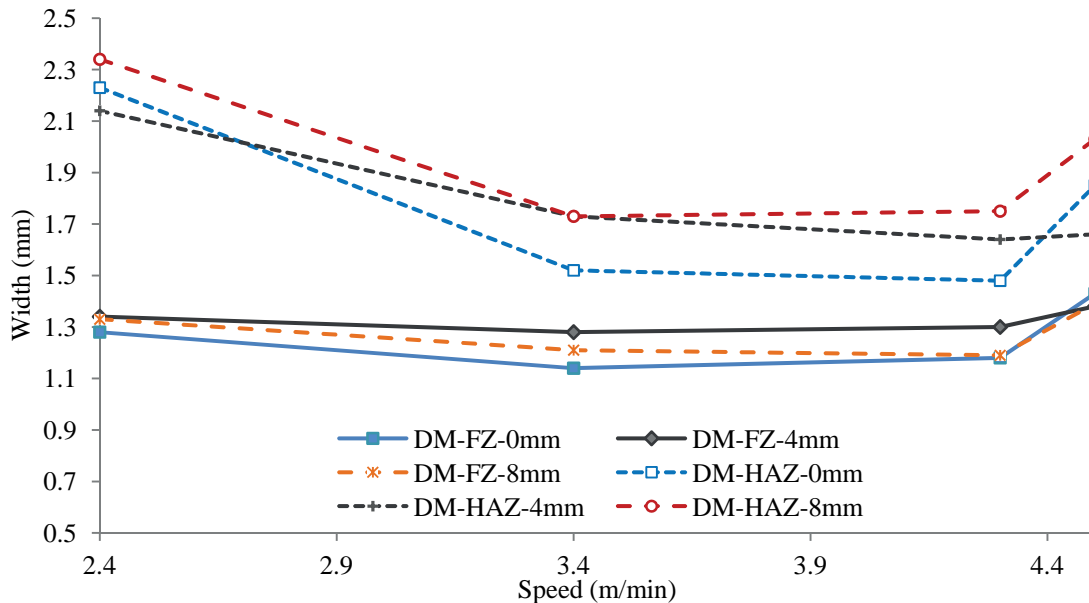

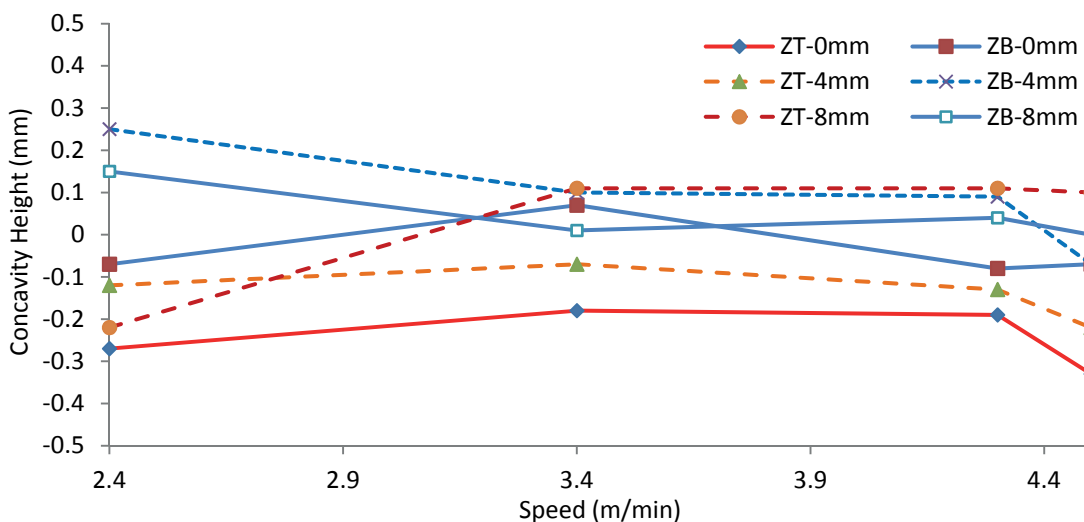Fig.3. 20 Dimension of FZ (mm) under effect of focal point position

Fig.3. 21 Lost of depth inside the FZ

The 4mm and 8mm focal point position can reduce the metal lost inside the FZ compared to the 0mm focal point position. But the 8mm focal position is more advantage in term of reduction the concavity height compared to the focal point situate at 4mm because of the divergence of laser beam on the top surface of sheet metal. The welding speed should be

93

more than or equal to 3.4m/min for 4kW welding power. Otherwise the concavity is still important even with 8mm focal point position because the power density is still high.

So, at the same welding speed and the same power used, the higher focal point position, 8mm, can also reduce the metal lost inside the FZ *(concavity)* and respectively enlarging the FZ and the HAZ widths as illustrated in Fig.3.22 (b and d).
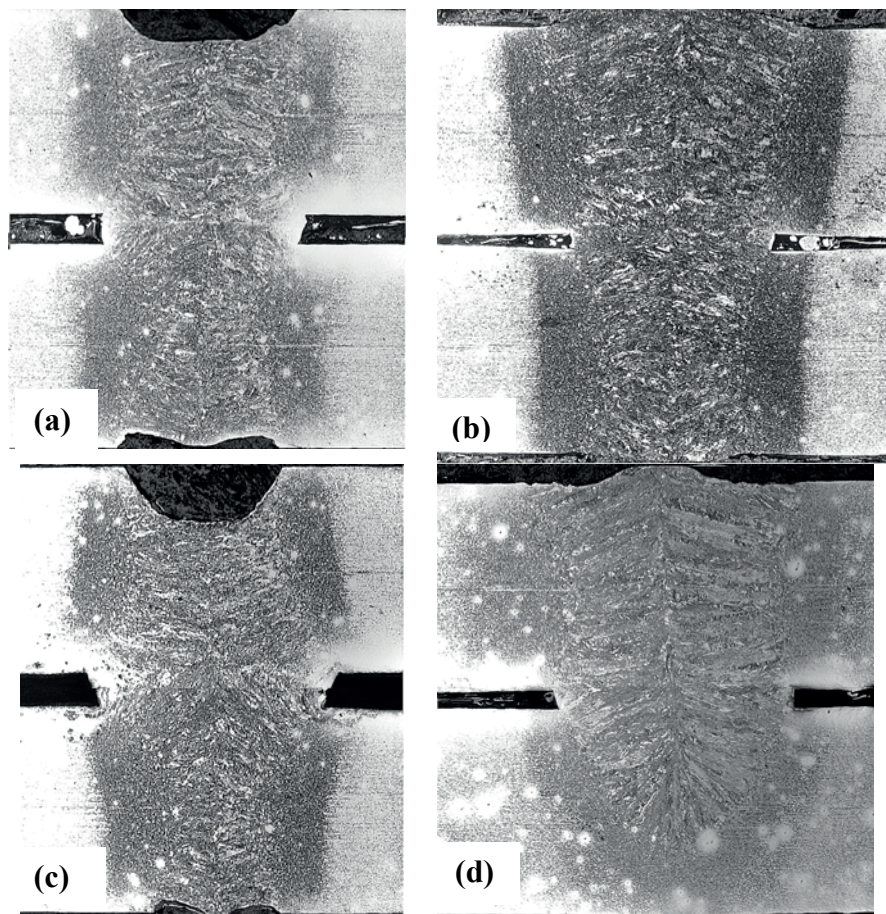

Fig.3. 22 Cross section lap joint under influence of focal point variation

From the illustration of HAZ width and the FZ widths on top sheet in Fig.3.19, the HAZ and FZ width of jointed area in Fig.3.20, and the lost of bead height in Fig.3.21, the focal position situated from 4mm to 8mm of top surface give better weld bead than 0mm focal point position. One can conclude that the focal point is a parameter that influent the imperfection of welded joint at higher power and higher speed of laser welding.

3.3.2.4   Influence of laser power

In this section the focal point position is on the surface of the top sheet that suppose to be the reference focal point position *(0mm)*, with a constant welding speed of 4.3m/min, the powers used are changed as shown in Tab.3.7 below.

Power (kW)	4	3.5	2.7	2.5	2.2
Sample index	P1	P2	P3	P4	P5

Tab.3. 7 Power variation

The variation of FZ and HAZ widths under influence of laser powers from 2.2kW to 4kW are shown in Fig.3.23.
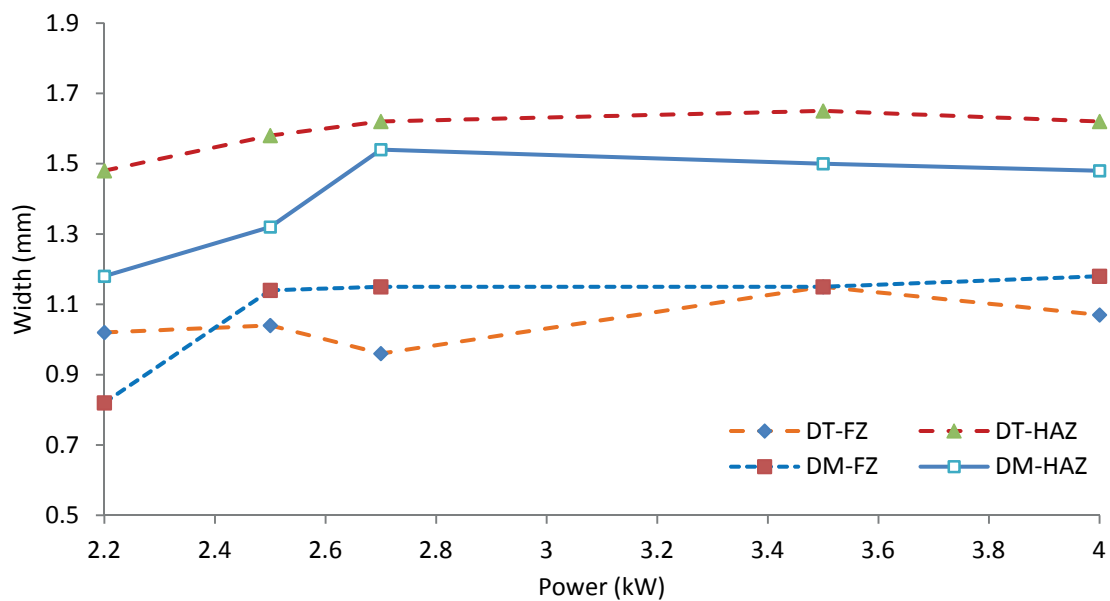

Fig.3. 23 Dimension of FZ and HAZ under effect of power variation

The HAZ widths, represented by the curve DT-HAZ and DM-HAZ, increase from laser power 2.2kW to 2.5kW and then become stable until maximum power. So the higher power used is not affected on the HAZ widths but the HAZ and FZ widths are sensitive to the lower power used as presented in Fig.3.23.

Fig.3.24 represents the variation of metal lost inside FZ represented by the curve *ZT-Power* for the concavity height on top surface and *ZB-Power* for the concavity height on bottom surface.
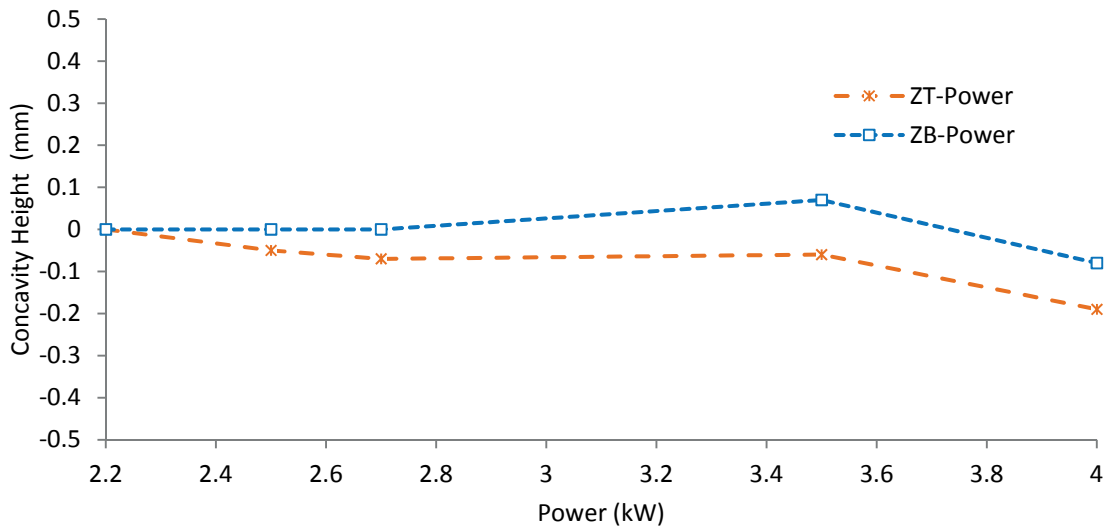
95

Fig.3. 24 Depth lost of FZ under effect of power variation

According to the results plotted in Fig.3.24, the higher power used causes concavity on top surface and excessive penetration on the root of the FZ and the lower power used creates an incomplete penetration as shown in Fig.3.25.

The different shapes of minimum and maximum power used are illustrated in Fig.3.25. The incomplete penetration is belonged to the lower power used, 2.2kW. The excessive penetration belonged to the 4kW power used that causes the concavity on top of the bead and undercut on the root of the bead.

So the laser power affects on the depth of the FZ but not affects on the width of the HAZ of the FZ as shown in Fig.3.23, and Fig.3.24. Furthers more it causes a concavity and excessive penetration at higher power used.
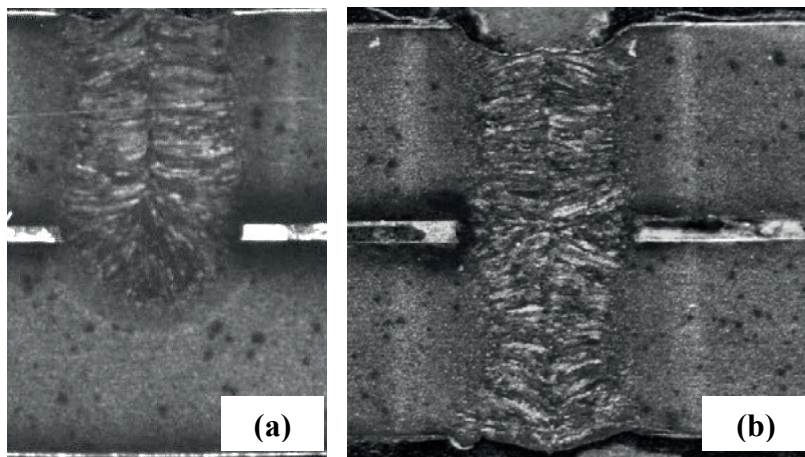

Fig.3. 25 Cross section of lap joint 2.2kW (a), and 4kW (b)

3.3.2.5 Synthesis

The analysis of lap joint dimension proves that:

- Increasing the focal point position can reduce the power density in the keyhole by increasing its volume and can increase the DM width and also reduce the geometric shape imperfection. But it causes a wider HAZ.

- Increasing welding speed cannot reduce the imperfection caused by the higher laser power used because the higher speed cannot reduce the power density inside the keyhole as much as focal point position, but rather it create a higher concavity on top and root of the weld bead by reducing the bead width.

- Increasing the laser power allows to have a deeper penetration. The variation of laser power affect less the width of FZ and the width of HAZ. Without increasing the focal point position, the higher power used create a higher concavity on top surface of the weld bead.

The observation of cross section of lap joint allows us to choose a better parameter of higher speed laser welding are, for power used more than 3.5kW to 4kW, a focal point position situate at 4mm to 8mm with a welding speed from 3.4m/min to 4.5m/min.

A furthers observations on mechanical properties of lap joint are presented in section 3.3.3 and section 3.3.4.

3.3.3 Hardness of welded joint

Hardness test is used to provide generic information on the material properties such as toughness and strength. Hardness measurements provide indications of metallurgical changes caused by welding and microstructural discontinuities in welded joints, brittleness, and relative sensitivity to cracking under structural loads.

Hardness testing of welds and its HAZ usually requires testing on a microscopic scale using a diamond indenter Fig.3.26. The Vickers Hardness test is the predominant test method compared to others hardness testing technique, the Vickers Hardness Number *(VHN)* is used to identify the level of hardness [20].

The observation on hardness of welding samples with different powers and speeds are base on the measurement of microhardness on the middle thickness of the sheet metal across the base metal *(BM)*, the heat affected zone *(HAZ)* and the fusion zone *(FZ)* of the joining section and also along the depth of the fusion zone from top to bottom sheet.

The comparison is separated to the different values under influence of welding speed and welding power as showing in the following section.
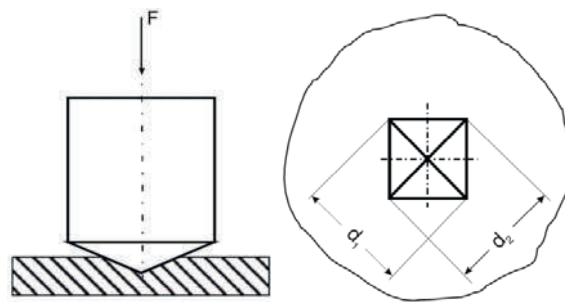
Fig.3. 26 Vickers microhardness

The peak of hardness and martensite volume fraction inside the FZ and the HAZ are due to high power density used, high welding speed and also the thickness of sheet metal [10] and also the nature of chemical composition of base metal too [16] as indicated in Fig 3.27.
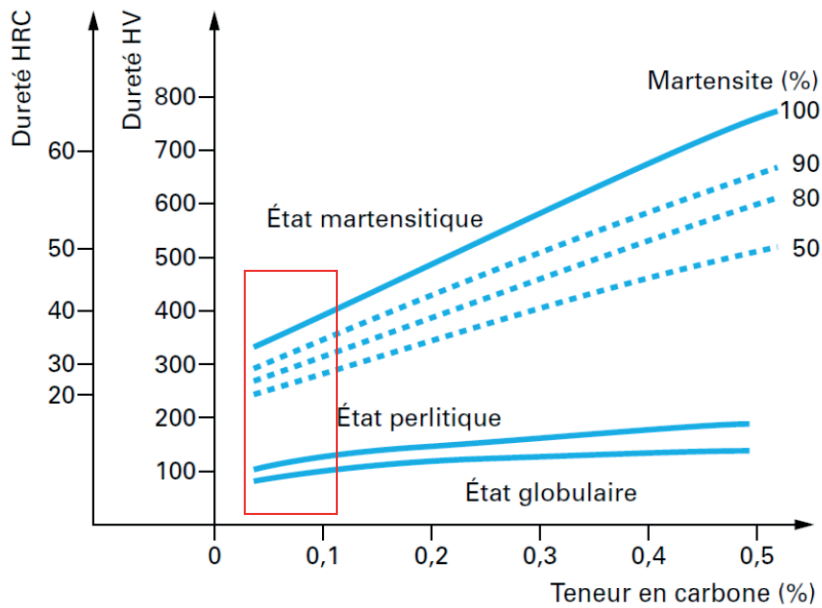
Fig.3. 27 Variations of hardness of steels according to their carbon content [16]

98

3.3.3.1 *Sensitivity of microhardness testing machine*

The different loads and the indent spaced are used with the sample dwell time of 15 seconds to test their effects on the value of hardness. The tests are done on the parent metal of DP600 and five indented point for each measurement. The Tab.3.8 below shows the values of loads and the indent spaced for each loads applied in the Miyutoyo microhardness testing machine Fig.3.28.

N°	Test force (kg)	Indent spaced (mm)
1	0.5	0.3,
2	0.3	0.1
		0.15
		0.3
3	0.1	0.1
4	0.05	0.15
		0.05
5	0.025	0.05

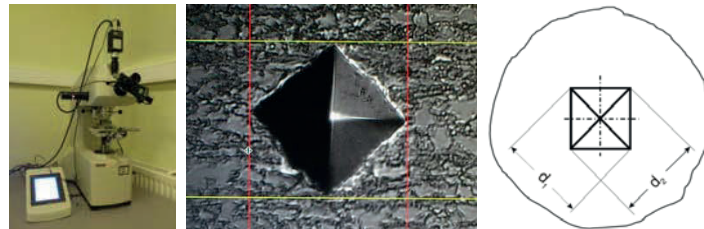Tab.3. 8 Testing parameter of hardness testing machine

Fig.3. 28 Mitutoyo Micro hardness testing machine

The peak value of hardness measured on base metal by a 0.3kg test force and different increment are shown in Fig.3.29. The maximum value, the minimum value and the medium value of the measurements are represented by Max, Min and Moy respectively.

Fig.3.29. show the hardness in function of indented loads (0.05, 0.25, 0.1 and 0.3kg) and different increment *(0.05mm, 0.10mm, 0.15mm and 0.3mm)*. The maximum value, the minimum value and the medium value of the measurements are represented by Max, Min and Moy respectively. The testing force 0.1kg- increment0.1mm, 0.3kg-increment 0.3mm

and 0.5kg-increment 0.3mm give a value of hardness of DP600 similar to the hardness of DP600 in literature[21]. But the test force 0.1kg give small indented shape so it needs more preparation time to get the value compared to the testing force 0.3kg and 0.5kg. The increment 0.3mm decreases the number of measurement across the weld joint cross section.
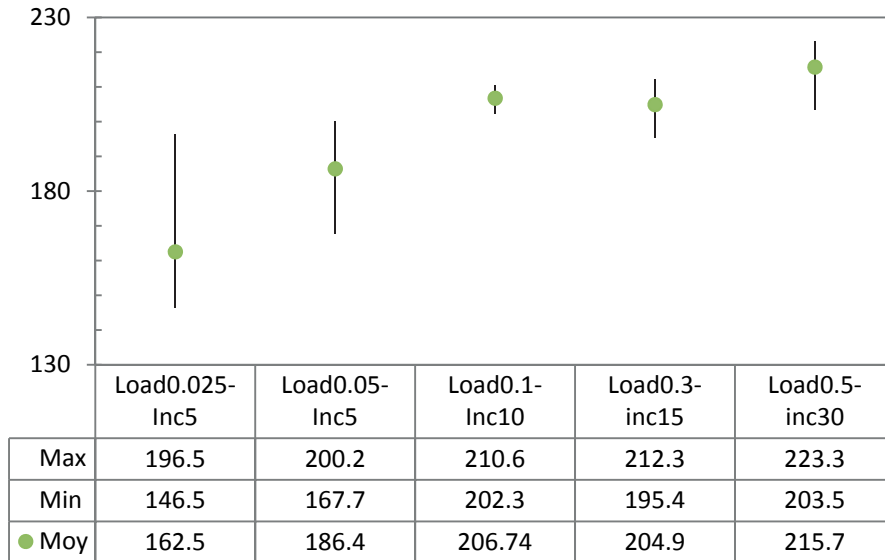

	Load0.025-Inc5	Load0.05-Inc5	Load0.1-Inc10	Load0.3-inc15	Load0.5-inc30
Max	196.5	200.2	210.6	212.3	223.3
Min	146.5	167.7	202.3	195.4	203.5
● Moy	162.5	186.4	206.74	204.9	215.7

Fig.3. 29 Variation of load and increment

Fig.3.30 shows the variation of precision getting from a test force 0.3kg with indented space 0.1mm, 0.15mm and 0.3mm. The indent spaced 0.15mm gives almost the same value of hardness sensitivity to the indent spaced 0.3mm and also it allows doubling the number of indent compared to a 0.3mm indent spaced. The indent spaced 0.30mm with a 0.3kg test force gives lower amplitude of hardness value *(low sensibility)* compared to the others indent spaced.

Base on the comparison of load and indent spaced, show in Fig.3.29 and Fig.3.30, the test force of 0.3kg with adequately space of 0.15mm and the test force of 0.1kg with indent spaced 0.1mm give the hardness value close to the hardness value in the literature of DP600[21]. So the couple load and indent spaced *(0.3kg, 0.15mm)* and *(0.1kg, 0.1mm)* are using in the measurement of hardness across the welded cross section.

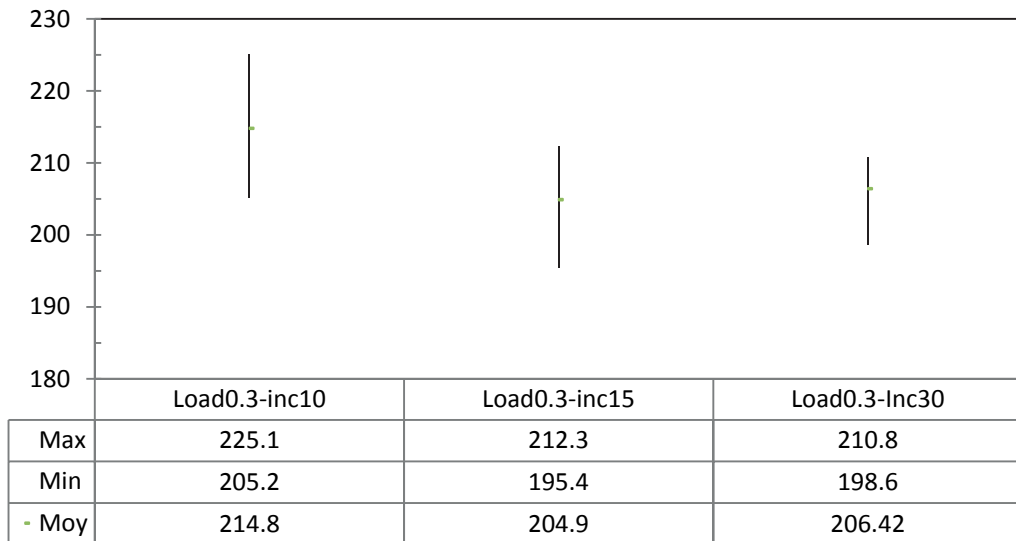|	Load0.3-inc10	Load0.3-inc15	Load0.3-Inc30
Max	225.1	212.3	210.8
Min	205.2	195.4	198.6
• Moy	214.8	204.9	206.42

Fig.3. 30 Test force 0.3kg with variation of increment

Fig.3.31 shows the microstructure and the indented shape on cross section of welded joint that include the indentation and microstructure inside the BM, HAZ and FZ. The size of indented shape is reduced from the BM to HAZ. One observed the same size of indented shape inside the HAZ and the FZ. These tests allow us to confirm the microstructure change inside the HAZ and the FZ.

Base Metal (BM)
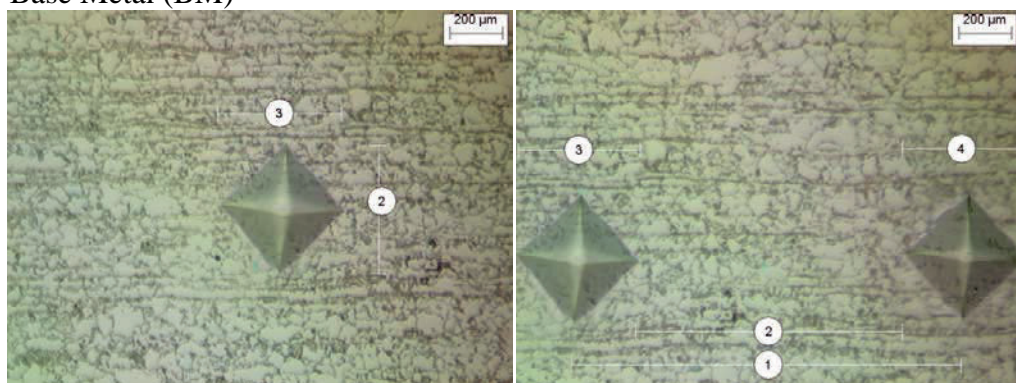
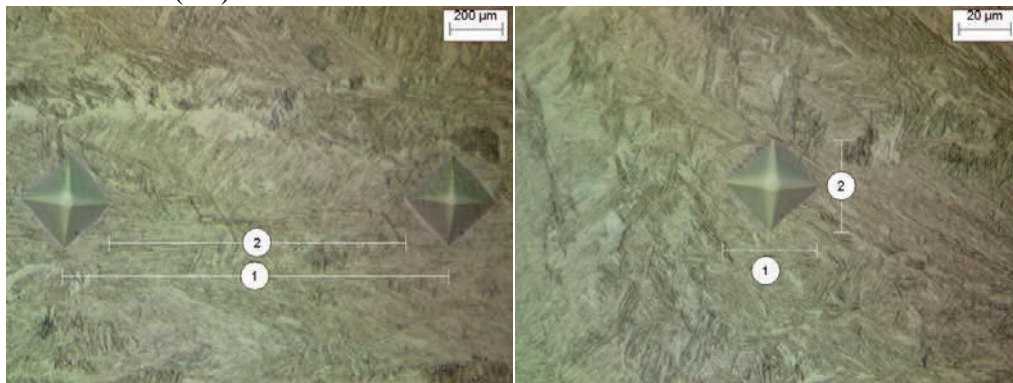Heat affected zone (HAZ)

Fusion zone (FZ)

Fig.3. 31 indented shape on metal

3.3.3.2 *Influence of laser power*

The microhardness measured along the horizontal mid-line *(0.62 mm from top surface)* on the top sheet of welded joint of laser power 2.2m/min to 4kW are presented in Fig.3.32. The microstructures along the vertical line inside FZ are presented in Fig.3.33.
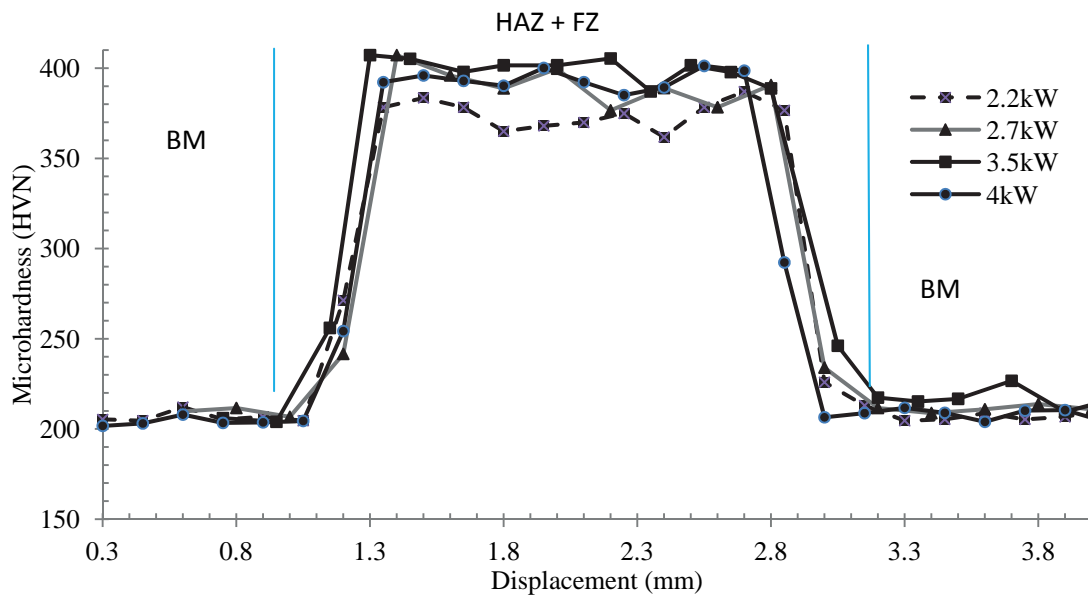
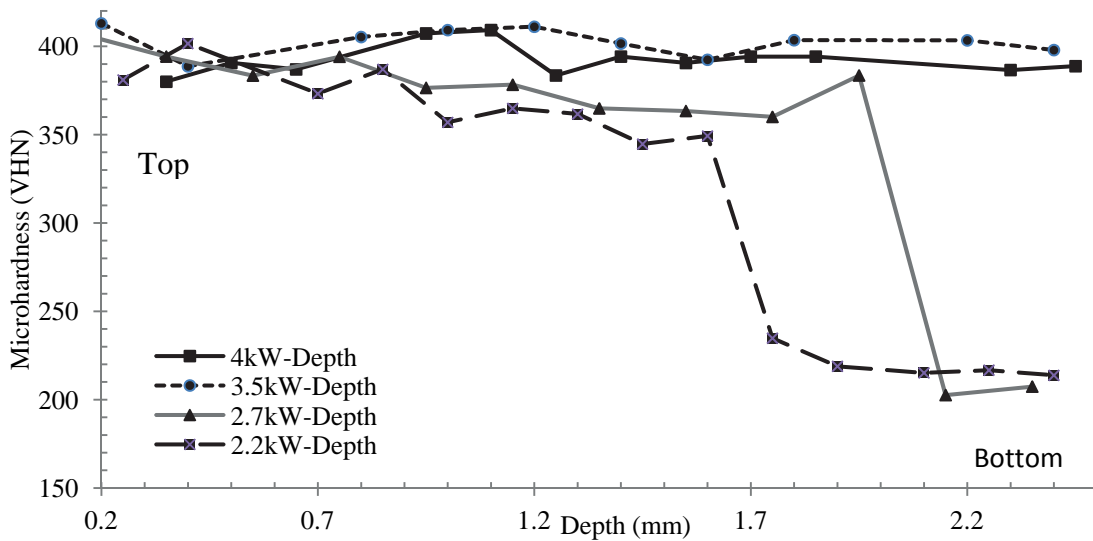Fig.3. 32 Microhardness under influence of power variation

Fig.3. 33 Microhardness along the depth of FZ

From the lower power (2.2kW) to the maximum power of the laser welding machine (4kW) at a constant welding speed (4.3m/min) and 0mm focal point position the hardness increase from 360+/-15VHN to 400+/-15 VHN inside the FZ and the HAZ. So one can assume that the hardness increases when the laser power increase, as indicate in Fig.3.33.

The decrease of hardness along the depth of FZ, from top to bottom sheet, is also under effect of power density reduction along the depth of FZ, in Fig.3.32, where the

hardness drop sharply, from 400+/-15VHN to 200+/-10VHN when the power is in minimum value, case of 2.2kW. Base on the illustration in Fig.3.32 and Fig.3.33, the power density played an important role in the formation of hardness inside FZ and HAZ. But the hardness inside FZ cannot be lower than 360+/-15 VHN for DP600 steel. The same hardness value has been conducted for two welding processes, in the work of XIA [21], by laser Nd: YAG *(power density of 10.6kW/mm²)* and diode laser *(power density of 0.67kW/mm²)* the measured hardness is 396 VHN and 322 VHN respectively.

So we can conclude that the power density variation has influence on the hardness inside FZ and HAZ.

3.3.3.3   *Influence of laser focal point position*

This study is base on the comparison of the hardness under influence of the focal point position 0mm and 8mm with two welding speeds, 2.4m/min and 4.5m/min at a constant welding power of 4kW.

Fig.3.34 shows the hardness of welded joint cross section on the top sheet at welding speed of 2.4m/min and focal point 0mm and 8mm from top surface. Fig.3.35 shows the hardness curve for welding speed 4.5m/ min with the same focal point position *(0mm, 8mm)*.
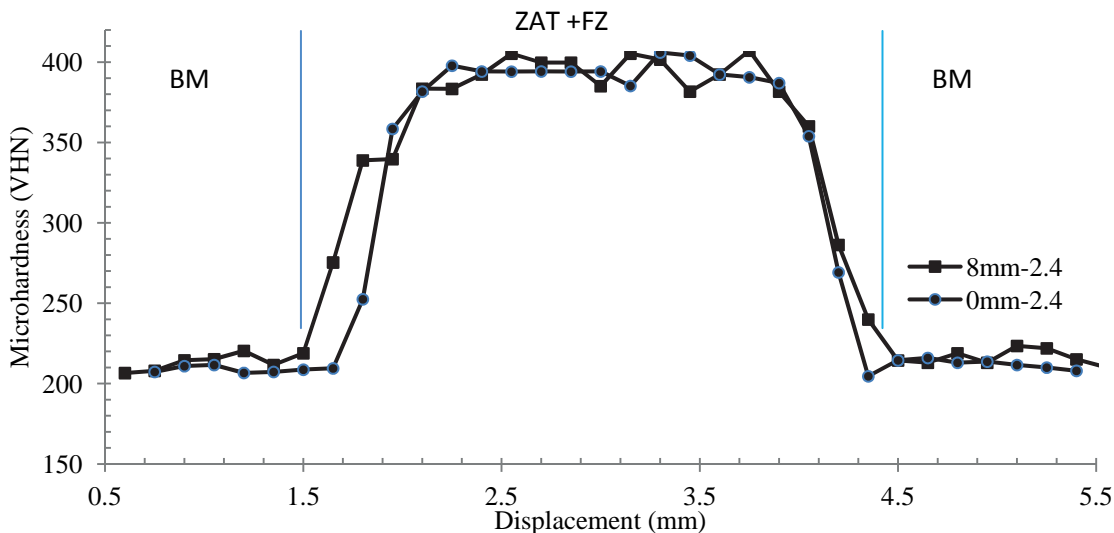

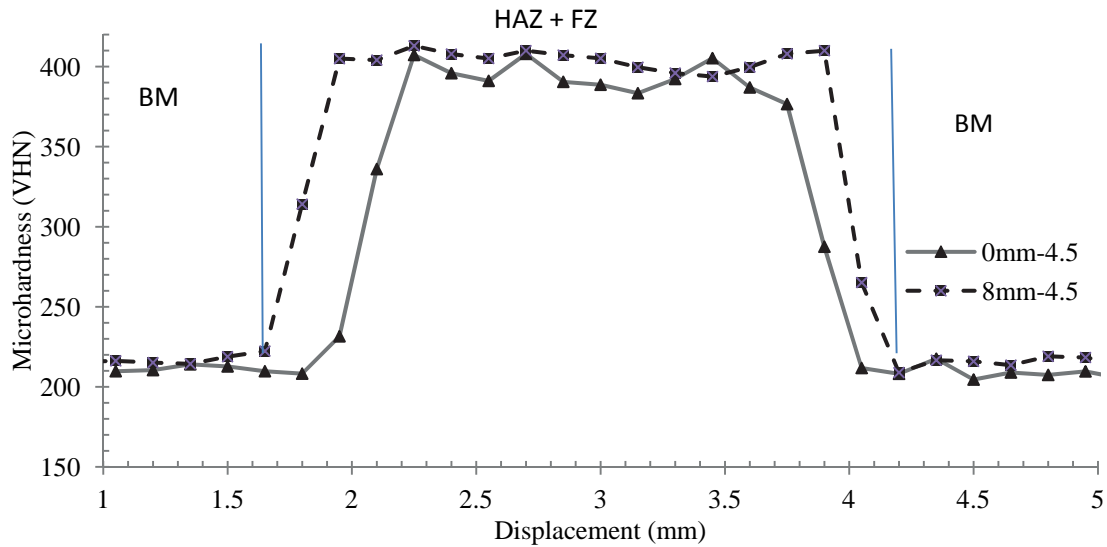Fig.3. 34 Hardness under influence of focal point of welding 4kW and 2.4m/min

Fig.3. 35 Hardness under influence of focal point for welding 4kW and 4.5m/min

The focal point position has less influence on the hardness inside the HAZ and no influence on the hardness inside FZ, for lower welding speed 2.4m/min, the hardness curve from difference focal point position are almost similar as indicated in Fig.3.34. But at higher welding speed 4.5m/min, Fig.3.35, increasing the focal point position enlarges significantly the hardness inside the HAZ. The maximum hardness inside HAZ and FZ are constant, 395+/-15 HVN, under influence of focal point position.

3.3.3.4   *Influence of welding speed*

Fig.3.36 shows the comparison of hardness getting from two welding speeds 2.4m/min, and 4.5m/min at reference focal point position. Fig.3.37 represents the comparison of hardness of welded cross section of two welding speed 2.4m/min, and 4.5m/m at 8mm focal point position.
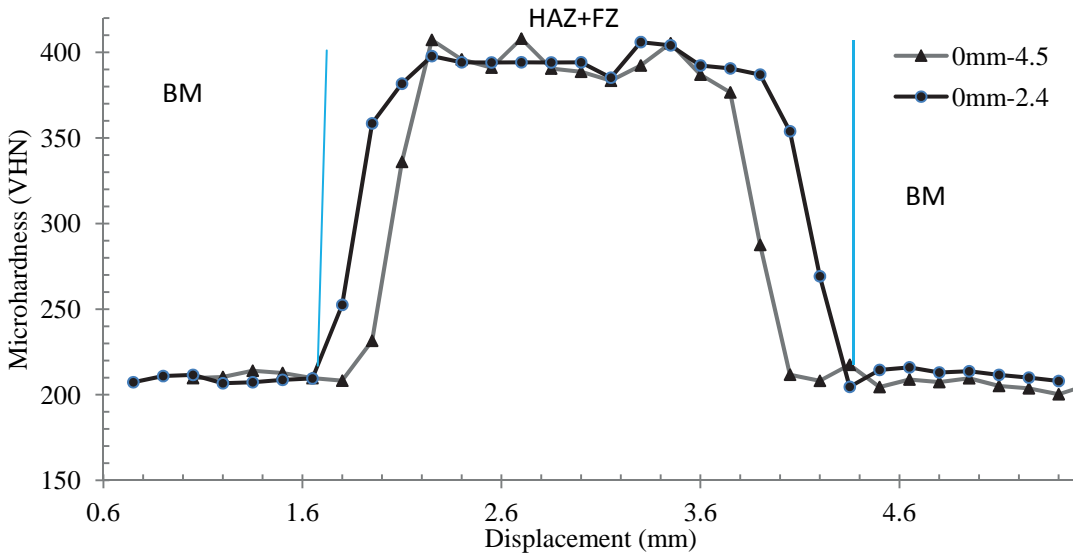
105

Fig.3. 36 Hardness under influence of welding speed at 0mm focal point position

In case of reference focal point position the variation of welding speed change significantly the hardness width inside the HAZ-FZ but don't cause any variation of hardening zone inside HAZ-FZ due to the parallel of hardness slope of these two curves as indicated in Fig.3.36. Conversely at 8mm focal point position, the welding speed variation does affect the hardening zone due to the difference slope as indicated in Fig3.37. But the maximum hardness inside these zones is similar 395+/-15 HVN.
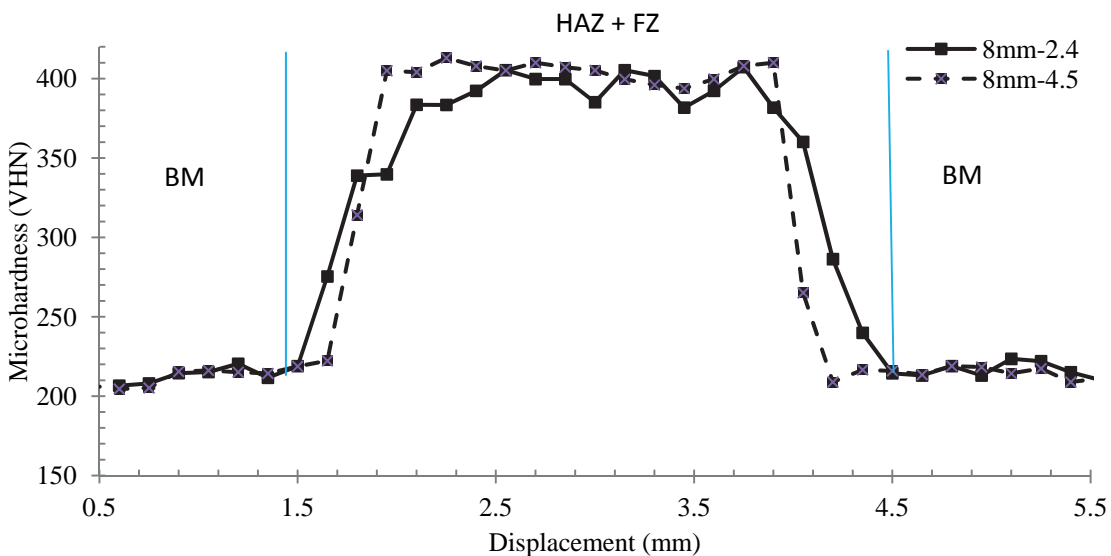

Fig.3. 37 Hardness under influence of welding speed at 8mm focal point position

Finally the speed and focal point play an important role in the variation hardness width inside HAZ and FZ but no influence on the maximum hardness inside these zones. One can conclude that the focal point position and the welding speed have almost no influence on the maximum hardness value but do affect the hardening width zone and maximum hardness inside the inter-zone *(BM-HAZ)*. But the maximum hardness inside these zones, HAZ and FZ, is similar *(395+/-15 HVN)*.

Base on the weldability of alloy steels, the HAZ hardness in excess of 350HV occur readily requiring high pre-heat temperatures, slow cooling and hydrogen controlled welding procedures [20]. So the precaution during laser welding Nd: YAG at any welding speed, focal point position and power should be considered.

3.3.3.5 *Influence of laser power on softening zone*

For studying the influence of the welding parameters on the softening zone under the tempering effect of martensite in the BM situate at the interface between BM and HAZ. We conducting two lines of micro-hardness measurements, the top line *(A)* separated from bottom line *(B)* by a distance of 0.25mm and 0.5mm from the top surface to the top line. The space between two points of measurement is 0.1mm with the 0.1kg load in the base metal and 0.08mm for the zone between the base metal and the fusion zone.

The points of the second line are situated on the middle of two points of the first line. The purpose of two lines methods here is to get small indent space distance. So we can observe the variation of hardness in a fine softening zone.

Two specimens from welding speed of 2.4m/min and 4.5m/min with the power of 4kW and focal point of 4mm from top surface are used in this observation.

Fig.3.38 represented the hardness measured on the top left of welded joint, *A4mm-2.4* represented the indent point along line A and *B4mm-2.4* represented the measured point along line B at welding speed 2.4m/min and 4kW. Fig.3.39 represented the hardness on line A, B at the welding speed 4.5m/min and 4kW.
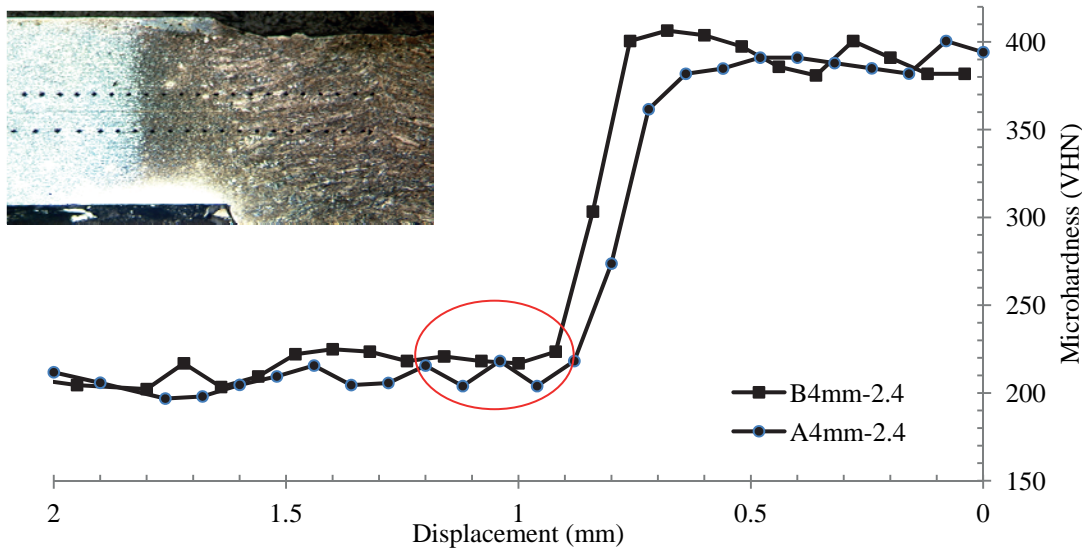
Fig.3. 38 Hardness on the top left side of laser welding 4kW, 2.4m/min
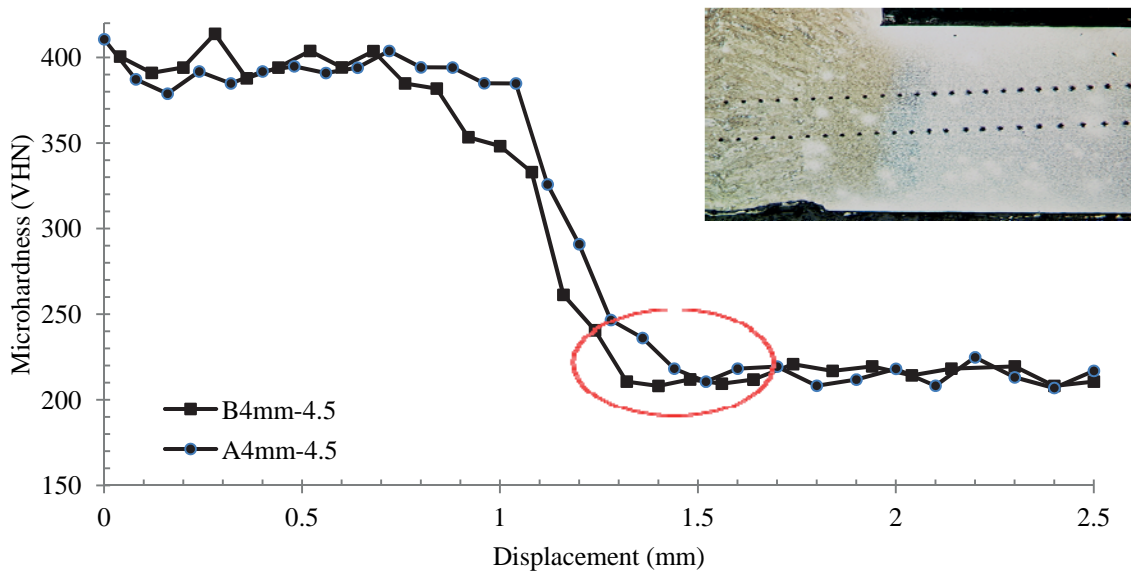

Fig.3. 39 Hardness on the bottom right side of laser welding 4kW, 4.5m/min

The two curves in Fig.3.38 and Fig.3.39 indicated no drop of hardness in the region close to the HAZ and the BM under effect of tempering martensite *(TM)* at a variation of welding speed from 2.4m/min to 4.5m/min. So there is no formation of the tempering martensite in the critical zone between HAZ and BM. One observes a slightly increase of hardness near the base metal, Fig.3.39, in which the aging of the ferrite phase by carbon segregation on the dislocation introduced by the welding process is the main cause of the

108

hardness. The microscopic observation inside the BM-HAZ gives also a supplementary proof of no softening zone to the measurement of hardness value.

So we can summary that there is no formation of TM in the zone located between BM and HAZ for laser welding type Nd: YAG with welding speed more than 2m/min with different powers and focal points parameters. The same results could be found in the hardness measurement done by Xia [21] of the laser Nd: YAG 6m/min 3kW for DP600.

3.3.4   Shear test

The laser power has a strong effect on the shear strength of the laser-welded joint (butt). The higher laser power resulted in a higher response value, due to the fact that using high laser power would increase the power density. This leads to more penetration results in an improved response. The shear strength is inversely proportional to the welding speed [17]. So the influence of laser welding speed is not studied here. Under influence of laser power, the shear load of lap joint is observed.

Sample N°	Power (kW)	Speed (m/min)	Focal (mm)
1	4	4.3	0mm
2	3.5	4.3	0mm
3	3.1	4.3	0mm
4	2.8	4.3	0mm
5	2.5	4.3	0mm
6	2.2	4.3	0mm

Tab.3. 9 Lap joint specimen for shear test

The shear load test is done by using samples prepared by laser welding with constant speed of 4.3m/min and variation of power from 2.2kW to 4 kW with focused point is on the top surface as indicated in Tab.3.9. The Instron shear testing machine as shown in Fig.3.40 (a) with the loading rate of 5mm/min is used for lap joint shear test. The preparation of specimen of shear test is based on the French standard NF EN 10002-1:2001 applied for

sheet metal testing. The loading rate using for shear test of base metal and lap joint is 5mm/min. two tests per specimen were applied to base metal and lap joint test.
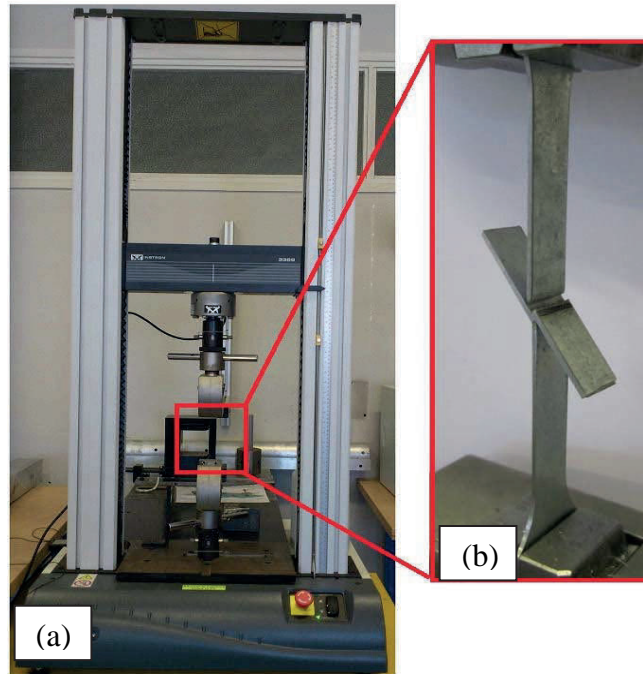

Fig.3. 40 Instron shear testing machine and specimen

3.3.4.1   *Shear test of base metal*

Specimen for shear testing of base metal is shown in Fig.3.41 and the results of testing are plotted in relation Fig.3.42 (a) for the Load-Extension curve and Fig.3.42(b) for Engineering Stress Strain curve.
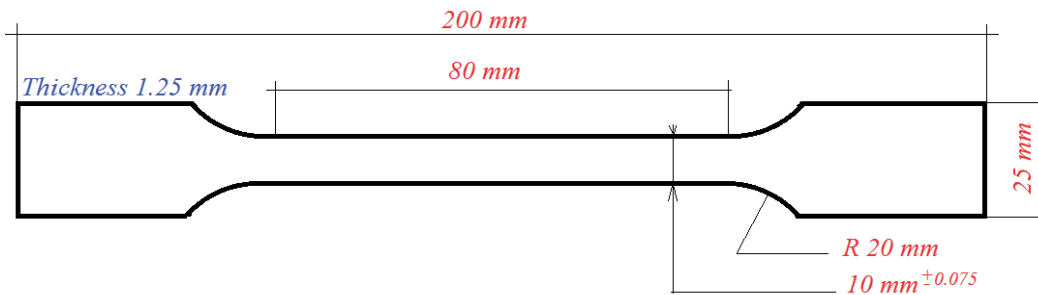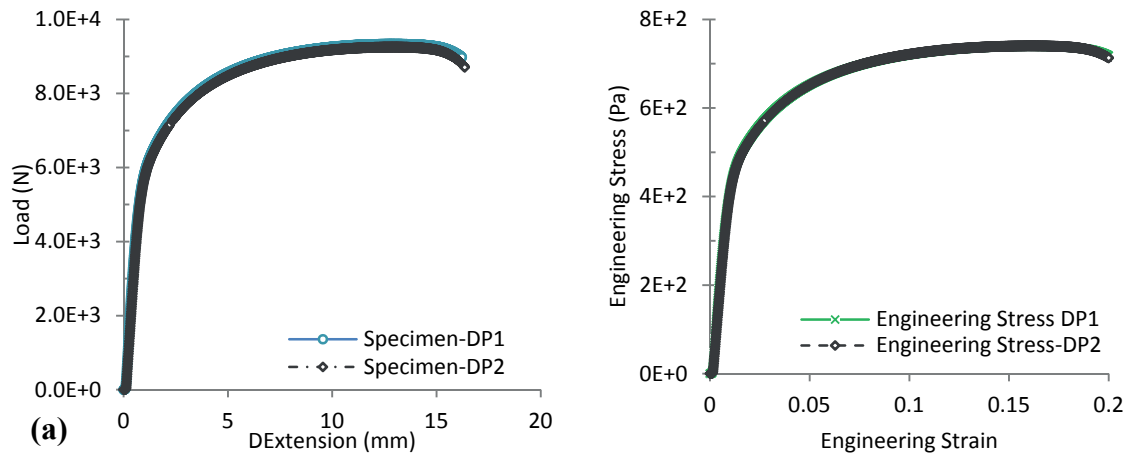

Fig.3. 41 Specimen of DP600

Fig.3. 42 Shear curve of DP600

Base on the engineering stress strain curve in FIg.3.42 (b), the mechanical properties of DP600 at room temperature are presented in Tab.3.10 which is compared to that of ArcelorMittal [3] and those of research of Bigot [7].

	Yield Strength (MPa)	Yield Strength 0.2% (MPa)	Utimate Tensile Strength (MPa)	Totale Elongation (%)
Experiment	360	440	740	22
ArcelorMittal[3]	330-410		600-700	>21
Bigot[7]	310+/- 40		654+/-14	22.9+/-1

Tab.3. 10 Mechanical properties of DP600
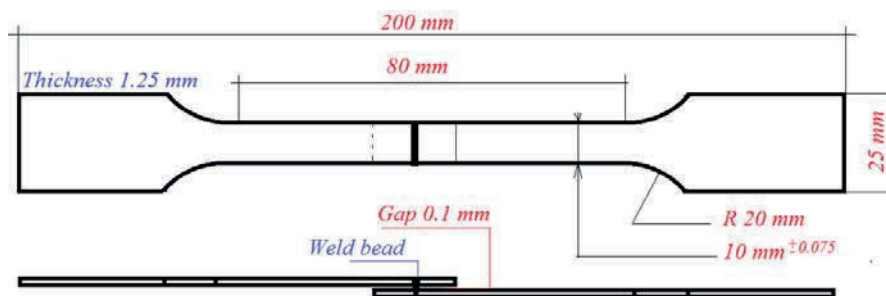
3.3.4.2   Shear test of lap joint

Fig.3. 43 Specimen for shear test of lap joint

Fig.3.44 shows the Loads-Extension curves of lap joint welding under variation of laser power. Increasing the laser power increase the depth of weld pool and cause the full penetration. This mechanics allow the lap joint to be strengthening than the lower power

welded. The curve prove also the increasing of displacement up to 11mm for 4kW laser welded joint and only 3.5mm for lower power 2.2kW welded joint.
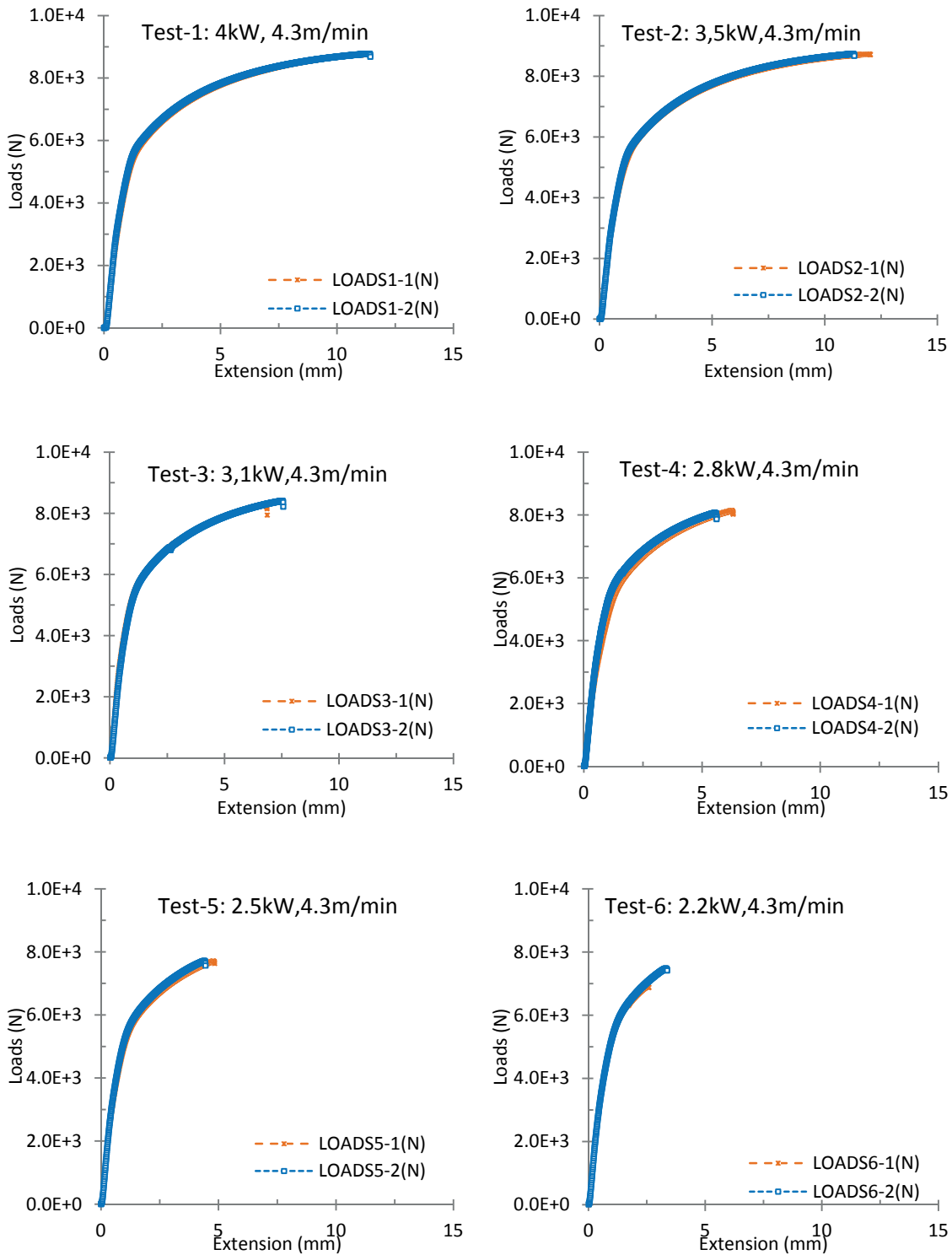

Fig.3. 44 Shear curve of lap joint under influence of laser power

112

The maximum shear load depended on the laser power are presented in Tab.3.11 and the extension of lap joint depended on laser power are presented in Tab.3.12.

	4kW	3.5kW	3.1kW	2.8kW	2.5kW	2.2kW
MIN	8752.45	8728.18	8283.12	8070.89	7703.83	6911.99
MAX	8776.97	8735.13	8405.22	8140.07	7712.97	7477.71
MOY	8764.71	8731.6	8344.17	8105.48	7708.4	7194.85

Tab.3. 11 Maximum loads of lap joint test *(N)*

	4kW	3.5kW	3.1kW	2.8kW	2.5kW	2.2kW
MIN	11.00	11.70	6.90	5.70	4.60	2.80
MAX	11.40	12.00	7.60	6.40	4.90	3.50
MOY	11.20	11.85	7.25	6.05	4.75	3.15

Tab.3. 12 Maximum extension of lap joint *(mm)*

The variation of maximum shear loads of lap joint is presented in Fig.3.45. It proved that the increasing the laser power not only cause full penetrate welded joint but also increase the shear strength of the lap joint too. It make about 1.5kN of different between the lower power used and the maximum power used. But at higher power used, 3.5 kW to 4kW, the maximum shear load became stable. In order to get higher maximum shear strength of lap joint the full penetration is recommended. With full penetration mode the molten pool is stable, less spatters and pores inside the welded joint compared to the none-penetration welded joint.

The maximum extension of lap joint, *curve Extension (mm) in Fig.3.45*, increasing significantly during increasing of laser power. The lower extension is about 3mm and higher extension is about 12mm.
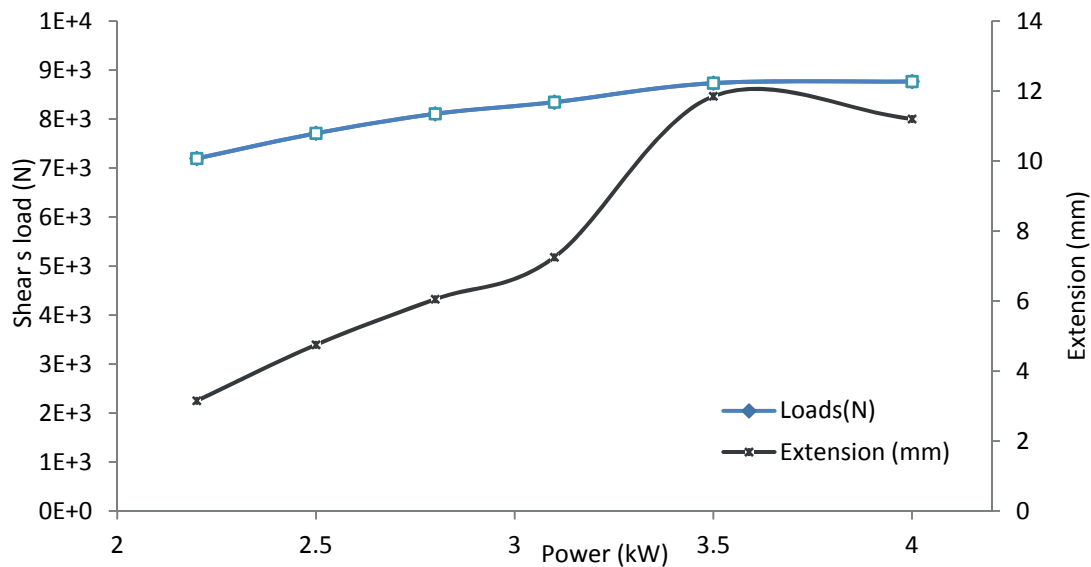
Fig.3. 45 Rupture load under influence of laser power

One notice that the rupture occurs at the HAZ of the bottom sheet metal of all welding parameters under influence of power variation as shown in Fig.3.32(b). The sample rupture location was found in laser welding of lap joint of DC56D steel with 0.8 of thickness and a joint gap ranged from 0.1mm to 0.15mm [9].

3.4 CONCLUSION

The conclusion of experiment of laser welding can be summery as follow:

- The position of focal point can reduce the power density in the keyhole by increasing its volume and can increase the FZ width at the middle depth of FZ and also reduce the geometric shape imperfection. The higher welding speed cannot reduce the imperfection caused by the higher laser power used because the higher speed cannot reduce the power density inside the keyhole as much as focal point position, but rather it create a higher concavity on top and root of the weld bead by reducing the bead width.

- No effect of tempering martensite in the softening zone by Nd: YAG laser welding process on the DP600 steel for welding speed upper than 2m/min.

114

- The speed and focal point have no influence on the maximum hardness value, but have effect on the width of HAZ and FZ. Power variation has a few influences on the maximum hardness inside the HAZ and FZ. The variation in range of 360VHN and 410VHN from the variation of laser power Nd: YAG, 2.2kW to 4kW.

- Another effect is the depth of the weld pool and also the maximum shear strength of the lap joint. It proved that the increasing the power not only cause full penetrate welded joint but also increase the maximum shear load of the lap joint too

REFERENCE

[1]   H. Al-Kazzaz, M. Medraj, X. Cao, and M. Jahazi. Nd:yag laser welding of aerospace grade ze41a magnesium alloy: Modeling and experimental investigations. *Materials Chemistry and Physics*, 109:61 – 76, 2008.

[2]   A.Murugaiyan, A.Saha Podder, A.Pandit, S. Chandra, D. Bhattacharjee, and R.K.Ray. Phase transformation in two c-mn-si-cr dual phase steels. *ISIJ International*, 46:1489–1494, 2006.

[3]   ArcelorMittal. Aciers dual phase et complex phase. Extrait du catalogue produit - édition européenne 2008, 2008.

[4]   G. Avramovic-Cingara, Y. Ososkov, M.K. Jain, and D.S. Wilkinson. Effect of martensite distribution on damage behaviour in dp600 dual phase steels. *Materials Science and Engineering: A*, 516(1-2):7 – 16, 2009.

[5]   V. Baltazar Hernandez, S. Nayak, and Y. Zhou. Tempering of martensite in dual-phase steels and its effects on softening behavior. *Metallurgical and Materials Transactions A*, 42:3115–3129, 2011. 10.1007/s11661-011-0739-3.

[6]   K.Y. Benyounis, A.G. Olabi, and M.S.J. Hashmi. Effect of laser welding parameters on the heat input and weld-bead profile. *Journal of Materials Processing Technology*, 164-165(0):978 – 985, 2005.

[7]   Julien BIGOT. Influence des paramètres process sur la tenue mécanique d'un assemblage soudé au laset l'études des règles de conception pour le soudage laser. Master's thesis, INSA de Rennes, 2007.

[8]   Régis Blondeau, editor. *Metallurgy and Mechanics of Welding: Processes and Industrial Applications*. ISTE Ltd, 2008.

[9]   Genyu Chen, Lifang Mei, Mingjun Zhang, Yi Zhang, and Zujian Wang. Research on key influence factors of laser overlap welding of automobile body galvanized steel. *Optics & Laser Technology*, 45(0):726 – 733, 2013.

[10]   Sylvian DANCETTE. *Comportement mécanique des soudures par points: mécanismes et stratégies de prédiction dans le cas des tôles pour aciers automobiles*. PhD thesis, INSA-lyon, 2009.

[11]   J.D. EMBURY E. BIRO, J.R. MCDERMID and Y. ZHOU. Softening kinetics in the subcritical heat-affected zone of dual-phase steel welds. *The Minerals, Metals & Materials Society and ASM International*, 41A:2348–2356, 2009.

[12]   N. Farabi, D.L. Chen, J. Li, Y. Zhou, and S.J. Dong. Microstructure and mechanical properties of laser welded dp600 steel joints. *Materials Science and Engineering: A*, 527(4-5):1215 – 1222, 2010.

[13]   Gejza Rosenberg Katarína Buriková. Quantification of microstructural parameter ferritic-martensite dual phase steel by image analysis. *Hradec nad Moravicí*, 5:19. – 21, 2009.

[14]   Tom Gray Malcolm S Loveday and Johannes Aegerter. Tensile testing of metallic materials: A review. Technical report, April 2004.

[15]   M.Brand and D.Siegele. Numerical simulation of distortion and residual stresses of dual phase steels weldments. In *IIW-1820-07*, 2007.

[16]   Guy MURRY. Transformation dans les aciers. Technical report, Techniques de l'Ingénieur, traité Matériaux métalliques.

[17]   U. Reisgen, M. Schleser, O. Mokrov, and E. Ahmed. Statistical modeling of laser welding of dp/trip steel sheets. *Optics & Laser Technology*, 44(1):92 – 101, 2012.

[18]   Christopher Schwenk. *FE-Simulation des Schweißverzugs laserstrahlgeschweißter dünner Bleche :Sensitivitätsanalyse durch Variation der Werkstoffkennwerte*. PhD thesis, Bundesanstalt für Materialforschung und prüfung, 2007.

[19]   WordAutoSteel. Advance high strength steel : Application guidelines. Technical report, June 2009.

[20]   WTIA. Hardness testing of welds. Technical report, Welding Technology Institute of Australia, 1-4, 1 March 2006. ABN 69003696 526.

[21]   Mingsheng XIA and Elliot BIRO. Effects of heat input and martensite on haz softening in laser welding of dual phase steels. *ISIJ International*, 48(6):809–814, 2008.

Résumé

Chapitre 4: Simulation Thermomécanique du soudage laser Nd:YAG

Ce chapitre est consacré au développement du modèle thermomécanique *(thermo-élasto-plastique)* pour décrire le comportement de l'acier à haute résistance DP600 pendant le soudage laser. L'objectif principal étant d'évaluer les contraintes résiduelles issues de ce modèle.

La démarche a été dans un premier temps de constituer un modèle géométrique proche de la réalité. Celui-ci a été représenté par le recouvrement de deux tôles d'acier d'une épaisseur de 1,25 mm avec un jeu de 0.1mm entre les deux tôles.

L'analyse numérique pour le modèle thermique, développée sur un code de calcul par éléments finis ABAQUS, repose sur la modélisation des phénomènes de transfert de chaleur au cours du soudage. Pour ce faire, le sous-programme DFLUX d'ABAQUS a été déployé pour réaliser ce modèle. Le chargement appliqué est une source de chaleur volumétrique de forme conique associée à des conditions aux limites. Les résultats de l'analyse thermique sont présentés sous forme d'évolution spatio-temporelle de la température dans les différentes régions des plaques soudées. Une comparaison des résultats numériques et expérimentaux a permis d'apprécier la pertinence du modèle thermique développé.

La deuxième étape concerne la simulation de l'évolution de l'état mécanique des pièces au cours de l'assemblage en introduisant les résultats du modèle thermique comme chargement.

La construction de ce modèle thermomécanique a été confortée par une étude de l'influence des différents paramètres physiques et de simulation sur le résultat final. Pour atteindre cet objectif, d'un point de vue méthodologique, nous avons étudié plusieurs sous-modèles en faisant varier :

- Les paramètres de maillage pour affiner les résultats finaux.
- Les paramètres physiques (les propriétés thermo-physiques dépendantes et indépendantes de la température, la valeur de la chaleur spécifique à la température de transformation de phase ainsi que la différence de température maximale) pour mieux appréhender leurs influences sur les résultats finaux.
- Les modes (faible, moyen et fort) de convection et de rayonnement sur la répartition de la température et des contraintes résiduelles.

A l'issue de cette étude paramétrique, nous avons identifié l'influence de la densité de maillage sur l'exactitude de la répartition de la température et des contraintes résiduelles ainsi que l'influence des paramètres physiques sur le modèle développé.

Abstract

Chapter 4: Thermomechanical simulation of Nd: YAG laser sheet metal welding

This chapter is devoted to the development of thermomechanical model *(thermo-elastic-plastic)* to describe the behavior of high strength steel DP600 during laser welding. The main objective was to evaluate the residual stresses resulting from this model.

The approach was initially to construct a geometric model. It was represented by the overlap of two steel plates with a thickness of 1.25 mm with a set of 0.1mm between the two sheets.

Numerical analysis for the thermal model, developed a finite element code of ABAQUS, based on the modeling of heat transfer phenomena during welding. To do this, the subroutine DFLUX of ABAQUS has been made to achieve this model. The applied load is a volumetric heat source conical associated with boundary conditions. The results of thermal analysis are presented in the form of spatio-temporal evolution of the temperature in different parts of the welded plates. A comparison of numerical and experimental results was used to assess the adequacy of the thermal model developed.

The second step involves the simulation of the evolution of the mechanical state of the assembled model by introducing the results of the thermal model as a load.

The construction of the thermomechanical model has been confirmed by a study of the influence of different physical and simulation parameters on the final result. To achieve this goal, from a methodological point of view, we studied several sub-models by varying:

- The mesh parameters to refine the final results.
- The physical parameters (*dependent and independent thermo-physical properties of the temperature, the value of the specific heat at the temperature of phase transformation as well as the maximum temperature difference*) to better understand their influence on the final results.
- Modes *(low, medium and high)* of convection and radiation on the temperature distribution and residual stresses.

At the end of this parametric study, we identified the influence of the mesh density on the accuracy of the temperature distribution and as well as the influence of physical parameters on the final results of developed model.

Contents

Figures

Tables

<div align="right">Chapter **4**</div>

Thermomechanical simulation of Nd: YAG laser sheet metal welding

4.1. INTRODUCTION

Welding simulation has been applied wildly to find the result of thermal and residual stresses. The precision of welding simulation is depended on many sources such as material data, type of welding model [2] and meshing dimension. The effect of thermo physical and mechanical of aluminum has been studied by Zhu [13]. The sensibility of thermomechanical data at +/-10 % of chart data on the result of welding simulation has been studied in the thesis of Schwenk [10].

The material properties functions of temperature play an important factor in the iteration of the numerical analysis [10]. Zhu [13] observed the influence of temperature dependent material properties on the welding simulation of 5052-H32 aluminum alloy. The thermal conductivity has an effect on the distribution of transient temperature field during welding analysis, the material density and specific heat have negligible effect on the temperature field. Regarding the material-dependent properties of steel that have a peak-point of specific heat at the phase transformation (Ac1) and some variations compared to aluminum. Another study for steel is necessary in order to understand those variations.

Conical heat source is a suitable volume heat source model for high intensity with small diameter laser beam welding simulation [7]. Facing some constraints in welding simulation laser Nd:YAG in which the laser seam is quite small and high speed welding, many simulators used refined mesh at the seam and rather coarse meshes far away from HAZ [9, 3, 4]. In thermal analysis, the mesh is not fine enough to solve the rapid rise in temperature in front of the weld pool. Their effect is that the computed strain rate can be much less than the real strain rate during the mechanical analysis. Consequently the computed stresses can be much less than the real stresses. The accuracy is limited by computational costs to rather coarse meshes [6]. Relation between mesh sizes and circular disc source model of laser forming process has been studied in the work of Zhang [12] for laser processes and also in the work of Schenk [9] for gas metal arc welding process, it showed that the mesh density is an important factor in determining the accuracy of distortion amplitude, the buckling shape as well as the critical bucking load and the stress. Grey [5] studied the effects of welding speed, energy input and heat source distribution on temperature variations in butt welding joint by metal inert gas process *(MIG)*. By using 2D model, he showed that the change of welding speed has mainly influenced on the peak temperature in FZ and that it has less effect on the temperatures in others areas. Variation of the heat source distribution and magnitude affect the shape and the boundaries of FZ and HAZ. The FZ was decreased *(lower peak values of heat fluxes)* when the parameters *(heat source's size)* increased. It also has a significantly effect on temperature distributions in the areas close to HAZ. The temperature decreases are none linear with the increasing of heat source parameters. The peak temperatures and temperature distributions are sensitive to small changes of heat source dimension. Therefore, it is important to define an accurate heat source model in order to predict the welding distortion and the residual stresses correctly.

A notable solution for surface treatment but not complete for full penetration welding model which used a tiny dimension. Minimum value of mesh dimension in [12] imposes constraint on time consuming of full penetration welding simulation applied to transparent welded joint because of high degree of freedoms *(DOFs)* and also limited by the capacity of

computing machine. Base on this idea we conduct a relation between the mesh density and the dimension of conical heat source model.

The quadratic interpolation function gives more accurate results for weld simulation [9] and is used in this thermal simulation.

Alberg [1] studied the comparison of mechanical model such as plastic model, viscoplastic model, and transformation induced plasticity model, the results show that the rate independent model, *elasto-plasticity*, gives results of residual stresses which are almost as good as from the rate dependent including microstructure calculation and Transformation induced plasticity model *(TRIP model)*, but with less costly material testing to obtain material parameter. Elastoplastic model with isotropic hardening or kinematic hardening gives a good result of residual stresses evaluation and using viscoplastic model is less important in prediction of residual stresses [2].

This part concentrates on the influence of the material properties, the meshing density, and the heat transfer condition with surrounding environment and the effect of peak temperatures on the simulation of full penetration mode of laser welding applied to dual phase steel DP600 within transparent mode include 0.1mm gap.

4.2. MODEL

4.2.1. Thermal model

The heat transfer from the volumetric heat source and the metal by conducting mode is expressed in equation 2.1 to 2.5 in chapter 2.

An initial condition is defined by the temperature of the model, T, equal to the surrounding temperature 25°C.

The boundary condition applied for thermal model are the heat dissipated by convection mode and radiation mode as shown in Fig 4.1 and are expressed by equation 2.4.and 2.5 respectively. The parameters concerned the thermal simulations are shown in section 4.2.2 and section 4.3.3.
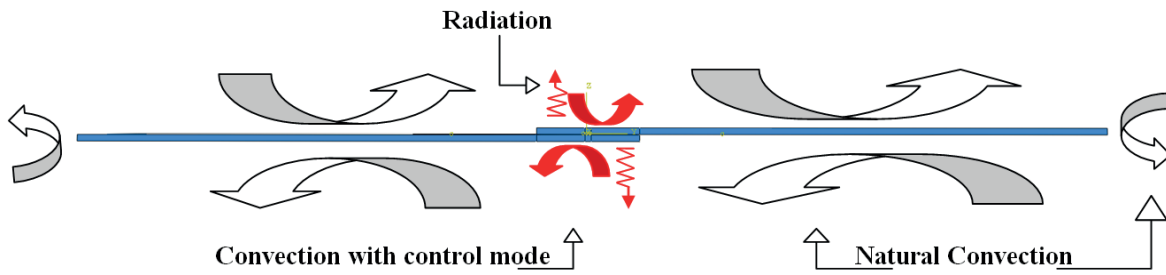
Fig.4. 1   Cross section of sheet metal assembled under heat transfer mode

4.2.2.   Parameters of heat source model

The conical heat source with Gaussian distribution [7] is used in modeling represented by the equation 2.19.

Tab.4.1 represents the parameters of conical heat source, showed in Fig.4. 21 used in thermal simulation.

Symbol	Quantity	Value
r_e	radius superior	0.65 m^{-6}
r_i	radius inferior	0.50 m^{-6}
r_c	distribution parameter	m^{-6}
z_e	position in Z axis of r_e	1.25 m^{-6}
z_i	position in Z axis of r_i	-1.26 m^{-6}
P	laser power	3.50 kW
η	efficiency	42.00 %
V	welding speed	0.05 m/s

Tab.4. 1 Parameters of Heat Source Model
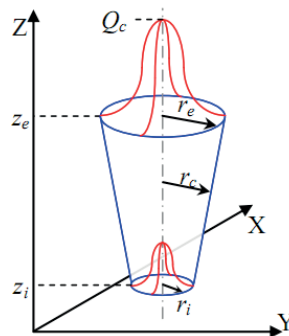
Fig.4. 2   Conical heat source

130

The dimension of heat source model is recommended to be 10% less than the real weld pool dimension [11]. But because of the high speed welding process and small weld pool, 10% less than the real value leads to a small value of efficiency in order to maintain the maximum temperature in weld pool. The number of elements in this section must be increase too in order to suite with the dimension of the model. So the real dimension from transverse section of weld pool is used in this work.

Zain [7] used the efficiency 37% for laser Nd:YAG simulation of aluminum AA 6056-T4 of the plate joint. Schenk [6] simulated with 64% for gas metal arc welding of 1mm overlap joint of DP600 steel. The same value of efficiency 64.3% for Gas Metal Arc *(GMA)* welding simulation of 5052-H32 aluminum alloy [9]. In the Nd: YAG laser welding simulation of ZE41A magnesium alloy show that the increasing of welding speed from 4 to $7m.min^{-1}$, the coupling efficiency increased from 25% to 42% [1].

According to the literatures [1, 7], the efficiency of 42% has been adopted in our work by the comparison of the cross section of the FZ between the thermal simulation and the experiment for laser Nd:YAG with success as shown in Fig.4.3. This value is also varied base on the dimension of the heat source model predefine by the measurement of the cross section of the FZ.
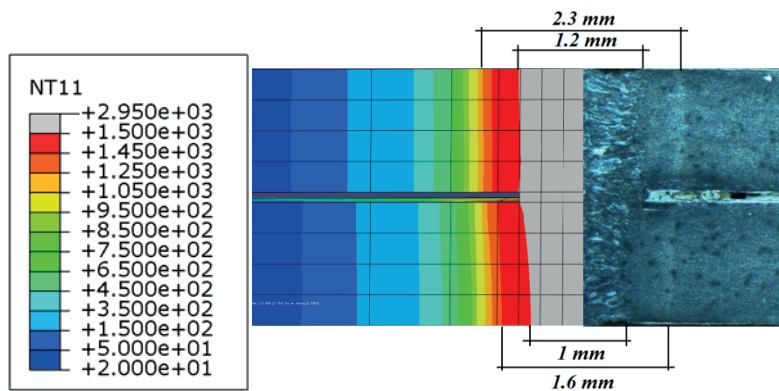
Fig.4. 3　Cross section FEA and experimental

The energy input and heat source distributions have important effects on the shape and the boundaries of FZ and HAZ, they also influent the peak temperature in FZ, which consequently affect the transient temperature distributions in the thermal model. The FZ and

the HAZ boundaries are sensitive to the variation of heat source parameters in welding simulation [4].

4.2.3. Mechanical Model

The resolution of the mechanical equation is based on the equation of static equilibrium [6] described in equation 2.35. The perfect elastoplastic model described in section 2.4.4.1 is used in the mechanical simulation.

During the analysis, the initial condition and the boundary condition applied for mechanical model are:

Initial condition: We considered that there was no stresses field before the welding process:

$\sigma(x_i, 0) = 0$ at instant $t = 0$

Boundary conditions: is based on the imposition of a zero displacement on the contact surface of the work pieces by:

- Position 1, 2, 4 and 5: Displacement Z =0 *(Z-SYMM mode)*. These BCs will relax at the end of mechanical analysis.

- Position 3: Lock the start of weld seam *(Encastre-mode)* and Displacement Z = 0 *(Z-SYMM-mode)* at the end of weld beam. These BCs are lock for all steps.
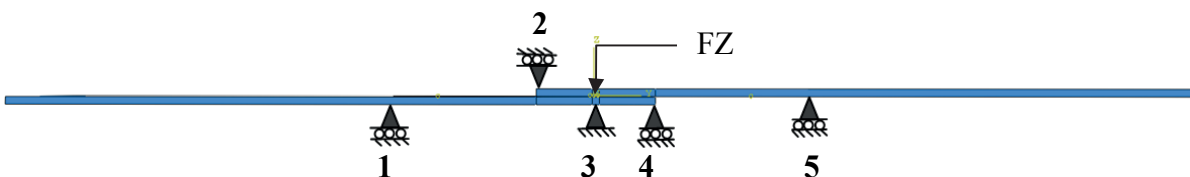
Fig.4. 4   Clamps condition during welding simulation

4.3. PROBLEMATIC OF SIMULATION

4.3.1. Thermal

Three models based on the properties of material were selected for studying the influence of materials properties.

- *Material Model 1* : density, conductivity and specific heat are at room temperature.

- *Material Model 2* : density at room temperature, conductivity and specific heat are function of temperature but the specific heat at phase transformation temperature (T= 600°C-800°C) is overlooked.

- *Material Model 3* : density at room temperature, conductivity and specific heat are function of temperature.

The dimensions of those models are the same as model 2 described in Tab.4.3.

Another 7 models are simulated for studying the influence of meshing dimension. Three zones of model are considered, Fusion Zone (FZ), Heat Affect Zone (HAZ) and Non Heat Affect Zone (NHAZ) located at 10mm from welded centerline in transverse direction. The meshes dimensions are different in each zone for better understanding the influence of discretization as indicated in Tab.4.2 and Fig.4.7.

Model	Zone1			Zone 2	Zone 3[a]
	DX	*DY*	*DZ*	*DY*	*BIASE*
Mesh 1	1.25	0.6	0.625	1.88	10:12
Mesh 2	1	0.6	0.625	0.94	10:25
Mesh 3	0.5	0.6	0.625	0.94	10:25
Mesh 4	0.5	0.6	0.625	0.47	20:25
Mesh 5	0.5	0.3	0.3125	0.313	20:25
Mesh 6	0.25	0.3	0.3125	0.313	20:25
Mesh 7	0.125	0.3	0.3125	0.313	20:25

[a]10:12 means 12 elements with biases factor of 10 from the small and the bigger one.

Tab.4. 2 Parameter of thermal mesh size (mm)
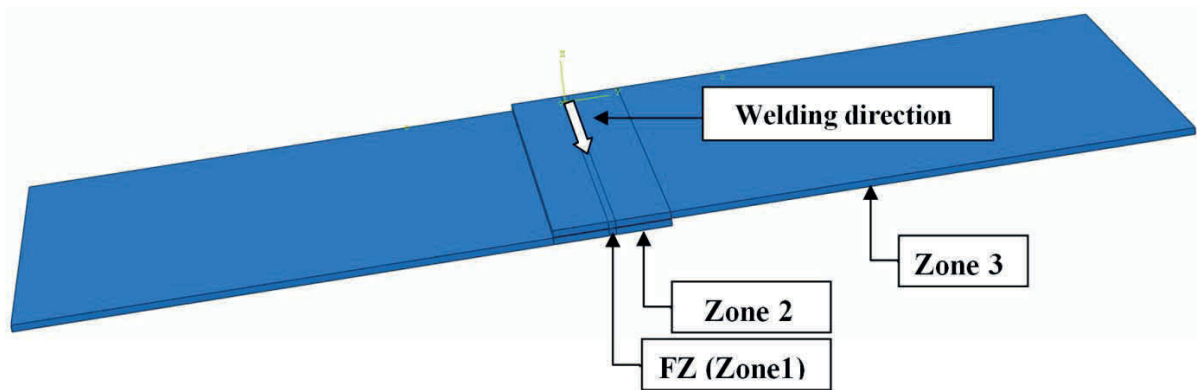
Fig.4. 5   Three zones used for meshing the sheet assembled
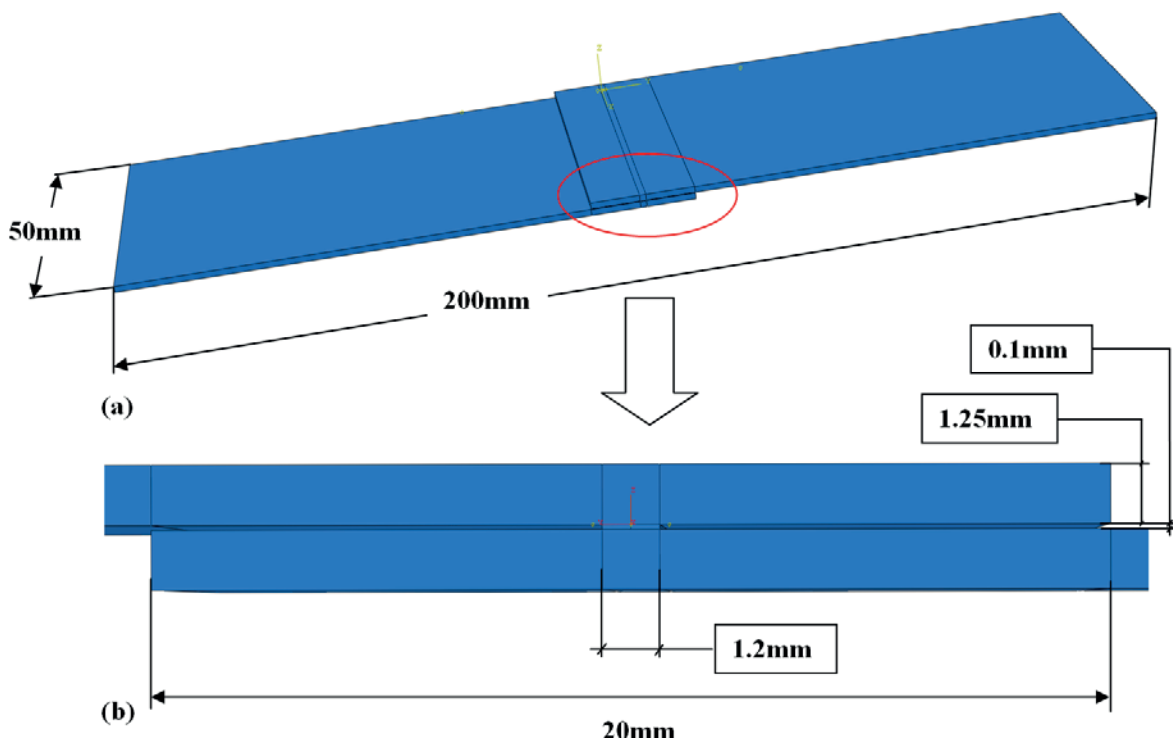
Fig.4. 6   Dimension of numerical modeling

4.3.2.   Mechanical

To construct the mechanical model, we considered various parameters and assumptions as follow:

The mesh density in mechanical analysis is the same to thermal analysis. Only six models are used in mechanical analysis for studying the influence of meshing dimension as shown in Tab.4.3 and Fig.4.7.

Model	FZ			HAZ	NHAZ[a]
	DX	*DY*	*DZ*	*DY*	*BIASE*
Model 1	1.25	0.6	0.625	1.88	10:12
Model 2	1	0.6	0.625	0.94	10:25
Model 3	0.5	0.6	0.625	0.94	10:25
Model 4	0.5	0.6	0.625	0.47	20:25
Model 5	0.5	0.3	0.312	0.313	20:25
Model 6	0.25	0.3	0.312	0.313	20:25

[a]10:12 means 12 elements with biases factor of 10 from the small and the bigger one.

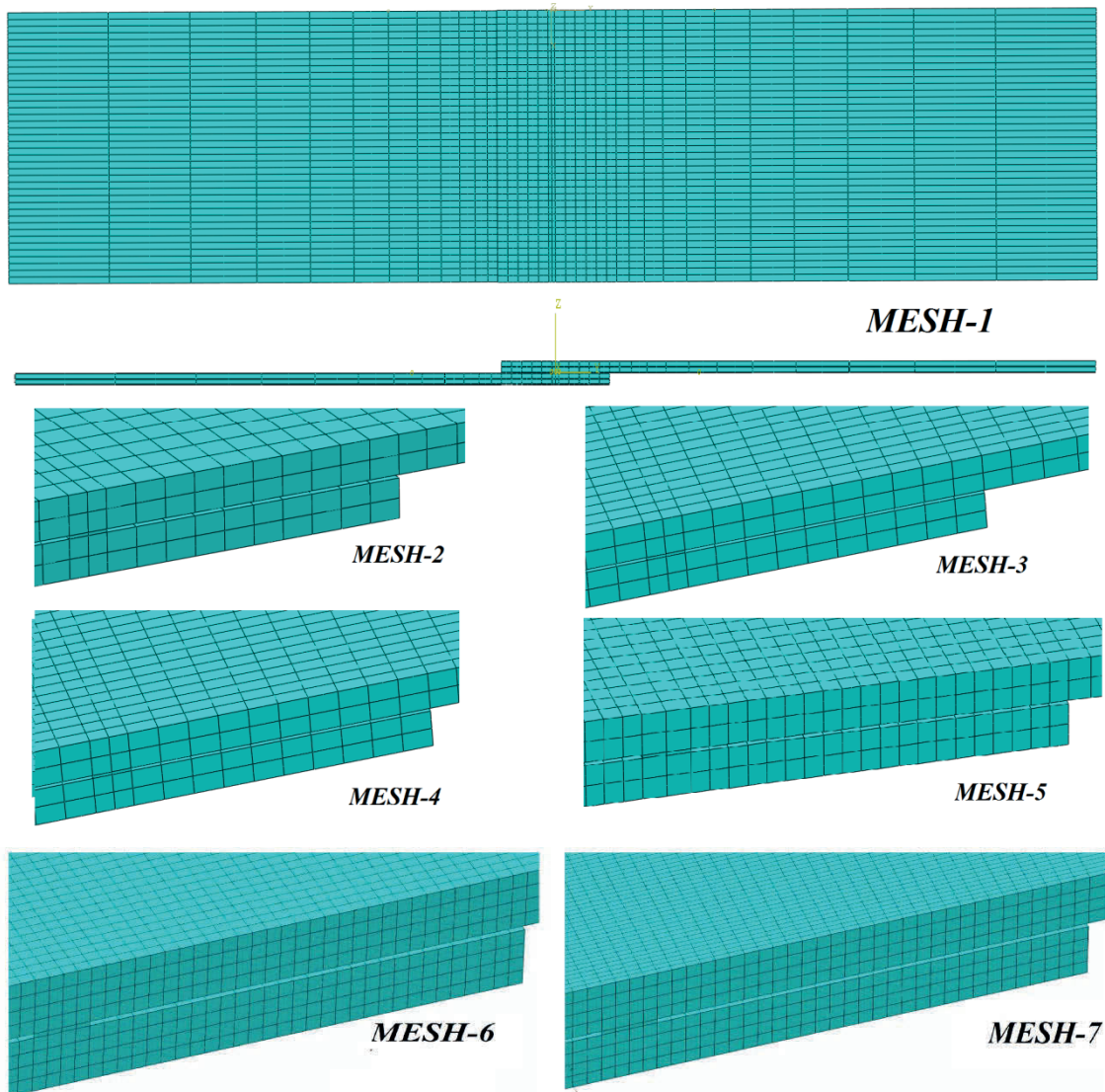Tab.4. 3 Parameter of mechanical mesh size (mm)

Fig.4. 7   Meshing parameters

4.3.3. Material Data

The influence of temperature dependent material properties on the welding simulation of 5052-H32 aluminum alloy are studied by Zhu et al [13]. They assumed that the thermal conductivity has some effects on the distribution of transient temperature field during welding. . The thermal effects due to solidification of the weld pool by the influence of latent heat for fusion is supposed to be less influence on the results of the simulation [10], and it is not counted in this work.

The material density and specific heat have negligible effect on the temperature field [9]. This is maybe the small variation of density and specific heat in function of temperature. Regarding the thermal properties of DP600 steel [6], the density is less changed with the variation of temperature. The density assumes to 7594 Kg/m^3 at room temperature.

The convection coefficient 73.5 W/m^2.K and emissivity of 0.25 is constant based on the result of [4]. The effect of shielding gas is translated by difference form of heat transfer modes. The influence of shielding gas on the top and bottom surface on the welding model is studied by 3 modes of heat transfer: *low convection and radiation* with a coefficient of convection of 15W/m².^{o}C and an emissivity of 0.25, *medium convection and radiation* with a coefficient of convection 75W/m².^{o}C and an emissivity of 0.35 and finally the *forced convection and radiation* with a coefficient of convection of 150W/m².^{o}C and an emissivity of 0.8. The Stefan Boltzmann coefficient is 5.6704E8 W/m^4.^{o}C^4 with absolute zero of -273.15°C. On the other hand, the specific heat reached the peak value at the phase change temperature from ferrite to austenite is around 750˚C. So the specific heat dependent of temperature is reconsidered in this work.

Thermal property of DP600 for *model 1*			
Specific heat		*Conductivity*	
Temperature (^{o}C)	Heat (J/kg.K)	Temperature (^{o}C)	Conductivity (W/m.K)
0	520	0	34.6
25	550	25	34.8

Thermal property of DP600 for *model 2*			
Specific heat		*Conductivity*	
Temperature (°C)	*Heat* (J/kg.K)	*Temperature* (°C)	*Conductivity* (W/m.K)
0	520	0	34.6
200	550	25	34.8
400	600	200	35
600	750	254	35
800	690	1200	25.5
1100	520	1300	60
1200	610	1400	70
3000	620	3000	70

Thermal property of DP600 for *model 3*			
Specific heat		*Conductivity*	
Temperature (°C)	*Heat* (J/kg.K)	*Temperature* (°C)	*Conductivity* (W/m.K)
0	520	0	34.6
200	550	25	34.8
400	600	200	35
600	750	254	35
740	1160	1100	21.4
800	690	1200	25.5
1100	520	1300	60
1200	610	1400	70
3000	620	3000	70

Tab.4. 4 Thermal property

Mechanical data for simulation				
Temperature(°C)	*Expansion*	*Poison ratio*	*Elastic(Pa)*	*Yield(Pa)*
0	1.20E-05	0.28	2.10E+11	3.8E+08
300	-	0.295	1.90E+11	-
400	1.60E-05	-	-	3.8E+08
550	-	-	-	3.1E+08
600	-	0.31	1.20E+11	1.6E+08
800	1.60E-05	0.33	3.00E+11	2.0E+07
1000	2.20E-05	-	-	3.0E+06
1200	2.50E-05	0.33	3.00E+11	3.0E+06
3000	2.50E-05	0.33	3.00E+11	3.0E+06

Tab.4. 5 Mechanical property of DP600

The thermal analysis by using Gaussian distribution of conical heat source model in the solid phase leads to higher maximum temperature, more than 3000˚C, in the center of the FZ. That is much more difference from reality. The effect of fluid flow and solidification of material have significant effects on the temperature distribution and on the shape of FZ. Deng [2] proposed an artificially increased thermal conductivity to be approximately twice of the value at room temperature when the temperature is higher than the melting point temperature.

Different maximum temperatures of the FZ were observed based on two maximum temperatures: the *first model* corresponded to the peak temperature in FZ about twice the fusion temperature, 3100°C, and the peak temperature close to the fusion temperature, around 1900°C, for the *second model*. The last model is getting from increasing the conductivity more than 2 times of its value at room temperature.

Based on the study of Goldak [6], the residual stresses take affect at cooling phase when the temperature drop to 800°C. The mechanical data for all mechanical simulations are considered as a function of temperature. Their sensitive analysis has been studied in the thesis of Schwenk [13]. The mechanical data are presented in Tab.4.6.

4.4. RESULTS OF THERMAL SIMULATION

The Fig.4.8 shows the evolution of thermal simulation during the welding cycle, Fig.4.8 (a) and during the cooling cycle, Fig.4.8 (b).
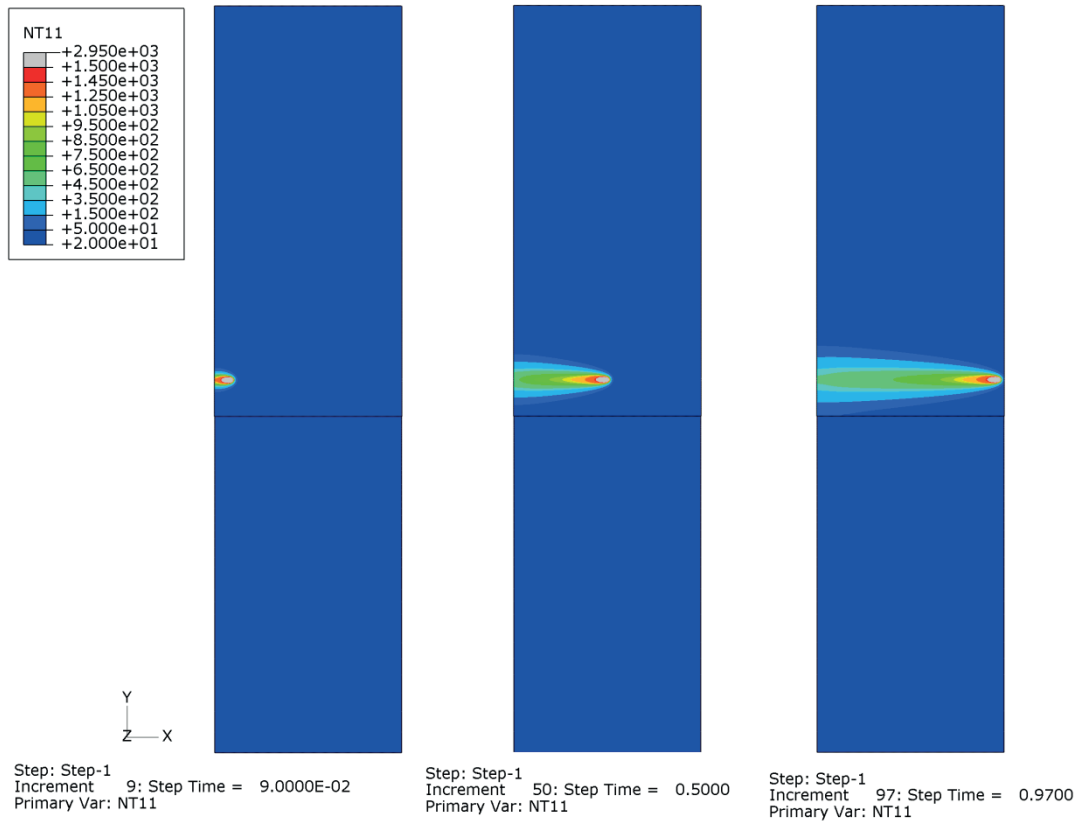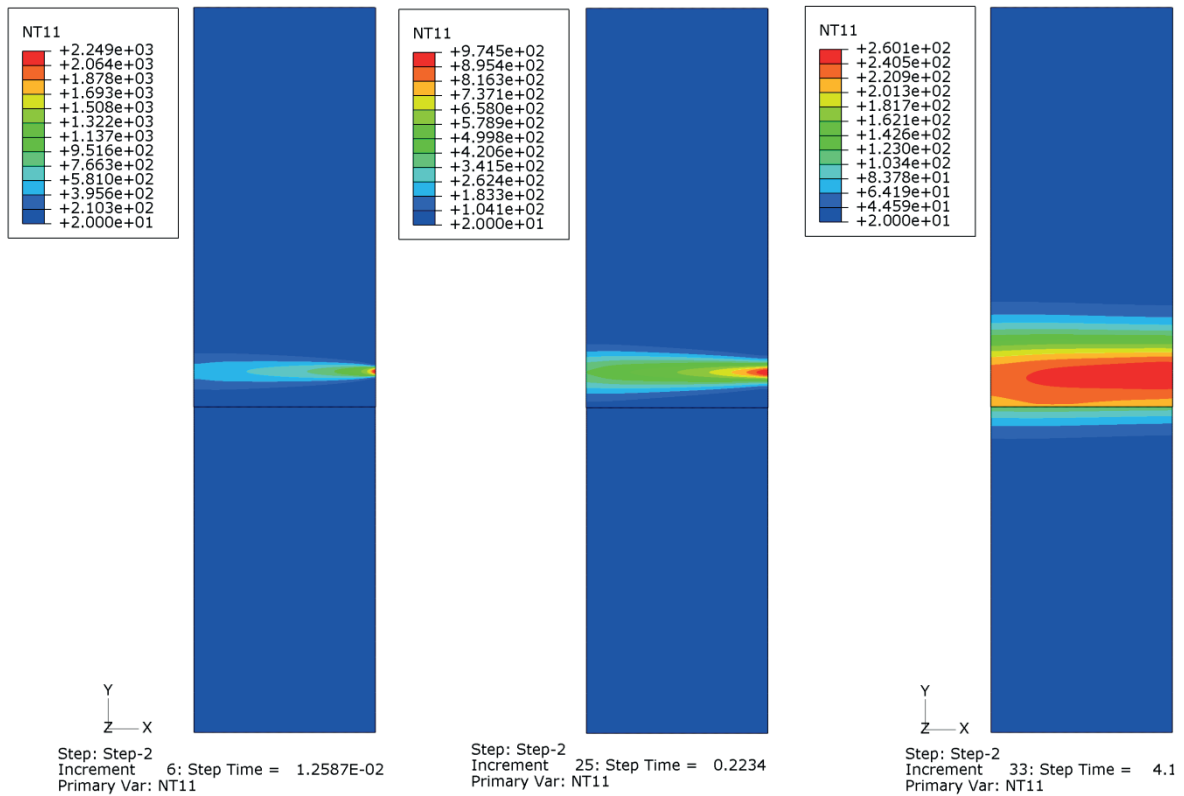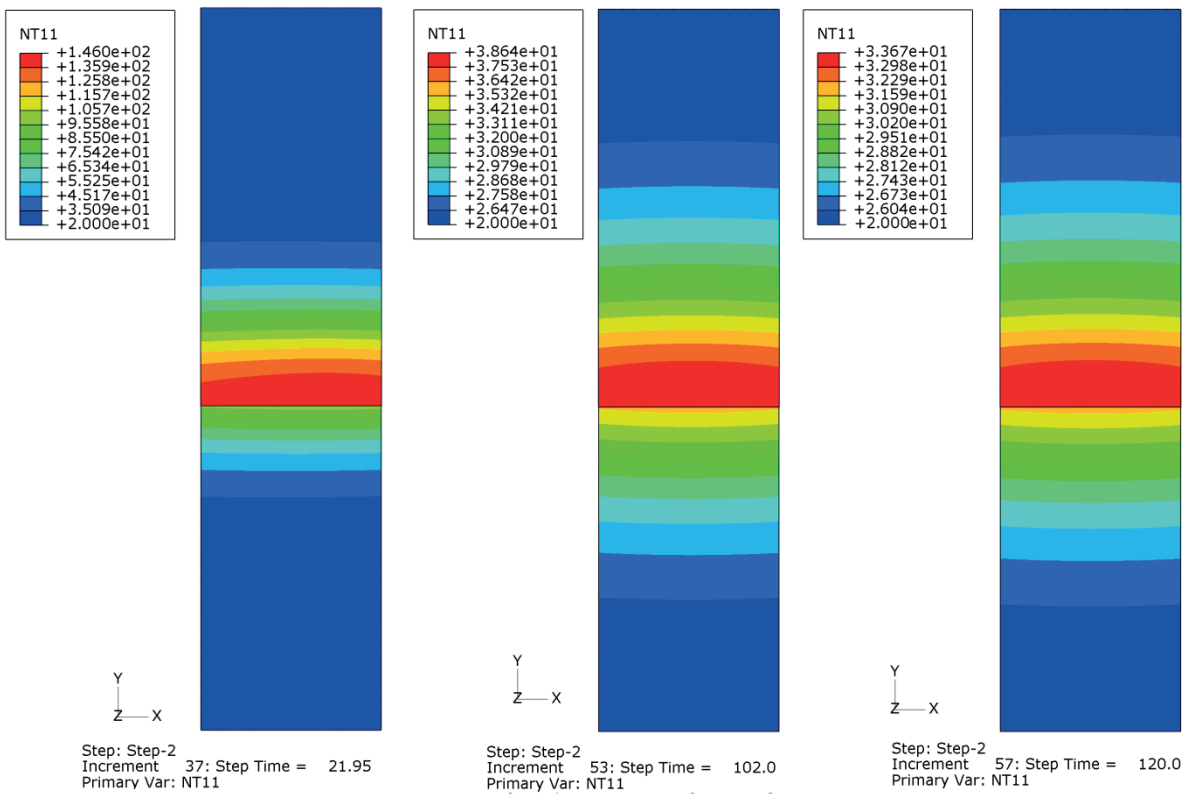
a) Welding cycle

b) Cooling cycle

Fig.4. 8   Temperature evolution during thermal simulation (°C)

4.4.1.   Effects of materials properties

Three points situated at the transverse line counted from center of the weld pool point A *(25, 0, 1.25)*, B *(25, 0.6, 1.25)* at the interface of solid and liquid phase and finally point C *(25, 5.3, 1.25)* at NHAZ are chosen to evaluate the evolution of temperature transient. Their locations are presented in Fig.4.9.

Fig.4. 9   Point A, B and C

140

4.4.1.1. Results at point A

Fig.4.10 represents the temperature evolution at point A by using three types of thermo-physical data.

Fig.4. 10   Temperature at point A

The results indicate that the simulation of model Material 1, *A-Material1*, with simplified material properties gives a high value of maximum temperature at the central of the weld pool compared to *A-Material 3* and *A-Material 2* from simulation of model 3 and model 2 seems to give the same value. The percentage of different is about 5.5% from model 1 and 3 and drop to 1.2% between model 1 and 2. In the cooling phase, the temperature drop on the same curve until 1500°C, below this temperature the difference between the curve *A-Material 1* and *A-Material 3* or *A-Material 2* appear clearly with 150˚C of the gap between them. So the material dependent temperature properties with or without peak-point at the phase change has no influence on the evolution of temperature in the weld pool.

The simplified parameter *A-Material 1* has signification influence on the temperature including the higher maximal value and also the curve of temperature during the cooling phase is faster than the two others models.

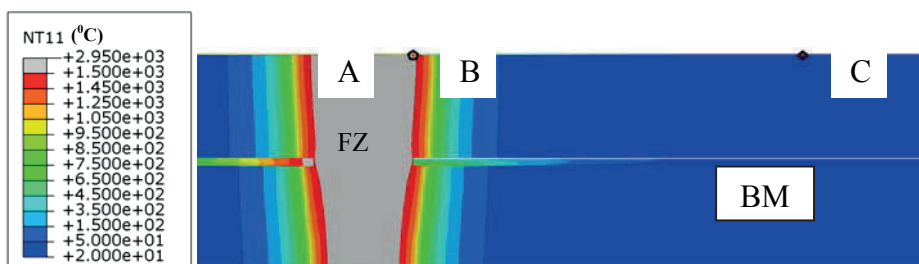### *4.4.1.2. Results at point B*

Fig.4.11 represents the temperature evolution at point B by using three types of thermo-physical data.

Fig.4. 11   Temperature at point B

The results on the Fig.4.11 show that the maximum temperature at the interface of solid and liquid of the weld pool is not quite different from the center of the welded pool of the point A, described in the Fig.4.10. Moreover, the percentage of *B-Material 2* compared to *B-Material 1* is to 1.5% and to 3.75% for simulation 1 *B-Material 1*. Otherwise the cooling curve translates, around 800°C-500°C, a different temperature between the curve *B-Material 3* and *B-Material 2*. This difference may be explained by the effect of the peak-point value of specific heat at Ac_1 when the maximum simulated temperature approach to the fusion temperature represented by curve *B-Material 3* and *B-Material 2* in Fig.4.11.

The curve *B-Material 1* still indicates the higher maximum temperature compared to others two models. The observation on the cooling phase shows that the temperature drop more rapidly than the two others models. That shows the same phenomena in the temperature at point A in Fig.4.10.

142

4.4.1.3. Results at point C

Fig.4.12 represents the temperature evolution at point C by using three types of thermo-physical data.

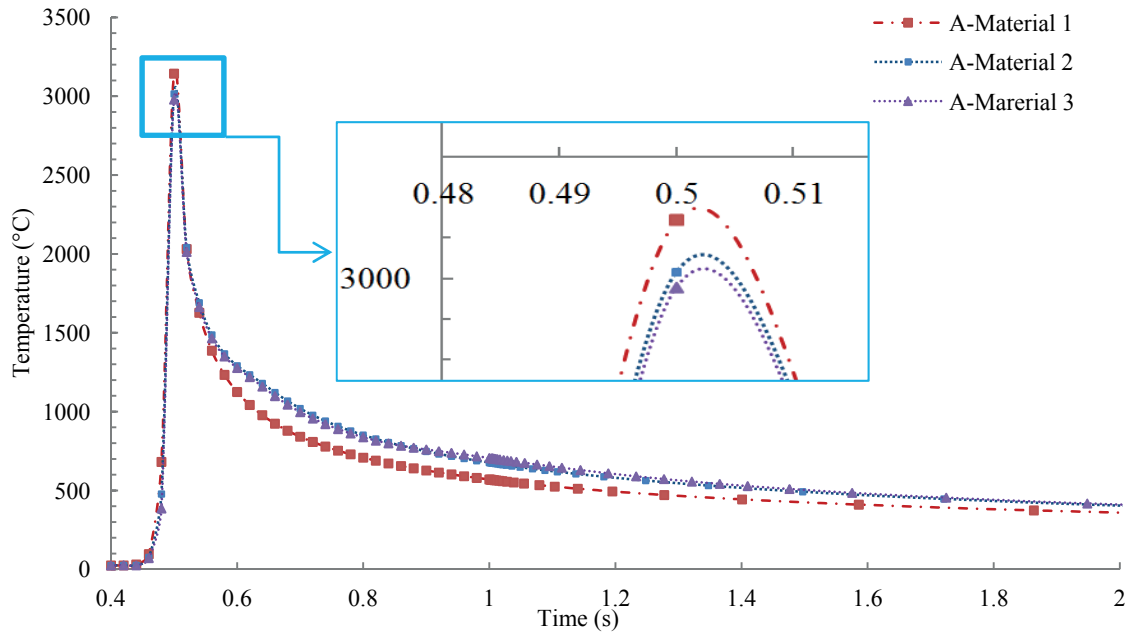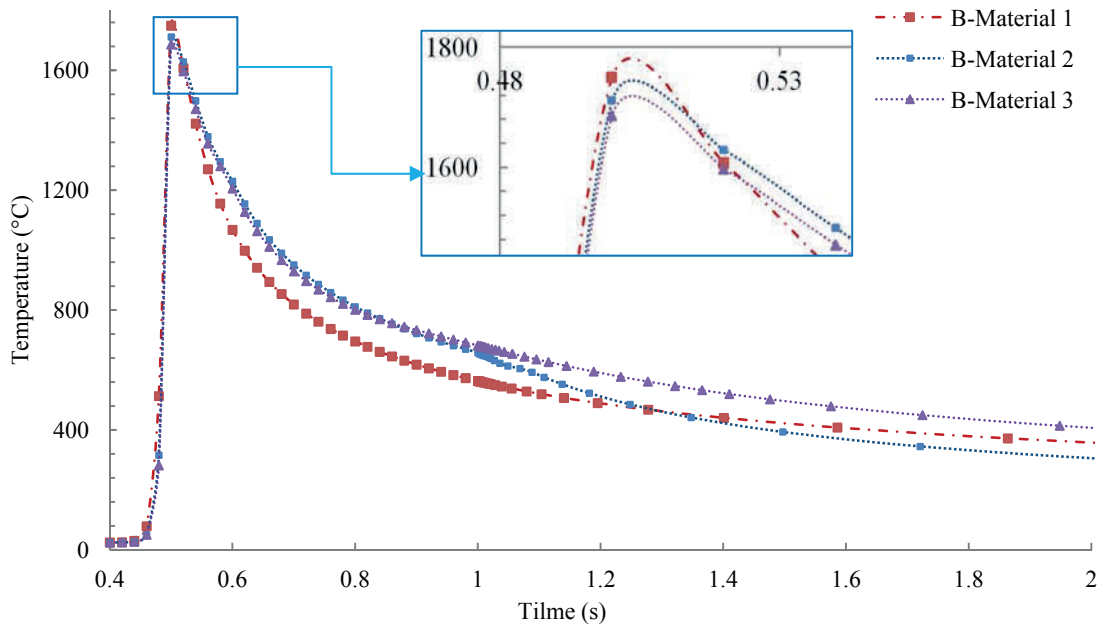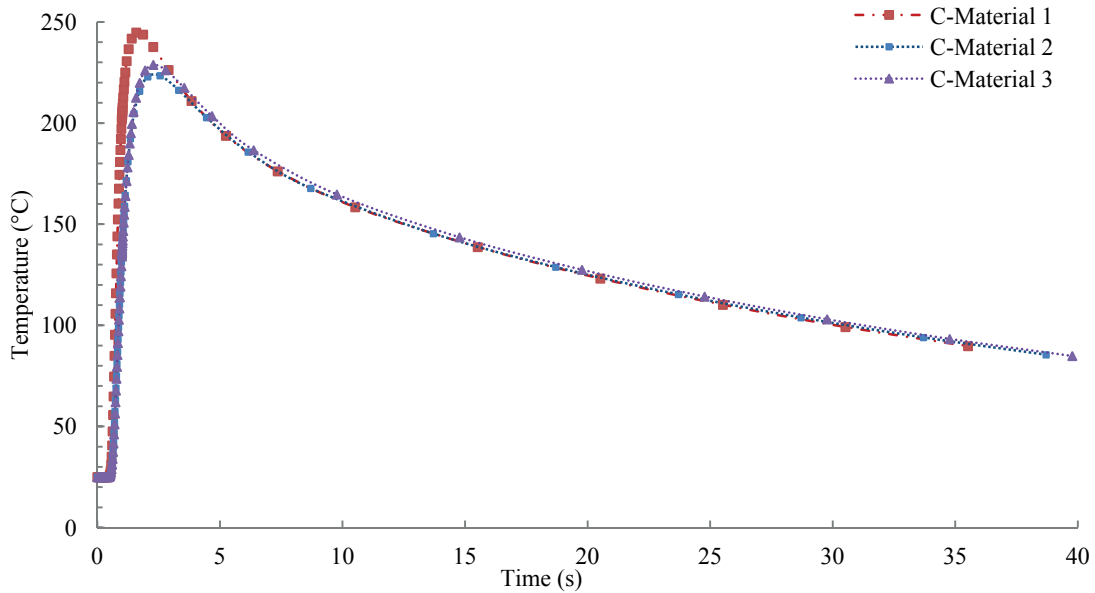Fig.4. 12   Temperature at point C

The point C represents the position far from the heat source, i.e in the base metal *(BM)*. The results in Fig.4.12 show the same higher maximum temperature belong to model number 1, *C-Material 1*. So the temperatures evolutions are the same for all simulations, in particular in the cooling phase where we observe the same temperature evolution during the cooling cycle.

So the constant thermo-physical property model gives a higher maximum temperature compared to the others two models but the same evolution of temperature cooling for the zone outside the FZ and HAZ.

4.4.1.4. Intermediate conclusion

Three points (A, B, C), located respectively in the FZ, interface between FZ and HAZ and the BM are studied by three simulations under influence of material properties. From the results, we can conclude that:

The temperature dependent material properties (*Material Model3)* have an influence on the temperature evolution inside the FZ and HAZ. Beside this zone, in the BM, no influence has been identified.

The temperature independent material properties *(Material Model 1)* have a significant influence on the maximum temperature in the FZ and HAZ. The results showed a difference of 5% and of 3.75 %, respectively in FZ, Point A in Fig.4.10, and the HAZ represented by point B in Fig.4.11.

The temperature dependent material properties overlook the phase transformation values *(Material Model 2)* have less effect on the temperature evolution. The results had shown a difference of 1.5% and of 1.2% respectively in the FZ and in the HAZ for the maximum temperature. So the peak value of the specific heat can be overlooked without influence on the maximum temperature even if the cooling curve indicates a different temperature evolution around 800˚C-500˚C.

The same declaration was found in the literature, which proved that the error percentage is less than 10% compared to the results getting from experimental for aluminum alloys [9].

4.4.2. Effects of meshing dimensions on the temperature evolution

In others to study the influence of meshing on the thermal simulation, we observes the maximum temperatures and also their evolution during the heating and cooling cycle at six points as shown in Fig.4.14 and Fig.4.15.

Six points ES*(25,0,1.25)*, EI*(25,0,-1.26)*, FS*(25,0.6,1.25)*, FI*(25,0.6,-1.26)*, GS*(25,10,1.25)* and *GI(25,10,-1.26)*, three situated on top surface ES, FS, GS and another three points on the bottom surface EI,FI, GI are used for examine the different values of temperature distributed on top and bottom surface of the model. The temperature distributed along the welding line on the top and bottom surface at instance 0.5s during welding process are also included in this observation.

144

Seven curves in each graph represent the temperature simulated by using seven values of meshes dimension of the quadratic element.

Fig.4.13 represents the points used to analysis the temperature under effect of meshing parameters.
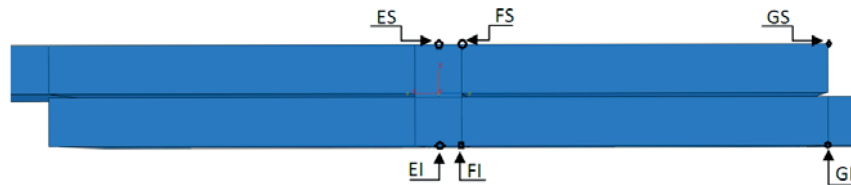
Fig.4. 13   Position of point E, F and G on top and bottom surface

4.4.2.1. *Temperature evolution at FZ*

Fig.4.14 presents the temperature evolution at the center of the weld pool respectively on the top and bottom surface. We can see in Fig.4.14 (a) that the effect of the mesh has little influence on the temperature at the center of the FZ. However, in Fig.4.14 (b), the mesh size has more influence on the evolution of temperature on the bottom surface.
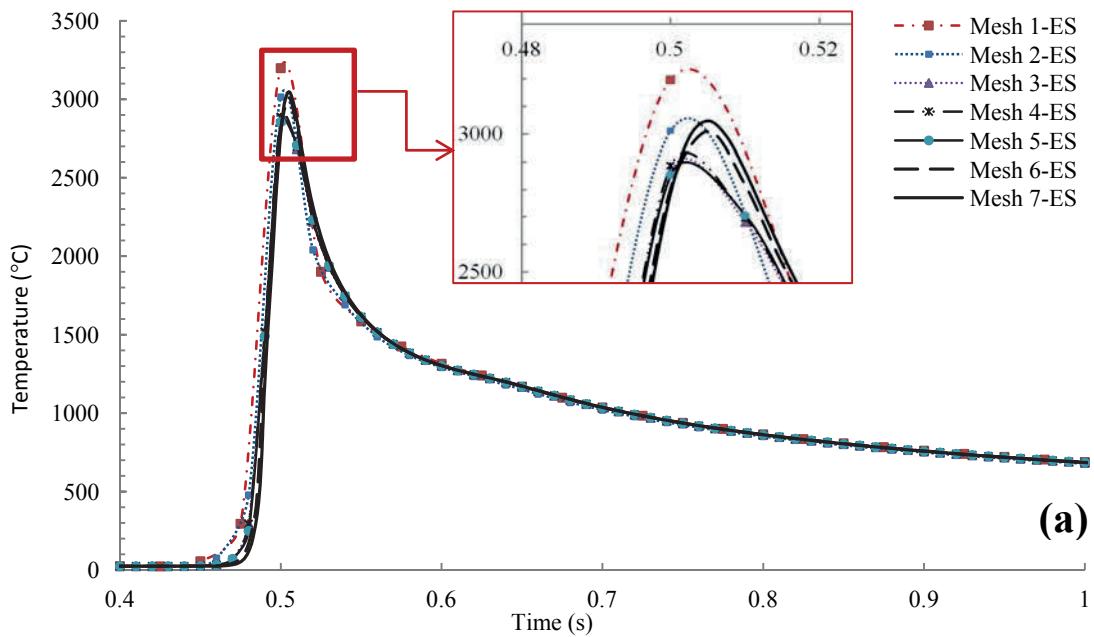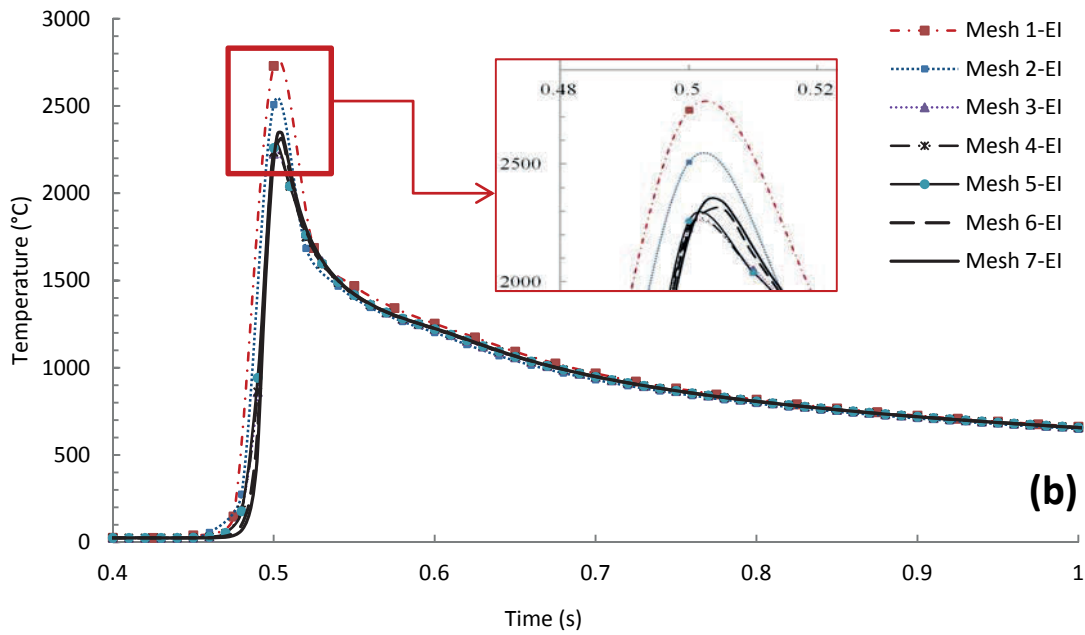
Fig.4. 14   Temperature at the center of FZ on top (a) and bottom surface (b)

4.4.2.2.   *Temperature evolution at the interface of FZ and HAZ*

Fig.4.15 shows the evolution of temperature at point F situated on top surface and bottom surface under influence of meshing dimension.
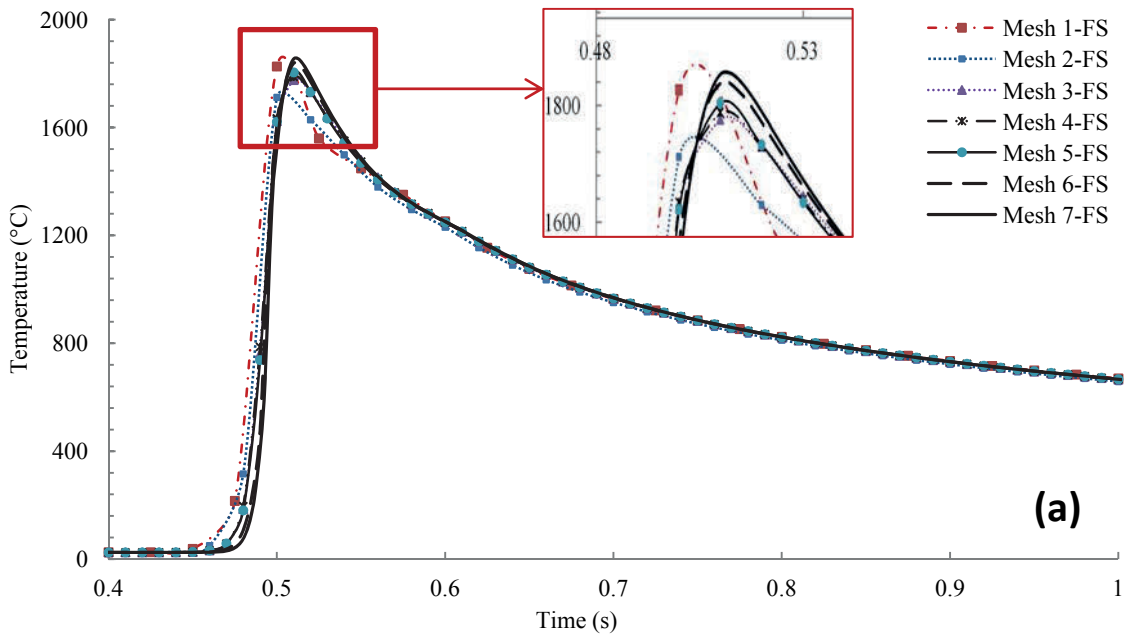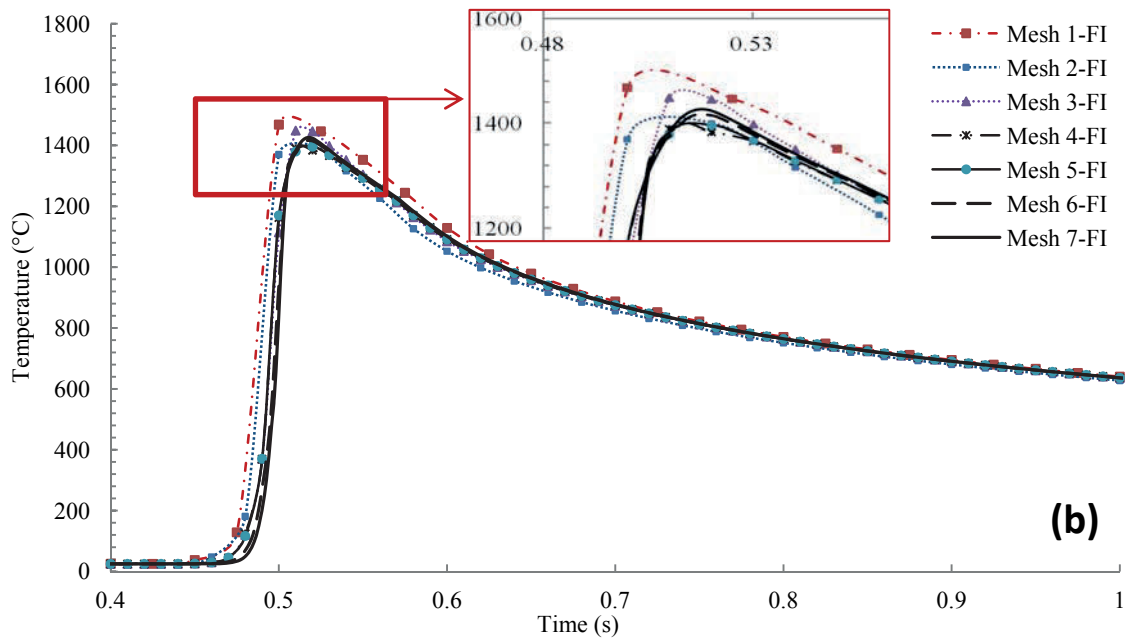
Fig.4. 15   Temperature at point F on top surface (a) and bottom surface (b)

The results of Fig.4.15 is identical to the previous results, Fig.4.14, where the effect of the mesh has little influence on the evolution of temperature at the interface FZ - HAZ on the top surface and a bit more influence on the evolution of temperature on the bottom surface.

4.4.2.3.   Temperature evolution at BM

Fig.4.16 shows the evolution of temperature at point G, Fig.4.13, situated on top surface and bottom surface under influence of meshing dimension. In the base metal *BM*, we find that there is no influence of the different mesh dimension on the temperature distribution on both top and lower surfaces.

147
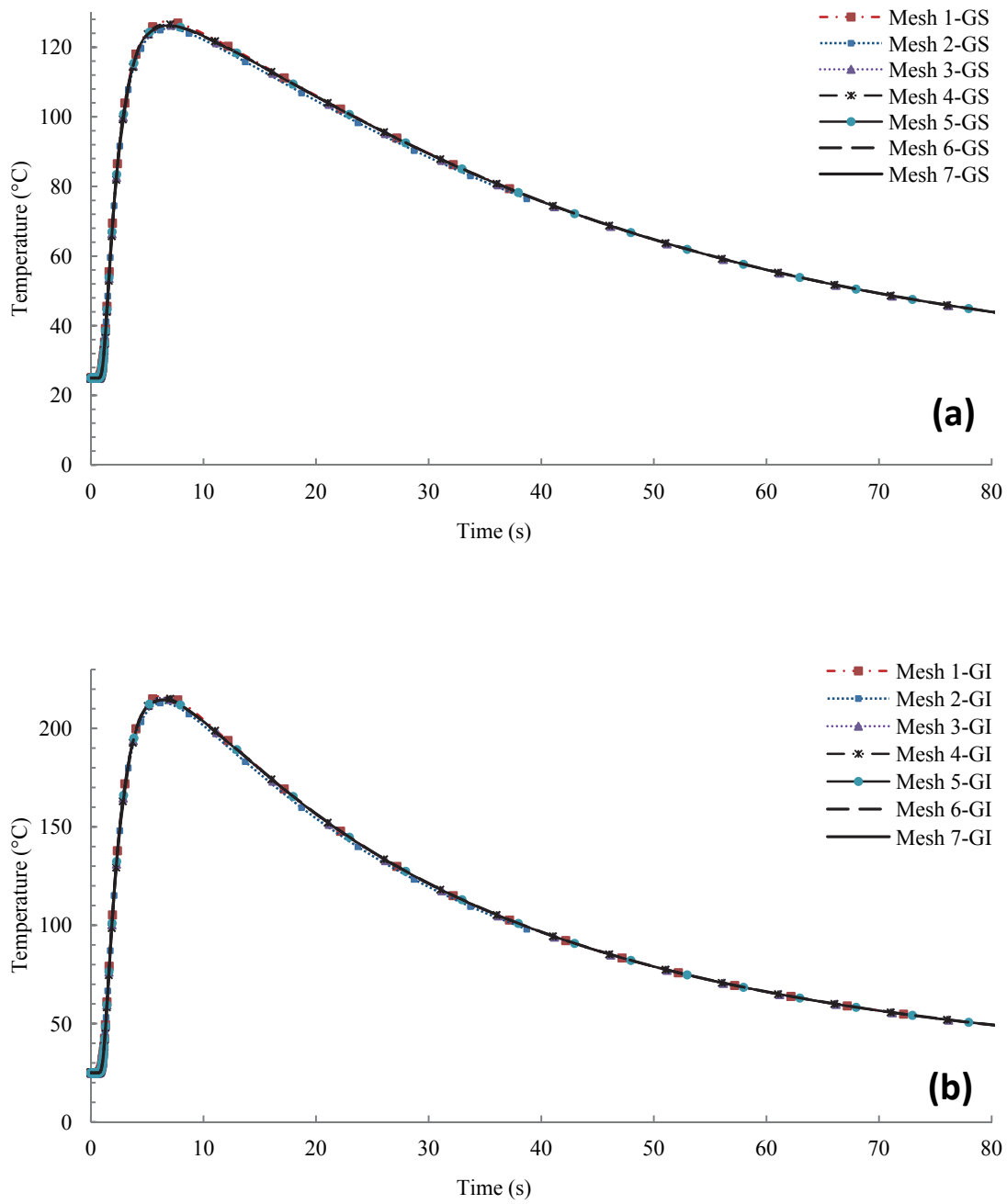
Fig.4. 16   Temperature at point G on top surface (a) and bottom surface (b)

4.4.2.4. *Effects of meshing dimensions on the temperature at instant 0.5 s*
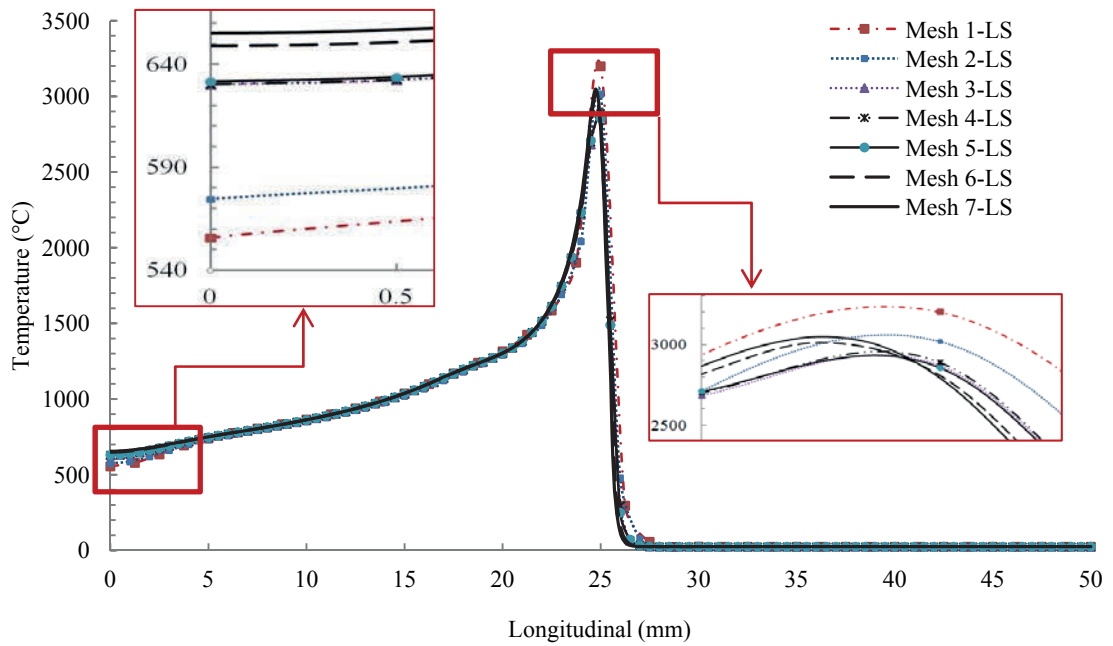
Fig.4. 17   Temperature along welding line on top surface at instant 0.5s
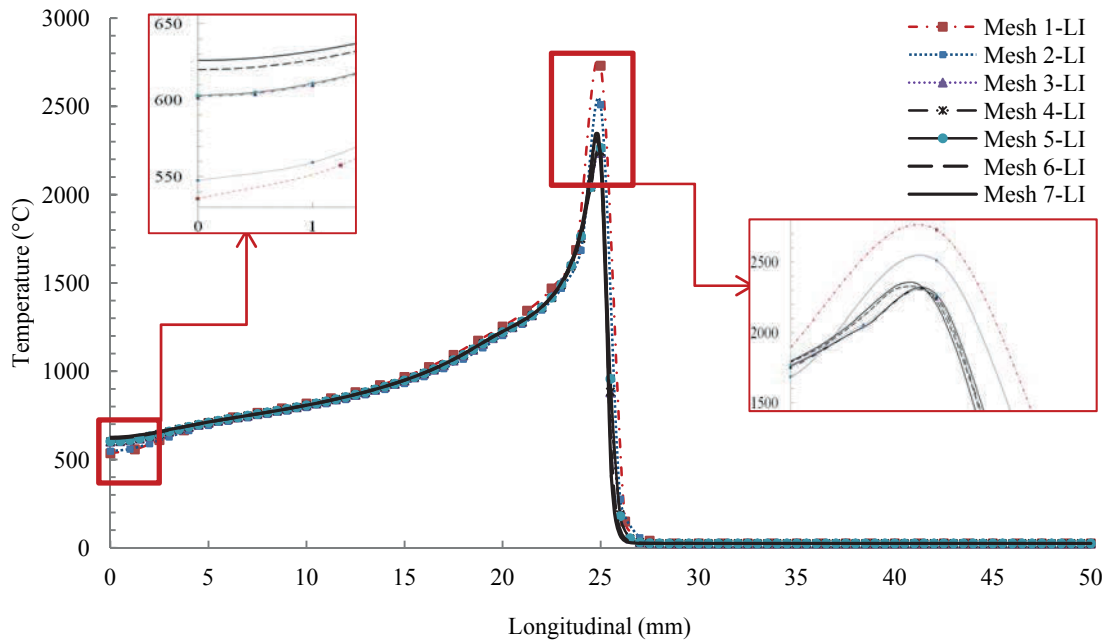
Fig.4. 18   Temperature along welding line on bottom surface at instant 0.5s

149

The two Fig.4.15 and Fig.4.16 represent the distribution of the maximum temperature along the welding line on top and bottom surface at instant of 0.5 second. They described the maximum temperature when the source heat located at point of 25 mm from the edge of sheet. The curve for a distance inferior to 25 mm describes the cooling after the pass of laser source heat.

In the two cases, we observe a maximum temperature of 3300°C and 2800°C respectively for the top and bottom surface in the weld pool. After heat by laser the temperature decreases quickly to achieve a temperature around 500°C in the weld bead in 0.5s as indicated in Fig.4.17 and Fig.4.18.

The maximum temperature distributed along the welding line, at instance of 0.5s, also proves the distinction by two curves for seven simulations with the gap of 100°C when the temperature at cooling stage less than 700°C. This is because of the different mesh inside the FZ and HAZ. The over preheat in front of the heat source by larger value of DX has been notified, but this error is overlooked by rapid welding speed.

4.4.2.5. Synthesis of meshing dimension

We can say that the coarse mesh size allows the nodes in front of the heat source heat faster than nodes in the fine mesh. This phenomena lead to higher maximum temperature for coarse mesh model than fin mesh model. During the cooling process the different values of mesh size are not affected on the evolution of temperature, as presented in Fig.4.14 to Fig.4. 16.

The maximum temperature getting from different mesh sizes are presented in Fig.4.19.

The peaks temperatures change with different mesh size in the FZ only, represented by the graphs ES and EI. The graphs FS and FI show less influence of mesh size on the peaks temperatures inside the HAZ. Furthermore, inside the BM, we observe no influence of meshing dimension on the peaks temperatures that are represented by the curves GS and GI in Fig.4.19.
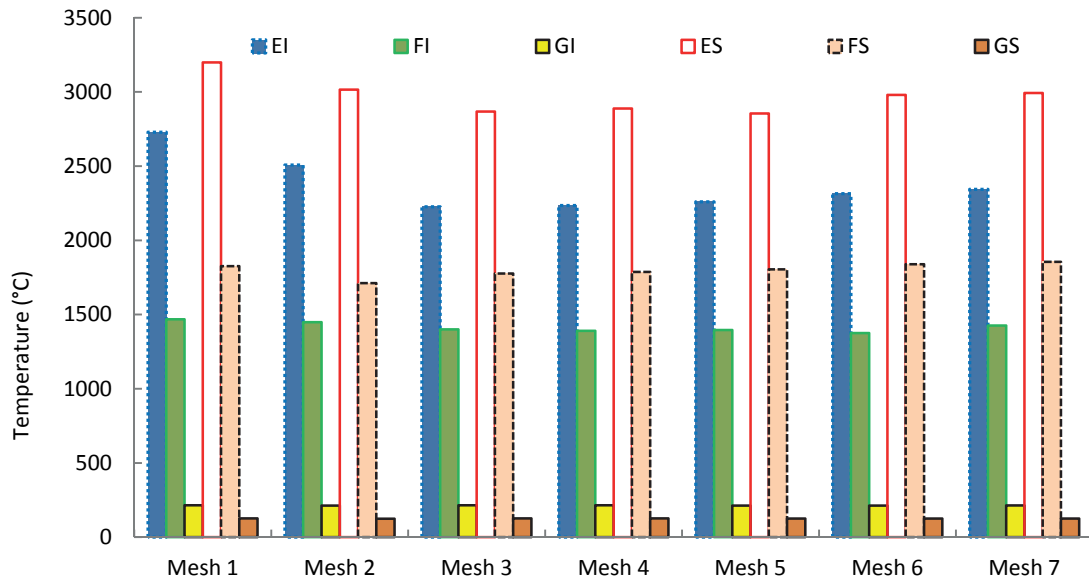
Fig.4. 19   Evolution of the maximum temperature in function of the mesh size at point E, F and G

Maximum temperature on the top surface of the FZ, represented by the graph *ES* in Fig.4.19, decreases from higher value in the model *Mesh 1* to a stabilized value in the models *Mesh 3, Mesh 4 and Mesh 5*. The same phenomena are found for peak temperature inside FZ on the bottom surface represented by graphs *EI* in Fig.4.19. This is due to the coarse mesh used in the model *Mesh 1*.

In model *Mesh 3*, *Mesh 4*, *Mesh 5* that use the same value of DX but a different value of DY and DZ, we decreased the elements sized in Y and Z direction by two for *Mesh 5* compared to *Mesh 4* or *Mesh 3*. These modifications cause a little influence on the maximum temperature, less than 1.5%, in weld pool. That is represented by the graph *ES and EI* in the Fig.4.19.

The graphs FS and FI in the boundary of FZ- ZAT of the models *Mesh 3, Mesh 4, Mesh 5* indicate the same meaning to the curve ES and EI. So the difference of DY and DZ has not influence on temperature in the FZ and ZAT.

The graphs *GS and GI* as indicated in Fig.4.19 represented the evolution of temperature in the BM, the horizontal line of this two curves show no sign of temperature variation during the variation from the coarse mesh to the fine mesh.

The model *Mesh 1* over evaluates the results, 19%, compared to *Mesh 5*, for EI and 11% for ES, because of the biggest mesh size in ZAT and FZ. Furthermore, the ratio of DX/R is not the same for top and bottom surface of the model that should be the cause of difference in percentage of the graphs EI and ES.

Passing from *Mesh 1* to *Mesh 2* by decreasing element size *DX*, the error reduce twice. For *Mesh 4* or *Mesh 3* the error drops to 1.5%. So it is clear that the element size along the welding direction plays an important role in precision of thermal analysis.

The model *Mesh 6*, consumes of 1608 minutes of analysis, with small mesh gives higher value of temperature on the top surface and slice difference on the bottom surface. This is because of the very small dimension mesh especially DX that let to overlap of heat flux in the same position on top surface than on bottom in the simulation.

The model *Mesh 7* with reducing DX from *Mesh 9* by factor of 2, using minimum value defined in [8], shows higher computing time compared to model and M9 around 3113 minutes of analysis. Maximum temperature in FZ increases less than 5% in FZ and less than 3% in HAZ compared to model *Mesh 5* and less than 1% compared to *Mesh 6*.

In general, the maximum temperature increases when the element size reduced. Model *Mesh 3, Mesh 4, Mesh 5, Mesh 6, Mesh 7* give the difference on maximum temperature less than 5% in FZ and less than 3% in HAZ by different mesh size elements.

Model	Zone1			Zone 2	Zone 3[a]
	DX/R_{Bottom}	DY/R_{Bottom}	DZ/R_{Bottom}	DY/R_{Bottom}	*BIASE*
Mesh 1	2.500	1.200	1.250	3.760	10:12
Mesh 2	2.000	1.200	1.250	1.880	10:25
Mesh 3	1.200	1.200	1.250	1.880	10:25
Mesh 4	*1.200*	*1.200*	*1.250*	*0.940*	*20:25*
Mesh 5	1.000	0.600	0.625	0.626	20:25
Mesh 6	0.500	0.600	0.625	0.626	20:25
Mesh 7	0.250	0.600	0.625	0.626	20:25

[a]10:12 means 12 elements with biases factor of 10 from the small and the bigger one.

Tab.4. 6 Mesh size and heat source dimension

The ratio of the element length and the minimum heat source radius, as presented in Tab.4.6, shows clearly the influence of element size and the heat source radius. One can see that the ratio *DX/R* must be smaller than two in order to get minimum accurate precision of thermal simulation. It has been used in the work of [6], [7] with success and has been verified experimentally. This ratio is sufficient and can reduce the numbers of element in the direction of welding. The modification of others dimensions DY and DZ have less influence in the results. Nevertheless, DY in the HAZ plays an important role because it defines the different temperature in the weld pool. In our work, the value of DY is fixed to 2 elements per radius and DZ to 4 elements per thickness. This choice is a minimum value and is verified in the literature in [8].

4.4.3.   Effects of maximum temperature
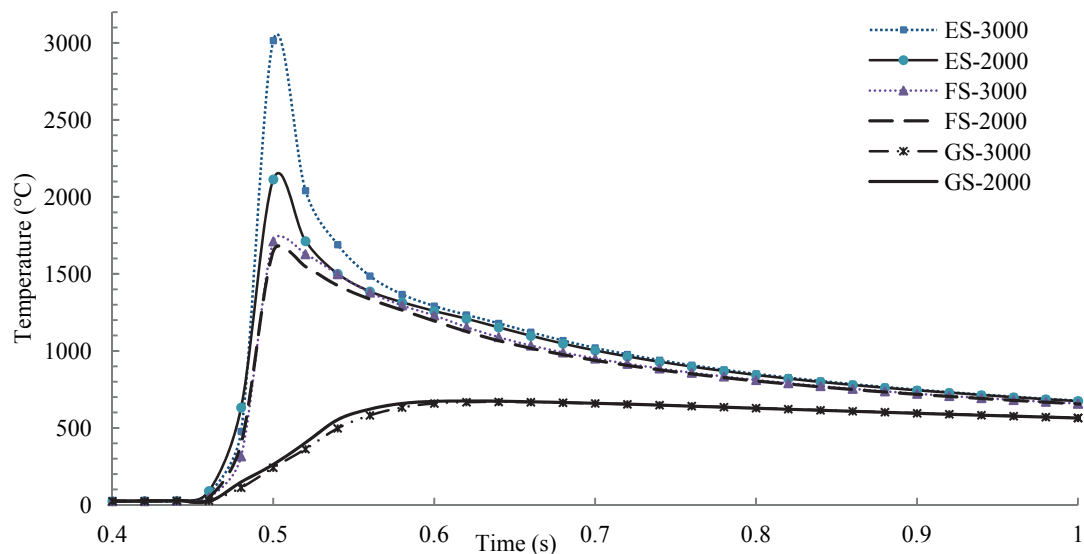
Fig.4. 20   Temperature at point ES, FS, GS

The distribution of temperature at point ES, FS and GS are presented in Fig. 4.20 where the peak temperature is about 1000°C of different at the central of the weld pool, curves ES-3000 and ES-2000, and 100°C of different at the edge of weld pool, the curves FS-3000 and FS-2000, and almost took the same peaks temperature in the region outside FZ

and HAZ, the curves GS-3000 and GS-2000. So the different peak temperature inside FZ has less effect on the cooling cycle after passing of laser beam.

4.4.4. Effect of convection

Three convection modes are used to study its influence on the laser welding process. Those convections conditions are described below:

- Convection 1: *low convection and radiation* with a coefficient of convection of 15W/m²C and an emissivity of 0.25.

- Convection 2: *medium convection and radiation* with a coefficient of convection 75W/m²C and an emissivity of 0.35.

- Convection 3: *forced convection and radiation* with a coefficient of convection of 150W/m²C and an emissivity of 0.8.

Fig. 4.21 shows the evolution of different temperature at point ES, FS and GS under effect of convections modes. The convection mode seems to affect the cooling process of region which has temperature bellow the Ac_1, 600°C, as indicated in Fig.4.21 (a, b, c). For the region which has temperature more than Ac_1, the convections modes do not affect on the cooling process. This is because of the laser welding is operated at higher speed so the dissipation of laser heat inside the metal after passing of laser beam is very important compared to the surface convection and radiation. The observation on influence of heat transfer during laser process Ferro et al [4] also proved that the heat conduction plays an important role in heat flow and the surface convection and radiation have little effect on FZ and HAZ boundaries.

(a)

(b)
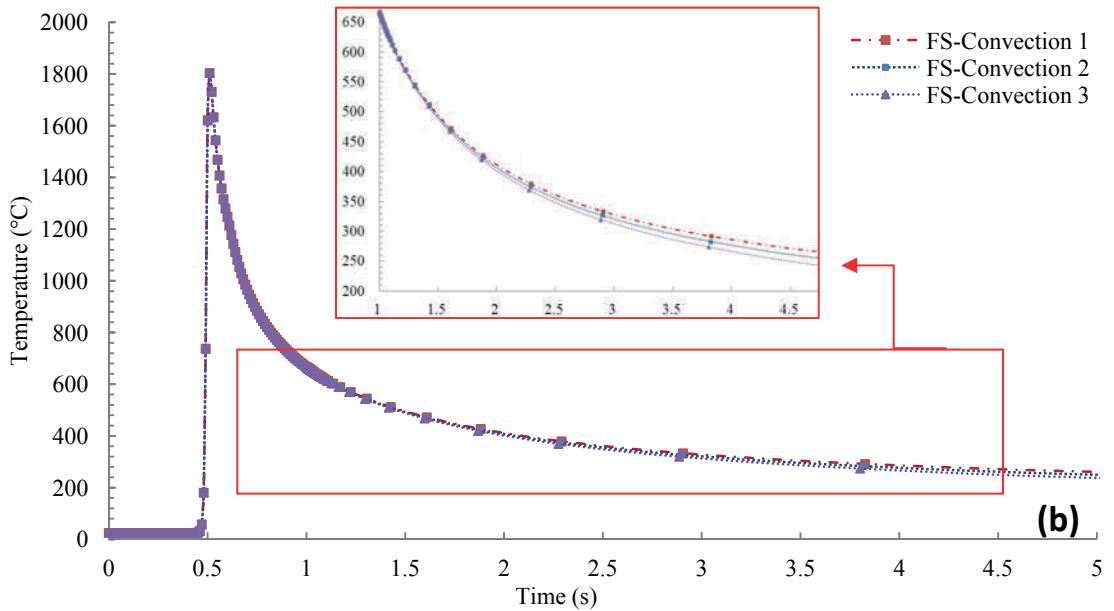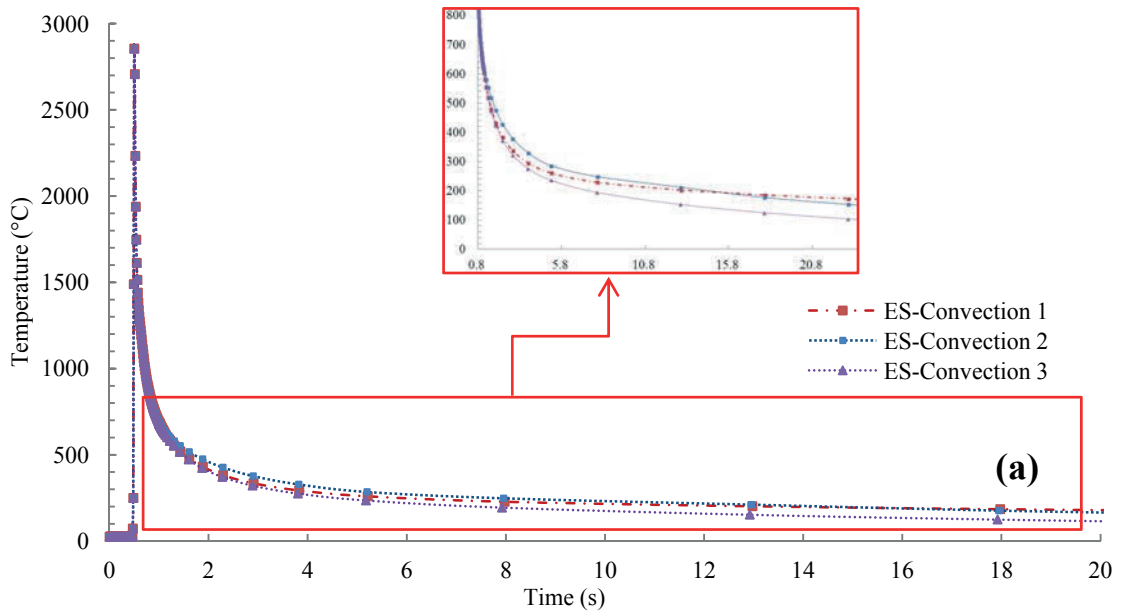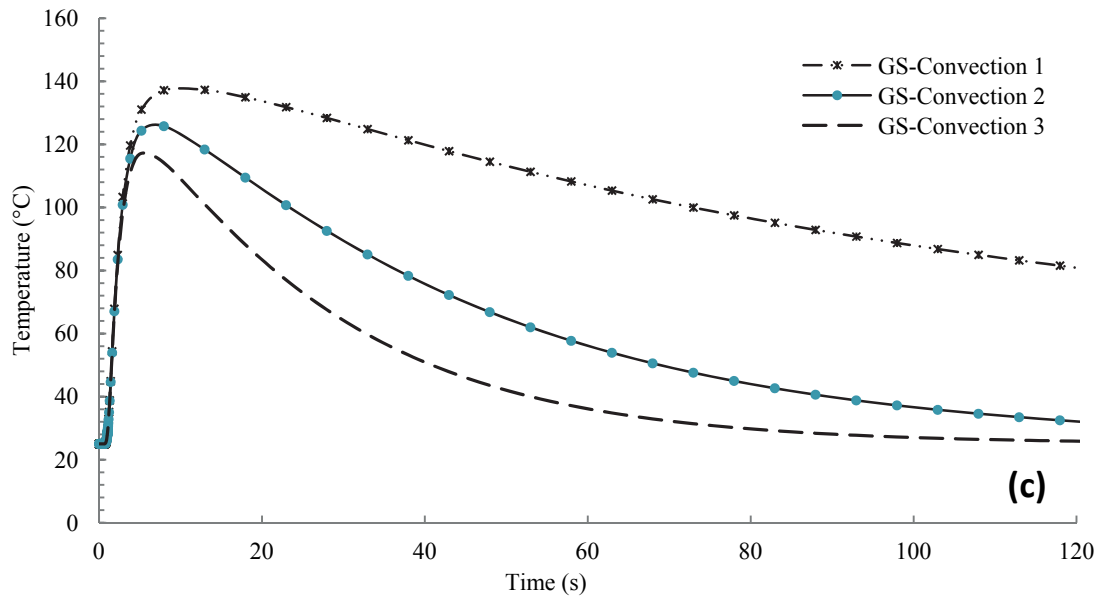
Fig.4. 21   Temperature at point ES (a), FS(b), GS(c)

4.4.5.   Intermediate conclusion

In conclusion, the maximum temperature increases when the element size reduced. The results show that the ratio of DX/R must be smaller than two in order to get minimum accurate precision of thermal simulation. This ratio is sufficient and can reduce the numbers of element in the direction of welding. The modification of others dimensions DY and DZ have less influence in the results. Nevertheless, DY plays an important role because it defines the different temperature in the FZ and in the HAZ. In our work, the value of DY is fixed to 2 elements per radius and DZ to 4 elements per thickness. The convection modes have less influence on the peak temperature and the cooling rate after passing of laser beam. The different peak temperature used in numerical simulation does not affect the temperature evolution outside the HAZ.

4.5. RESULTS OF MECHANICAL SIMULATION

The Fig.4.22 shows simulation results of Von Mises residual stresses of welding.
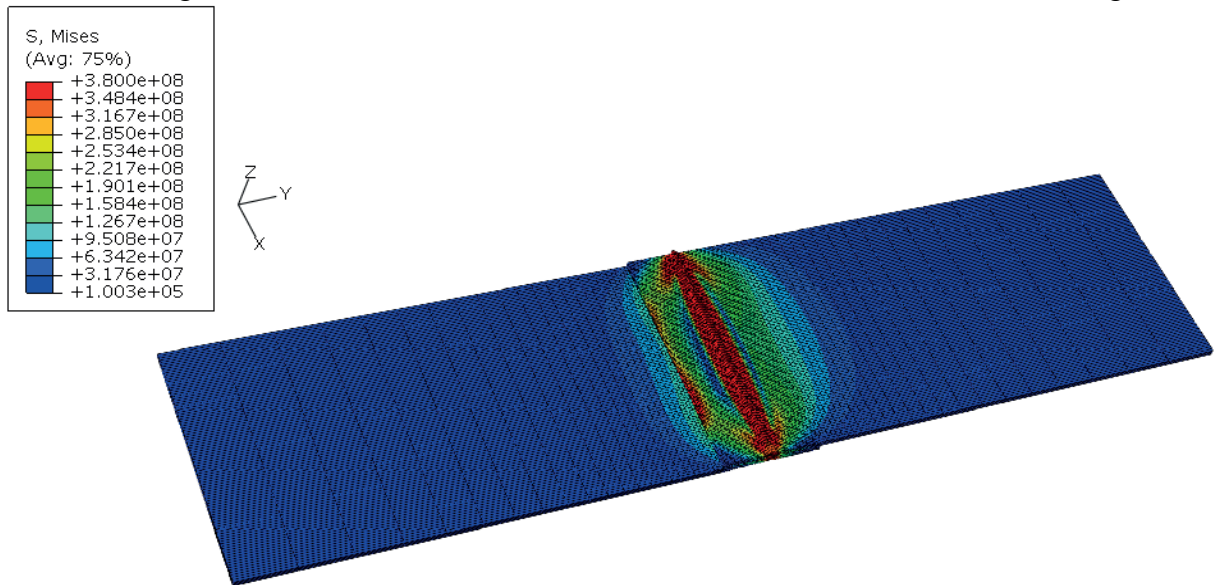
Fig.4. 22   Von Mises residual stresses of mechanical simulation

4.5.1. Effects of Mesh size

In order to study the influence of mesh size on the mechanical simulation results, the residual longitudinal stresses S_{11} and the Von Mises residual stresses *VM* along the longitudinal line, *on the welding line*, and transverse line are considered. The positions of these two lines are presented in Fig.4.23.
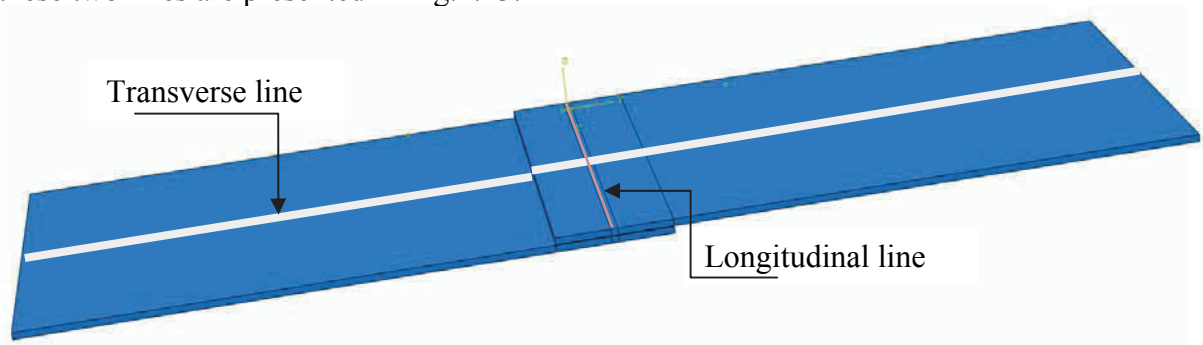
Fig.4. 23   Position of longitudinal and transverse line

The curve of Von Mises stresses gives a clear difference of the results from different meshes than the curve of longitudinal stresses because the equivalence value of the three axial residual is a medium values of the triaxial stresses. Among these triaxial stresses the

longitudinal stresses is higher than other residual stresses so most of the graph showing in this chapter is the equivalence Von Mises stresses and longitudinal stresses as presented in Fig.4.24, Fig.4.25, Fig.4.26 and Fig.4.27.

4.5.1.1. *Stresses along longitudinal line*

Fig.4.24 and Fig.4.25 represents respectively the curve of the Von Mises stresses and longitudinal stresses along longitudinal line on the top surface of the model, Fig.4.23, getting from six simulations.

Base on Fig.4.24 and Fig.4.25, all the simulations give almost the same values of maximum stresses around 380MPa. We observe on Fig.4.24 a small difference in VM-Model 1 with a decreasing of the maximum Von Mises stresses around 20MPa compared to others simulations at the middle of the longitudinal line. The more significant results are seen on Fig.4.24 where the mesh has significant influence on the Von Mises stresses at the start and the end of edge sheet model. The coarse mesh seems to over evaluate the residual stresses compared the value of residual stresses of the fine mesh as shown in Fig.4.24 and Fig.4.25. The observations show that the meshing dimension has influence on the residual stresses.
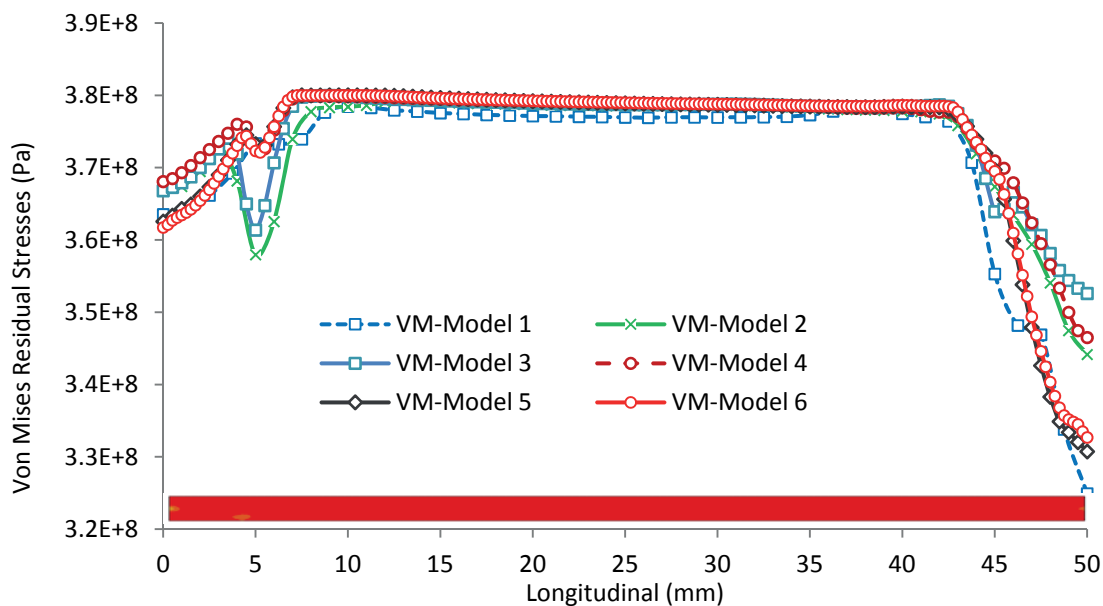
Fig.4. 24   Von Mises residual stresses along the top longitudinal line
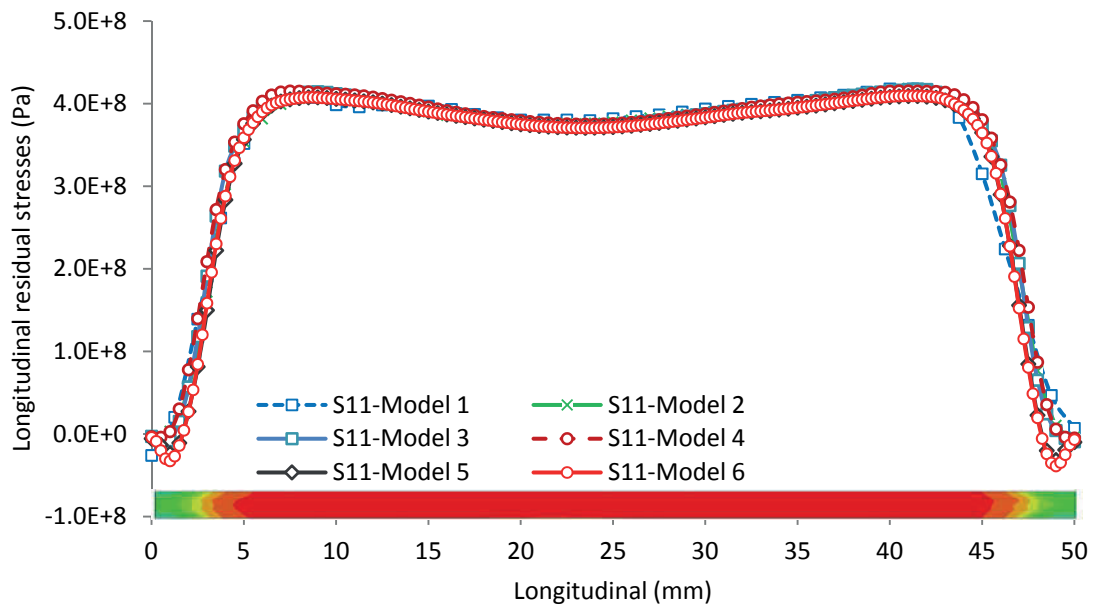
Fig.4. 25   Longitudinal residual stresses along the welding line

The *Model 5* and *Model 6* give the same value of residual stresses closes to each others, the same results for *Model 4* and *Model 3*. For the *Model 4 and Model 3*, it is normal because these two models have the same meshes parameters in the FZ.

But for the *models 5* and *Model 6*, the meshes sizes are the same in Z and Y directions and different in the X-direction. The simulated results between these two models confirmed that there is no influence of mesh size in X-axis on the residual stresses.

4.5.1.2. *Residual stresses along transverse line*

Fig.4.26 and Fig.4.27 represent respectively the curve of the Von Mises stresses and longitudinal stresses along transverse line on the top surface of weld zone getting from six simulations.

The maximum Von Mises stresses (375MPa), presented on the transverse line in Fig. 4.26, and are situated around 3 mm from fusion centered line. These stresses drop to a minimum value of 30MPa situated around 4mm from the weld center. The edge of plat that close to the weld pool presents a maximum Von Mises stresses.

Regarding the longitudinal stresses showed in Fig.4.27, the maximum tensile longitudinal residual stress is around 400MPa situated approximately 3mm from welded pool centered line. Because of dissymmetry of weld plat, the compression stresses drop to maximum compression stress on the edge closed to the weld pool, -300MPa, and minimum compression stress, -150MPa, on the others side.

Fig.4.26 and Fig.4.27 show that the curves of residual stresses of *Model 4, Model 5* and *Model 6* are the same value. Indeed, the curves of these three simulations are confused to a single curve for the residual longitudinal stresses and residual Von Mises stresses along the transverse line. Compared to these models, *Model 3* gives some different values at the minimum value outside the ZAT. Only the curves represented the *Model 2* and *Mode 1* that give different value in tensile and compression stress from the curves of *Models 3, 4, 5, 6*.

The mesh density at the HAZ and NHAZ of *Model 3* arrives at the maximum mesh size as indicated in the residual Von Mises stresses, Fig.4.26. The results show an over estimate of compression stress in this zone compare to the results of fine mesh in *Model 5 and 6*. From the mesh size point of view, the difference of maximum and minimum stresses in the HAZ and in the NHAZ of *Model 3 and Model 4* can be explained by the influence of the doubling mesh elements from *Model 3* to *Model 4*.
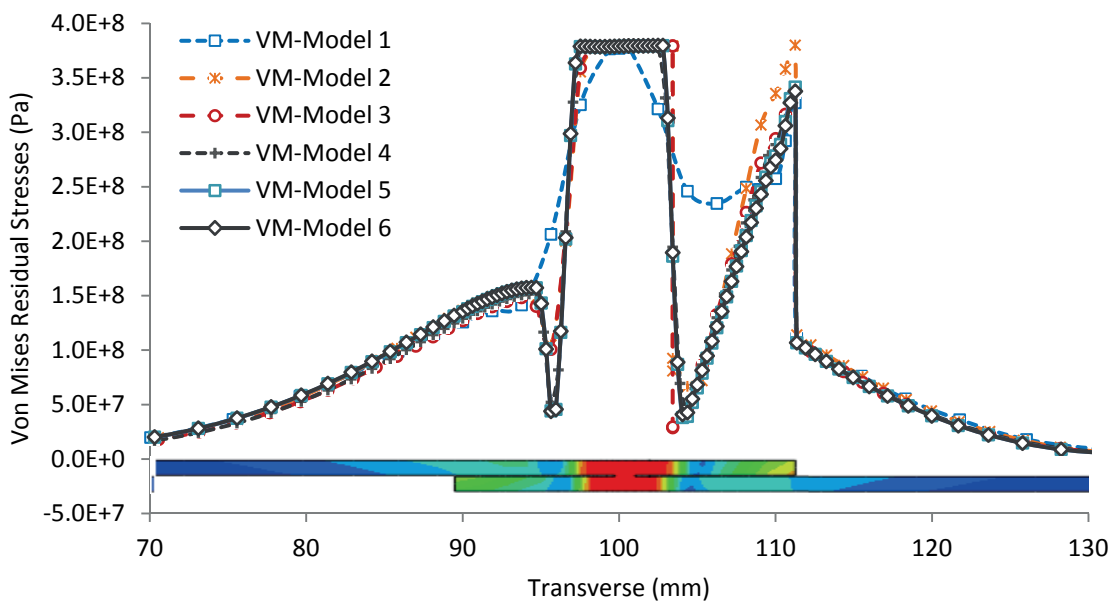
Fig.4. 26   Von Mises residual stresses on the top transverse line
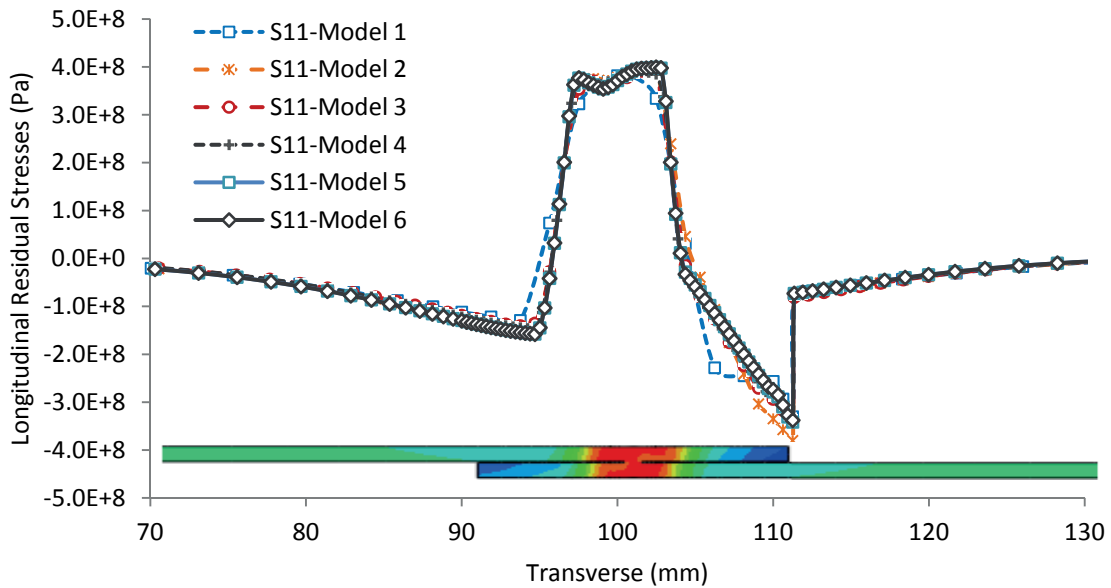
Fig.4. 27   Longitudinal residual stresses on the top transverse line

Regarding to the *Model 4*, the compression stress is similar to the *Model 5* and *Model 6* that is the same as the results indicated in Fig.4.24 and 25. If the side effect is less considered the *Model 4* also gives an interesting results compared to *Model 5 and Model 6*.

The *Model 5* gives a similar result to *Model 6*, although the mesh elements along the weld direction have been multiplied by factor of 2. No influence of finer mesh affects the results for these two models.

Compared to residual stresses of *Models 5 and 6*, the results show that the mesh of *Model 4* is sufficient and so acceptable for mechanical simulation.

4.5.1.3.   Syntheses of meshing dimension

After observing the residual stresses along the longitudinal and transverse line we can conclude that the mesh element in *Model 4* is sufficient and so acceptable for simulation of residual stresses in laser welding in condition the side effect *(start and stop of laser heat source)* is not taken into account. Otherwise *Model 5* give the same results for residual stresses in transverse direction and also give better residual stresses *(along longitudinal line)* for side effect compared to the residual stresses of *Model 4*.

Model	Zone1			Zone 2	Zone 3[a]
	DX/R_{Bottom}	DY/R_{Bottom}	DZ/R_{Bottom}	DY/R_{Bottom}	$BIASE$
Mesh 1	2.500	1.200	1.250	3.760	10:12
Mesh 2	2.000	1.200	1.250	1.880	10:25
Mesh 3	1.200	1.200	1.250	1.880	10:25
Mesh 4	*1.200*	*1.200*	*1.250*	*0.940*	*20:25*
Mesh 5	1.000	0.600	0.625	0.626	20:25
Mesh 6	0.500	0.600	0.625	0.626	20:25

[a]10:12 means 12 elements with biases factor of 10 from the small and the bigger one.

Tab.4. 7 Mesh size and heat source dimension

The ratio of the element length and the minimum heat source radius, as presented in Tab.4.7, shows clearly the influence of element size and the heat source radius on the results of mechanical simulation. The approach between the mesh size of *Model 4* and the minimum radius of heat source R_{Bottom}, one found out that the mesh size equal to the radius of laser heat source give the results of residual stresses close to the results of finer mesh size in *Model 5 and 6*. So the mesh size equal to the radius of heat source can be the minimum requirement for the minimum precision of residual stresses simulation of laser welding. It required less element in mechanical simulation compared to thermal simulation.

The mesh size in HAZ and FZ, DX, should be less or equal to the radius of heat source radius for better results of simulation. So the minimum mesh size along the welded direction and in transverse direction is equal to the value of radius of heat source model for minimum precision of the mechanical simulations.

The mesh density at the HAZ and NHAZ of *Model 3* reaches at the maximum mesh size as indicated in the residual Von Mises stresses, Fig.4.26, theirs values reach two times the radius of the conical heat source. The results show an over estimate of compression stress in this zone. Regarding *Model 4* with mesh size close to the radius of heat source, the compression stress is similar to *Model 5* and *Model 6* that is the same as the results indicated in Fig.4.26 and Fig.4.27.

4.5.2. Residual stresses on top and bottom surface

In order to observe the influence of different temperatures from top and bottom surface of welding sheet, we compare the longitudinal residual stresses along the welding direction, represented by the curve *VM-Model 6-Top* for Von Mises residual stresses on top surface and *VM-Model 6-Bottom* for bottom surface longitudinal line showed in Fig.4.28. We also compared the longitudinal stresses on the transverse line of top surface, *S11-Model 6-Top* and bottom surface corresponded to the curve *S11-Model 6-Bottom* in Fig.4.29.
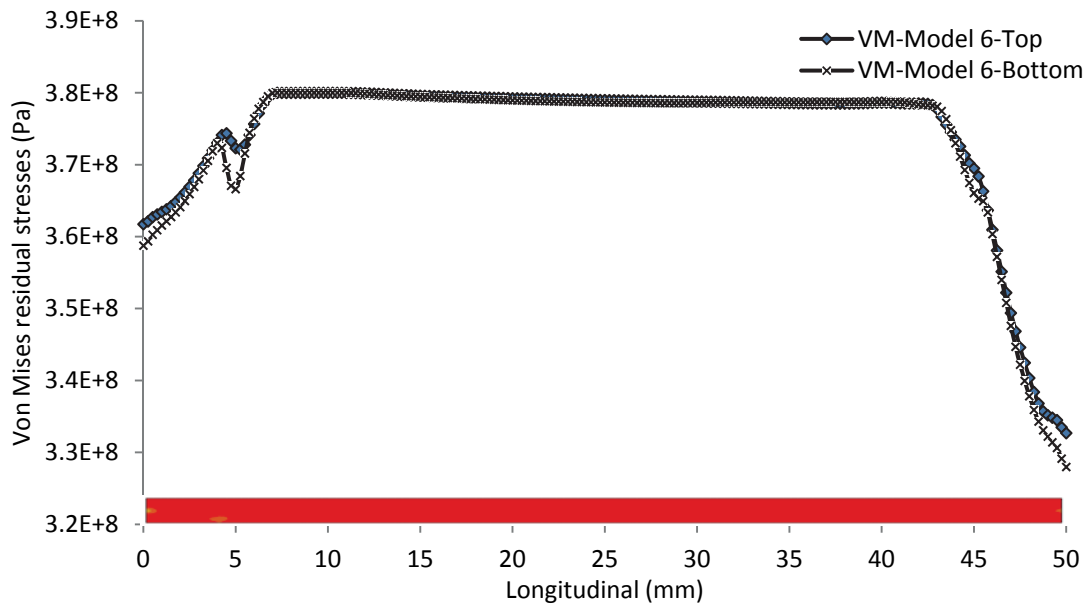
Fig.4. 28   Von Mises residual stresses on top and bottom longitudinal line

163
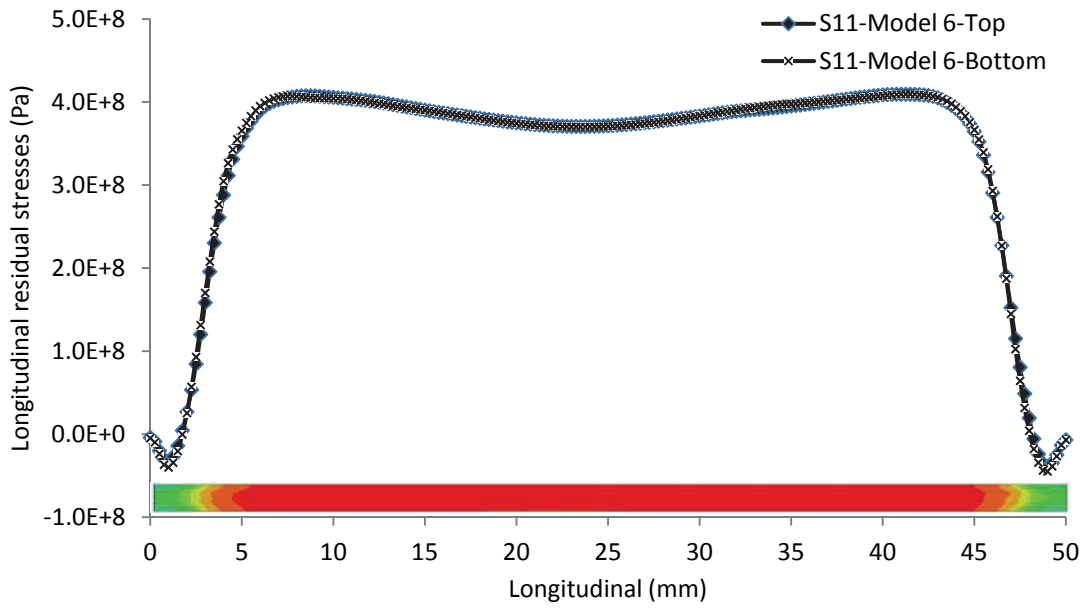
Fig.4. 29   Longitudinal residual stresses on top and bottom longitudinal line
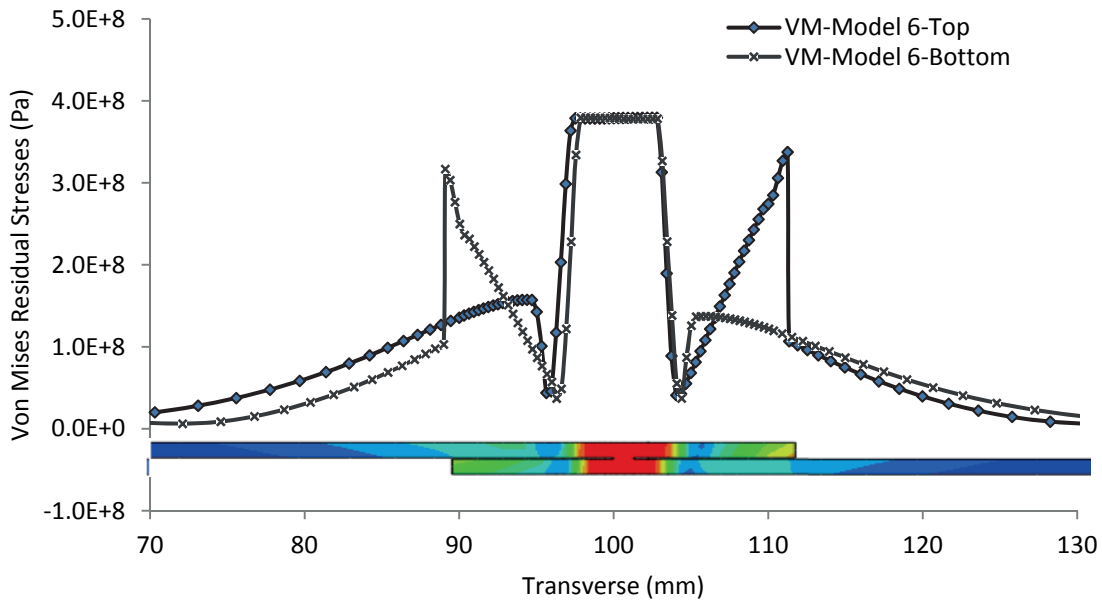
Fig.4. 30   Von Mises residual stresses along transverse line of top and bottom surface
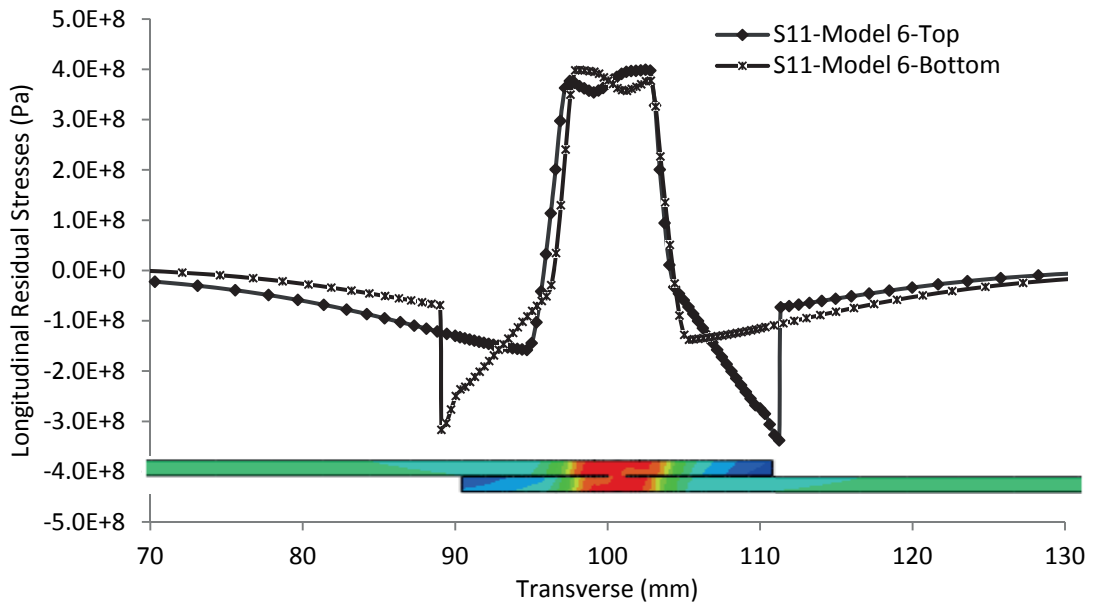
Fig.4. 31   longitudinal residual stresses along transverse line of top and bottom surface

Because of full penetration of welding are used in our simulation with small variation of heat source dimension from bottom to top surface, the longitudinal residual stresses on both surfaces along the longitudinal or transverse line give the same values as indicated in Fig.4.30 and Fig.4.31. So there is no variation of residual stresses between the top and the bottom surface of the full penetration welding mode on sheet metal.

4.5.3.   Effects of thermal properties

The objective was to observe the influence of thermo-physical properties on the residual stresses. Three mechanical analysis bases on different parameter of thermo-physical model represented as follow:

- *Material-1* is the results of simulation from using the thermo-physical dependent of temperature.
- *Material-2* is the results of simulation from using the thermo-physical dependent of temperature without peak point at phase transformation, Ac_1.
- *Material-3* is the results of simulation from using the thermo-physical independent of temperature.

Fig.4.32 and Fig.4.33 show the distribution of Von Mises *VM* and longitudinal residual stresses *S11* under influent of thermo-physical properties along the longitudinal line.

Fig.4.34 and Fig.4.35 present the curves of equivalent Von Mises residual stresses and longitudinal residual stresses along the transverse line.
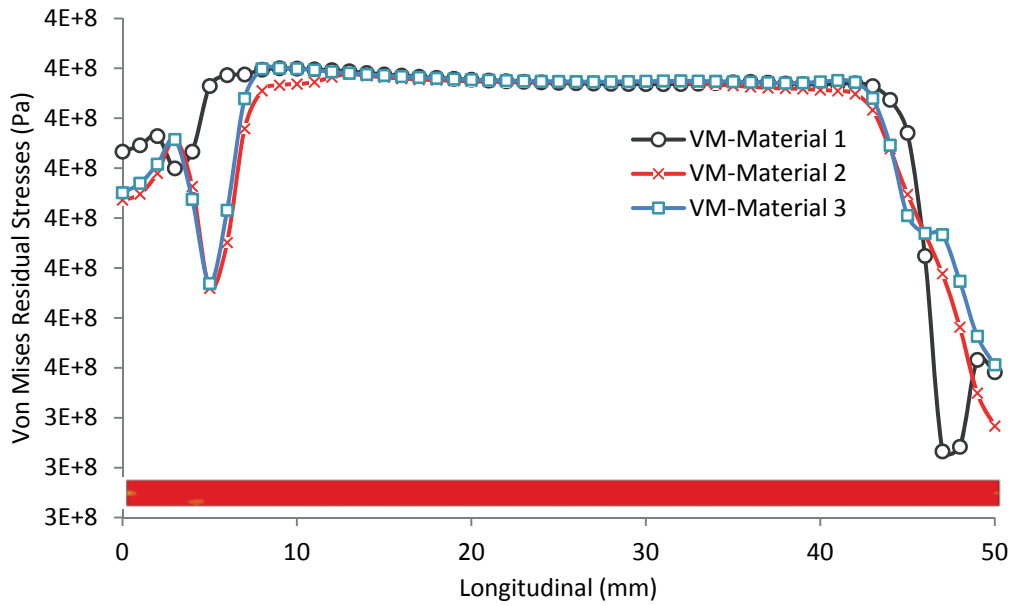
Fig.4. 32   Residual Von Mises stresses on the top longitudinal line

Fig.4. 33   Longitudinal residual stresses on the top longitudinal line

166

Fig.4. 34   Von Mises residual stresses on the top transverse line

Fig.4. 35   Longitudinal residual stresses on the top transverse line

The thermo-physical properties have some influences on the residual stresses especially outside the FZ and HAZ but there is no effect inside the HAZ and FZ as indicated

in Fig.4.34 and Fig.4.35. It also gives a different longitudinal residual stresses at the start and stop of simulation as indicated by the curve *S11-Material 1* in Fig.4.32.

The residual stresses are similar for all values of thermo-physical properties *(Material-1, Material-2, and Material-3)* inside HAZ and FZ. But a notable different of residual stresses outside these zones are appeared, the model with constant parameters give a higher Von Mises residual stresses compared to the two others models as shown in Fig.4.34.

4.5.4.   Effects of different maximum temperature

The variation of Von Mises residual stresses and longitudinal residual stresses along the transverse line are figured in Fig.4.36 and Fig.4.37.

The different maximum temperatures have no influence on the residual stresses inside and outside FZ and HAZ. The results of simulation show clearly that the different temperatures in fusion have no effect on the result of residual stresses in case where the dimension of welding pool is not change as indicated in Fig.4.36 to Fig.4.37. Because of the formation of residual stresses in cooling process is below the cut-off temperature [7].

Fig.4. 36   Von Mises residual stresses on the top transverse line
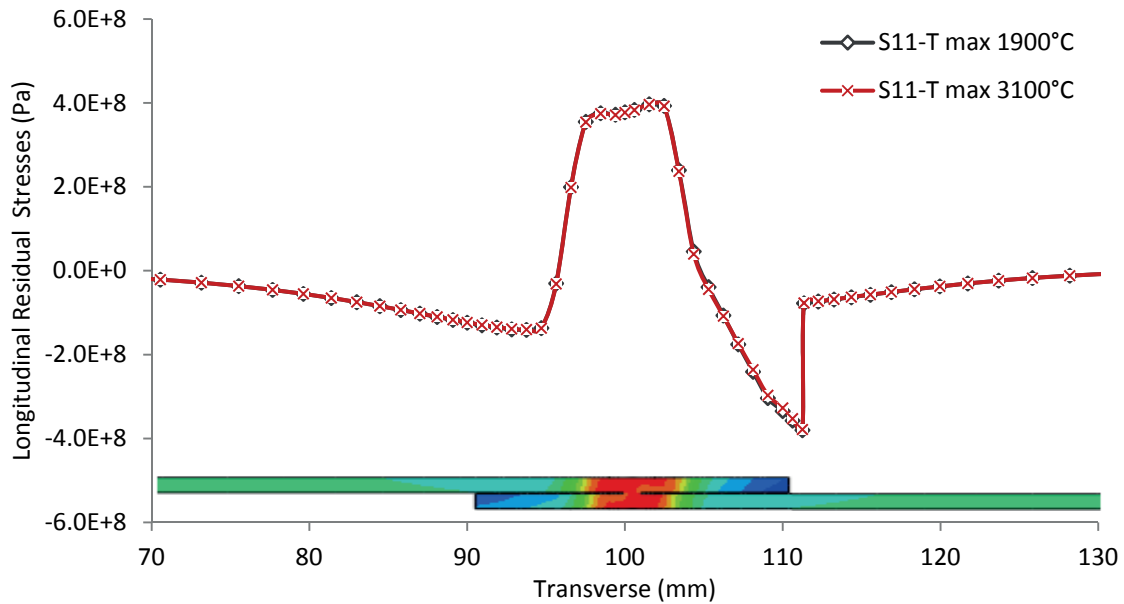
Fig.4. 37   Longitudinal residual stresses on the top transverse line

4.5.5.   Effects of convection

In this part, the residual stresses on the longitudinal line on the top surface of weld seam and the residual stresses along the transverse line are considered to study the influence of three modes of convection.

- The residual stresses under low convection, represented by the curve *Low Convection*.

- And under medium convection represented by the curve *Medium Convection*.

- Finally under forced convection represented by the curve number *fort convection*.

The results are presented in the Fig.4.38 to Fig.4.41. Where the variation of Von Mises residual stresses and Longitudinal residual stresses along the longitudinal and transverse on top surface are used to observe this effects.
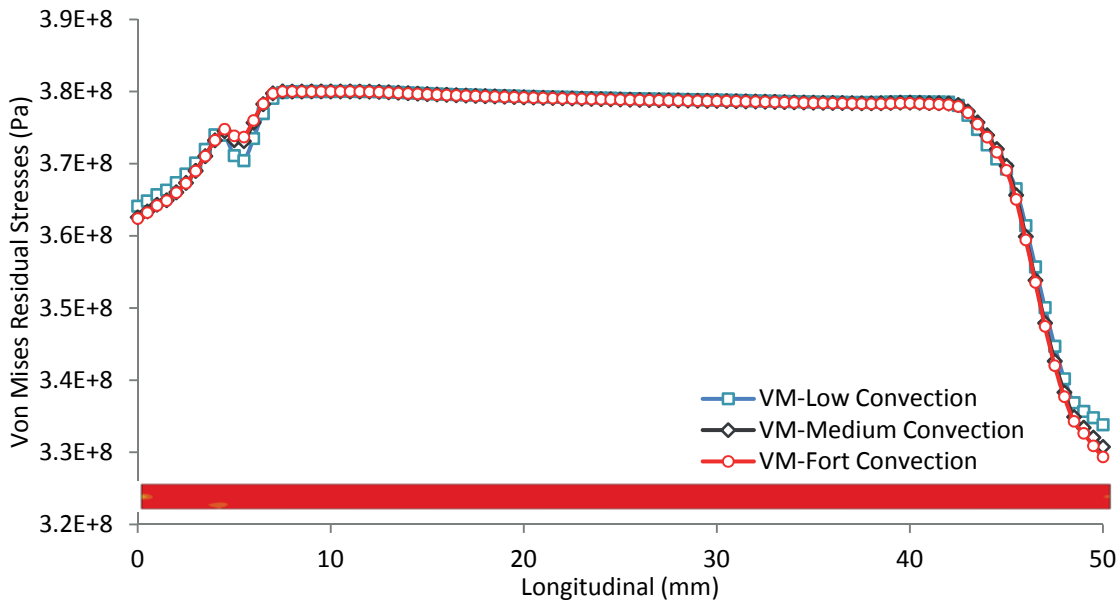
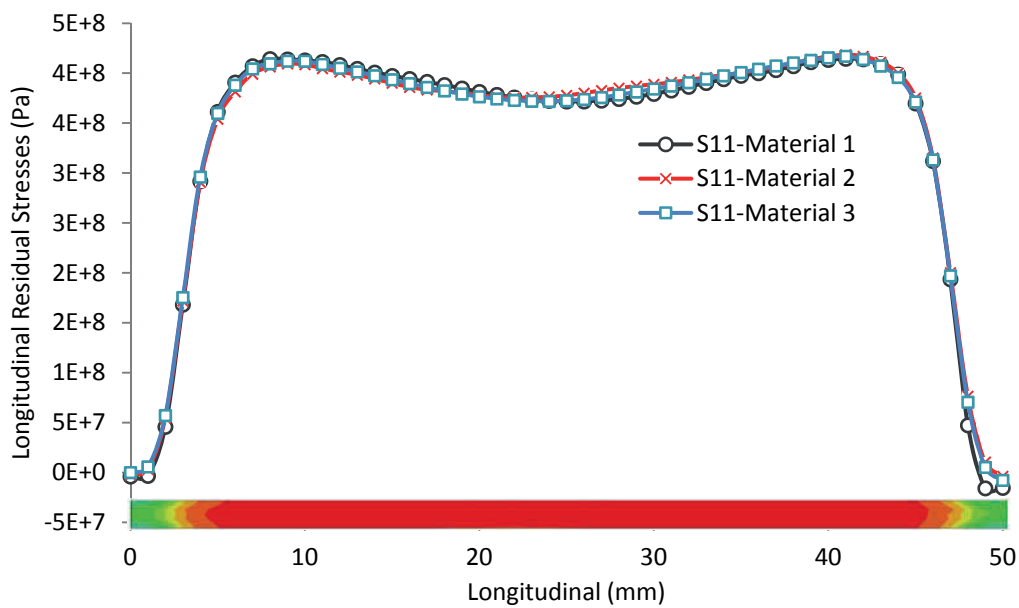Fig.4. 38   Von Mises residual stresses along longitudinal top line
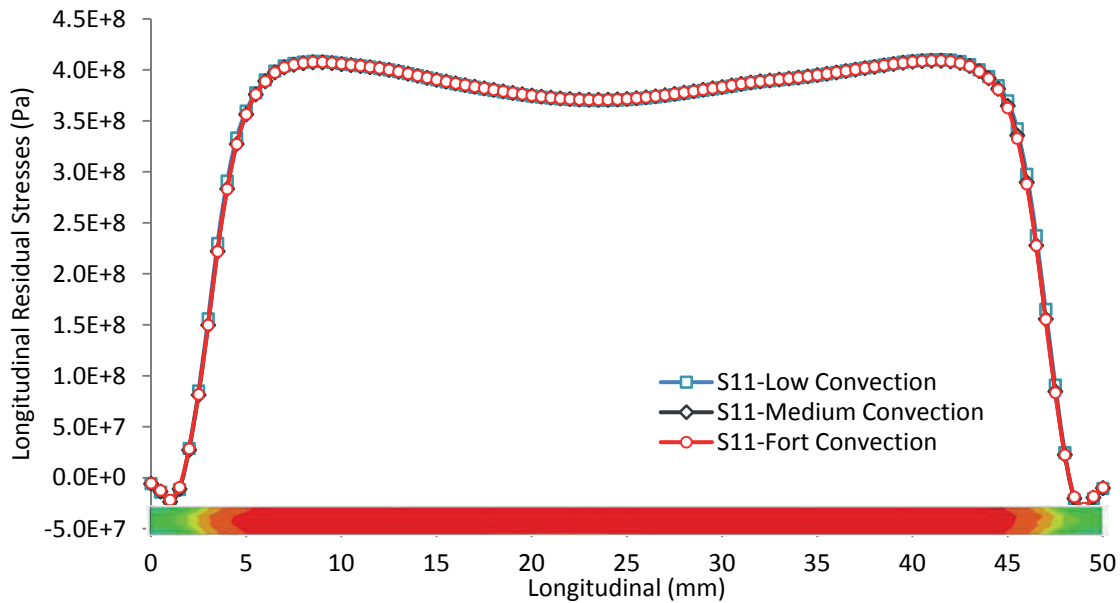
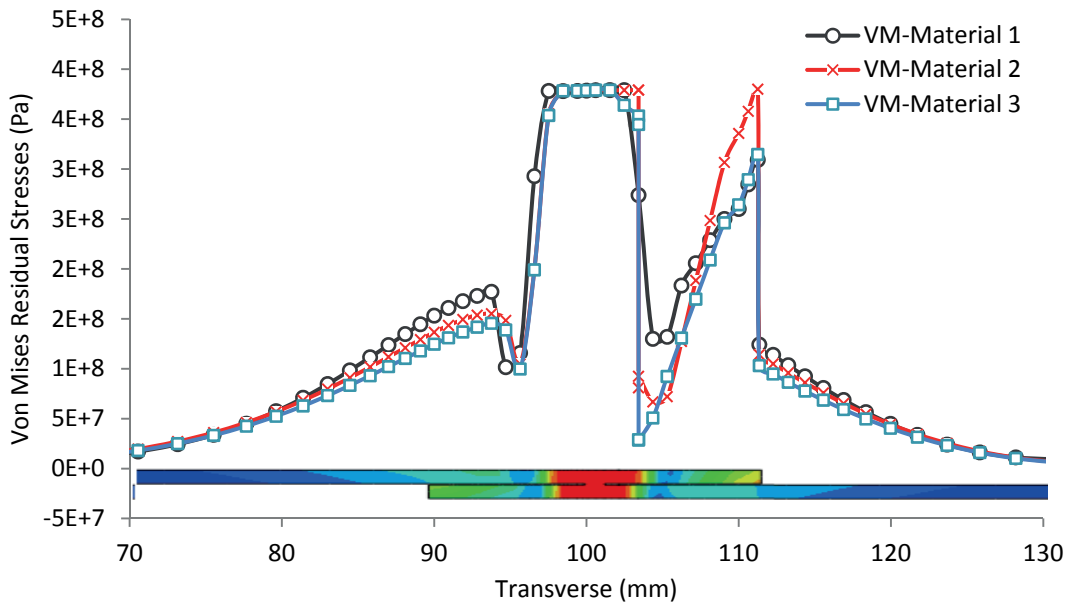Fig.4. 39   Longitudinal residual stresses along longitudinal top line
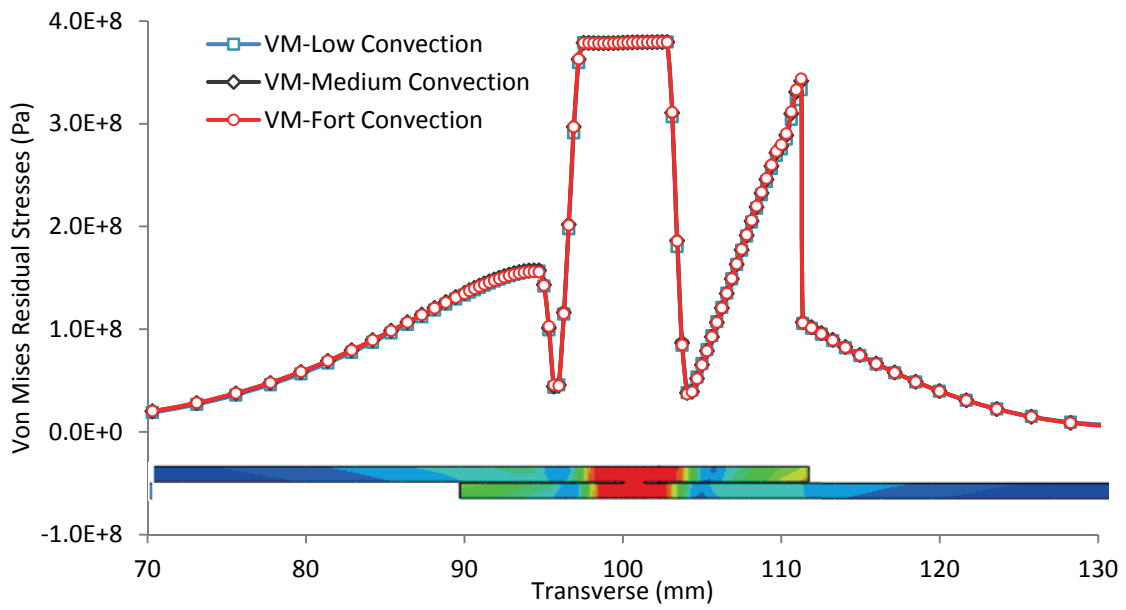
Fig.4. 40   Von Mises residual stresses on the transverse top line

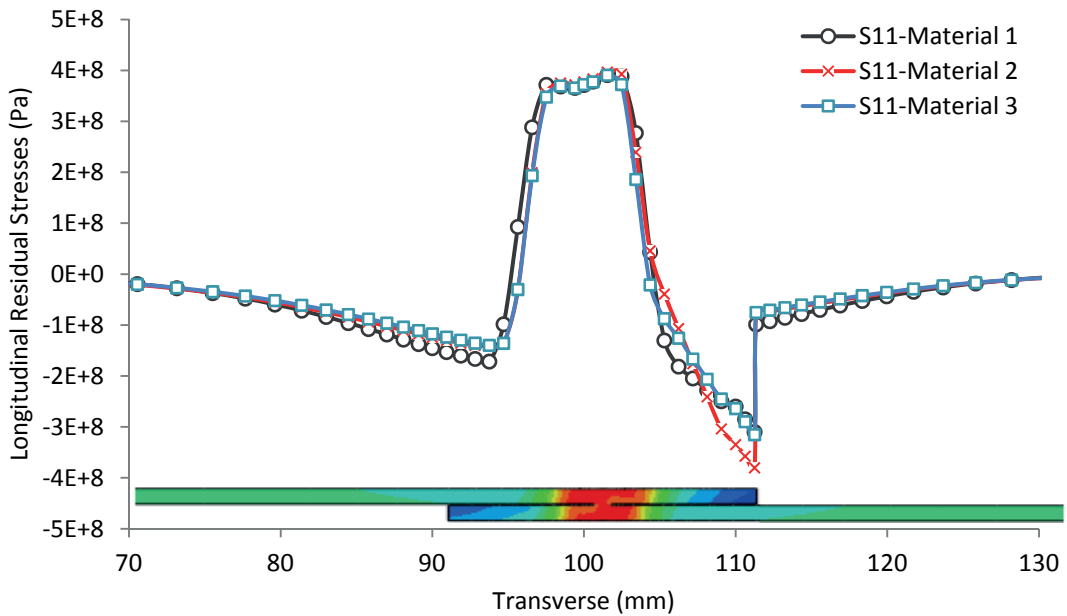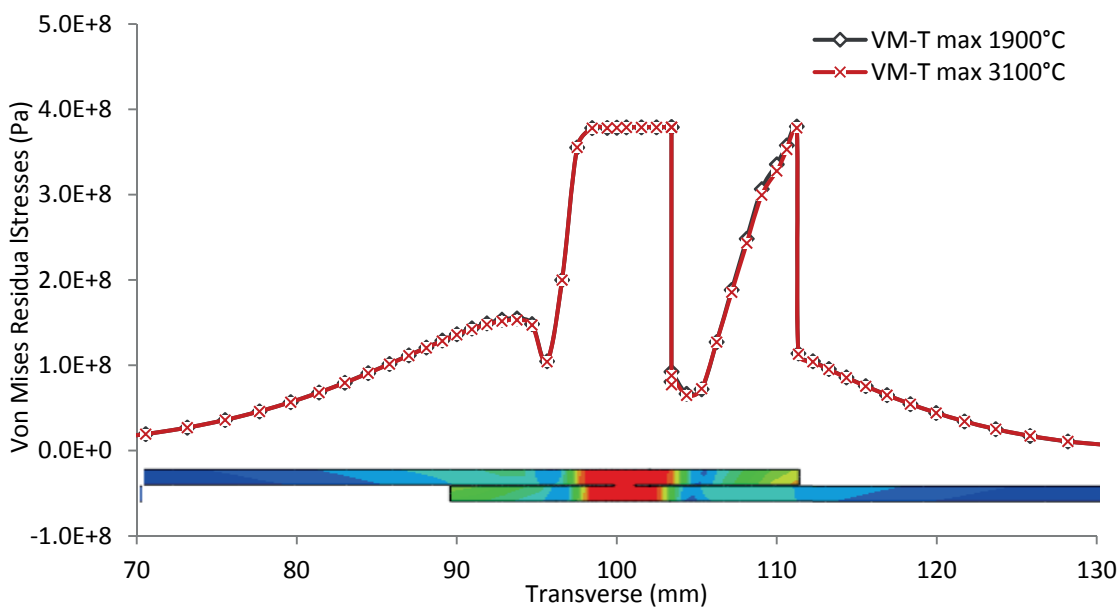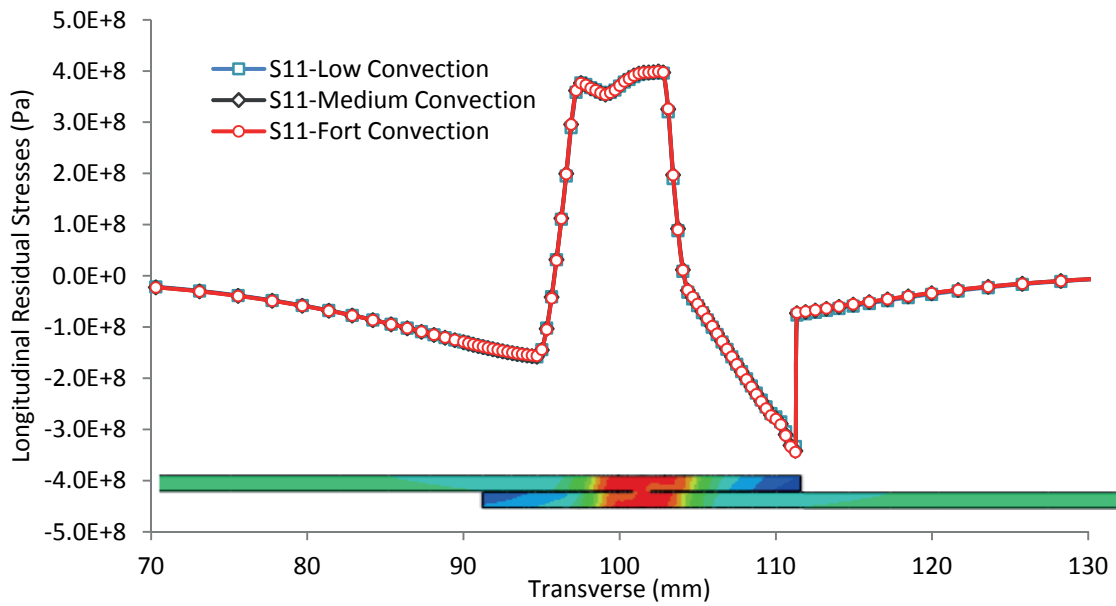Fig.4. 41   Longitudinal residual stresses along the transverse top line

The analysis on residual stresses, interpreted from Fig.4.38 to Fig.4.41, show no variation in residual stresses along the transverse line, Fig.4.40 and Fig.4.41, and neither

along the longitudinal line, Fig.4.38 and Fig.4.39, causing by the different intensity of convection mode.

The reasons maybe come from the welding speed of laser Nd: YAG is very fast, the diameter of laser in sheet welding process is very small. These two reasons allow the FZ and HAZ getting cool at the same cooling rate.

Similarly, these observations have been realized in others process such as grinding. Indeed, the convection heat coefficient, with high or low convection, does not have any considerable effect on the surface residual stresses in the grinding process [8]. But the cooling rate from water cooling, 1000W/m²°C, has a significant effect on both magnitudes and overall spatial distribution patterns of weld-induced residual stresses. It can considerably reduce the residual stress magnitudes from tensile to compression and would undesirable increase stresses at another location [11].

4.6. CONCLUSION

In case of thermal analysis we conclude as follow:

- The ratio of R/DX along the welding step must be greater than two in order to get minimum accurate precision of thermal simulation. The others dimensions of mesh elements such as DY and DZ have less influence in the results.

- The effects of material properties on the thermal results have been classified by percent of errors with the material dependent temperature properties from 1.5% to 5% in the model that overlooked the peak specific heat at phase transformation to the material independent of temperature.

In case of mechanical analysis we also conclude as follow:

- The thermo-physical properties have small affect on the residual stresses outside the FZ and HAZ of laser welding but have no influences on the residual stresses inside the FZ and HAZ.

- The different convection mode and the different maximum temperature inside FZ during laser welding simulation give the same value of the residual stresses inside

and outside the FZ and HAZ. So no influence of convection mode and different maximum temperature on the laser simulation.

- Full penetration mode of laser weld applied for thin metal give a constant value of residual stresses through the thickness. We observe no sign of difference has been indentified from top to bottom surface.

The mesh size, DX along the welding direction of meshing edge, equal to the radius of laser heat source is the minimum requirement for the precision of laser welding. It is clear that the ratio R/DX in thermal analysis is less affect on the results of mechanical analysis.

REFERENCE

[1] H. Alberg and D. Berglund. Comparison of plastic, viscoplastic, and creep models when modelling welding and stress relief heat treatment. *Computer Methods in Applied Mechanics and Engineering*, 192(49-50):5189–5208, December 2003.

[2] Jean-Michel BERGHEAU. Modelisation numerique de soudage. *Technique de l'ingénieur*, 2004.

[3] Dean Deng. Fem prediction of welding residual stress and distortion in carbon steel considering phase transformation effects. *Materials & Design*, 30(2):359 – 366, 2009.

[4] Paolo Ferro, Andrea Zambon, and Franco Bonollo. Investigation of electron-beam welding in wrought inconel 706–experimental and numerical analysis. *Materials Science and Engineering: A*, 392(1-2):94 – 105, 2005.

[5] D. Gery, H. Long, and P. Maropoulos. Effects of welding speed, energy input and heat source distribution on temperature variations in butt joint welding. *Journal of Materials Processing Technology*, 167(2-3):393 – 401, 2005.

[6] John A. Goldak. *Computational Welding Mechanics*. Springer, 2005.

[7] Dieter Radaj. *Welding residual stresses and distorsion : calculation and measurement*, volume 2. DVS, 2003.

[8] G. H. Farrahi S. H. H-Gangaraj and H. Ghadbeigi. On the temperature and residual stress field during grinding. In *Proceeding of the Congress on Engineering*, volume 2, july 2010.

[9] T. Schenk, I.M. Richardson, M. Kraska, and S. Ohnimus. Modeling buckling distortion of dp600 overlap joints due to gas metal arc welding and the influence of the mesh density. *Computational Materials Science*, 46(4):977 – 986, 2009.

[10] Christopher Schwenk. *FE-Simulation des Schweißverzugs laserstrahlgeschweißter dünner Bleche :Sensitivitätsanalyse durch Variation der Werkstoffkennwerte*. PhD thesis, Bundesanstalt für Materialforschung und prüfung, 2007.

[11] Kadda Yahiaoui Wei Jian. Influence of cooling rate on predicted weld residual stress buildup in a thick-walled piping intersection. *Pressure Vessel Technology*, 132(021205), april 2010.

[12] L. Zhang, E. W. Reutzel, and P. Michaleris. Finite element modeling discretization requirements for the laser forming process. *International Journal of Mechanical Sciences*, 46(4):623 – 637, 2004.

[13] X. K. Zhu and Y. J. Chao. Effects of temperature-dependent material properties on welding simulation. *Computers & Structures*, 80(11):967 – 976, 2002.

Résumé

Chapitre 5: Simulation Thermo-Métallurgique du soudage laser Nd:YAG

L'objectif principal de ce chapitre est de prendre en compte l'effet métallurgique associé au soudage lors du chauffage et du refroidissement et en particulier la nature des phases en présence et celles apparaissant lors de la transformation des phases. Deux modèles ont été utilisés, le modèle thermique et le modèle métallurgique. Ces deux modèles ont été codés à l'aide des sous-fonctions DFLUX et UMAT d'Abaqus respectivement. Pour prendre en compte les effets métallurgiques, l'étude numérique s'est appuyée sur l'intégration des modèles de Waeckel et de Koistinen-Marburger. Le modèle de Waeckel nous permis de simuler et de prendre en compte le phénomène d'austénitisation pendant le chauffage. Le modèle de Koistinen-Marburger permet de tenir compte du phénomène de transformation de la martensite généré pendant le refroidissement dans le procédé de soudage laser. Nous avons également implémenté un modèle nous permettant d'obtenir les valeurs de micro-dureté à partir de la loi de combinaison linéaire de la dureté de chaque phase. Les propriétés mécaniques comme la limite d'élasticité et la résistance maximale à la traction ont été également obtenues par l'introduction d'un modèle mécanique basée sur un modèle permettant de convertir la valeur de la dureté en propriétés mécaniques.

D'un point de vue résultat, la simulation a révélé que la principale phase présente dans la zone de fusion à l'issue du soudage laser est la martensite. La fraction volumique de celle-ci est très élevée dans la zone de fusion comparée à celles des phases ferrites et austénites. Nous avons pu également dans ce chapitre évaluer les propriétés de la dureté en Vickers et la résistance à la traction dans les différentes zones de soudure. Ces résultats seront comparés avec ceux de l'expérience pour conforter l'analyse numérique

Abstract

Chapter 5: Thermo-metallurgical simulation of laser welding Nd:YAG

The main objective of this chapter is to consider the metallurgical effect on the mechanical model during heating and cooling process, and in particular the nature of the initial metallurgical phases and those occurring during phase transformation.

Two models were used, the thermal model and metallurgical model. These two models have been encoded using sub-functions DFLUX and UMAT of Abaqus respectively. To take into account the metallurgical effects, the numerical study was based on the integration of models Waeckel and Koistinen-Marburger. Waeckel model allowed us to simulate and to take into account the phenomenon of austenitization during heating. Model Koistinen-Marburger takes into account the phenomenon of transformation of martensite generated during cooling in the process of laser welding. We also implemented a model that allows us to obtain the values of micro-hardness from the law of linear combination of the hardness of each phase. Mechanical properties such as yield strength and maximum tensile strength was also obtained by the introduction of a mechanical model allow converting the value of hardness to the mechanical properties.

From a point of view results, the simulation revealed that the main phase present in the melting zone after the laser welding is martensite. The volume fraction thereof is very high in the melting zone as compared to those of ferrite and austenite phases. We also, in this chapter, evaluate the properties of the Vickers hardness and tensile strength in different areas of welding. These results will be compared with the experience to reinforce the numerical analysis.

Contents

Figures

Tables

Chapter **5**

Thermo-Metallurgical simulation of laser welding Nd: YAG

5.1. INTRODUCTION

High speed laser Nd:YAG welding has more advantage in the industrial application of welding especially the assembly of sheet metal series. But the fast welding speed have different influences on the cooling cycle in the Heat Affected Zone (HAZ) and in the Fusion Zone (FZ) compared to others welding process, MIG/MAG, TIG that operate at low welding speed. The metallurgical and mechanical behavior of the welded structure depends on the welding condition, welding type and also the chemical composition of base material (BM). Different processes give different effects on the welding structure. Seeing these constraints, the numerical simulation of welding is used to predict their behavior such as the temperature evolution, the metallurgical phase transformation, the hardness and the resistance. Four models are use in this simulation, the heat source model developed in the subroutine DFLUX for thermal analysis and the model of phase transformation, model of the mean hardness and also the model tensile strength are coding in UMAT subroutine.

The welding simulation of laser Nd:YAG, in which the laser seam is quite small and high speed welding, is sensitive to the numerical parameter. So the refined mesh at the seam

and rather coarse meshes far away at the specimen edge are used by many simulation works [19, 5, 8]. The mesh density has been studied in the work of Schenk [19], which shown that the mesh density plays a very important role in determination of the accuracy of the distortion amplitude. The quadratic interpolation function gives more accurate results close to the weld seam.

The fast cooling phase in the laser welding slows down some phase transformations such as the transformation from austenite to ferrite, pearlite and bainite, and they observe the predominant of volume fraction of martensite in FZ [7, 10].

The micro-indentation hardness measured profile of diode laser welded DP600 steel with laser speed of 1m/min show a significantly higher hardness values approximately 1.5 times higher than those in the base metal (BM). The SEM examination of this region indicated that the phase apparent in the FZ included predominately martensite in conjunction with some sideplates ferrite and bainite [7]. But the metallurgical structure of welded joint by Nd:YAG laser is different from the same assembly by diode laser and it will study in this part.

5.2. THERMO-METALLURGICAL MODEL

This section describes the different models of simulation introduced in this work. It consists of a thermal model and a metallurgy model and finally the model of hardness and mechanical properties.

5.2.1. Thermal model

The thermal models contain of the heat transfer equation and the conical heat source model was described in chapter 2. It is not re-described in this section.

182

5.2.2. Metallurgical model

The chosen model, the Model Waeckel [25, 24, 6], allows describing the anisothermes metallurgical transformation provided by a differential equation. This model was described in section 2.3.3 and section 2.3.7.

The volume fraction functions of the model Waeckel are resolved by the Euler explicit methods as the expression below:

$$Z_{n+1} = Z_n + \dot{Z}_n.\Delta t \tag{5.1}$$

$$\Delta t = t_{n+1} - t_n \tag{5.2}$$

Where Z_{n+1} is the new volume fraction at time increment n+1, Z_n is the volume fraction at the time increment n and Δt is the time increment.

During rapid cooling, the austenite with a face centered cubic structure changes to martensite with a body centered tetragonal structure. This phase transformation is described by the Koistinen and Marburger model [13]. It was described in section 2.3.7.

5.2.3. Hardness Model

The hardness value of steel can be calculate from on the chemical composition such as the model proposed by Kirkaldy and their derivative or by the linear mixed rule of hardness value got from measurement data.

The models of hardness based on the chemical composition and the cooling rates of low alloy steel [15, 18, 12] which are improved from the original work of Kirkaldy are not fit to the data from experiment of DP600 steel. The values of hardness from the results of those models are about 10% lower than the measurement value. The hardness is very sensitive to the volume fraction of martensite [9]. The metallurgical structure of dual phase steel composed of ferrite and martensite in volume fraction that ease use in another approach that is based on the measurement data of each phase independently in the thesis of Prodromos [22]. This approach gives a hardness value close to the measurement value.

A linear rule of mixture:

$$HV_{DP} = HV_F + V_M (HV_M - HV_F) \tag{5.3}$$

Where HV_{DP}, HV_F and HV_M stand for the microhardness of dual phase steel, of ferrite and of martensite, respectively, while V_F and V_M express the volume fraction of ferrite and martensite. The values of HV_F and HV_M were experimentally determined. The minimum hardness value of martensite 395HVN at 100% of volume fraction and 160HVN of pure ferrite volume fraction are used that is confirmed to be fit with experimental results [22].

5.2.4. Tensile Model

The knowledge of tensile properties is more significant in most cases for the welding engineer, the relationships between the hardness and tensile properties can be established by [18] :

$$UTS (MPa) = 19.13.10^{-4}.HV^2 + 1.89HV + 181.5 \tag{5.4}$$

$$YS02(MPa) = -266.8 + UTS + 30.41 \log(VR) + 51.01 \tag{5.5}$$

Where

UTS and YS02 are the ultimate tensile strength and yield strength at 0.2%.

VR is the cooling speed in degree Celsius per hour defined in equation 5.6.

These relationships have been correlated with measurement of various welding processes include the electron beam welds with a good accuracy.

5.3. SIMULATION OF LASER WELDING

5.3.1. Simulation parameters

The meshing dimension along the welding direction DX is fixed to 0.3125mm. In transverse direction DY is 0.2mm in FZ and 0.175mm in HAZ and progressive cores mesh in the BM. The mesh dimension in the depth DZ is 0.3125mm. The quadratic mode is used for thermal analysis and linear mode for metallurgical analysis of thermo-metallurgical

simulation of dual phase steel DP600, 1.25mm x 50mm x 110mm, within transparent mode include 0.1mm gap as presented in Fig.5.1 and Fig.5.2. The value of mesh dimension are summarize to Tab.5.1

The thermo metallurgical simulation is done in two steps. Each step corresponds to a specific time of welding and cooling as presents below:

- The welding step : 0.8818s
- The cooling step: 120s

The boundary conditions included the convection and radiations with the surrounding environment are applied in the cooling step was presented in Fig.4.1.
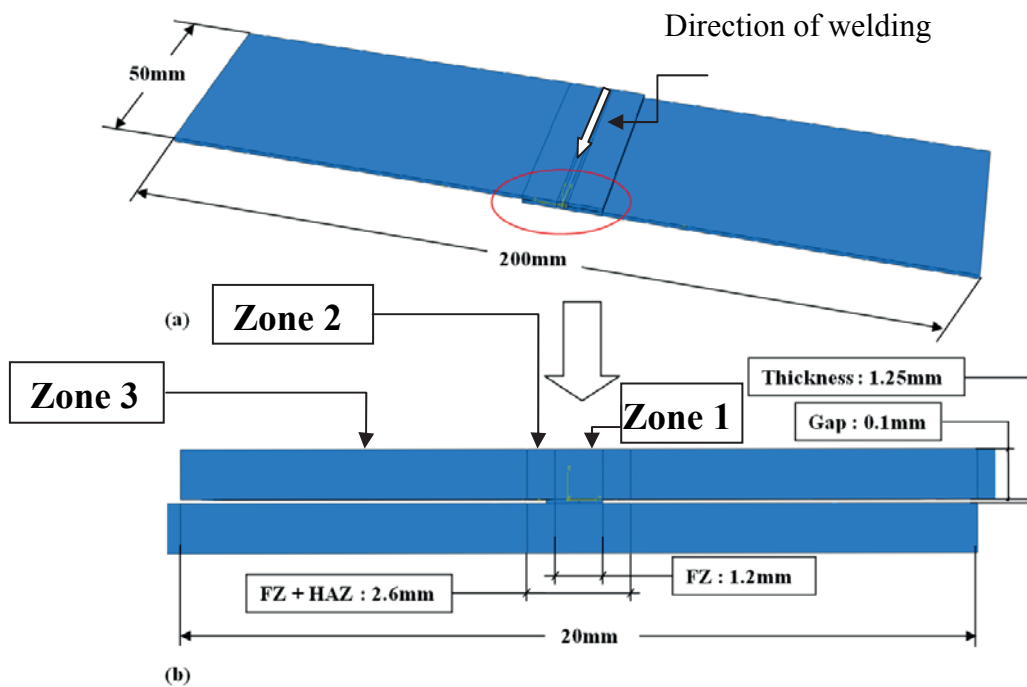
Fig.5. 1   Model of sheet joint
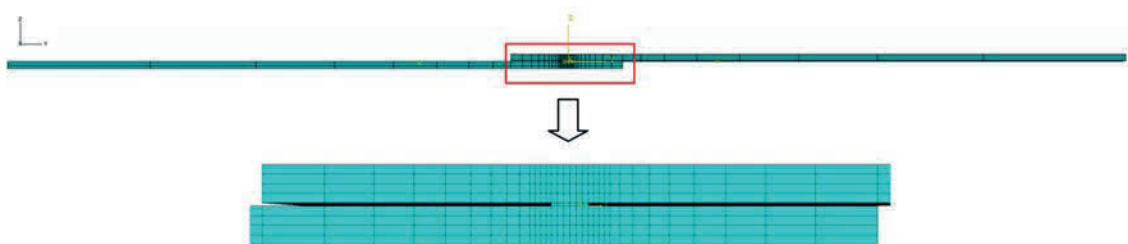
Fig.5. 2   Mesh of the sheet metal model

Model	Zone1			Zone 2	Zone 3[a]
	DX	DY	DZ	DY	BIASE
	0.25	0.2	0.3125	0.175	10:17

[a]10:17 means 17 elements with biases factor of 10 from the small and the bigger one.

Tab.5. 1 Parameter of thermal mesh size (mm)

5.3.2. Thermal Data

The convection coefficient 73.5 W/m^2.K and emissivity of 0.25 [16] are used in thermal model with the control mode and natural convection with the convection coefficient of 20 W/m^2.K.

The value of the conical heat source model are presented in Tab.5.2

Symbol	Quantity	Value
r_e	radius superior of cone	0.8 m^{-6}
r_i	radius inferior of cone	0.35 m^{-6}
r_c	distribution parameter	m^{-6}
z_e	position in Z axis of r_e	2.6 m^{-6}
z_i	position in Z axis of r_i	0 m^{-6}
P	laser power	3500 W
η	Efficiency	42%
V	welding speed	0.0567m/s

Tab.5. 2 Parameter of Heat Source Model

5.3.3. Metallurgical Data

The dual phase DP600 steel microstructure consists of a matrix of soft α-ferrite grains, strengthened by a finely dispersed, hard Martensite-Austenite constituent, the presence of small amounts of others constituents, such as bainite and a lesser degree of pearlite. Those compositions can be tolerated because it does not significantly alter the specific dual phase properties as long as a sufficient amount of low temperature martensite has been formed [23]. The volume fraction of martensite is approximately 20% for DP600 steel [2, 19].

- The parameter for austenitization (Waeckel model).

The growth parameter τ from ferrite, pearlite, bainite or martensite to austenite has been set to 0.05s in order to obtain a good agreement to the results of the phase field predictions for welding of DP600. This value was use in [21, 19]. With the constant value of the function τ (T), the volume fractions of all phases inside the FZ are reached but volume fraction of bainite obtained is higher compared to experimental results. Otherwise in the HAZ of a gas metal arc welding simulation, the predicted martensite volume fraction is underestimated. This is the reason that the austenite growth is overestimated by the present transformation model. Hence, the CCT diagram might be employed to model the transformation, but one has to be careful with the austenitization on heating of the material. [19].

Several investigations have showed that for very fast heating rates and low carbon contents, which occur in almost every weld, the end of austenitization (γ) transformation does not depend on chemical composition, the Ac_3 was close to 910˚C for all grades of steel [18]. For higher rate of heating corresponding to laser welding, the volume fraction of austenite is reached at the fusion temperature but not at Ac_3[10], and Ac_1 is 720°C with temperature of fusion $T_{liquidus}$ equal to 1530°C [26] and with the temperature of solidus $T_{Solidus}$ equal to 1440°C [20].

- The parameter of martensite transformation (Koistinen Marburger model)

The CCT diagram of DP600 austenitization at 800°C during 86s is used as reference for cooling model of the welding simulation show in Fig.5.4.
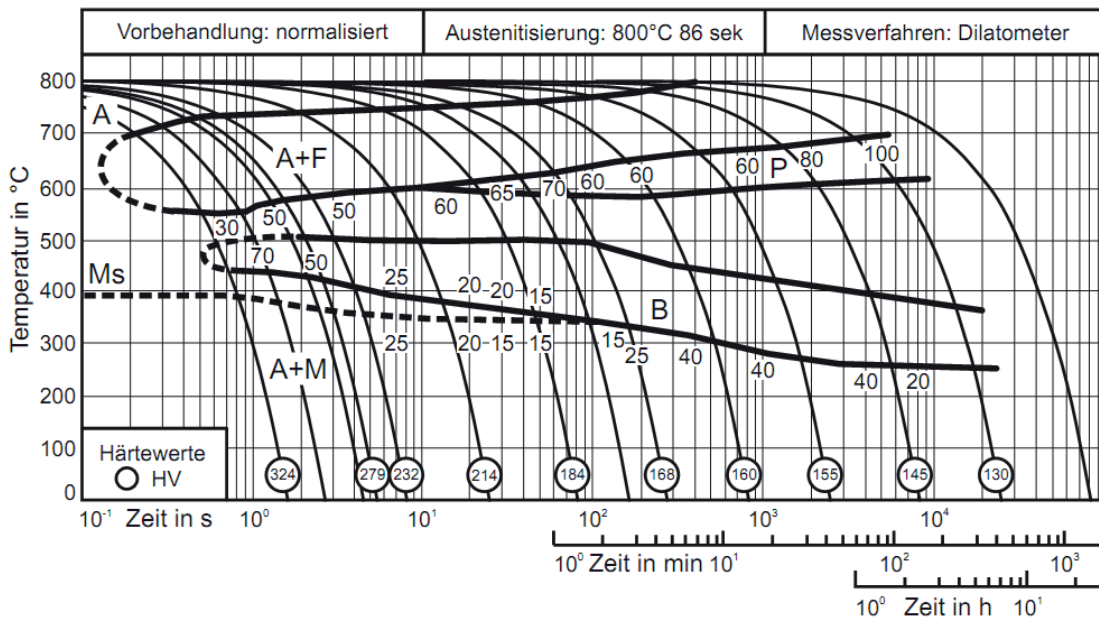
Fig.5. 3   Continuous Cooling Transformation Diagram of DP600-W austenitized at 800°C for 86s [20]

Based on the cooling curve, Fig.5.3, situated between the hardness 324HV and 279HV of DP600, consists of 70% of martensite and 30% of austenite, with cooling time from 800˚C to 500˚C, $t_{8/5}$, of 1s. The hardness 400HVN inside the HAZ and the FZ for laser welding Nd: YAG with welding speed 6m/min [26] and 310-350VHN for diode laser welding 1m/min [7]. It indicates that the hardness or the martensite volume fraction really function of the welding speed and heat density that corresponds to the time of material expose to heat source.

Mean time the $\tau_{8/5}$ equal to 0.7s measure from experiment of laser welding Nd:YAG, 3Kw and 4m/min of DP600W of 2mm thickness [20]. The same value had been found in the thermal analysis in section 5.5.2.1 in which the hardness are about 400HVN *(section 5.5.1.2).*

The cooling rate at 700˚C (˚C/h) or cooling rate from 800°C-500°C using in the calculation of hardness, can be obtain from 800°C-500°C expression:

$$VR = \left(\frac{800-500}{\tau_{8/5}}\right) 3600 \tag{5.6}$$

188

Phase transformation parameter of DP600 of gas metal arc welding process [19], the formation of bainite starts at cooling time $t_{8/5}$ around 1.5s and 5.3s for ferrite transformation.

The phase transformation of volume fraction of ferrite and pearlite is limited to the cooling rate less than 20°C/s and the martensite transformation start from the cooling rate more than 10°C/s, The bainite phase increases from cooling rate 0.1°C/s to 50°C/s and end of transformation when the cooling rate is more than 100°C/s. The formation of bainite is strongly affected by higher chemical composition in the DP600 steels [1].

The curves in Fig.5.5 translate the volume fraction of martensite during the cooling cycle from austenite to martensite by using the Koistinen-Marburger model. Three coefficients of material parameter β, 0.011, 0.018 and 0.2, are used to study their influence on the martensite transformation. Where the coefficient β equal to 0.011, used for carbon steel, reduces and retards the formation of martensite volume fraction. With increasing the value of β to 0.2 the transformation from austenite to martensite is completed around the martensite start temperature. This relationship is confirmed by the dilatometer test in the thesis of Schwenk [20] presented in the Fig.5.6 in which the controlled cooling time $t_{8/5}$ equal to 0.8s indicates a start and finish of martensite transformation around the martensite start temperature.

The curves in Fig.5.4 represent the thermal expansion of DP600-W with 4 cooling times. The measurement $t_{8/5}$ equal to 3.1s occurred without active cooling, while other measures with active cooling time [17]. The expansion curve during cooling phase deviate upward, around 900°C, when the cooling time is in active controlled mode (from 2s to 0.8s of cooling time).
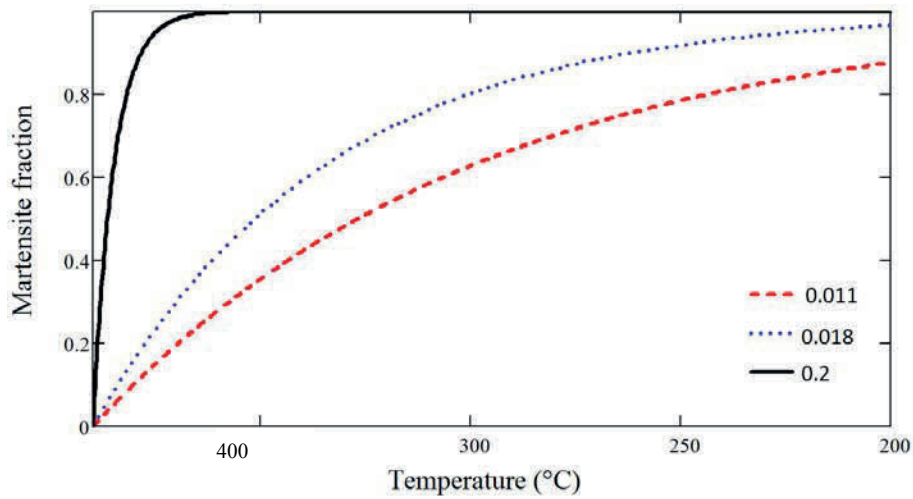
Fig.5. 4   Influence of martensite coefficient β
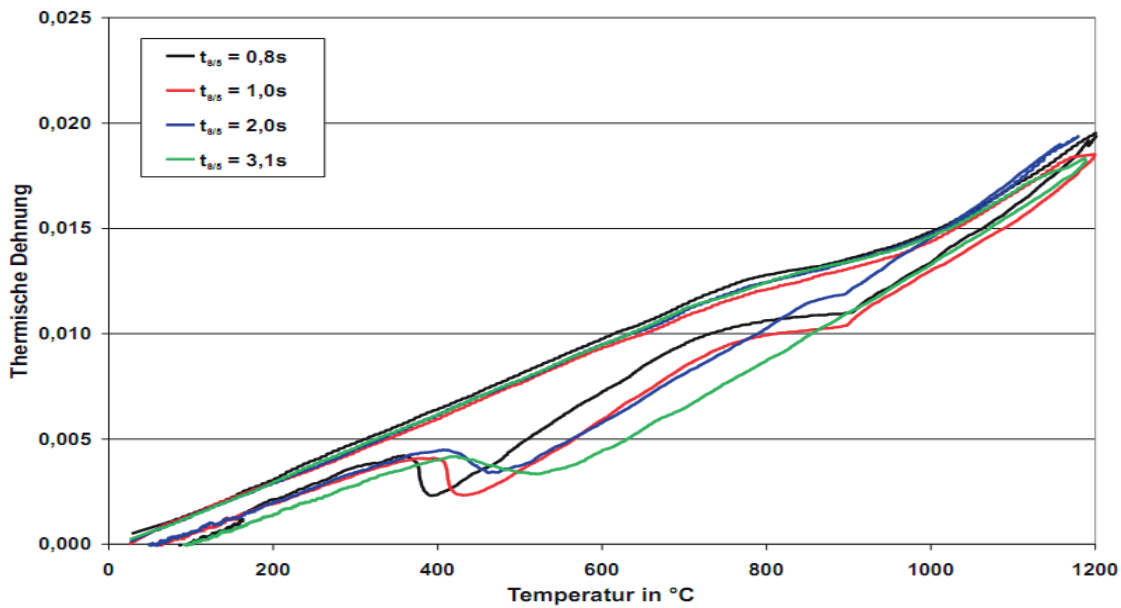
Fig.5. 5   Dilatometer curves determined experimentally for DP-600 W [20]

The approach of the cooling time $t_{8/5}$ between the results of thermal simulation and the curve of material parameter, Fig.5.4, and the curve of thermal expansion, Fig.5.5, show that the coefficient β of the Koistiten-Marburger model, applied for DP600-W, is 0.2 with the martensite start temperature Ms equal to 390°C [17] and these values are used in this simulation.

5.4. MICROSTRUCTURE AND HARDNESS ANALYSIS

The standard metallographic sample of weld cross section were prepared and examined for microstructural detail under Leica optical microscope after etching by solution Nittal 4% during 10 seconds then the samples were immediately washed with water follow by ethanol, and then were blown dry in hot air. The hardness measurement is done by Mitutoyo Instrument of Microhardness with a load of 0.3kg and a dwell time of 15 seconds were used during testing with an adequate spacing of 0.15mm from each point of measurement by Vickers indenter for preventing interfere with each other.

5.5. RESULTS

5.5.1. Experimental results

5.5.1.1. Microstructure

Optical metallographic was carried out to observe the variation of microstructure content in HAZ and FZ. From these micrographs it is evident that the formation of martensite is increased successively from the HAZ to the maximum volume fraction inside the FZ, as showed in Fig.5.6-A, B, C, D, E and F. The volume fraction of ferrite, grain with white color, are decreased to almost zero in the HAZ, Fig.5.6-B-C, that is dominated by the volume fraction of martensite. The welding speed has influenced on the cooling time, $t_{8/5}$, is an important factor of the martensite formation and others phases, ferrite, bainite. Based on the CCT diagram the formation of pearlite occurred at a very slow cooling time compared to the formation of bainite and ferrite so it is impossible to have the transformation from austenite to bainite and pearlite of the laser welding with higher speed of DP600 steel.

The martensite experience coarsening in the FZ, Fig.5.6-C-D, The coarsening martensite is observed high in the FZ compared to the HAZ because the degree of coarsening increase with an higher degree of austenitizing temperature during the cooling phase after passed by heat source. The cooling parameters, t8/5, are almost the same for FZ and HAZ as indicated in thermal simulation.
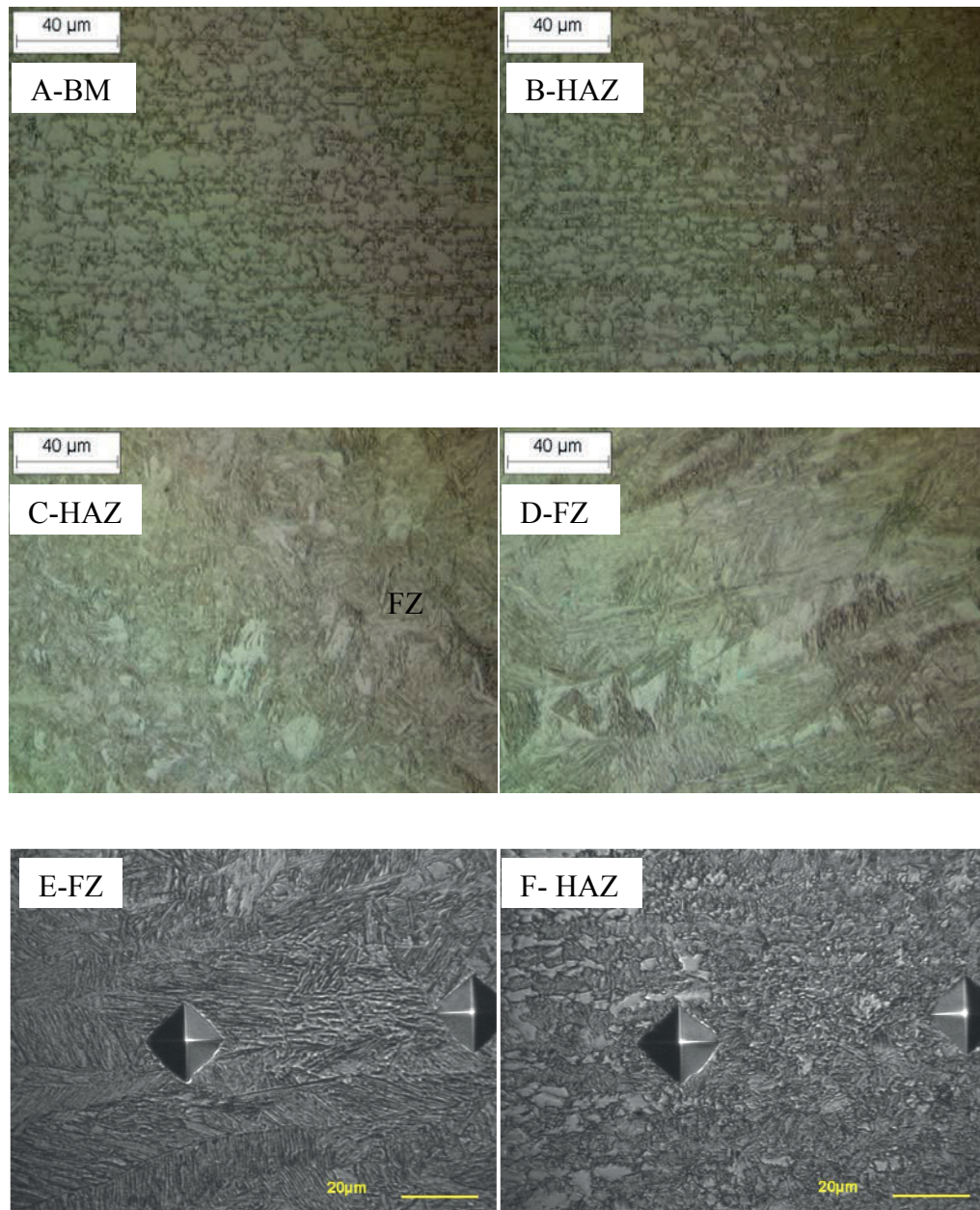
Fig.5. 6   Optical microstructure of welds in BM, HAZ and FZ: A: BM, B:HAZ, C:HAZ close to the ZF, D: FZ, E: Prisme microhardness in FZ and F : Prisme microhardness in HAZ.

5.5.1.2. Microhardness

Micro-hardness survey was carried out by Mitutoyo Microhardness tester using a Vickers indenter. Two lines of hardness measurement are done successively, the first line is

along the horizontal line at the middle of the first sheet and the second line is the vertical line situated at the middle of the FZ as shown in Fig.5.7-E and Fig.5.6-F.

The formation of martensite in the FZ and the HAZ resulted from the rapid cooling of weld pool during laser welding process. Beside the martensite volume fraction, the cooling speed plays an important role in the hardness value, the cooling time t8/5 of difference points of thermal simulation in the FZ and the HAZ is not quit difference, less than 0.1s, this is the reason that causes the same hardness value is ZF and HAZ, around 400HVN as indicated in Fig.5.7, and depends only the volume fraction of martensite. Based on the microscopic and the hardness, one resumes that the volume fraction of martensite inside de FZ is 100%. The same hardness value had been found in the mesurement along the vertical line across the FZ as indicated in Fig.5.8.

In the region, between the HAZ and BM, near the base metal, the hardness value drop sharply from the maximum value to a minimum value of base metal, 200HVN, in a small width approximate to 0.2-0.3mm but no presence of soft zone near this area that is in agreement with early studies [26]. The higher laser welding speed reduces the size of HAZ and no sign of soft zone at BM close to HAZ that is depends on the martensite contents [4].

Tempering of martensite is dependent on time and temperature of thermal exposure. The diode laser full penetration welding, 1m/min, lead to the formation of soft zone in the sub-critical area of HAZ [7]. Nonisothermal tempering occurs generally during manufacturing processes such as welding and joining involving rapid heating, negligible holding time at tempering temperature, and rapid cooling. it is strongly affected by the heating rate. Temperature of start and end of tempering is 250°C to less than Ac_1. The sub-critical HAZ counted from the temperature Ac_1, in case of resistance spot welded DP980 steel, showing that the microstructure at $800\mu m$-$1000\mu m$ far from Ac_1 indicated no sign of decomposed appearance, compared the original BM microstructure [11].

Based on literatures [7, 11, 4, 26] and measurement results in section 3.3.3.5, we can conclude that there are no tempering effects on the laser Nd: YAG of DP600 because of higher welding speed and volume fraction of martensite of this steel.
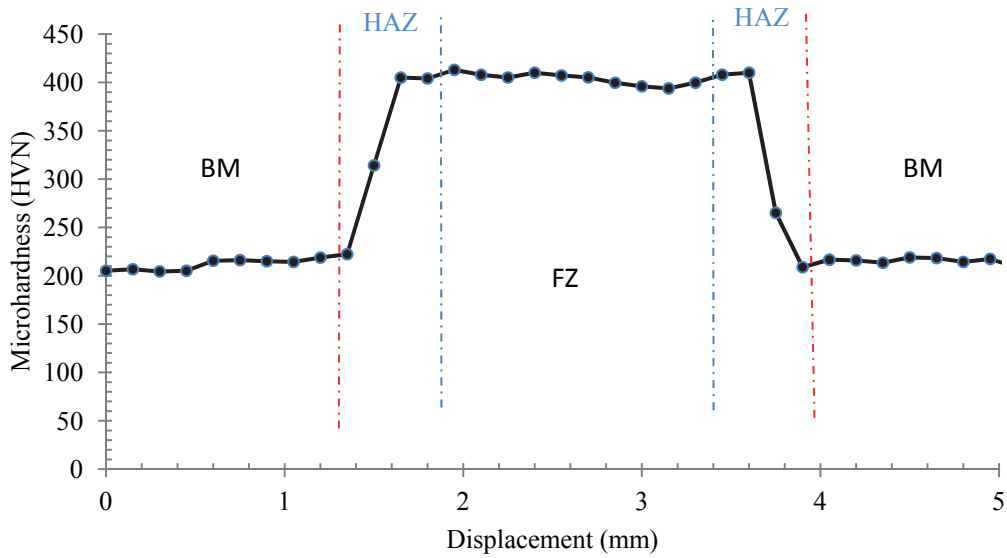
Fig.5. 7   Microhardness across the first sheet of weld sample
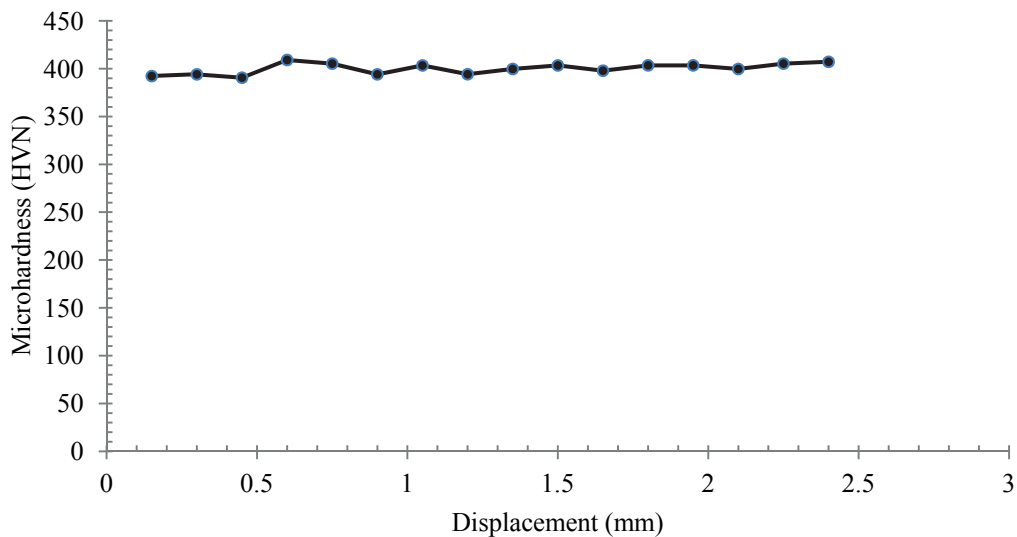
Fig.5. 8   Microhardness along the vertical line at the middle of FZ

5.5.2.   Simulations Results

5.5.2.1.   *Thermal*

The temperature evolution at different points in the FZ, HAZ is used to study the temperature distribution and also their cooling speed during the cooling cycle. Fig.5.9 shows the temperature histories at five points situated inside the top sheet. Its positions are presented in Tab.5.3.
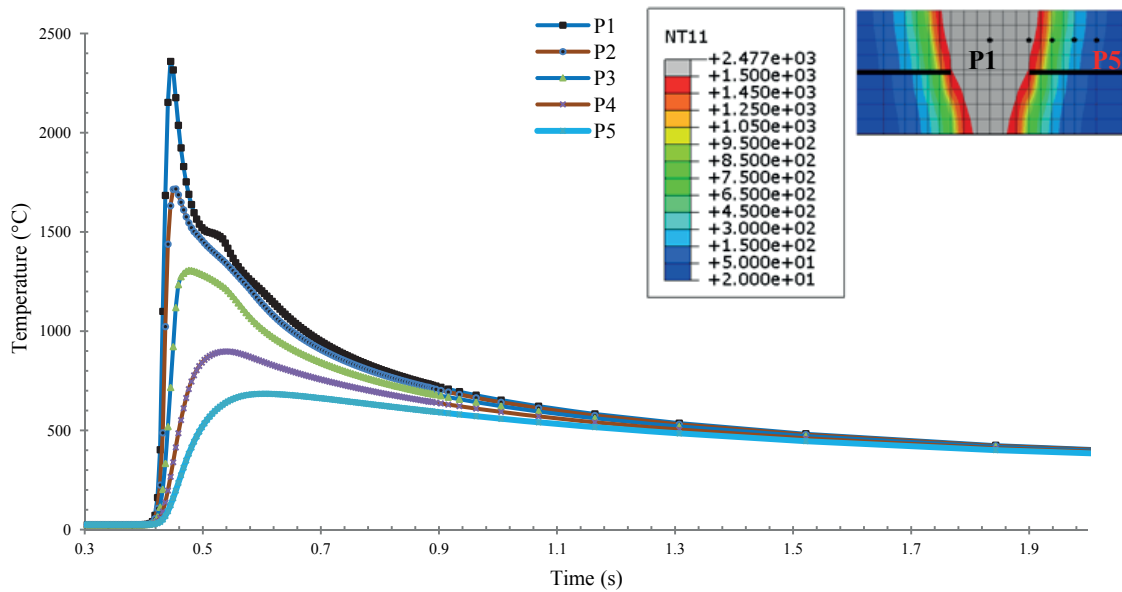
Fig.5. 9   Temperature evolution during welding and cooling cycle

The material properties used in thermal simulation have influence on the evolution of temperature during the welding process. Material dependent temperatures have been supposed to give this evolution fit to the real case getting from experimental measurement [3, 10, 27]. The study of thermal distributions is important in the transformation of metallurgical phase and mechanical structure of welding joint. The cooling curve from 800°C to 500°C is the important parameter in this evolution.

Points	P1	P2	P3	P4	P5
Distance (mm)	0	0.6	0.95	1.3	1.6219
Max T (°C)	2359	1716	1306	898	684
$t_{8/5}$ (s)	0.7	0.72	0.72	0.75	NO

Tab.5. 3 Cooling times from 800°C to 500°C and maximum temperatures at different positions located on the middle line of the top sheet, counted from centre of welded pool.

The high speed laser welding increases the cooling speed inside the FZ and HAZ. In others to study their influences we observe the cooling time, t8/5, between 800°C and 500°C from simulation results at 4 points, two points, P1 and P2 situated inside FZ and another 2 points P3 and P4 located inside HAZ show small difference between them as indicated in Tab.5.3 This small difference causes no difference in metallurgical transformation at those

points. These values are similar to the cooling time in previous work [20]. We can conclude that the simulation of laser welding gives a small difference of the cooling time t8/5 (s) in the ZF and also the HAZ.

5.5.2.2. Metallurgy

The macroscopic image of the weld cross section allows us to measure the dimension of FZ and the HAZ and calibrating with the value from simulation. The dimension of weld cross section is showed in Fig.5.10.
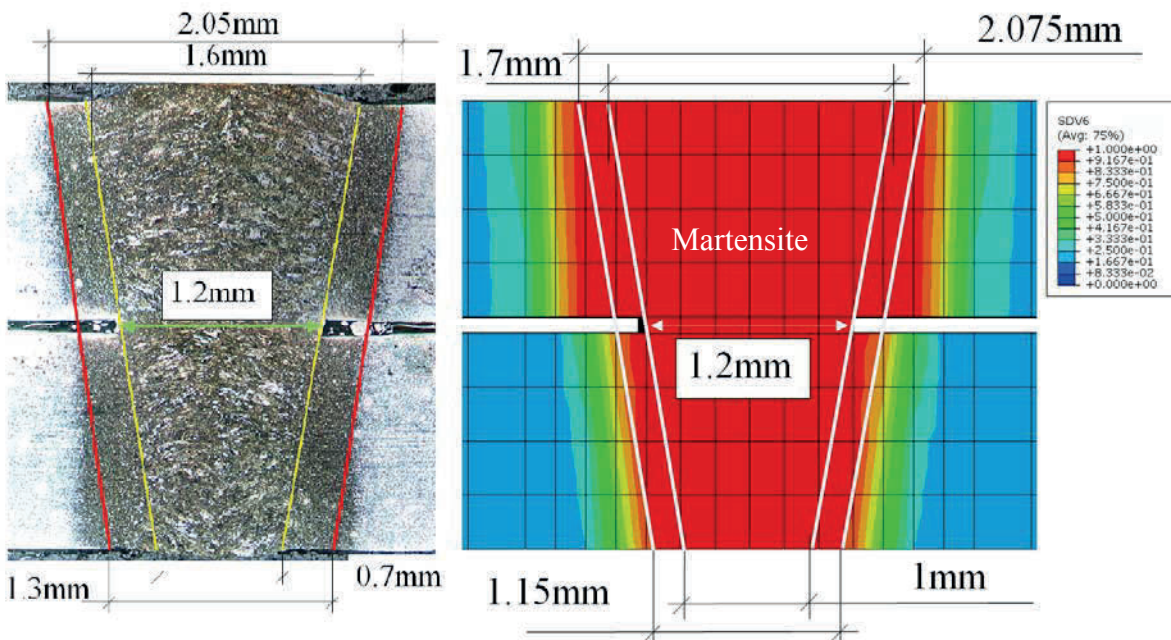
Fig.5. 10   Cross section of weld joint

The difference of cooling time, get from thermal simulation, in FZ and HAZ are less than 0.1s that leads to the same phase transformation in these two areas in the cooling cycle. Base on the cooling curve in the CCT diagram, the image from optical microscope and microhardness measurement, we can assume that the phase transformation inside the fusion zone is 99.9% martensite. The heat affected zones HAZ are included the complete martensite transformation and the incomplete phase transformation. The width of incomplete phase transformation zone is tiny, around 0.2-0.3mm, showed in Fig.5.6-F and Fig.5.7.

The start and stop austenitizing temperature are the main factor of metallurgical simulation. 830°C and 1150°C give a solution close to experimental. Another factor is the growth parameter, τ, that control the slope of the volume fraction from base metal to the complete martensite transformed phase as showing in the hardness curve Fig.5.11. When τ becomes small the slopes become vertical. Finally in orders to have a complete transformation, the growth parameter equal to 0.05s is used in this work.
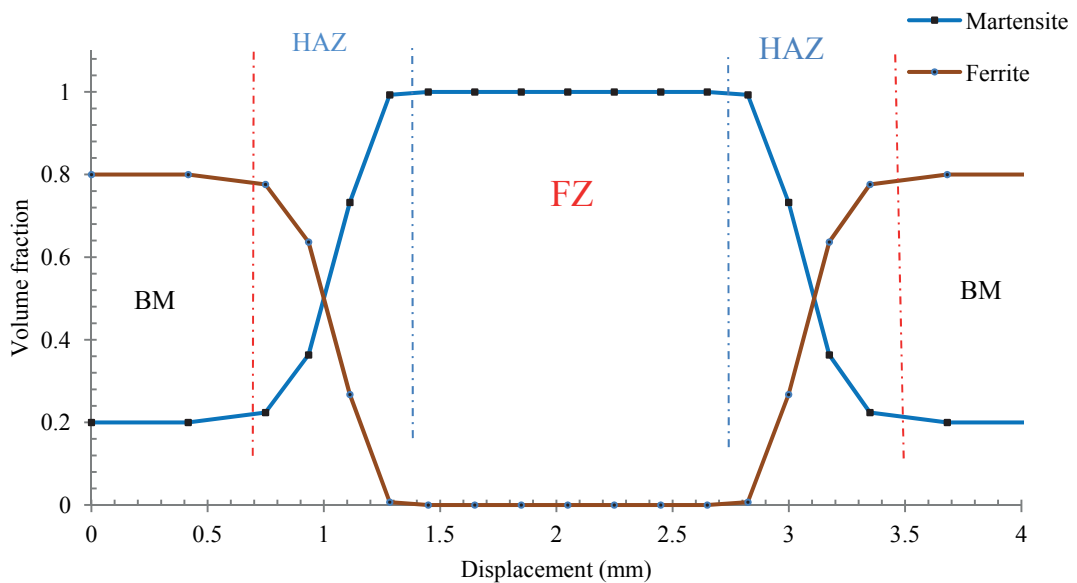
Fig.5. 11   Volume fraction across the weld zone at the middle line of top sheet

5.5.2.3. Hardness and tensile properties

The volume fraction of martensite is the main factor of the increasing hardness inside the material, the curve of hardness from simulation across the weld joint reflex their proportion of martensite. Fig.5.12 showed that the hardness drops sharply from maximum value of the FZ and HAZ to the minimum value of BM. These values are close to the value getting from measurement in Fig.5.12.

The ultimate tensile strength and the 0.2% yield strength are increasing parallel to the hardness value, and because of no tempering martensite near the ZAT, their minimums values are equal to the values of BM and maximum inside the FZ as indicated in Fig.5.13.
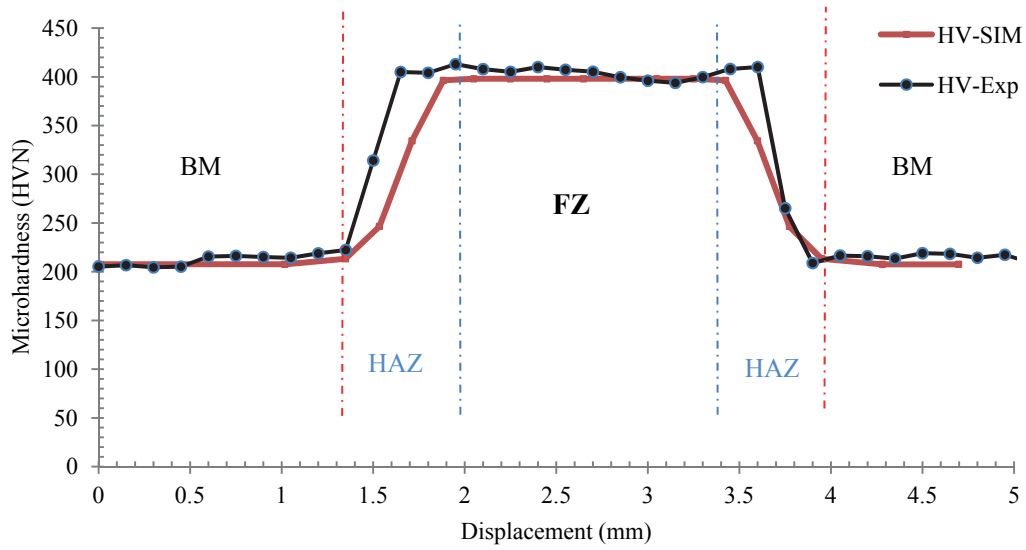
Fig.5. 12   Hardness at the middle line of top sheet
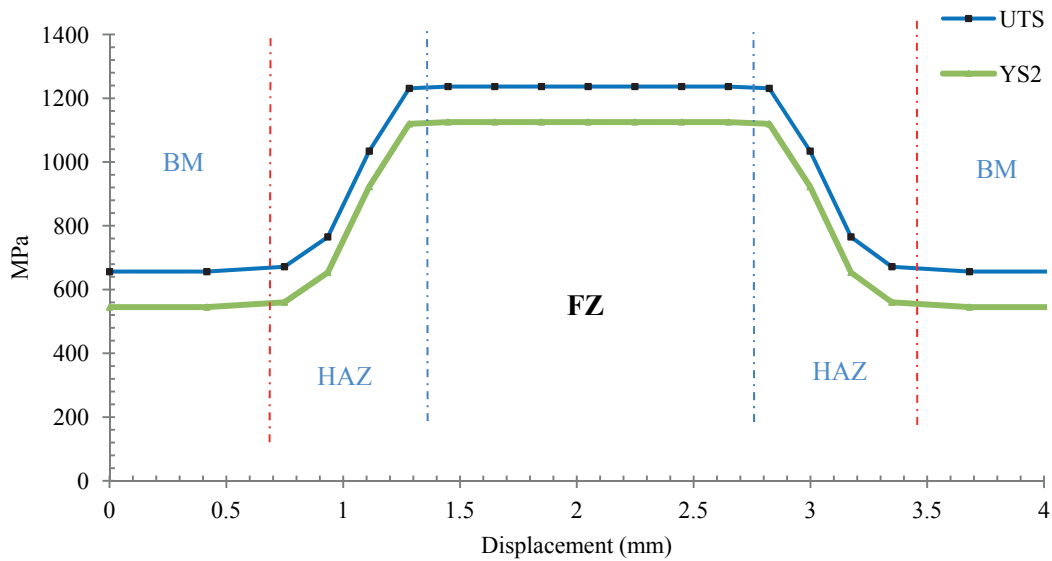
Fig.5. 13   Tensile properties at the middle line of the top sheet

5.6.   CONCLUSIONS

The phase transformation of DP600 during laser ND: YAG welding in this study by calibrates with image from optical microscopy and microhardness is achieved. The model of phase transformation and hardness prediction has been applied for dual phase steel with

success that allow to predict the volume fraction of the final phase and hardness of laser welding.

The hardness inside the fusion zone is an indicator of dominated martensite over volume fraction of austenite and ferrite inside the weld cross section.

The measurement of hardness is also an alternative solution with optical microscope to validate the simulation model with higher percentage of martensite.

No softening zone created by high speed laser Nd: YAG welding process on the DP600 steel.

REFERENCES

[1]   A.Murugaiyan, A.Saha Podder, A.Pandit, S. Chandra, D. Bhattacharjee, and R.K.Ray. Phase transformation in two c-mn-si-cr dual phase steels. *ISIJ International*, 46:1489–1494, 2006.

[2]   G. Avramovic-Cingara, Y. Ososkov, M.K. Jain, and D.S. Wilkinson. Effect of martensite distribution on damage behaviour in dp600 dual phase steels. *Materials Science and Engineering: A*, 516(1-2):7 – 16, 2009.

[3]   Jean-Michel BERGHEAU. Modelisation numerique de soudage. *Technique de l'ingénieur*, 2004.

[4]   E. Biro, J. McDermid, J. Embury, and Y. Zhou. Softening kinetics in the subcritical heat-affected zone of dual-phase steel welds. *Metallurgical and Materials Transactions A*, 41:2348–2356, 2010. 10.1007/s11661-010-0323-2.

[5]   Dean Deng. Fem prediction of welding residual stress and distortion in carbon steel considering phase transformation effects. *Materials & Design*, 30(2):359 – 366, 2009.

[6]   Waeckel F. Modélisation du comportement thermo-métallurgique des aciers. volume 4. EDP Sciences, févier 1994.

[7]   N. Farabi, D.L. Chen, J. Li, Y. Zhou, and S.J. Dong. Microstructure and mechanical properties of laser welded dp600 steel joints. *Materials Science and Engineering: A*, 527(4-5):1215 – 1222, 2010.

[8]   Paolo Ferro, Andrea Zambon, and Franco Bonollo. Investigation of electron-beam welding in wrought inconel 706–experimental and numerical analysis. *Materials Science and Engineering: A*, 392(1-2):94 – 105, 2005.

[9]   John A. Goldak and Mehdi Akhlaghi. *Computational Welding Mechanics*. Springer, 2005.

[10]   Christophe Grignon, Eric Petitpas, Robert Perinet, and Jean Condoure. Modélisation thermométallurgique appliquée au soudage laser des aciersthermometallurgical modeling applied to laser welding of steels. *International Journal of Thermal Sciences*, 40(7):669 – 680, 2001.

[11]   Victor Hugo Baltazar Hernandez, Sushanta Kumar Panda, Yasuaki Okita, and Norman Y Zhou. A study on heat affected zone softening in resistance spot welded

dual phase steel by nanoindentation. *Journal of material sciences*, 45:1638–1647, 2010.

[12] J.Trzaska, A.Jagietto, and L.A. Dobrzanski. The calculation of cct diagrams for engineering steels. *World Academy of Materials Science and Manufactueing Engineering*, 39:13–20, september 2009.

[13] D.P. Koistinen and R.E. Marburger. A general equation prescribing the extent of the austenite-martensite transformation in pure iron-carbon alloys and plain carbon steels. *Acta Metallurgica*, 7(1):59 − 60, 1959.

[14] J.B. Leblond and J. Devaux. A new kinetic model for anisothermal metallurgical transformations in steels including effect of austenite grain size. *Acta Metallurgica*, 32(1):137 − 146, 1984.

[15] Victor LI, Davide V. Neiburhr, Lemmy L. Meekisho, and David G. Atteridge. A computational model for the prediction of steel hardenability. *Metallurgical and materials transactions B*, 29B:661–672, june 1998.

[16] P. Martinson, S. Daneshpour, M. Koçak, S. Riekehr, and P. Staron. Residual stress analysis of laser spot welding of steel sheets. *Materials & Design*, 30(9):3351 − 3359, 2009.

[17] M.Brand and D.Siegele. Numerical simulation of distortion and residual stresses of dual phase steels weldments. In *IIW-1820-07*, 2007.

[18] Ph.Bourges, L.Jubin, and P. Bocquet. Prediction of mechanical properties of weld metal based on some metallurgical assumptions. *Mathematical Modelling of Weld Phenomena*, pages 201–212.

[19] T. Schenk, I. M. Richardson, M. Kraska, and S. Ohnimus. Non-isothermal thermomechanical metallurgical model and its application to welding simulations. *Science and Technology of Welding and joining*, 14(2), 2009.

[20] Christopher Schwenk. *FE-Simulation des Schweißverzugs laserstrahlgeschweißter dünner Bleche :Sensitivitätsanalyse durch Variation der Werkstoffkennwerte*. PhD thesis, Bundesanstalt für Materialforschung und prüfung, 2007.

[21] R.G. Thiessen, I.M. Richardson, and J. Sietsma. Physically based modelling of phase transformations during welding of low-carbon steel. *Materials Science and Engineering: A*, 427(1-2):223 − 231, 2006.

[22] Prodromos Tsipouridis. *Mechanical properties of Dual-Phase steels*. PhD thesis, Technischen Universität München, 2006.

[23]   T.Waterschoot, K. Verbeken, and B.C. Decooman. Tempering kinetics of the martensite phase in dp steel. *ISIJ International*, 46(1):138–146, 2006.

[24]   Anrieux S. Waeckel F. Thermo-metallurgical modelling of steel cooling behaviour during quenching or welding. In *14th Internatiinal Conference on Structural Mechanics in Reactor Technology (SMiRT), Lyon, France*, August 17-22, 1997.

[25]   P. Dupas Waeckel F. and Andrieux. A thermo-metallurgical model for steel cooling behaviour: Proposition, validation and comparison with the sysweld's model. In *Journal de physique IV*, volume 6. EDP Sciences, Janvier 1996.

[26]   Mingsheng XIA and Elliot BIRO. Effects of heat input and martensite on haz softening in laser welding of dual phase steels. *ISIJ International*, 48(6):809–814, 2008.

[27]   X. K. Zhu and Y. J. Chao. Effects of temperature-dependent material properties on welding simulation. *Computers & Structures*, 80(11):967 – 976, 2002.

Résumé

Chapitre 6: Simulation Thermo-Métallo-Mécanique du soudage laser Nd:YAG

Après avoir identifié l'effet thermo-métallurgique, ce chapitre présente le couplage des modèles thermiques, métallurgiques et mécaniques. Dans ce dernier cas, deux modèles élasto-plastiques ont été étudiés : avec et sans effet métallurgique *(modèle classique)*. Pour prendre en compte l'effet métallurgique, les transformations de phases métallurgiques pendant le chauffage et pendent le refroidissement ont été utilisées comme des paramètres dépendant de la dilatation thermique *(modèle thermo-métallo-mécanique)*. Dans ce cas, l'évolution de la dilatation thermique en fonction de la fraction volumique de chaque phase a été intégrée à la place du coefficient de dilatation thermique classique utilisé précédemment *(chapitre 4)*. Ces paramètres ont été utilisés comme chargement dans le modèle mécanique.

A travers cette démarche, nous avons obtenues les effets de la déformation thermo-métallurgique, nous permettant d'évaluer l'état des contraintes résiduelles longitudinales et transversales et de les comparer aux contraintes résiduelles issues du modèles mécanique classique. Les résultats ont montré que la répartition des contraintes résiduelles dans la zone de fusion (FZ) et dans la zone affectée thermiquement (ZAT) sous l'effet de la déformation thermo-métallurgique donne des valeurs légèrement supérieures à celle du modèle élastoplastique classique.

Abstract
Chapter 6: Simulation thermo-metallo-mechanical of laser welding Nd: YAG

After identifying the thermo-metallurgical effect, this chapter presents the coupling of thermal, metallurgical and mechanical models. In the latter case, two elastic-plastic models have been studied: with and without metal effect *(classic)*. To take into account the metallurgical effect, the metallurgical phase transformations during heating and cooling hang were used as dependent parameters of thermal expansion *(model thermo-metallo-mechanical)*. In this case, the evolution of thermal expansion as a function of the volume fraction of each phase was incorporated in place of the conventional thermal expansion coefficient used previously *(Chapter 4)*. These parameters were used as loading in the mechanical model.

Through this approach, we obtained the effects of thermo-metallurgical strain, allowing us to assess the state of longitudinal and transverse residual stresses and compare the residual stresses from the classical mechanics models. The results showed that the distribution of residual stresses in the fusion zone *(FZ)* and heat affected zone *(HAZ)* due to deformation thermo-metallurgical gives slightly higher than conventional elastoplastic model values.

Contents

Figures

Tables

<div align="right">Chapter **6**</div>

Simulation Thermo-Metallo-Mechanical of laser welding

6.1. INTRODUCTION

The phase transformation affects the welding process in a number of ways. Under the transformation induced volume strain effect, it influences the welding distortion and stresses due to their accompanied volume expansion [13] which is theoretically 1.3% of volume expansion for the austenite - ferrite transformation and 4% for austenite - martensite transformation [14]. If 100% ferrite is transformed to 100% martensite due to heat treatment, this results in a volume different of 2.7%. In order to predict the welding stresses and distortions as adequate as possible, it appears to be indispensable to incorporate phase transformations in the model due to the strong spatial dependency of the phase transformations under effect of different cooling rates [13]. Studies performed by Taljat et al [1] indicated that this volumetric expansion on cooling phase lowers the residual stresses in the fusion zone of a weld metal. Mikami et al [19] reported by means of numerical simulations that angular distortion of T-Joints can be reduced significantly by an increased martensite volume fraction. Beside the physical properties of sheet metal, the welding process plays an important factor in the formation of welding pool and its evolution during cooling phase. It affects on the heating rate, the cooling rate and finally the metallurgical and mechanical property of the welded joint as mention in the previous research works. The

residual stresses along the transverse line were observed by Kong [8]. The numerical and X-ray diffraction analysis had been used to study the influence of different welding processes of lap joint, laser, GTAW, hybrid laser-GTAW. He found out that the maximum normal stress components are located at the HAZ and its peak value increases with the decrease of welding speed. He also notice that, from X-ray diffraction technique increasing the welding speed *(1.2 m/min to 2.4m/min)*, the longitudinal stress at the center of the weld bead *(FZ)* changes from compressive state to the tensile one.

So the implement of metallurgical effect in mechanical model is important in numerical analysis of welding residual stresses and residual distortion. The elastoplastic model includes the transformation induced volumetric strain is used to compare with the classical elastoplastic model applied to the analysis of Nd: YAG laser welding of sheet metal joining process.

6.2. MODELS

6.2.1. Thermo-metallo-mechanical model

The thermo-metallo-mechanical model constitutes of three models separately, the thermal model, the metallurgical model and the mechanical model. The thermal model constitutes of heat transfer equation and heat source model had been presented in *Chapter four* and *Chapter five*. The metallurgical model used in this simulation is based on Waeckel model, which is developed from the model Leblond as presented in *Chapter five*. The elastoplastic model with linear isotropic hardening under Von Misses criteria can be found in *section 2.4.4.2*. All of these models are not re-described in this section. But the transformation induced volumetric strain is described in this section.

The separation between the rate of volume changed and rate of thermal deformation by changing the coefficient of thermal expansion allows having the flexibility to describe the behavior of the material [6]. The phase transformation plays an important role in modeling the residual stresses [9]. To count these changes in volume, just replace the thermal

deformation by a thermo-metallurgical strain [2] or transformation induced volumetric strain [17]. Its expression was described in section 2.4.3.

In the literature, the reported volume changes $\Delta V_{\gamma \to \alpha}$ from austenite to ferrite vary strongly. For instance, Velthuis et al. [16] reported an expansion of 1% for Fe-Cu and Fe-Co steels. The measurement operated by Chen et al. [11] found in an expansion of 2.6 %. Dean et al [5] reported 0.75 % expansion for 9Cr-1Mo steel. Moyer and Ansell [7] reported values between 1.3 % and 2.7 % for various tool steels and stainless steels.

The volume change, applied for DP600 steel [13] from austenite to ferrite is assumed to be 1.4 % and from austenite to martensite 1 % which is in accordance to values reported in the research [5, 7, 16] of the steels alloys transformation.

6.2.2.   Parameters of thermo-metallo-mechanical model

The thermal model and thermal condition using in this analysis are the same to those used in chapter 5. Their properties could be found in section 4.3.3.

The mechanical data used in the model thermo-elastoplastic classic *(EP model)* and VEP model was presented in section 4.3.3.

The thermo-metallurgical data of DP600 for thermo-elastoplastic model with the transformation induced volume strain *(VEP model)* are presented in Tab.6.1. The mechanical data could be found in section 4.3.3.

The thermo metallurgical expansion used in the elastoplastic model with volume change *(VEP model)* is considered to be constant in each phase and is shown in Tab.6.1 where the thermal expansion interpolated by these values during heating and cooling are presented in Fig.6.1 which is similar to the curves of experimental results of thermal expansion DP600 presented in Fig.5.5 *(Chapter 5)* for the four cooling time *(from 800^0C to 500^0C)* 0.8s, 1s, 2s and 3.1s [15].

Thermo metallurgical expansion coefficient	
γ-base (Austenite)	$2.13\ 10^{-5}$
α-base (FM, M)	$1.68\ 10^{-5}$
$\Delta\varepsilon_{\alpha\gamma}^{25°C}$	0.01375

Tab.6. 1   Thermo metallurgical expansion coefficient of DP600
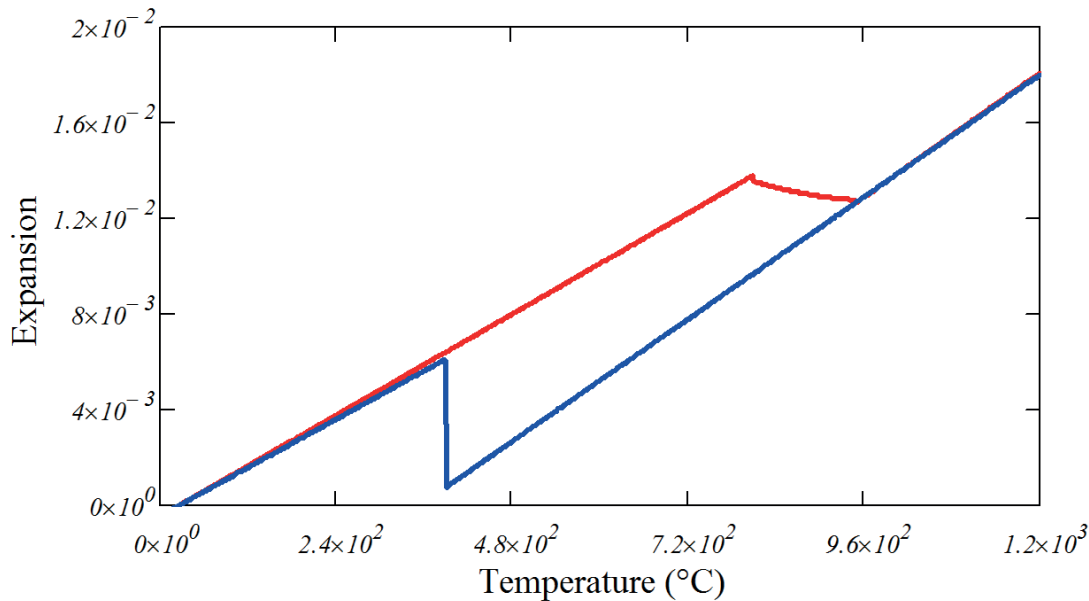
Fig.6. 1   Thermal expansion of DP600

6.3. SIMULATION AND PREPARATION

The simulation is done in two states, the thermal state and mechanical state where three steps are considered, the welding step for 0.8823 seconds, the cooling step for 120 seconds and relaxing step for 120 seconds with the laser power of 4kW and laser speed of 4.3m/min. The quadratic interpolation function gives more accurate results close to the weld seam and is used in this simulation to solve the thermal analysis of welding and linear interpolation was used to solve the mechanical analysis.

Two mechanical models are used here, the elastoplastic model *(EP model)* and the elastoplastic with the transformation induced volume strain model *(VEP model)*. The simulation of these two models were done at the same condition and meshing parameters in order to evaluate its different outputs such as residual stresses.

6.3.1. Boundary Condition
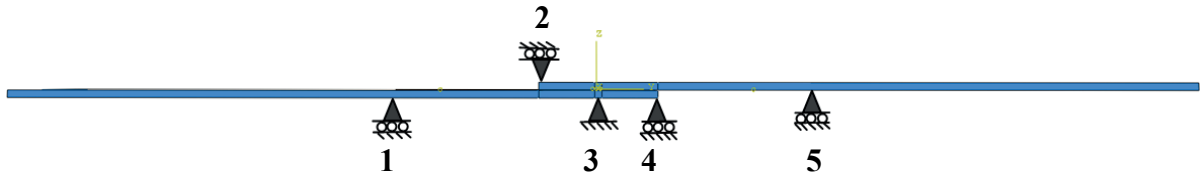
Fig.6. 2   Mechanical boundary condition

The boundary condition plays an important role in the formation of residual stress and deformation of the welding joint. The nature of contact surface between the clamping system and the sheet metal is also influenced on the cooling rate of the welding process. Numerical predictions performed by Schwenk [4] for a case study where the cooling rate is increased by a factor of two. The influence of the distance of the clamping, the clamping force as well as the release time after welding have been studied by many authors [12, 3, 10, 13]. There are some compromise and contradiction on the clamping position on the distortion prediction.

The boundary conditions BCs, as illustrated in Fig.6.2, using in this model are:

- Position 1, 2, 4 and 5: Displacement Z =0 *(Z-SYMM mode)*. These BCs *(BCs at position 1, 2, 4 and 5)* will relax at third step.

- Position 3: Lock the start of weld seam *(Encastre-mode)* and Displacement Z = 0 *(Z-SYMM-mode)* at the end of weld beam. These BCs are lock for all steps.

6.3.2. Meshing parameter

The model is separated into three zones, the FZ, the HAZ and the BM. The first order element with 8-nodes brick technique is used for the HAZ and the FZ in purpose to assure a constant and small element size inside these two zones. On the other hand the sweep technique with advancing front algorithm is used to reduce the number of elements inside the BM as shown in Fig.6.3.

The mesh dimension of the FZ and the HAZ are presented in the Tab.6.2 below.
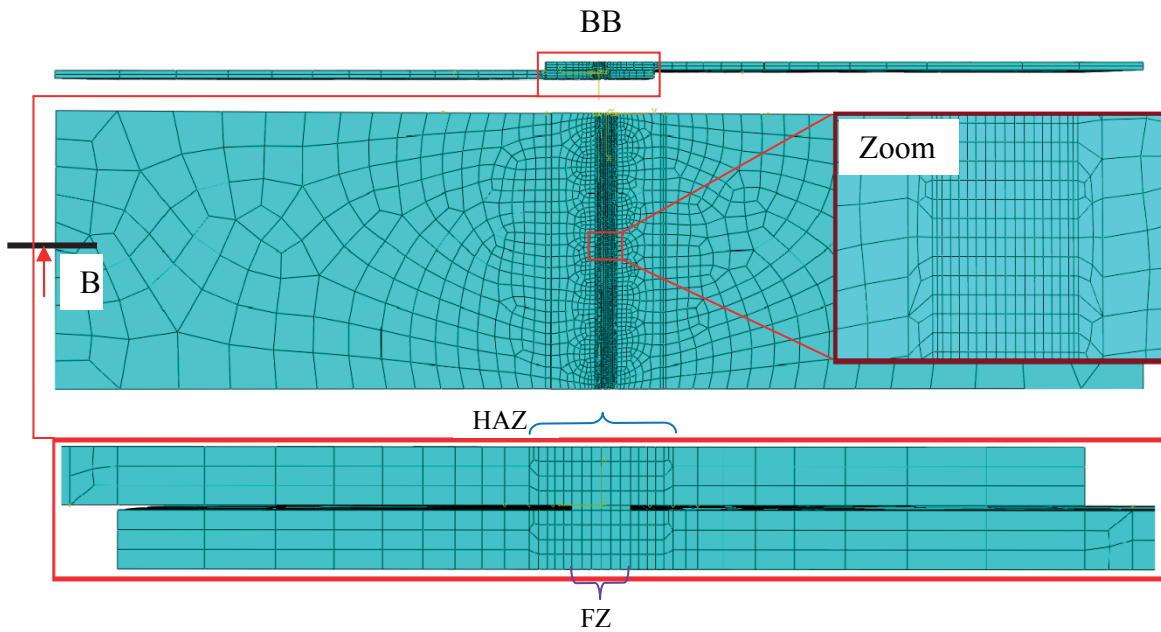
Fig.6. 3   Meshing element

	FZ-HAZ	Ratio in BM
DX	0.4mm	125:62:31:25:10
DY	0.2mm	biase 5:15
DZ	0.3125mm	4:3:2

Tab.6. 2   Mesh size of FZ and HAZ

6.4. RESULTS

The magnitude of residual stresses present after welding is important in the prediction of resistance to fracture [6]. To study the different residual stresses getting from the elastoplastic model *(EP model)* and the elastoplastic with volume change model *(VEP model)*, one has to observe on:

The Von Mises stresses VM, the longitudinal stresses S11, the transverse or hoop stresses S22 and the shear stresses S12 along the transverse line and the longitudinal line at the end of cooling cycle.

212

6.4.1.   Residual stresses

The influence of transformation induced volume strain on elastoplastic model is observed based on the comparison of the residual stresses analysis such as Von Mises stresses VM, longitudinal stresses S11, transversal stresses S22 and shear stresses S12 of the elastoplastic model, *EP model*, shown in Fig.6.4 (a-b-c-d) and those of elastoplastic model with transformation induced volume strain model, *VEP model*, presented in Fig.6.5 (a-b-c-d).

The magnitudes of maximum residual stresses of these two models located in the FZ and HAZ which was depended almost entirely on the ambient temperature yield strength.

The general aspects of residual stresses of these models are almost similar but a few different aspects of residual stresses are found. The longitudinal residual stresses distribution along the transverse direction of VEP model, Fig.6.5 (b), is wider than that of the EP model, Fig.6.4 (b). The transverse residual stresses of VEP model, Fig.6.5 (c), seem to give more effects, higher residual stresses S22, than that of EP model as indicated in Fig.6.4 (c). The same results has been found in the shear residual stresses as shown in Fig.6.4(d) and Fig.6.5 (d). A further analysis are based on the study of residual stresses distribute along the transverse line and longitudinal line and presented in section 6.4.1.1 and section 6.4.1.2 respectively.

(a)
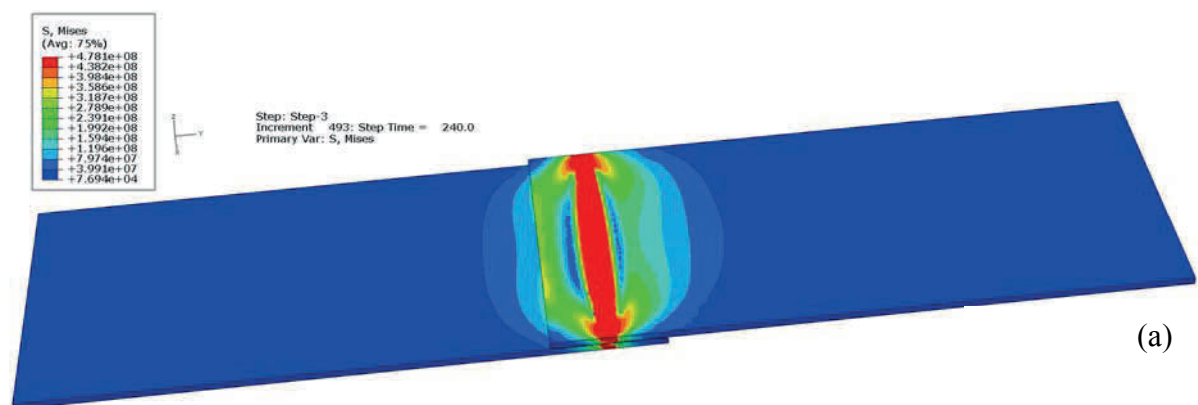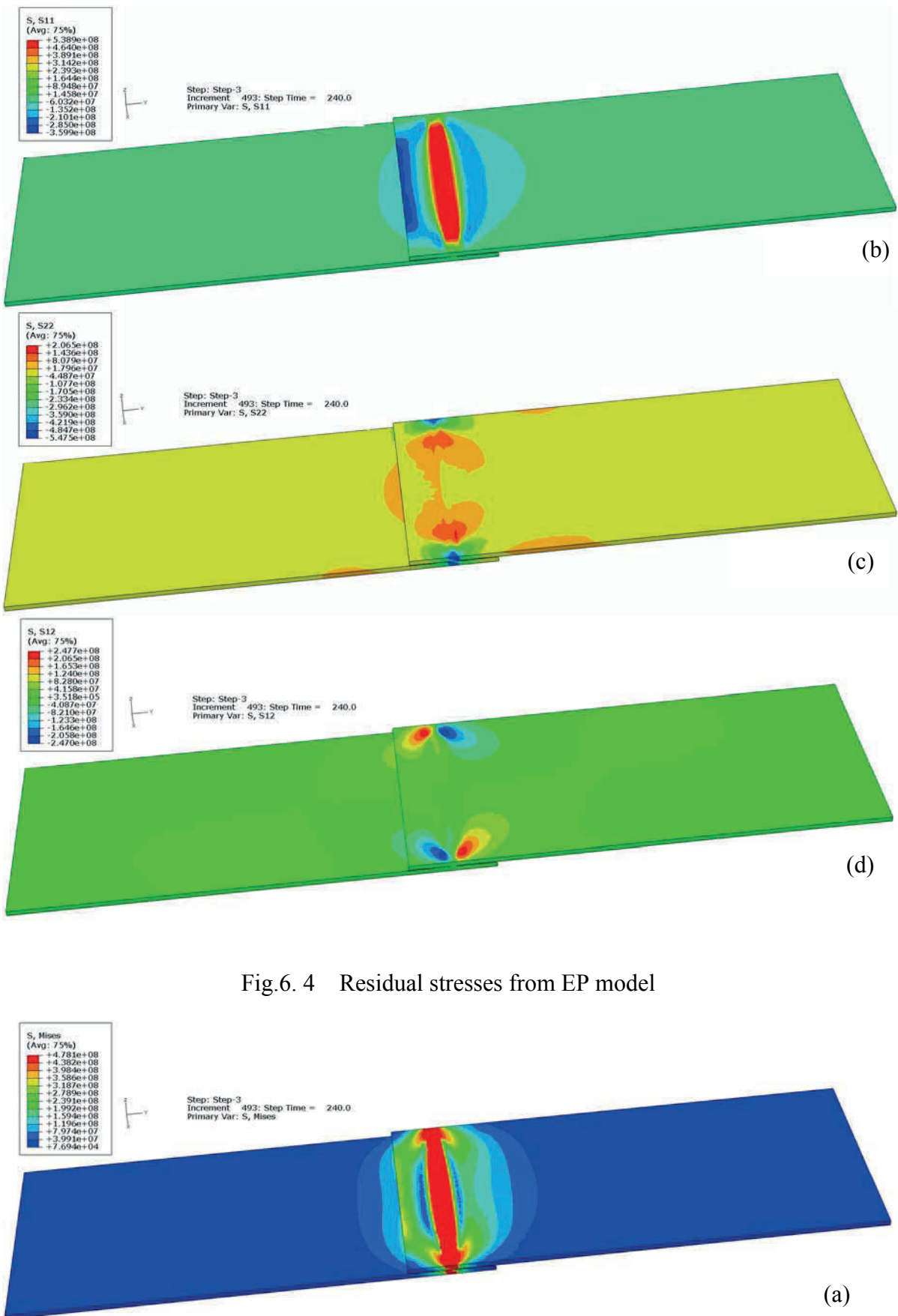
Fig.6. 4   Residual stresses from EP model

(b)

(c)

(d)
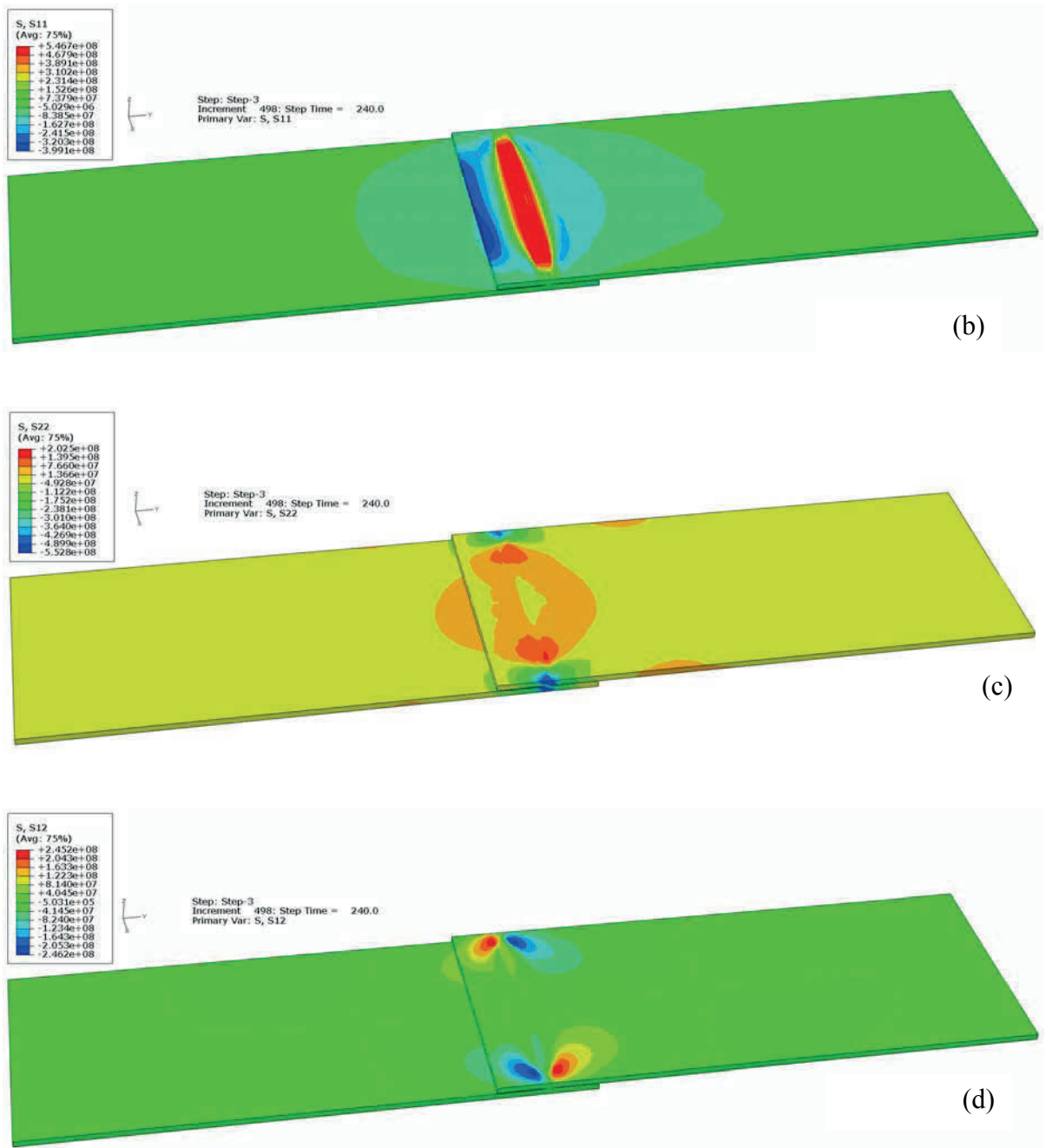
Fig.6. 5   Residual stresses from VEP model (Pa)

6.4.1.1.   *Residual stresses along the transverse line*

Fig.6.6 presents the transverse line situated on top right of the numerical model in purpose to study the variation of residual stresses.
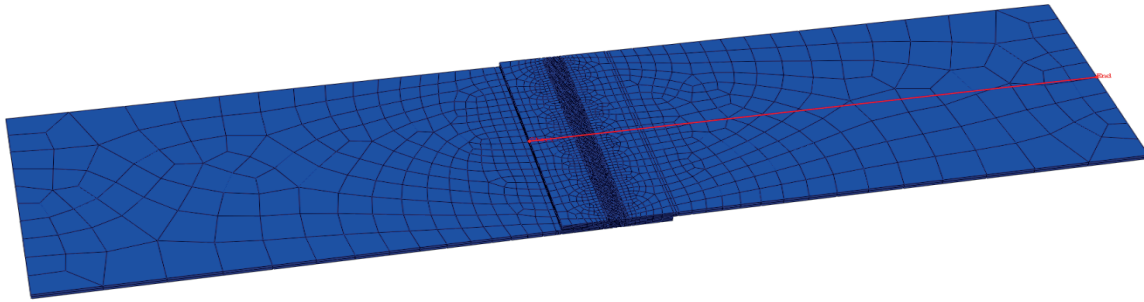
Fig.6. 6   Transverse line on the top right of welding model (Pa)

The comparison of residual stresses along the transverse line as shown in Fig.6.7, Fig.6.8, Fig.6.9 show the distribution of the Von Mises residual stresses VM, the longitudinal residual stresses S11, the transverse residual stresses S22 and the shear residual stresses S12 respectively.

Only a slightly different was found. The VEP model gives a higher value of the Von Mises residual stress VM, the longitudinal residual stresses S11, the transverse residual stresses S22 and the shear residual stresses S12 than those of the EP model as shown Fig.6.7 and Fig.6.10 respectively.

The curves represent of these residual stresses emphasize the intensity of residual stresses. It proved that the residual stresses of these models followed the same distribution with just a few different *MPa* on its intensity. The difference of residual stresses along the transverse line is considered to be negligibly small.

216
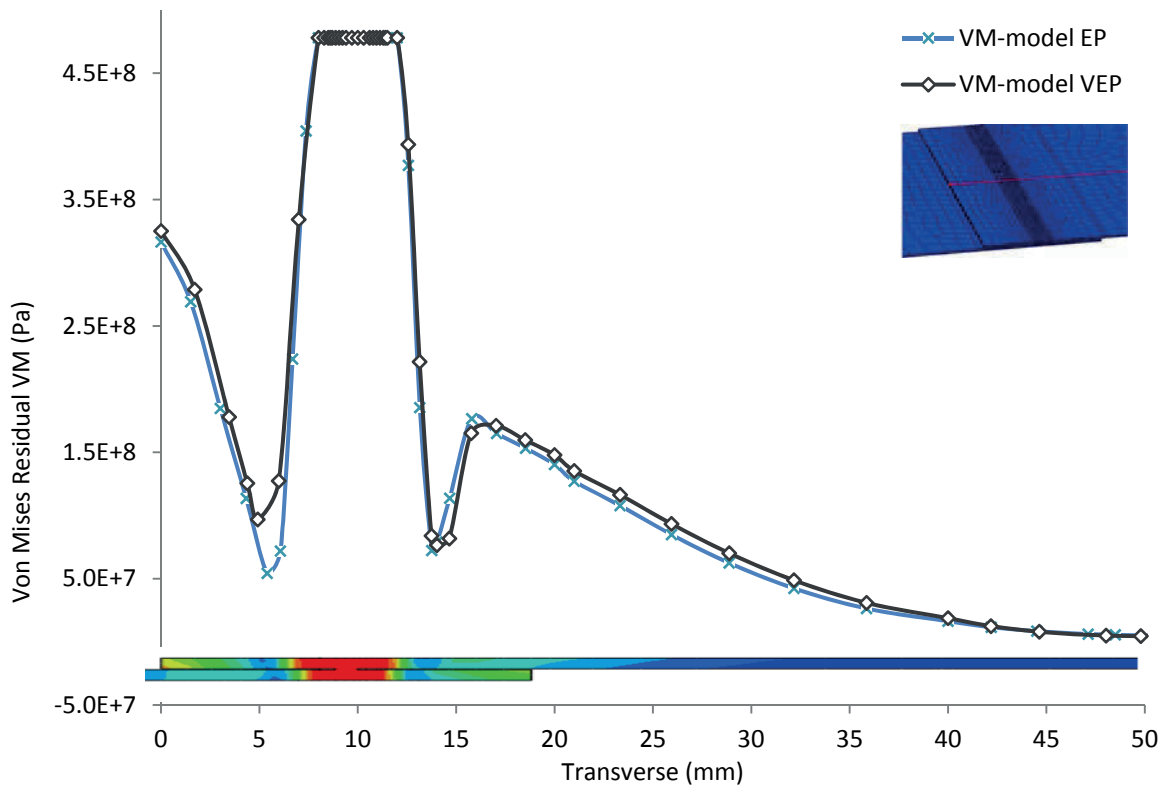
Fig.6. 7   Von Mises residual stresses VM along the top-right transverse line
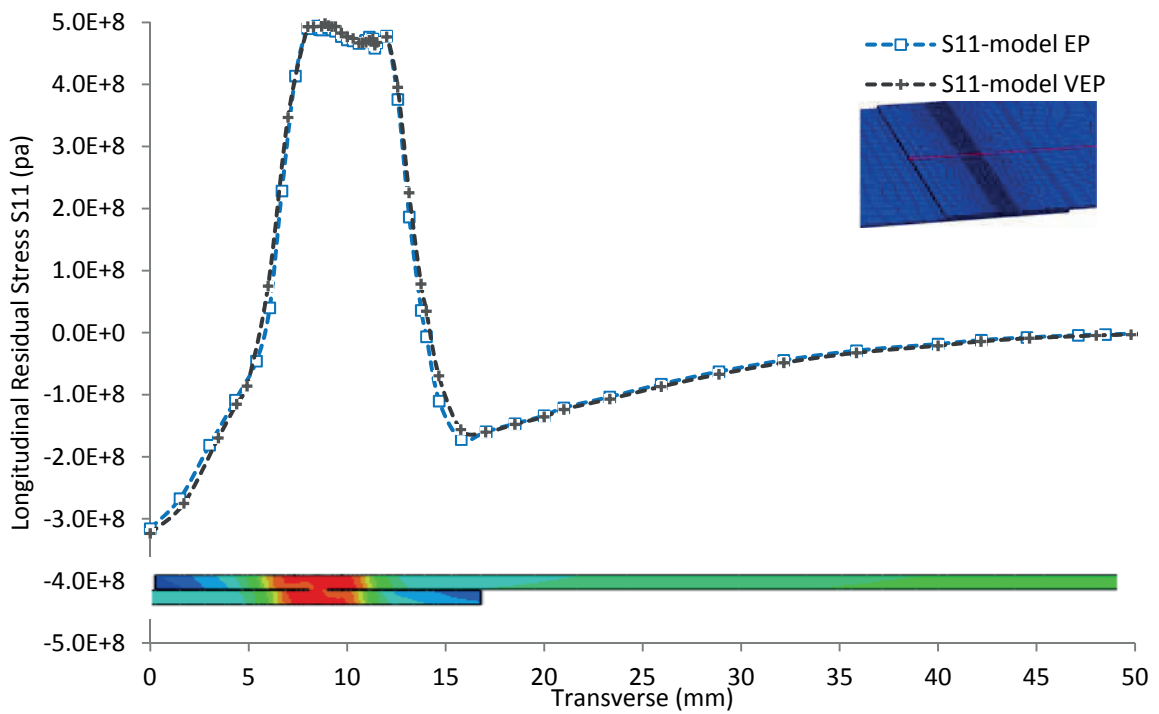
Fig.6. 8   Longitudinal residual stresses S11along the top-right transverse line
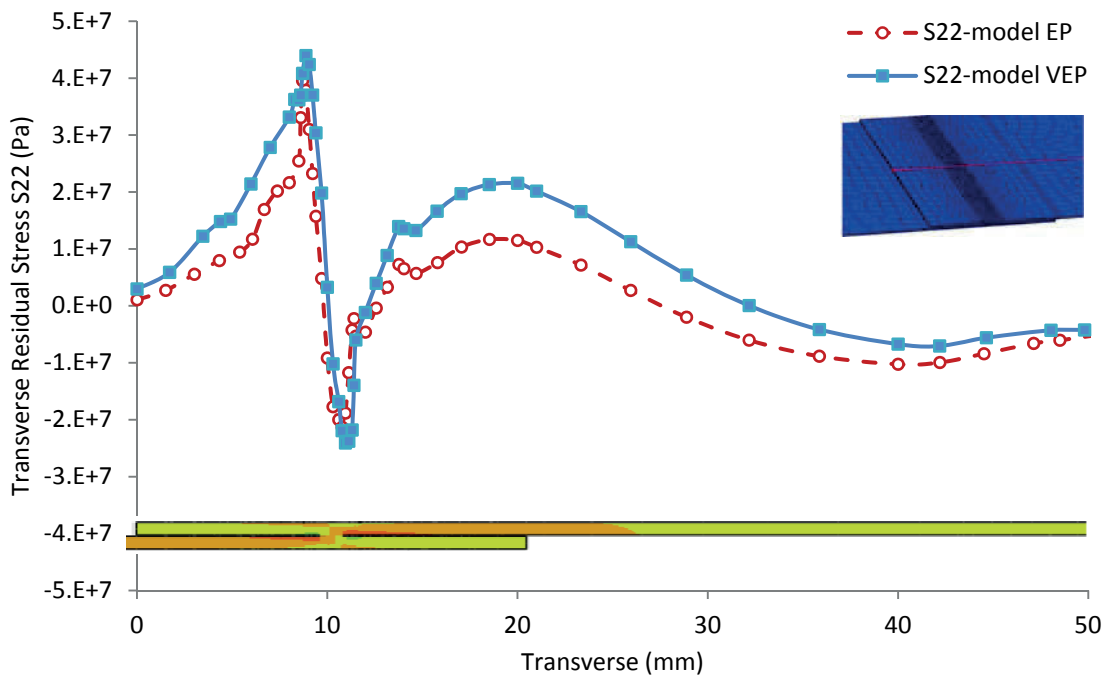
Fig.6. 9   Transverse residual stresses S22 along the top-right transverse line
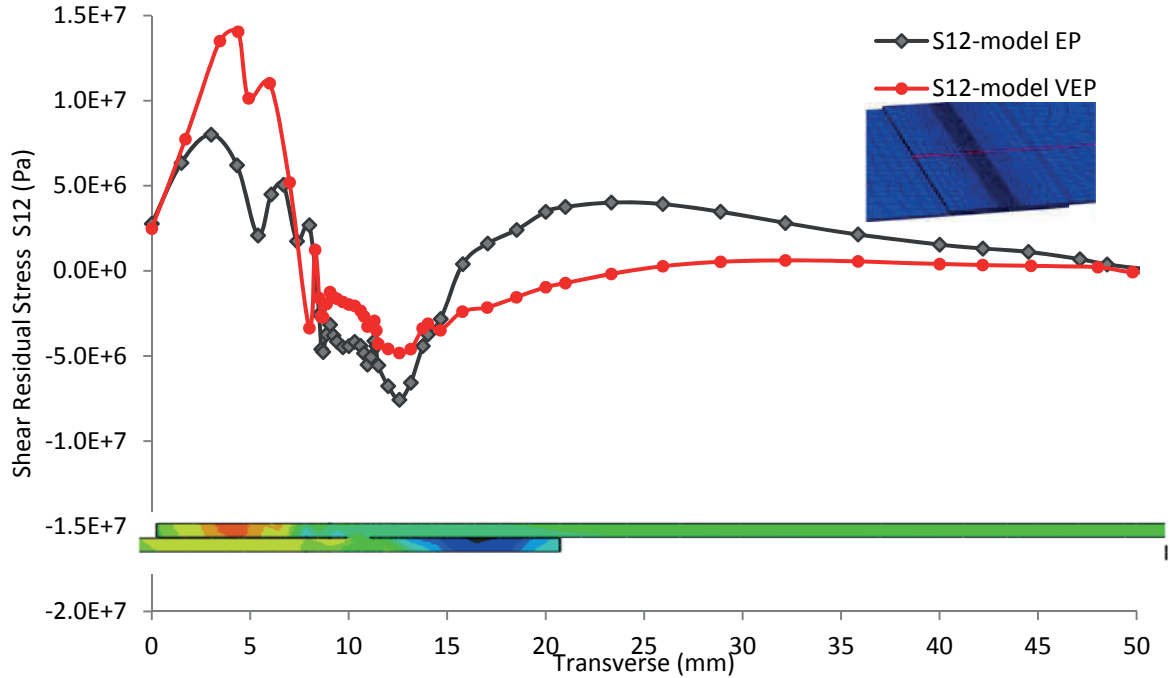
Fig.6. 10   Shear residual stresses S12 along the top-right transverse line

6.4.1.2. *Residual stresses along the longitudinal line*

The longitudinal line on top of the weld seam is presented in Fig.6.11.
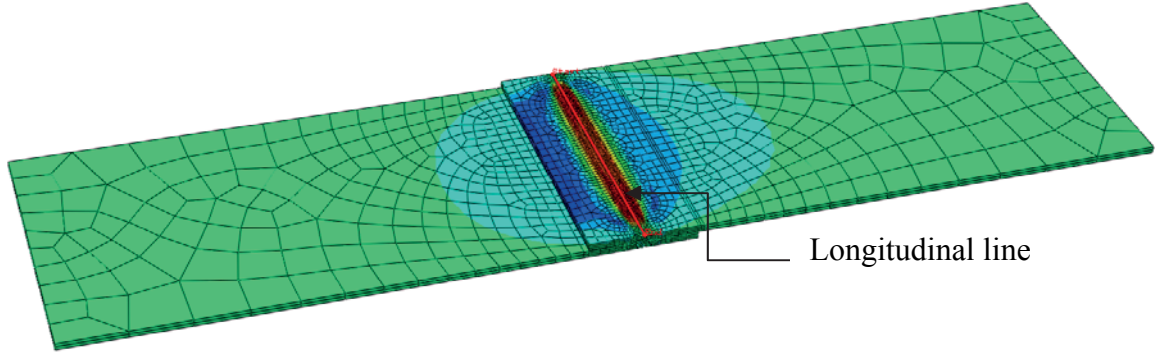
Fig.6. 11   Longitudinal line on top of welding model

The residual stresses along the longitudinal line *(along the weld center line)* as shown in Fig.6.12, Fig.6.13, Fig.6.14 present clearly the Von Mises residual stresses VM, the longitudinal residual stresses S11 and the transverse residual stresses S22 respectively.
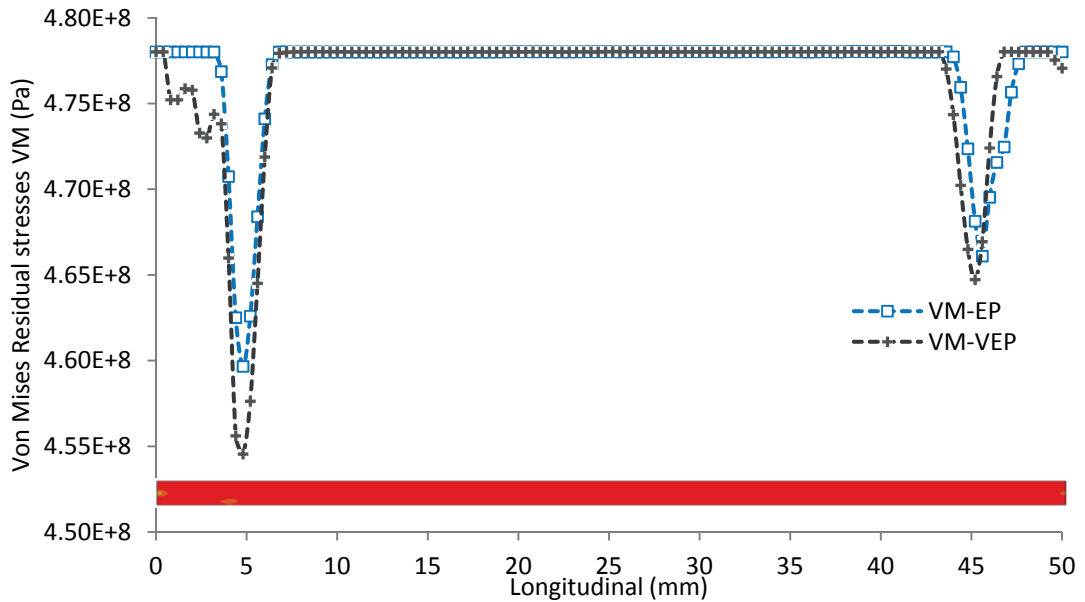
Fig.6. 12   Von Mises residual stresses VM along the longitudinal line

219
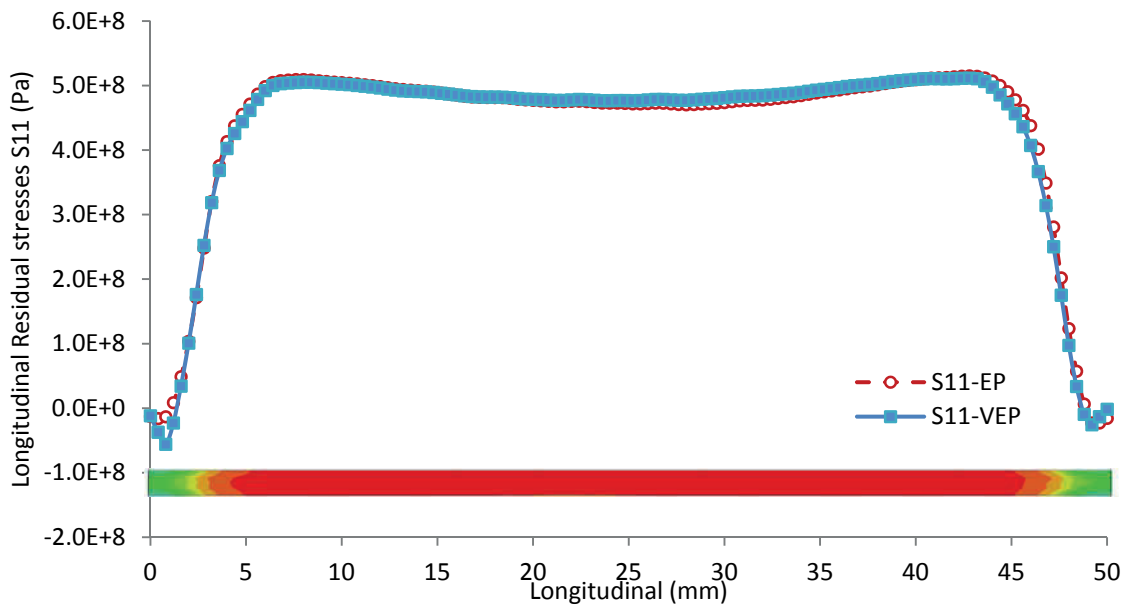
Fig.6. 13   Longitudinal residual stresses S11 along the longitudinal line
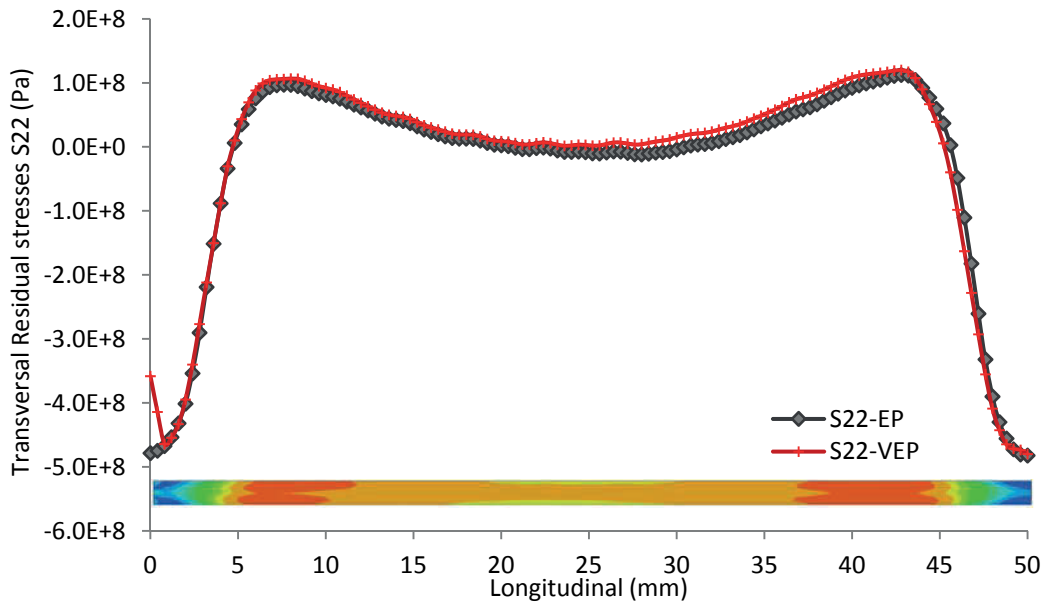
Fig.6. 14   Transverse residual stresses S22 along the longitudinal line

The distribution of residual stresses of EP model and VEP model are almost similar. Only a slight different of Von Mises residual stresses, Fig.6.11, situated near the start and ended point of weld bead was found. And a very small difference of longitudinal residual stresses, Fig.6.12, and transverse residual stresses, Fig.6.13, are found and considered to be negligible.

Along the longitudinal line inside the FZ of the weld seam center, The VEP model give a slightly higher of longitudinal stress and transverse stress than that of the EP model.

Observation of the residual stress on the aspect general and its distribution along the longitudinal and transverse line proved that the results of residual stresses from VEP model are a slightly higher than that of the EP model but the difference is negligibly small.

6.5. CONCLUSION

The effect of transformation induced volumetric strain had been identified. The global distribution of residual stresses such as the Von Mises residual stresses, the longitudinal residual stresses and transversal residual stresses has shown clearly the different residual stresses from these models. The VEP models gives a slightly higher value of longitudinal residual stresses S11 and transversal residual stresses S22 in the FZ and HAZ than that of the EP model. Anyway the different of residual stresses of these models is very low and can be consider being negligible small. One can conclude that the transformation induced volume strain has less affect on the results of the elastoplastic model applied for laser welding of thin sheet metal DP600.

REFERENCE

[1]   Z. Zacharia B. Taljat, B. Radhakrishnan. Numerical analysis of gta welding process with emphasis on post-solidification phase transformation effects on residual stresses. *Mater. Sci. Eng*, A246:45–54, 1998.

[2]   Jean-Michel BERGHEAU. Modélisation numérique de soudage. *Technique de l'ingénieur*, 2004.

[3]   J.X. Zhang C. Liu. Numerical simulation of transient welding angular distortion with external restraints. *Science and Technology of Welding and Joining*, 14(1):26–31, 2009.

[4]   K. Dilger V. Michailov C. Schwenk, M. Rethmeier. Schweißsimulation im fahrzeugbau - möglichkeiten, grenzen und herausforderungen. Technical report, DVS Report, Nr. 237, pp. 353, 2005.

[5]   M. Hidekazu D. Dean. Prediction of welding residual stress in multi-pass butt-welded modified 9cr–1mo steel pipe considering phase transformation effects. *Computational Material Science*, 37:209–216, 2006.

[6]   John A. Goldak. *Computational Welding Mechanics*. Springer, 2005.

[7]   G.S. Ansell J.M. Moyer. The volume expansion accompanying the martensite transformation in iron-carbon alloys. *Metallurgical Transactions*, 6A:1785–1791, 1975.

[8]   Fanrong Kong and Radovan Kovacevic. 3d finite element modeling of the thermally induced residual stress in the hybrid laser/arc welding of lap joint. *Journal of Materials Processing Technology*, In Press, Accepted Manuscript:–, 2010.

[9]   Lars-Erik Lingren. *Computational Welding Mechanics: Thermomechanical and microstructural simulations*. Woodhead Publishing in Materials, 2007.

[10]   M. Siddique M. Abid. Numerical simulation of the effect of constraints on welding deformations and residual stresses in a pipe-flange joint. *Modelling Simul. Mater. Sci. Eng*, 13:919–933, 2005.

[11]   R. Kaspar Q. Chen, O. Pawelski. Contribution to the deformation characteristics of dual-phase steels. *Z. Metallkunde*, page 348–352, 1985.

[12] M. Rethmeier S. Roeren, C. Schwenk. Different approaches to model clamping conditions within a weld simulation. In *Proceedings of the 8th Conference on Mathematical Modelling of Weld Phenomena*, 2006.

[13] Tobias Schenk. *Modeling welding Distortion Influence of Clamping and Sequencing*. PhD thesis, Material Innovation Institute, www.m2i.nl, 2011.

[14] H. Schumann. *Metallographie*. ISBN: 3342004312, 1991.

[15] Christopher Schwenk. *FE-Simulation des Schweißverzugs laserstrahlgeschweißter dünner Bleche :Sensitivitätsanalyse durch Variation der Werkstoffkennwerte*. PhD thesis, Bundesanstalt für Materialforschung und prüfung, 2007.

[16] J. Sietsma M. T. RekveldtS. Van der Zwaag S.G.E. Velthuis, J.H. Root. The ferrite and austenite lattice parameters of fe-co and fe-cu binary alloys as a function of temperature. *Acta Materialia*, 46(15):5223–5228, 1998.

[17] Yannick Vincent, Jean-Michel Bergheau, and Jean-Baptiste Leblond. Viscoplastic behaviour of steels during phase transformations. *Comptes Rendus Mecanique*, 331(9):587 – 594, 2003.

[18] Yannick Vincent, Jean-François Jullien, and Philippe Gilles. Thermo-mechanical consequences of phase transformations in the heat-affected zone using a cyclic uniaxial test. *International Journal of Solids and Structures*, 42(14):4077 – 4098, 2005.

[19] M. Mochizuki M. Toyoda Y. Mikami, Y. Morikage. Angular distortion of filler welded t -joints using low transformation temperature welding wire. *Science and Technology of Welding and Joining*, 14(2):97–105, 2009.

Résumé

Chapitre 7 : Approche Numérique et Expérimentale du Soudage Laser

Ce chapitre est une comparaison des résultats issus de l'analyse numérique avec les résultats expérimentaux. Pour avoir une comparaison fiable entre l'approche numérique et expérimentale, nous avons utilisé la même géométrie et les mêmes dimensions de l'échantillon, à savoir une dimension de 110x250mm. Les conditions aux limites et les conditions initiales de l'analyse numérique ont été simplifiées pour être similaires à celles de l'installation expérimentale afin de faciliter le travail de comparaison entre l'analyse numérique et l'analyse expérimentale.

Pour valider la robustesse de notre modèle, la comparaison entre les résultats expérimentaux et numériques est réalisée. Les paramètres comparés sont :

- Les courbes d'évolution de la température en fonction du temps réalisées expérimentalement à l'aide de thermocouples.

- Les dimensions géométriques du bain fondu (section transversale).

- Les déplacements hors plan mesurés expérimentalement à l'aide de machine à mesure trois dimensions.

- Enfin, le profil de l'analyse numérique des contraintes résiduelles a été comparé à celle fournie par la littérature.

Abstract

Chapter 7: Numerical and Experimental approach of laser welding

This chapter is a comparison of the results of numerical analysis with experimental results. For a reliable comparison between the numerical and experimental approach, we used the same geometry and the same sample size, namely a size of 110x250mm. The boundary conditions and initial conditions of numerical analysis have been simplified to be similar to the experimental setup in order to facilitate the work of comparison between the numerical analysis and experimental analysis.

To validate the robustness of our model, the comparison between experimental and numerical results is performed. The parameters to be compared are:

• The evolution of the temperature versus time curves produced experimentally using thermocouples.

• The geometrical dimensions of the melt (cross section).

• The out of plane displacements measured experimentally using three-dimensional measuring machine.

• Finally, the profile of the numerical analysis of residual stress was compared to that provided by the literature.

Contents

Figures

Tables

Chapter 7

Numerical and Experimental Approach of Laser Welding

7.1 INTRODUCTION

This part of work consists of approaching the experimental results to that of the numerical analysis. The numerical analysis had been studied in the previous chapter 4, 5 and 6. Its optimized parameters are using in this numerical analysis in order to approach to the experimental results. The parameter used to evaluate this difference includes the temperature evolution in the vicinity of weld seam during laser welding process, the out of plane displacement of welding specimen and the residual stresses after welding process.

7.2 NUMERICAL MODELS

In the previous research work, the out of plane displacement from elastoplastic model *(EP model)* and elastoviscoplastic model *(EVP model)* are compared in the thesis of Zain [11], the amplitude of out of plane displacement, U3, using EP model seem to be higher than that of EVP model, but the difference of these two models is negligible small. Another observation by numerical methods to the experiment found out that the out of plane amplitude from isotropic hardening model is higher that the kinematic hardening model compared to the measurement value, the deviation is about 10% which is still acceptable for welding simulation [9] . So the elastoplastic with linear isotropic hardening model include the transformation induced volumetric strain are used in this part. The thermo-metallo-

mechanical models and the physical properties of DP600 steel are the same as models and properties used in chapter 6.

7.3 EXPERIMENT AND SIMULATION PREPARATION

The experimental processes for laser welding include the welding specimen mounting, fixing the thermocouple and finally the out of plane displacement measurement of the specimen after welding by three dimensional measuring machines. Each of these processes is described in the following case.

7.3.1 Experiment setup

The experimental campaigns of laser welding Nd: YAG was prepared at the institute Maupertuis, Fig.7.1. Two sheets metal with the dimension 110mm x 250mm are joined by transparent mode, or lap joint, with an overlap of 20mm and 0.1mm gap between two sheets. The mounting system is presented in Fig.7.1 and also in Fig.7.2 (a) and Fig.7.3 (b). The sheet metals are clamped by a screw-nut system that allows locking the sheet metal between the top bar *(Upper clamps)* and the bottom fixed table *(Lower clamps)*.

Robot

Laser Head

Clamping system

Laser Nd: YAG
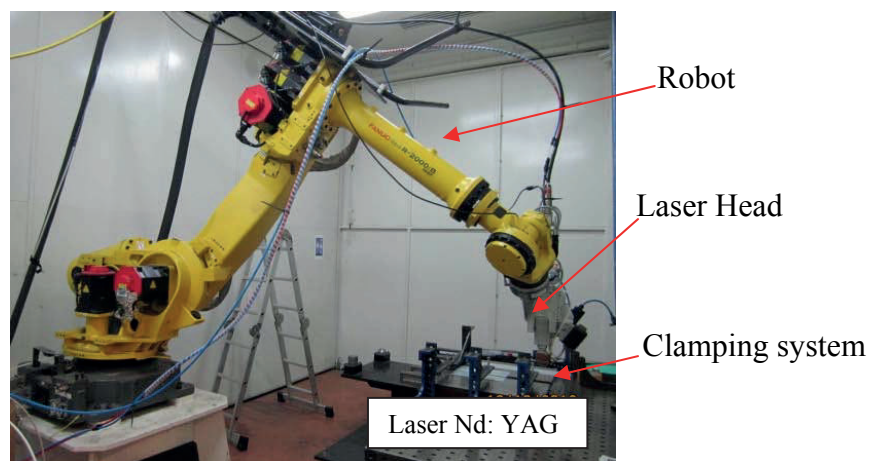
Fig.7. 1   Sheet metal assembled with laser welding robot
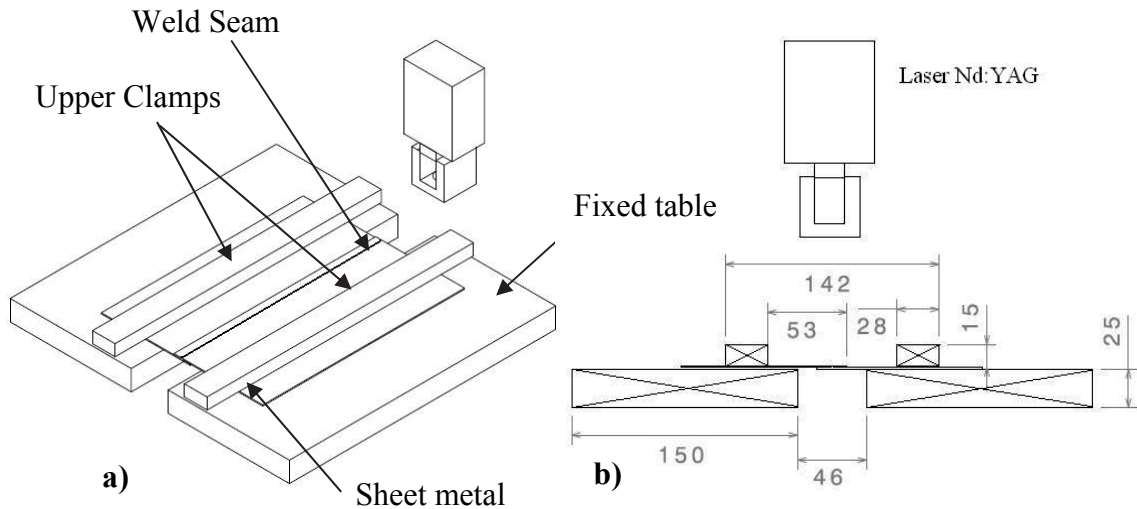
Fig.7. 2   Clamping system during laser welding a) isometric view, b) front view (mm)

7.3.1.1   Thermocouple

The temperature evolution on the top surface of the sheet metal in the vicinity of the lap joint was measured by three K-type (Chromel-Alumel) thermocouples with wire diameter of 300 micrometers. Those thermocouples are fixed to the top sheet metal by resistance spot welding technique as indicated in Fig.7.3. The coordinate positions of thermocouples for experimental measurement are shown in Tab.7.1.

Temperature acquisition during welding and cooling process was made by NI-DAQ, NI-9214 of National Instruments, which is capable of treating 16 differential inputs from thermocouple. The accuracy of temperature measurement for NI-9214 is $0.02^{o}C$ and the accuracy of K-type thermocouple is $1.1^{0}C$ in range of $-180^{0}C$ to $+1300^{o}C$.

Coordinate	Thermocouples		
	TC1	TC2	TC3
X	125	125	125
Y	2.5	5.5	7.2
Z	1.25	1.25	1.25

Tab.7. 1   Coordinate positions of thermocouple (mm)
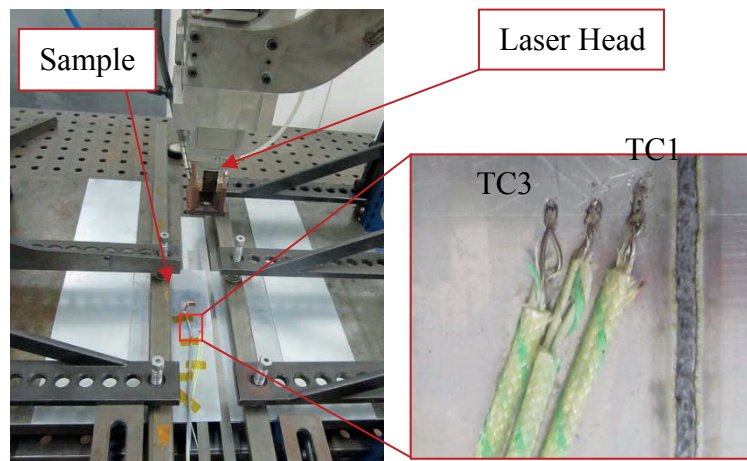
Fig.7. 3   Position of thermocouples

7.3.1.2   *Three dimensional measuring machine*

The out of plane displacement was measured by the three dimensional measuring machine, RENISHAW-Prelude inspection machine as shown Fig.7.4(a), at the department of mechanical and control systems engineering , Institute National of Applied Sciences of Rennes. The measurement samples constitute of 120 points measurement as indicated in the model present in Fig.7.4 (b) which was drawn in commercial CAD software, Catia, and then generated in Prelude Inspection software. The coordinate *(X, Y, Z)* data are treated in MATLAB in order to plot the deformation of the surface profile.
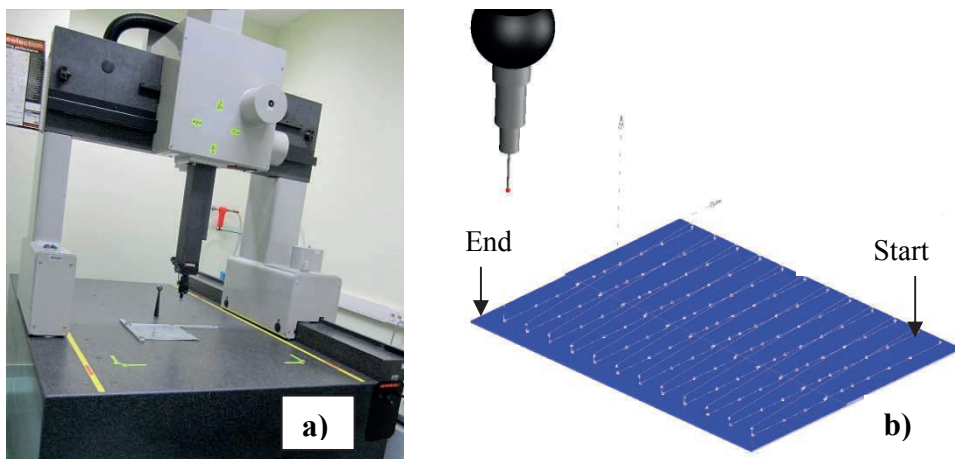
Fig.7. 4   Three dimensional measuring machine (a) and measurement preparation plane (b)

7.3.2   Boundary Condition

The boundary and initial condition caused by clamping mode play an important role in the cooling mode and residual stresses and also residual deformation of sheet metal assembling. Numerical predictions performed by Schwenk [2] presented results for a case study where the cooling rate is increased by a factor of two. The contact conduction of DP600 has been determined experimentally to be h_c = 100W/m²K and the emissivity coefficient of radiation is $\varepsilon(T) = 0.2 + 0.5(1 - \exp(900/T))$ [12]. The influence of the distance of the clamping, the clamping force as well as the release time after welding have been studied by many authors [8,1,5,10]. There are some compromise and contradiction on the clamping position on the distortion. Influence of welding speed and penetration depth has been determined experimentally by Lenz [4], for low speeds, there is a full penetration and no out of plane bending distortion but the bucking might occurred since the bending moment is zero [10]. While for very high welding speeds there is no shrinkage [6].

During clamping, the models suppose to be a Z symmetry plane condition, Z-SYMM-mode, on both left side and right side at a distance of 43mm from the weld seam line as shown in Fig.7.5. In order to stabilize the model after welding the Encastre-Mode is used to lock the start point of FZ and the Z-SYMM-Mode at the ended point of laser welding model.
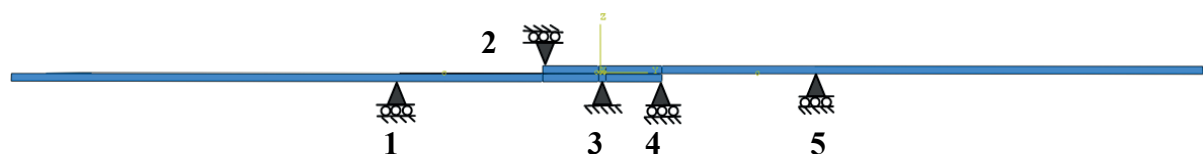
Fig.7. 5   Boundary Condition

The thermal and mechanical analyses are performed in three steps.

- Welding step: 4.3179 seconds for calculating the thermal and mechanical response during welding process. The length of weld bead is 240mm compared to 250mm of the total length of the model. So it starts 5mm from the start edge and end 5mm before the last edge.

- Cooling step: 60 seconds for calculating the mechanical response during cooling process.

- Relaxation step: 440 seconds for calculating the mechanical response after mechanical constrain released.

The laser is moving in the first step called the welding step. The heat loses by convection and radiation is set in the second to third step during thermal simulation which was called the cooling step and the relaxation step. In mechanical simulation the clamping condition are set in the first and second step and relax on the third step. Only the BCs at FZ are maintained to well position the model after relaxation.

7.3.3 Meshing parameter

The model, presented in Fig.7.6, is separated into three zones, the fusion zone *(FZ)*, the heat affected zone *(HAZ)* and the base metal *(BM)*. The hexahedra element shape is used for this simulation. The structured technique is used for the HAZ and the FZ in purpose to assure a constant and small element size inside these zones. On the other hand the sweep technique with advancing front algorithm is used to reduce the number of elements next to the HAZ and the BM. The mesh dimension of the FZ and the HAZ are presented in Tab.7.2.

The total number of elements used is 63480 with 321520 nodes for thermal model and the same elements with only 85876 nodes for mechanical model.

The quadratic interpolation function is used in this thermal simulation and linear interpolation function is used for metallo-mechanical simulation in FEA analysis software ABAQUS. During thermal analysis, the fixed time increment is used due to a constant welding speed, the automatic increment is used for cooling step and relaxation step. But for mechanical analysis, all step use automatic increment. Total CPU time for simulation is 3.64116E5 seconds *(101h)* for thermal analysis and 3.62752E5 *(100h)* for mechanical analysis running on PC 8-Cores 8GB RAM *(only 6 cores processors used)*.
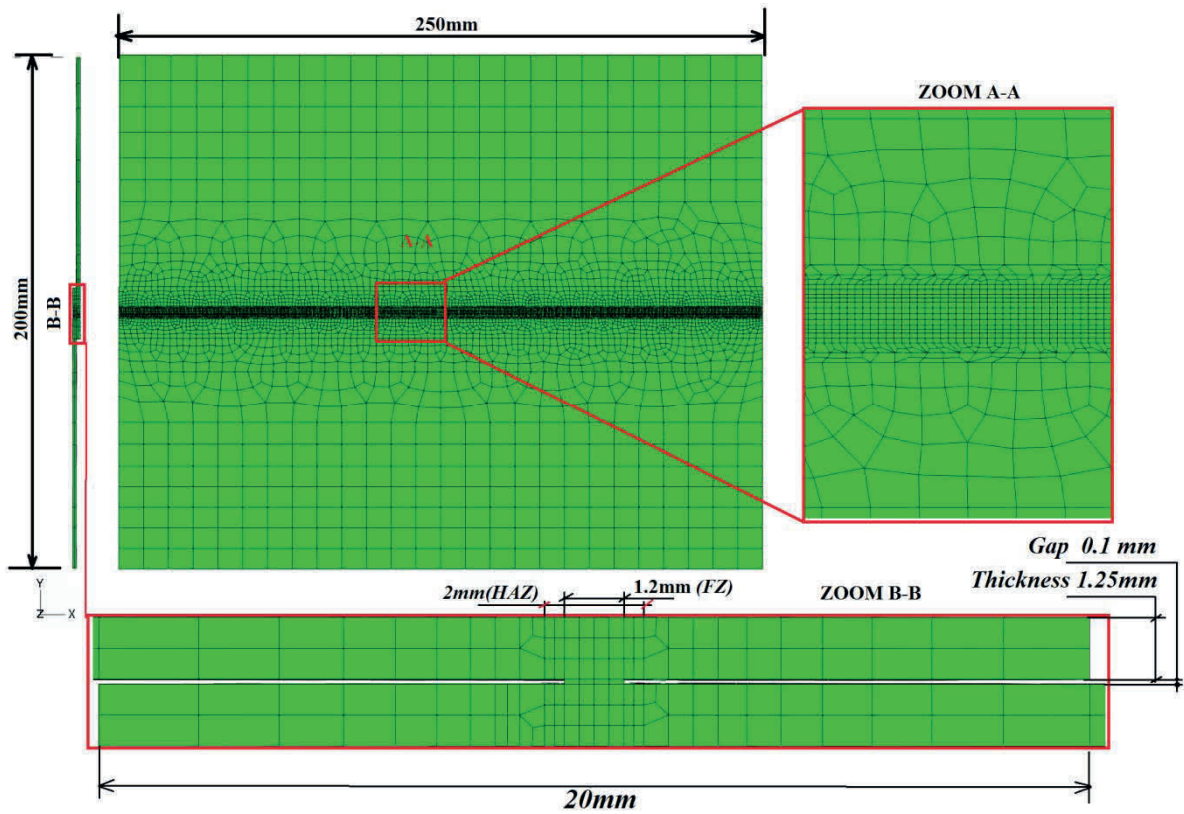
Fig.7. 6   Meshing model

Element length	FZ	HAZ
DX	0.4mm	0.4mm
DY	0.3mm	0.2mm
DZ	0.4166mm	0.4166mm

Tab.7. 2   Mesh size of FZ and HAZ

7.4 RESULTS

7.4.1 Temperature distribution

Fig.7.7 shows the half model of thermal simulation and that of experimental sample. A coherent of dimension of simulated temperature distributed inside the FZ and the weld seam size from experiment was reached.

235
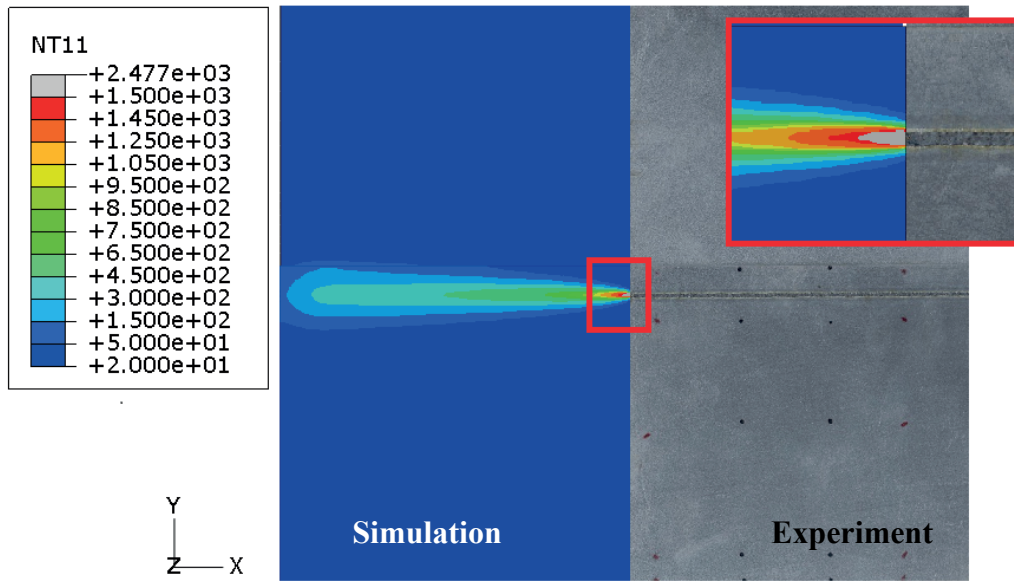
Fig.7. 7　Thermal simulation and experimental of lap joint (^{o}C)

The FZ cross section along the X-Z and Y-Z cutting plan are presented in Fig.7.8. It shown the important variation of temperature along the weld center line plan (X-Z plan) after laser heat source passed and the surrounding heat source temperature (Y-Z plan). These two figures prove that the temperature is heating very fast inside the keyhole and cooling down rapidly afterward.

Fig.7. 8　Temperature distribution in cross section (^{o}C)
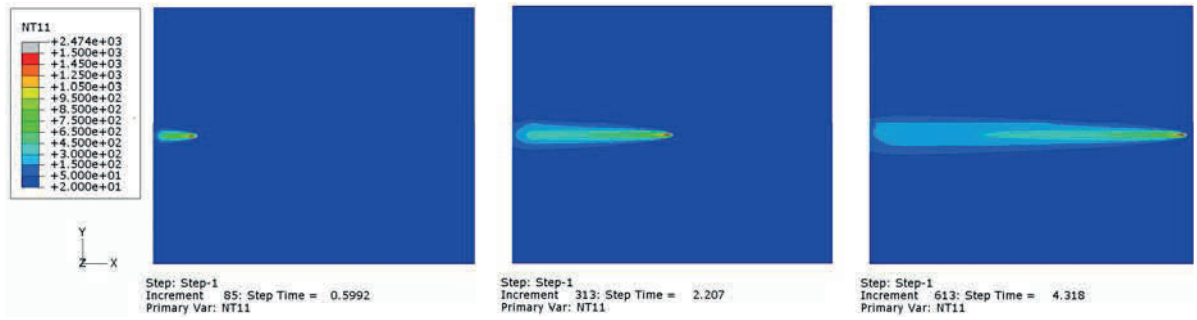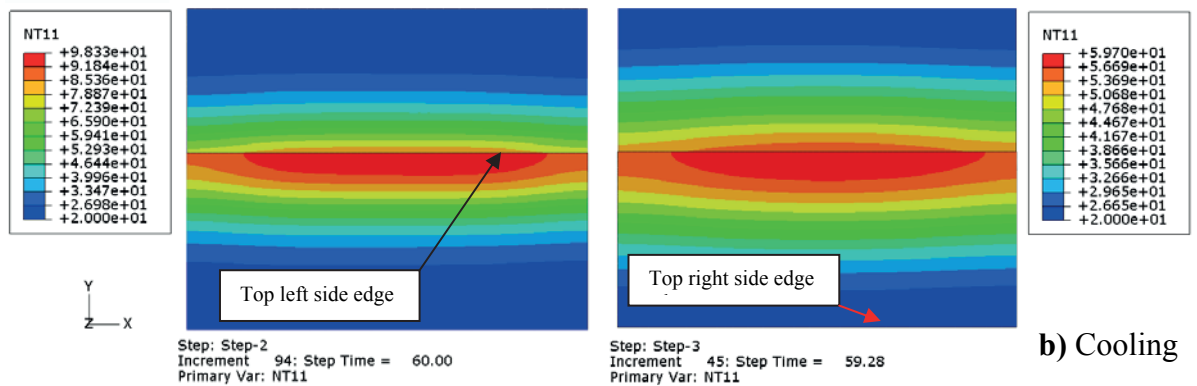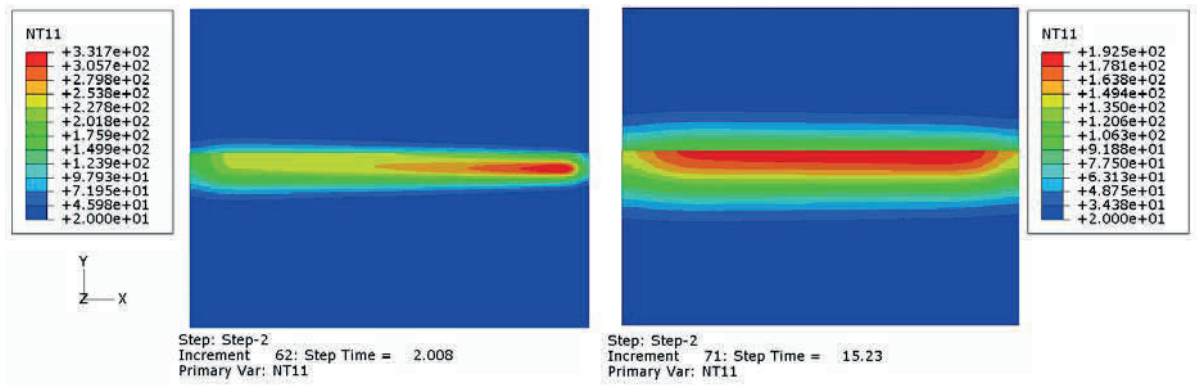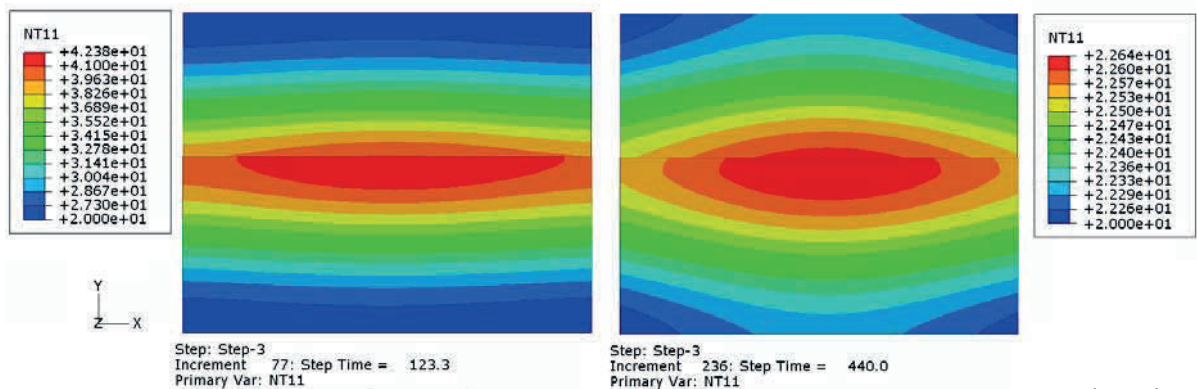
a) Welding

b) Cooling

c) Relaxation

Fig.7. 9   Temperature contours (^{o}C)

Fig.7.9 described the thermal evolution during welding, cooling and relaxation. Due to a higher welding speed of laser welding, the heat dissipation within the model is quite rapid that is the reason why the temperature contour during the welding process confines to a small region around the heat source. The temperature evolution from the beginning to the end of welding cycle indicate that the width of fusion zone is just about 20mm around the heat source within a range of 150°C at the a distance of 10mm from weld seam centerline as indicated in Fig.7.9(a). During cooling cycle the temperature drop sharply from maximum temperature inside the keyhole center to 330°C in just two seconds after end of laser heat, at this instant, the width of fusion zone is still in a limit area *(less than 30mm around the weld seam)* as indicated in Fig.7.9(b). The short distance from weld line center *(in welding direction)* of the top left side edge compared to the top right side edge of the top sheet, the heat dissipation on the top right side is more rapid that the top left side edge *(short distance)* and the finally the heat concentrates to the top left side edge as indicated in Fig.7.9 (b) and Fig.7.9 (c). Inside the relaxation phase the influence of low convection with the surrounding environment the heat lost become less important and it take about 120 seconds to cool the model from 100°C, at the beginning of relaxation, to 40°C and another 320 seconds more for cooling the thermal model from 40°C to 20°C as shown in Fig.7.9 (c).
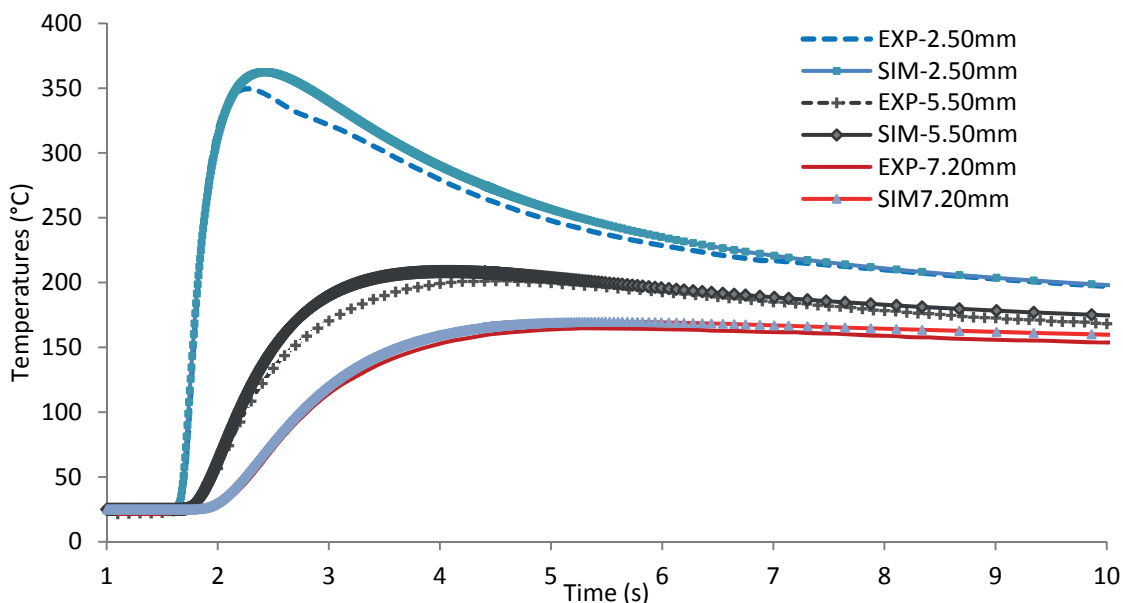
Fig.7. 10　Comparison of temperature at 3 points from simulation and experiment

238

The temperatures evolution curve, described in Fig.7.10, shows the evolution of temperature during welding and cooling cycle at three points A, B and C getting from experimental and numerical analysis. The approach of temperature between the experiment and simulation are reached, the different between the simulations and experimental is less than 10%. The thermal simulation give higher values of maximum temperature compared to the experimental results.

7.4.2 Residual stresses

In most of the welding processes, the longitudinal stresses, *stress in the welding direction*, have maximum influence over distortions and failure of the material. The next significant stresses are the transverse stresses, while the remaining stress components generally have less effect [13].

The residual stresses distributed on the numerical model at the end of relaxation are presented here, the longitudinal residual stresses S11 shows in Fig.7.11, the transverse residual stress S22 shows in Fig.7.13 and finally the shear stress S12 shows in Fig.7.16 respectively.

7.4.2.1 Longitudinal residual stresses S11

The longitudinal residual stresses presented in Fig.7. 11 indicated the maximum tensile stresses inside the HAZ and the FZ. It is surrounded by the tensile residual stresses up to 10mm *(in transverse direction)* from the weld center line and then by the compressive residual stresses next to the tensile residual stresses zone. There are less tensile residual stresses and the start and the end of the weld seam and the magnitude of residual stresses become maximum and commence to reduce at the mid-length of the model, however, the stress level outside the tensile and compressive zone remains considerably low. The cross section of the lap joint shows that the variation of longitudinal residual stresses across the thickness of lap joint was indifferent.

Fig.7. 11   Longitudinal stress S11(Pa)

The residual stresses along the transverse line are also observed by Kong [3]. The numerical and X-ray diffraction analysis had been used here to observe the influence of different welding processes, laser, GTAW, hybrid laser-GTAW and welding parameters on lap joint. He found out that the maximum normal stress components are located at the HAZ and its peak value increase with the decrease in welding speed. The level of residual stress concentration in the welded joint obtained by hybrid laser-GTAW is lower than ones present in the weld joints obtained by either laser welding alone or GTAW. He also notice that, from X-ray diffraction technique increasing the welding speed *(1.2 m/min to 2.4m/min)*, the longitudinal stress at the center of the weld bead changes from compressive state to the tensile one. The maximum residual stress occurs at the top of weld seam because of maximum heat density in this zone which was found in laser welding [11] and the longitudinal residual stresses are proportional to the heat source intensity.

During higher welding speed *(3.4m/min)*, the maximum tensile longitudinal stress occurred inside the HAZ and the FZ as presented in Fig.7.12. It is similar to the studies in literatures [9,3].

240

Fig.7. 12   Longitudinal residual stresses along the transverse line
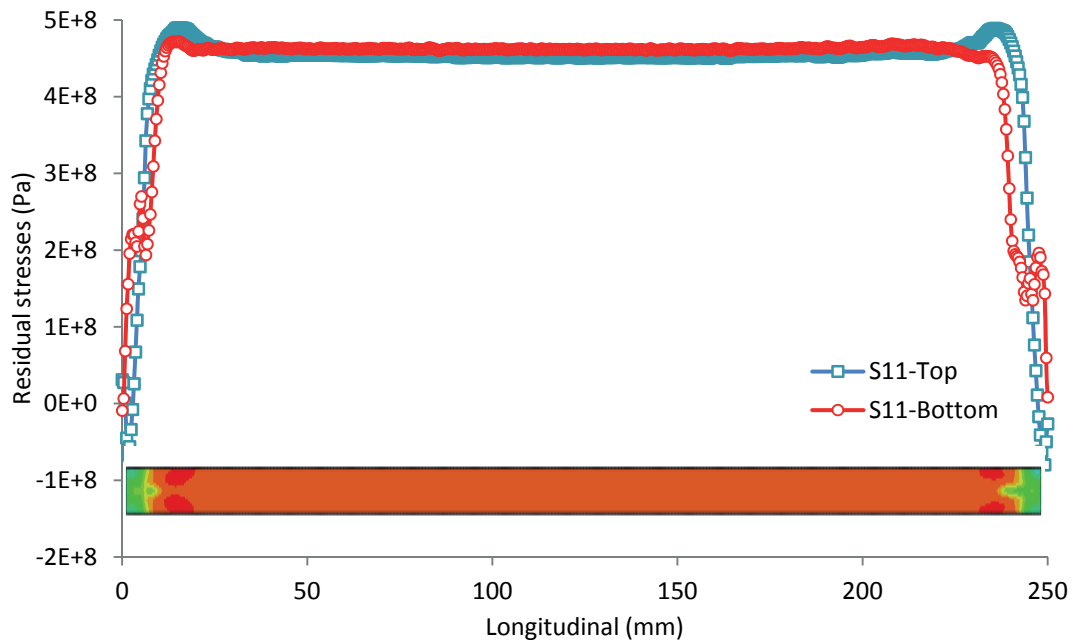
Fig.7. 13   Longitudinal S11 and transverse S22 stresses along the longitudinal line

Fig. 7.13 shows the stress distribution along the longitudinal line situated on the top and bottom surface of the top sheet model. The stress level remains uniform over the entire length of the fusion zone except the start and end of weld bead. The higher welding speed of laser causes a compressive transverse stress on the start and end of the weld bead. The

distributions of the longitudinal residual stress along the top and along the bottom line are similar.

7.4.2.2 Transverse residual stresses S22

Fig.7.14 shows the distribution of transverse residual stresses at the end of relaxation. The observation of transverse residual stresses distributed from the top to the bottom sheet model by the weld seam shows by a cross section in Fig.7.14. The main reason of this distribution is the clamping condition on the two sheet models, as shown in the clamping condition of this chapter, which allows the model to expand free in transverse direction. But the stresses still occur at the moment of transverse displacement direction is out of restrain due to the self restrain inside the material model.

The side effect have more influence on the transverse stresses, one observed the maximum of tensile shear residual stresses and maximum compressive transverse residual stresses take place at the start and end of weld bead.
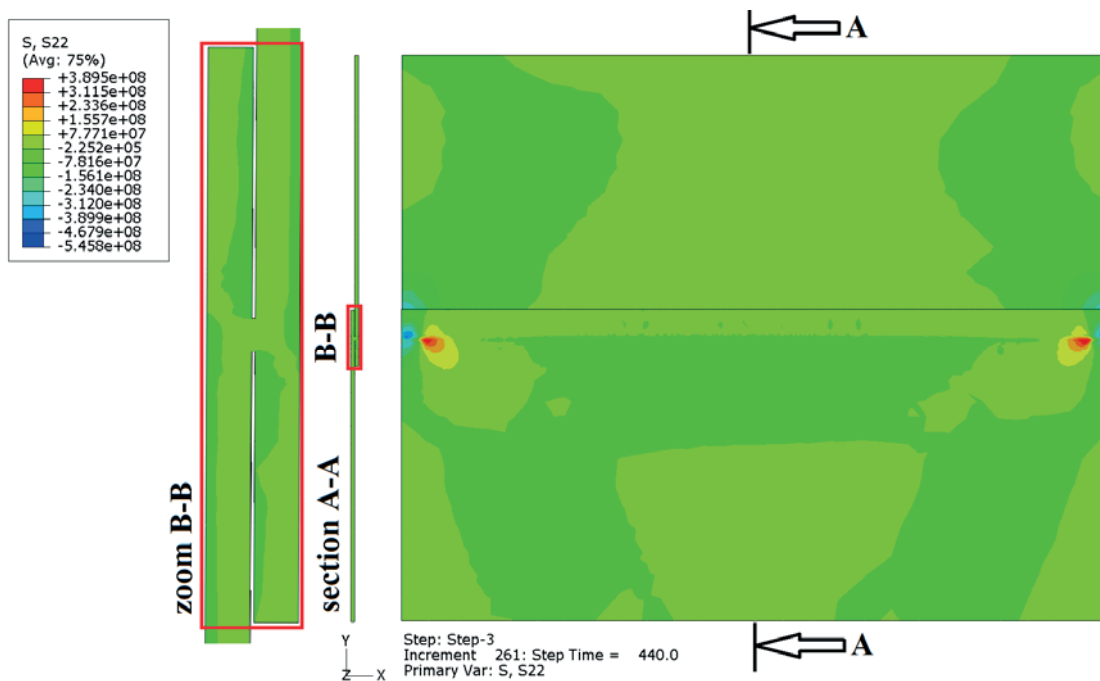
Fig.7. 13   Transverse stress S22 (Pa)
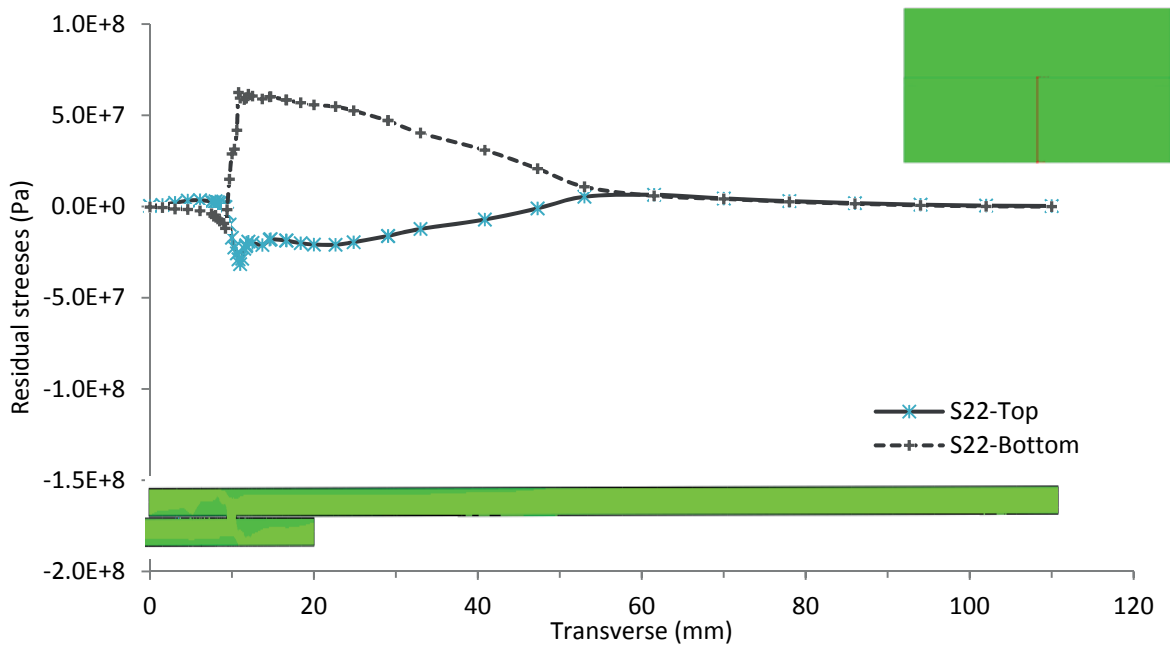
Fig.7. 14   Transverse residual stress along the transverse line

Fig.7.15 presents the transverse residual stresses on top and bottom line of the top sheet model in the transverse direction. On the top line, the compressive transverse residual stress occurred inside the HAZ, FZ and also the zone close to the HAZ. But on the bottom line, the transverse residual stresses became tensile. The weld seam at the interface of the top and bottom sheet plays an important role in the switching from compressive state to tensile state of the transverse stresses on top and bottom surface.
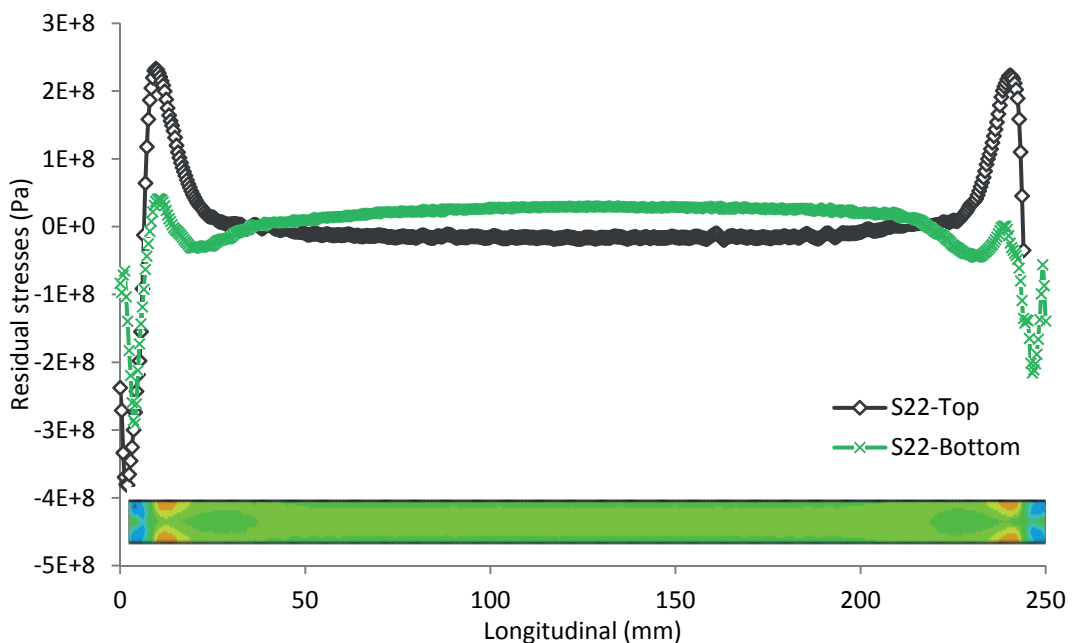
Fig.7. 15   Transverse residual stresses along the longitudinal line

Fig.7.16 shows the transverse residual stresses along the longitudinal line on top and bottom line of the top sheet model.

The transverse residual stresses on the weld seam *(interface between the top and bottom sheet model)* seem to be higher than that of the top surface as express in Fig.7.16. One observes also a higher maximum tensile stresses and maximum compressive stresses on top surface compared to those on the bottom surface at the start and end of weld bead but a slightly difference outside these zones.

7.4.2.3 *Shear stresses S12*

The shear stresses presented in Fig.7.16 is the shear stresses on top view of numerical model at the end of relaxation cycle.
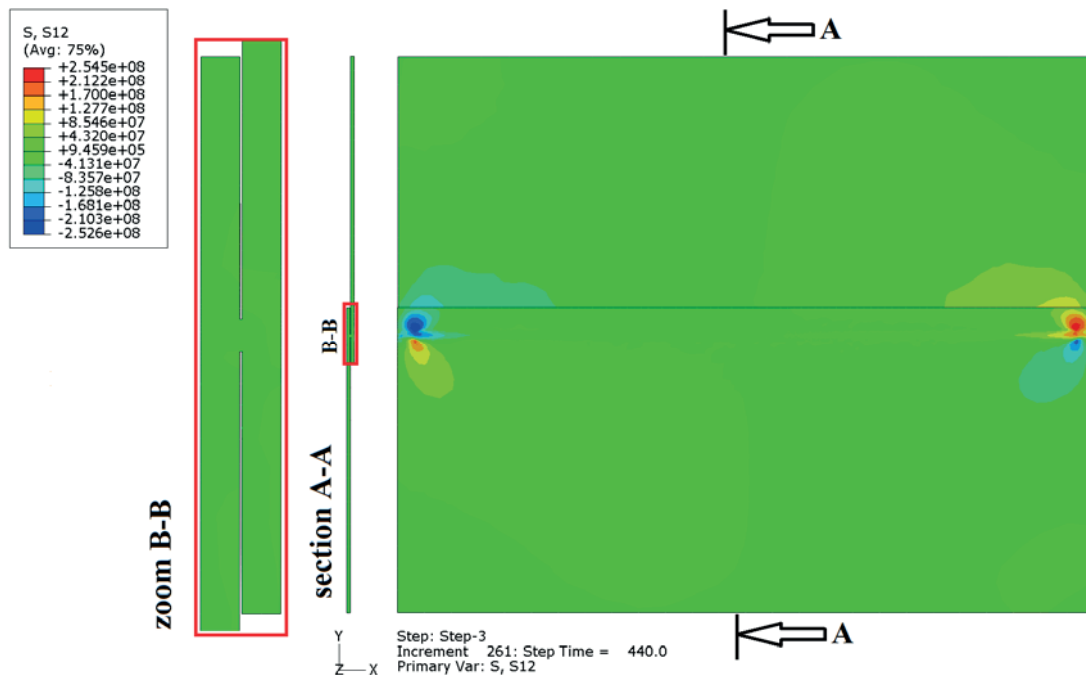
Fig.7. 16   Shear stress S12 (Pa)

The maximum shear stresses occurred only next to the beginning and the end of weld bead. The maximum shear stresses S12 occurred at the start and end of weld bead as shown in Fig.7.17. Otherwise the distribution of shear stresses on top and bottom line of top sheet

model, as shown in Fig.7.17, are similar to the distribution of transverse stresses. The positive shear stress distribute on top surface and negative shear stresses on the bottom line of the top sheet. But the distribution of shear stress seems to be in random in the HAZ and the FZ compared to those of the longitudinal and transverse stresses.
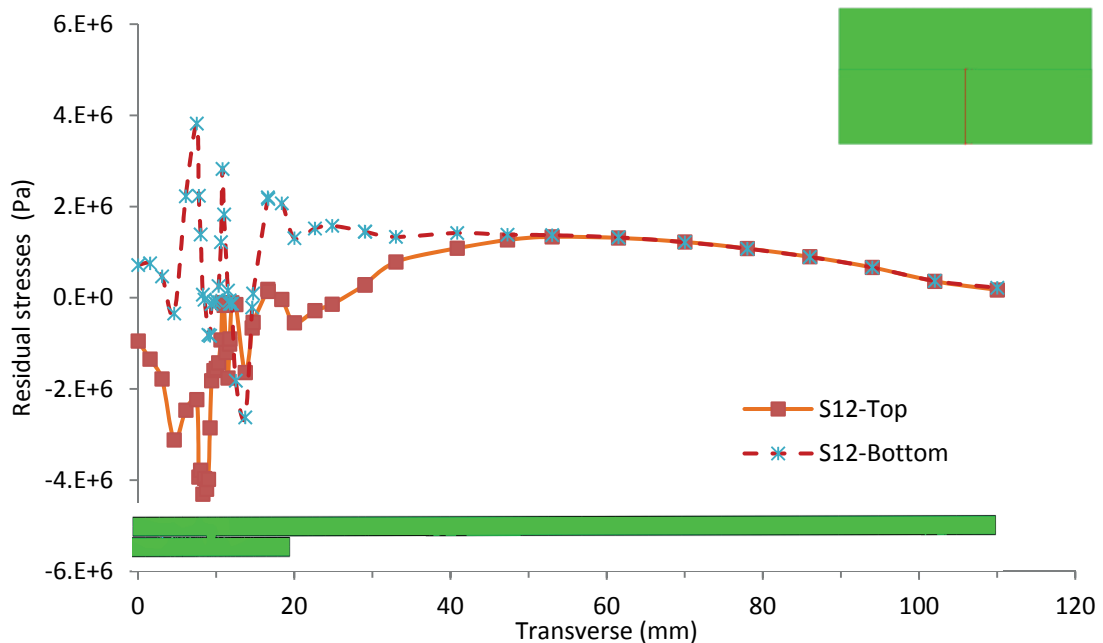
Fig.7. 17   Residual stresses along the longitudinal line

7.4.3   Out of plane displacement (U3)

The out of plan displacement is a result of non-uniform heating and cooling during welding. These mechanisms, also known as angular deformation, result due to the existence of temperature gradient in the through thickness direction [11].

The final out of plane displacement is a balance between the initial imperfection profile and the residual out of plane displacement under effect of welding process. The initial surface profiles play an important role in defining the distortion pattern of the test plates. The initial surface profiles not only affect the maximum displacement level but also affect the distribution pattern of deformation, thereby, given rise to different distorted shapes of the test plates. However, the maximum out of plane displacement values mainly depend upon the heat energy input, the effect of geometric imperfections *(initial deformation)* over these

values is small [11]. The imperfection of sample, caused by preparation of the sample, cutting etc, is around [0.12mm, 0.34mm] measured on two hazardous samples. It is not present in this report because it not affect on the maximum out of plane displacement as mention by Zain [11].

The out off plane displacement U3 measured on the top surface of the sheet metal assisted by the MNT machine are presented in the Fig.7.18. The specimen for measured is presented in Fig.7.18 (a). Three specimens with the same welding condition are prepared for measurement. The two dimensional profiles of specimens are presented in Fig.7.18 (b) for the first sample, Fig.7.18 (c) for the second specimen and Fig.7.18 (d) for the third specimen respectively.

The out of plan displacement U3 patterns getting from these measurements are almost similar. The profile of *specimen-1* is similar to that of the *specimen-2* but different to the profile of *specimen-3*. The amplitude of the out of plane displacement is:

- Specimen-1 [-2.0mm, 2.5mm]   : 4.5mm
- Specimen-2 [-0.25mm, 4.0mm]   : 4.25mm
- Specimen-3 [-0.7mm, 3.0mm]   : 3.7mm

The maximum amplitude of out of plane displacement is about [3.7mm, 4.5mm]. It is about 0.8mm of different between those three models with the same welding condition. Beside the initial imperfection of the specimen others parameters also affect the results of displacement such as the different clamping load, the imprecision of specimen mounted inside the clamping system during welding process and the positioning of specimen on MNT table that doesn't count in this study.
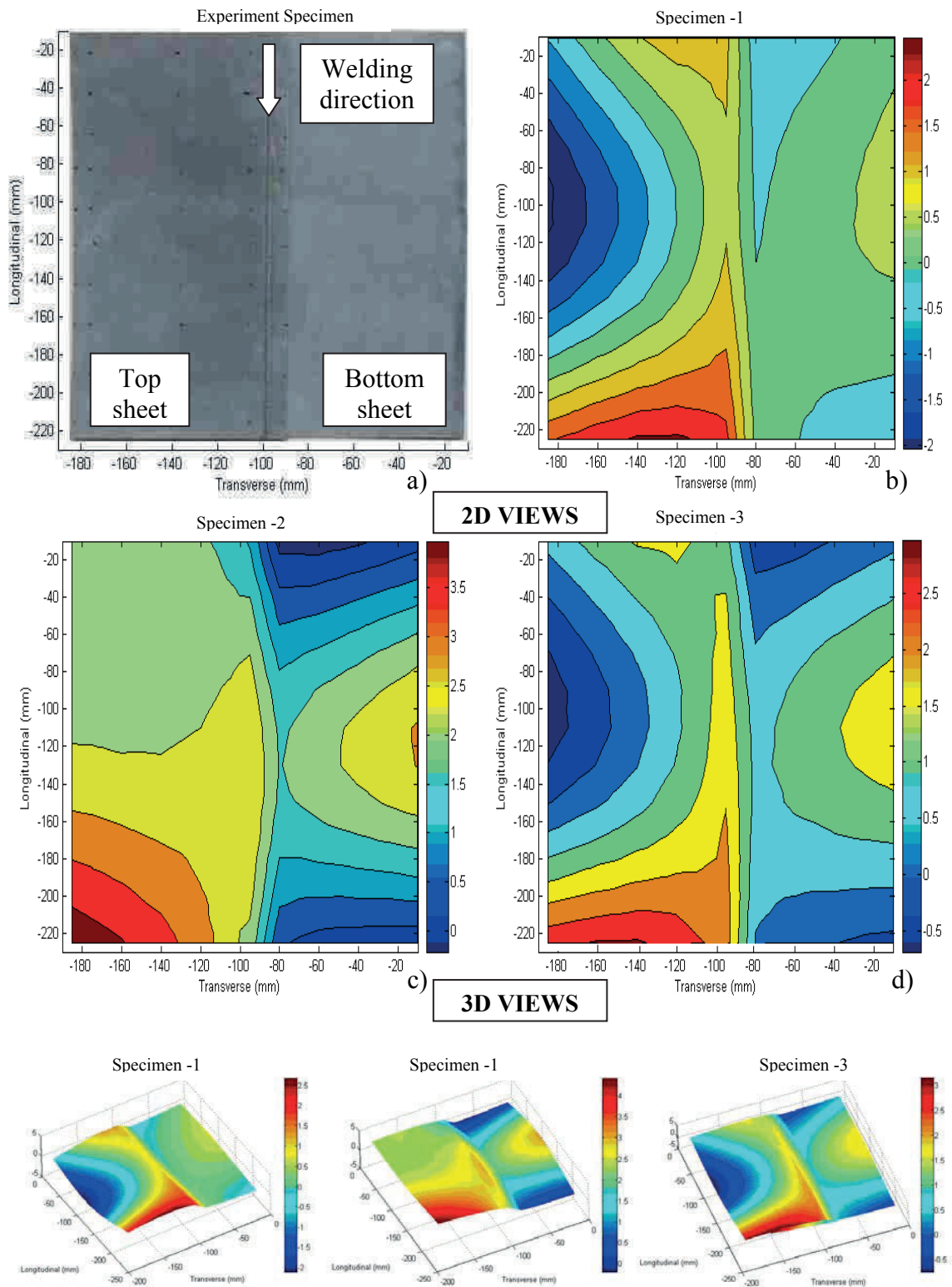
Fig.7. 18   Measured out of plane displacement by MNT Machine (mm)
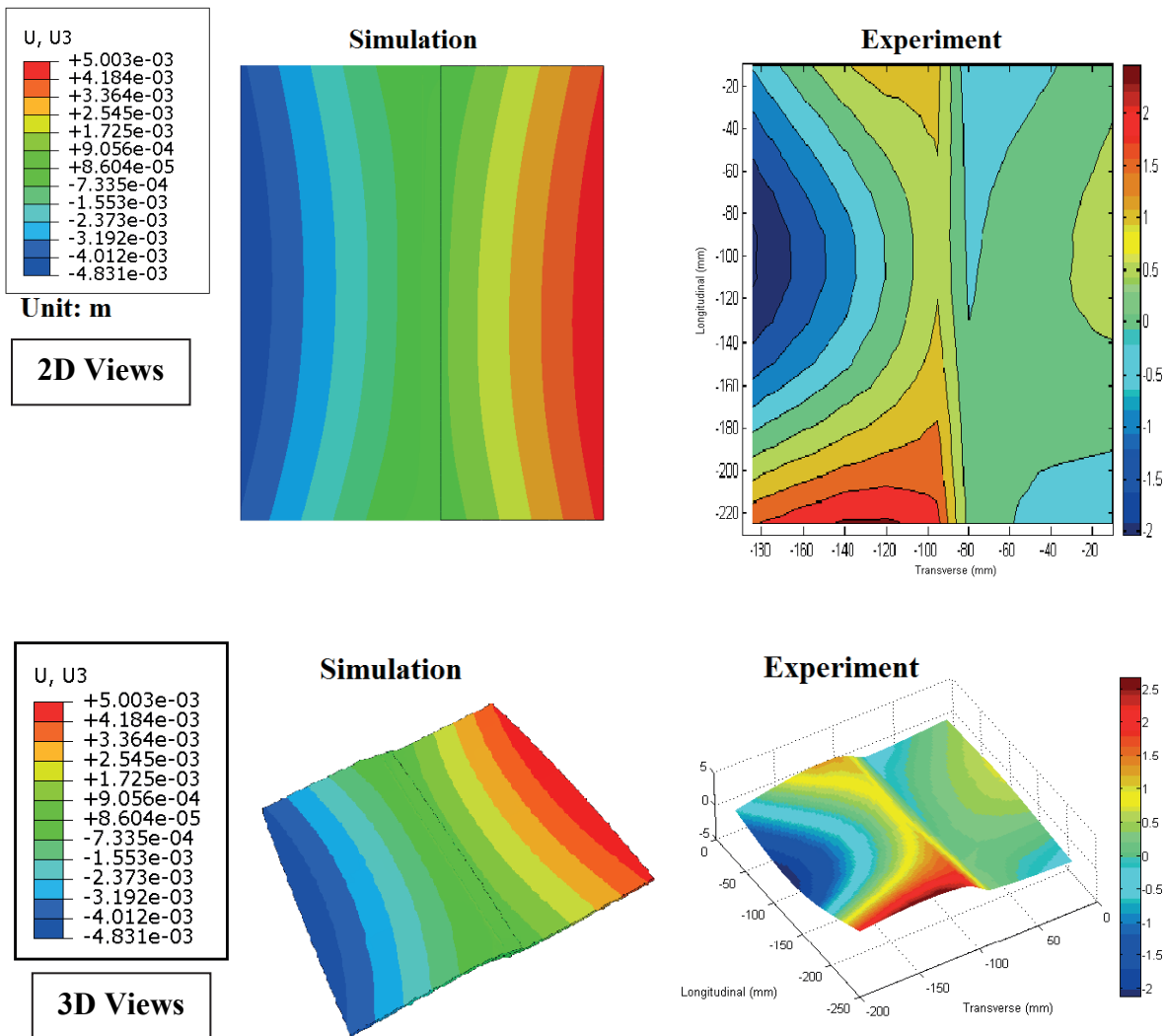
Fig.7. 19   Predicted out of plan displacement U3 (m)

From numerical analysis, the residual out of plan displacement U3 presented in Fig. 7.19 (a). The predicted out of plan displacement profile is almost symmetric to the welded seam and one obtain the maximum and minimum amplitude on each side of the welded line. Its profile is almost similar to that of measurement in Fig. 7.19 (b). The minimum amplitude situated on the middle edge of the top left sheet and the maximum amplitude situated on the middle edge of the bottom right sheet. But some difference are found out between these two approaches such as the predicted amplitude of out of plan displacement is two times higher than that of the experiment, the measured maximum amplitude of out of plan displacement is located at the end of weld seam on top left sheet. The mains source of difference may come

from the different factor that didn't count in this analysis such as the clamping force, the friction coefficient between the clampers and the sheet metal, the meshing parameter and also the numerical models used.

7.5 CONCLUSION

The interaction between numerical analysis and experimental methods was carried out. The evolution of temperature in function of time, the residual stresses and finally the out of plan displacement from experiment give a very good reference of numerical analysis. The conclusion can be obtained as follow:

The temperature profile has been validated by two techniques, first the comparison of weld cross section between the numerical analysis's results and the experimental results and secondly is the comparison of temperature evolution at three points on top surface of the sample. The results show a good agreement between experiment and numerical analysis.

The numerical analysis of out of plan displacements gave the same deformation profile to that of the experiment but its amplitude is two time higher than that of experiment. The measurement of residual stresses by X-rays diffraction is in process, anyways the profile of numerical analysis of residual stresses are similar to that of lap joint of DP600 by GMA welding process with approximate maximum amplitude of longitudinal residual stresses [10] and also the same profile to lap joint of laser/GTAW [3].

Conclusion générale

Cette thèse nous a permis d'étudier l'assemblage par recouvrement de tôles fines d'épaisseur 1,25 mm soudées laser Nd: YAG. Le matériau étudié est un acier dual phase de haute résistance, DP600, utilisé dans la construction automobile. L'objectif étant de valider la soudabilité de cet acier et en particulier sa tenue mécanique, nous avons réalisé cette étude par une approche numérique et expérimentale. L'approche numérique concerne la simulation du procédé laser, l'évaluation de certaines propriétés géométriques du bain fondu, des propriétés microstructurales *(fraction volumique des phases)*, mécaniques *(dureté, traction)* et principalement l'évaluation des contraintes résiduelles. L'approche expérimentale nous a permis à la fois de caractériser le matériau de base et soudé. Les différents paramètres obtenus nous ont permis d'une part d'enrichir notre modèle de simulation et de l'affiner et d'autre part de comparer la robustesse de nos modèles numériques avec ceux de l'expérience.

L'étude expérimentale, présentée dans le troisième chapitre, nous a permis de connaître les effets du procédé de soudage par faisceau laser sur la qualité de la structure soudée et d'acquérir des résultats expérimentaux pour la validation du travail numérique. Cette démarche nous a permis également de construire un support de données expérimentales pour les implémenter dans nos différents modèles numériques. Ce dernier point a été une étape fondamentale de notre travail pour assurer la robustesse des modèles numériques développés. Pour ce faire, nous avons réalisé une étude paramétrique du procédé laser pour comprendre l'influence des paramètres technologiques du laser sur les qualités aussi bien géométriques que dimensionnelles des soudures. L'analyse des cordons a permis de montrer que les paramètres déterminants pour la faisabilité du procédé laser de l'acier étudié sont la puissance du faisceau, la vitesse de soudage et la position du point focale. D'un point de vue géométrique, les résultats ont montré que la vitesse du soudage et la distance focale sont les facteurs qui influencent principalement la largeur de la zone soudée. La puissance du laser

présente une contribution moindre sur la largeur de la zone de fusion. Elle influence cependant la profondeur de pénétration. D'ailleurs une optimisation de la puissance et de la position du point focal a permis d'obtenir une profondeur de pénétration et une largeur de la zone de fusion de qualité.

A l'issue de cette phase paramétrique, un domaine de soudabilité a été déterminé pour l'assemblage par faisceau laser Nd-YAG, des plaques en acier DP600 de 1.25 mm d'épaisseur. La puissance et la vitesse minimales de soudage ont été respectivement fixées à 3,5 kW et 3,4 m/min. Le balayage de l'ensemble des paramètres technologiques, nous a permis de réaliser une analyse fine des conséquences thermique, métallurgique et mécanique du soudage par faisceau laser sur des cordons de soudure obtenue par des paramètres appartenant au domaine de soudabilité.

L'approche métallurgique nous a permis de considérer les transformations microstructurales dans les pièces soudées. Elle a révélé, qu'après le soudage par faisceau laser, la structure à gros grain du métal de base constitué de ferrite (80 %) et de martensite (20%) est transformée en une structure martensitique dominante au niveau de la zone fondue. Au niveau de la zone affectée thermiquement, nous avons remarqué une diminution de la taille de la phase primaire. Cette zone a été assimilée à une zone de transition avec la présence de ferrite du métal de base et une fraction plus importante de martensite formée par l'opération de soudage.

La seconde partie de l'analyse a été consacrée à la détermination des caractéristiques mécaniques du métal de base et de la zone de fusion. Les résultats ont montré une augmentation de la dureté dans la zone fondue. Les observations ont montré l'absence d'une zone de revenu dans la ZAT. Les mesures de micro-dureté réalisées dans la profondeur de la zone de fusion ont montré que la puissance joue un rôle conséquent sur les résultats. Pour des puissances supérieures à 3 kW, la dureté est relativement stable sur l'ensemble de la profondeur. Pour des puissances inférieures, les résultats ont montré des gradients avec une chute conséquente à partir de 1,7 mm de profondeur. D'un point de vue des essais mécaniques, une influence des paramètres du laser a été également observée. Une diminution

de l'allongement maximal dans l'assemblage par faisceau laser a été observée de façon générale et de façon spécifique, une diminution de la puissance conduit à une diminution de l'allongement. Inversement, la résistance mécanique au cisaillement est maximale lorsque la puissance du faisceau laser est augmentée.

La dernière partie de l'analyse expérimentale a concerné la mise en œuvre d'une chaîne d'acquisition de la température par des thermocouples implantés en différents points des pièces soudées et à proximité du cordon de soudure. L'enregistrement de l'évolution de la température en fonction du temps au cours du soudage par faisceau laser ont montré que ce procédé génère d'importants gradients thermiques temporel et spatial qui sont responsables de l'apparition des contraintes résiduelles dans les pièces soudées.

Dans la partie analyse numérique, nous avons développé et étudié plusieurs modèles numériques : un modèle thermo- mécanique, un modèle thermo-métallurgique et un modèle thermo-métallo-mécanique. Les deux premiers modèles nous ont permis d'une part d'évaluer les différentes propriétés recherchées et d'autres part d'utiliser les résultats issus de ces modèles pour réaliser le dernier modèle plus complet : thermo-métallo- mécanique. Ces trois modèles numériques ont été développés sur un code d'éléments finis ABAQUS. Chaque modèle nous a permis d'appréhender l'état mécanique et métallurgique en simulant la distribution spatio-temporelle de la température *(modèle thermique)*, les transformations de phase et les phénomènes de dilatations *(modèle métallurgique)*. Ces deux modèles nous ont permis de déterminer l'état mécanique dans l'assemblage en particulier l'état résiduel après soudage. D'un point de vue méthodologie, nous avons ensuite couplé les deux modèles thermique et métallurgique pour appréhender au mieux l'état mécanique final par la prise en compte simultanée de la thermique et de la métallurgie inhérents au procédés de soudage. Outre cet objectif, cette démarche nous a permis d'une part de mieux comprendre et d'optimiser les paramètres influents du procédé laser et les conséquences sur le cordon de soudure.

Concernant la démarche thermomécanique, nous avons développé dans un premier temps deux modèles découplés : thermique et mécanique. Concernant le modèle thermique,

l'étude numérique s'est appuyée sur la résolution de l'équation transfert de chaleur *(Equation de Fourier)*. Nous avons utilisé l'équation de transfert thermique en mode conduction entre la source de chaleur et le métal pendant la phase de chauffage lors de l'opération de soudage. Cette équation a été également utilisée pour résoudre l'équation de transfert de chaleur en mode convection et radiation pour prendre en compte les phénomènes de dissipation entre le métal et l'environnement extérieur pendant la phase de refroidissement. L'effet de la convection sur les résultats a été étudié en considérant une faible, moyenne et forte convection. Concernant le modèle mécanique, nous avons utilisé le modèle élastoplastique classique.

Pour optimiser les résultats de ce modèle thermomécanique, la simulation prend en compte la non-linéarité introduite par le chargement dépendant du temps et de l'espace et par les caractéristiques thermo-physiques indépendantes de la température et celles qui varient en fonction de la température. Il présente la particularité de prendre en considération l'apport énergétique du keyhole. Le chargement est représenté par une source de chaleur mobile : une source volumique de forme conique avec une distribution gaussienne modélise le keyhole. La spécification géométrique et analytique est définie à partir des caractéristiques du faisceau laser utilisé et des paramètres technologiques du soudage déterminés par l'étude expérimentale. Les résultats du modèle thermique sont présentés sous forme d'isothermes de refroidissement à chaque instant du traitement décrivant l'évolution de la température en fonction du temps dès le début du soudage jusqu'au refroidissement final des pièces. Ces résultats ont permis de suivre l'évolution du gradient thermique au cours de l'assemblage. Celui-ci est très important durant la phase d'application de la source laser, vue l'importance de la densité de puissance introduite, mais beaucoup plus faible au cours de la phase de refroidissement. Ce gradient thermique va être responsable de l'apparition, au cours du soudage, d'un gradient de déformation qui peut générer des contraintes résiduelles. Les résultats thermiques ont montré que les propriétés thermo-physiques ont une faible influence sur le résultat thermique avec une variation de moins de 10%. Le ratio R/DX doit être supérieur à deux afin d'obtenir une précision maximale pour la simulation thermique. Par

contre les autres dimensions de maillage, DY et DZ, ont peu d'influence sur les résultats finaux. Les modes de convection ont peu d'influence sur la température maximale et la vitesse de refroidissement après le passage du faisceau laser. L'utilisation de pics de températures différents utilisés dans la simulation numérique ne semble pas influencer l'évolution des températures en dehors de la zone affectée thermiquement. Le modèle thermomécanique nous a permis d'avoir les résultats des contraintes résiduelles. Celles-ci ont été optimisées. L'optimisation a montré que la variation des propriétés thermo-physiques, les différents modes de convection et la différence des températures présentent peu d'influence sur la valeur des contraintes résiduelles.

Le modèle thermo-métallurgique a été réalisé par couplage du modèle thermique *(décrit précédemment)* et par la réalisation d'un modèle numérique métallurgique. Dans ce dernier cas, l'étude numérique s'est appuyée sur l'intégration des modèles de Waeckel et de Koistinen-Marburger. Le modèle de Waeckel nous a permis de simuler et de prendre en compte le phénomène d'austénitisation pendant le chauffage. Le modèle de Koistinen-Marburger permet de tenir compte la fraction volumique de martensite générée pendant le refroidissement et donc de prendre en compte les phénomènes de transformation de phases lors du soudage. Nous avons également implémenté un modèle nous permettant d'obtenir les valeurs de micro-dureté à partir de la loi de combinaison linéaire de la dureté de chaque phase. Les propriétés mécaniques comme la limite élastique et la résistance maximale à la traction ont été également obtenues par l'introduction d'un modèle mécanique basée sur un modèle permettant de convertir la valeur de la résistance mécanique à partir de la valeur de dureté.

A l'issue du couplage thermique et métallurgique, les résultats de la simulation nous ont permis d'obtenir les fractions volumiques de la ferrite, de l'austénite et de la martensite. Nous avons pu également avoir des caractérisations mécaniques comme la dureté et ainsi que les propriétés en traction du joint de soudure et ceux du métal de base. Les résultats issus de cette simulation thermo-métallurgique ont montré que la principale phase présente dans la zone de fusion du soudage laser est la martensite. Ce résultat numérique a été validé

par microscope optique et microscopie électronique à balayage. Cette observation a également été validée par les valeurs de micro-dureté élevée dans la zone soudée (400 HVN). La comparaison des résultats numériques et expérimentaux confirment la concordance et la robustesse de la simulation. La simulation nous a permis également d'obtenir les valeurs de la résistance de traction dans le métal de base, les zones soudées et affectées thermiquement.

Enfin, dans la dernière partie de simulation, nous avons réalisé le couplage thermo-métallo-mécanique. Les résultats obtenus dans la partie précédente, ont été implémentés dans différents modèles mécaniques : le modèle mécanique classique et le modèle mécanique avec prise en compte de la déformation liée aux effets de dilatations. Cet effet a été intégré à travers le coefficient de dilatation thermique des phases ferritiques et martensitiques et des fractions volumiques obtenues à partir du modèle thermo-métallurgique. Les résultats ont montré que la répartition des contraintes résiduelles dans la zone de fusion et dans la zone affectée thermiquement sous l'effet de la déformation thermo-métallurgique donne des valeurs supérieures à celles estimées par le modèle élastoplastique classique. Il semblerait que la déformation thermo-métallurgique a moins d'influence sur le modèle élastoplastique concernant le soudage laser.

Pour valider la robustesse de notre modèle, la comparaison entre les résultats expérimentaux et numériques a été réalisée.

- Le profil de température a été validé. Les courbes d'évolution de la température en fonction du temps réalisées expérimentalement à l'aide de thermocouples sont identiques à celles obtenues par l'analyse numérique.

- D'un point de vue géométrique, les dimensions du bain fondu (largeur, profondeur, section transversale) sont similaires.

- Les observations micrographiques et métallurgiques concordent sur les phases en présence en particulier sur une fraction de martensite majoritaire dans la zone de fusion.

- Les micro-duretés mesurées à la fois dans le métal de base, dans la zone affectée thermiquement et de fusion concordent avec celles prédites par l'analyse numérique.

- Les déplacements hors plan mesurés expérimentalement et obtenus numériquement présentent des évolutions similaires. Néanmoins l'analyse numérique donne des amplitudes plus élevées que celles obtenues expérimentalement.

- Enfin, le profil de l'analyse numérique des contraintes résiduelles a été comparé à l'expérience fournie par la littérature. La comparaison avec nos résultats numériques a montré des évolutions et des valeurs proches de celles obtenues expérimentalement dans le cas des joints assemblés dans le cas d'un recouvrement des tôles d'acier de DP600 par d'autres procédés de soudage.

En résumé, la majorité des résultats expérimentaux et numériques concordent. Une analyse expérimentale plus fine des contraintes résiduelles seraient appropriées.

Perspectives pour la prochaine recherche

A l'issue de ce travail, de nombreuses questions se lèvent et qui peuvent être des orientations pour les travaux à suivre. Ils peuvent être classés en deux catégories:

Caractérisation thermomécanique

L'essai de traction a été effectué sur l'acier DP600 à température ambiante dans le but de caractériser ses propriétés mécaniques. Ainsi, une campagne d'expérimentation à différentes températures (400°C à 800°C) doit être envisagée. En effet, les propriétés mécaniques dépendantes des phases dues au chauffage et au refroidissement rapide inhérentes au soudage laser doivent être prises en compte dans l'analyse numérique.

Analyse numérique du soudage laser Nd: YAG

Mettre en œuvre la plasticité induite par la transformation (TRIP) pour le modèle mécanique. Sous l'influence de ce paramètre, les contraintes résiduelles prédites de joint soudé est inférieure à celui du modèle sans effet TRIP. Cette prise en compte nécessite un ensemble de données lourdes sur les propriétés mécaniques en fonction des phases. Donc une campagne de caractérisation de l'expérience est nécessaire.

Prendre en compte l'influence du facteur de forme du cordon de soudure sur les contraintes résiduelles. Cette idée est basée sur l'effet de concentration de contraintes sur les discontinuités géométriques.

L'état de serrage doit être analysé afin d'optimiser la distorsion du modèle sans oublier l'effet de différents modèles mécaniques et le maillage technique.

General Conclusion

This thesis has allowed us to study the assembly by coating thin sheet of thickness 1.25 mm welded Nd: YAG laser. The material studied is a dual phase high strength steel, DP600, used in the automotive industry. The aim is to validate the weldability of the steel and in particular its mechanical strength, we conducted this study with a numerical and experimental approach. The numerical approach for the simulation of laser process, the evaluation of some geometrical properties of the melt, the microstructural properties *(volume fraction of phases)*, mechanical *(hardness, tensile strength)* and mainly the evaluation of residual stresses. The experimental approach allowed us to characterize both the base material and weld material. The different parameters obtained allowed us to both enrich our simulation model and refine it and secondly to compare the robustness of our numerical models with those of the experiment.

The experimental study presented in the third chapter, we were able to know the effects of the laser welding parameters on the quality of the welded structure and acquire experimental results for the validation of numerical results. This has also allowed us to build a support experimental data for implementing our various numerical models. This last point has been a fundamental part of our work to ensure the robustness of the developed numerical models. To do this, we conducted a parametric study of laser process to understand the influence of technological parameters on the quality of welded joint as well as the geometric. The analysis of the weld bead has shown that determining the feasibility of laser process parameters are the study of the laser beam power, the welding speed and the position of focal point. From a geometrical point of view, the results showed that the welding speed and focal length are the factors that mainly affect the width of the weld zone. The laser power has a lower contribution to the width of the melting zone. However, it influences the penetration depth. So optimizing the power and position of the focal point allow to qualify the penetration depth, a width of the melting zone.

At the end of the parametric phase, field weldability has been determined for the assembly by Nd-YAG laser beam, steel plates DP600 1.25 mm thick. The power and the minimum welding speed have been fixed respectively 3.5 kW and 3.4 m/min. The observation of all technological parameters, allowed us to make a detailed analysis of thermal, metallurgical and mechanical effects of laser welding on welded structure obtained by parameters belonging to weldability.

Metallurgical approach allowed us to consider the microstructural changes in the welded parts. It showed that after the laser beam welding, the large grain structure of the base metal consisting of ferrite (80%) and martensite (20%) is converted into a predominantly martensite structure at the weld bead *(FZ)*. At the heat affected zone *(HAZ)*, we noticed a decrease in the size of the primary phase. This area was considered to be a transition zone with the presence of ferrite of the base metal and a higher fraction of martensite formed by the welding operation.

The second part of the analysis was devoted to the determination of the mechanical properties of the base metal and the fusion zone. The results showed an increase in hardness in the melted zone. Observations have shown the absence of a softening zone in the HAZ. The micro-hardness measurements made in the depth of the fusion zone showed that power plays a relevant role in its results. For more than 3 kW, the hardness is relatively stable over the entire depth. For lower powers, the results showed gradients with a consequent fall from 1.7 mm deep. From a viewpoint of the mechanical tests, the influence of laser parameters was also observed. A decrease in the maximum elongation in the assembly by laser beam was observed in general and specifically, a reduction in the power leads to a decrease in elongation. Conversely, the shear strength is maximized when the laser beam power is increased.

The last part of the experimental analysis concerned the implementation of an acquisition channel temperature by thermocouples installed at different points of the welded parts and near the weld. The recording of the change in temperature as a function of time during the laser welding showed that this process generates large temporal and spatial

temperature gradients are responsible for the appearance of residual stresses in the welded parts.

In the numerical analysis part, we have developed and studied several numerical models: a thermo-mechanical model, a thermo-metallurgical model and metallo-thermo-mechanical model. The first two models have allowed us to both evaluate various desired properties and on the other hand to use the results from these models to achieve the latter more complete model: metallo-thermo-mechanics. These three numerical models have been developed on a finite element code of ABAQUS. Each model has allowed us to understand the mechanical and metallurgical state by simulating the spatio-temporal distribution of temperature *(thermal model)*, phase transformations and the phenomena of expansion *(metallurgical model)*. Both models have allowed us to determine the mechanical condition in the assembly in particular the residual state after welding. From a methodological point of view, we then coupled both thermal and metallurgical models for better assessment of the final mechanical condition by simultaneously taking into account the thermal and metallurgical inherent in welding processes. Besides this objective, this approach has enabled us to both better understand and optimize the important parameters of the laser process and consequences of the welding parameters.

On the process in the thermomechanical model, we developed initially two decoupled models: thermal and mechanical. On the thermal model, the numerical study is based on solving the heat transfer equation *(Equation Fourier)*. We used equation conduction heat transfer mode between the heat source and the metal during the welding phase during the welding operation. This equation was also used to solve the equation of heat transfer in convection and radiation to take into account the phenomena of dissipation between the metal and the external environment during the cooling phase. The effect of convection on the results was studied by considering a low, medium and strong convection. On the mechanical model, we used the classical elastoplastic model.

To optimize the results of the thermomechanical model, the simulation takes into account the non-linearity introduced by the loading time dependent and space and

independent thermo-physical characteristics of the temperature and those which vary depending on the temperature. A keyhole mode of laser welding is represented by a mobile heat source *(conical volume source with a Gaussian distribution models)*. The geometric and analytical specification is defined based on the characteristics of the laser beam used and technological welding parameters determined by the experimental study. The results of the thermal model are described by the evolution of the temperature over time from the start of welding process to the end of cooling cycle. These results were used to monitor the temperature gradient in the assembled model. This thermal gradient will be responsible for the appearance of strain gradient that can generate residual stresses during welding. The thermal results showed that the thermo-physical properties have a small influence on the thermal output with a variation less than 10%. The R/DX ratio must be greater than two to obtain maximum accuracy for thermal simulation. Anyways other mesh sizes, DY and DZ, have little influence on the final results. Convection modes have little influence on the maximum temperature and the cooling rate after the passage of the laser beam. The use of different peak temperatures used in the numerical simulation does not seem to influence the evolution of temperatures outside the heat affected zone. The thermomechanical model allows having the results of residual stresses. These have been optimized. Optimization showed that the variation of thermo-physical properties, different modes of convection and the difference in temperature have little influence on the value of the residual stresses.

The thermo-metallurgical model was built by coupling the thermal model *(described above)* and by carrying out a metallurgical numerical model. In the latter case, the numerical study is based on the integration of models Waeckel and Koistinen-Marburger. Waeckel model allowed us to simulate and to take into account the phenomenon of austenitization during heating. Koistinen-Marburger model takes into account the volume fraction of martensite generated during cooling and therefore to take into account the phenomena of phase transformations during laser welding. We also implemented a model that allows us to obtain the values of micro-hardness from the law of linear combination of the hardness of each phase. Mechanical properties such as yield strength and maximum tensile strength was

also obtained by the introduction of a model based on a mechanical model to convert the value of the mechanical strength from the hardness value.

At the end of metallurgical and thermal coupling, the simulation results have allowed us to obtain the volume fractions of ferrite, austenite and martensite. We could also evaluated the mechanical characterizations as well as the hardness and the tensile properties of the weld bead and those of the base metal. The results of the simulation by using thermo-metallurgical model showed that the main phase present in the weld bead of the laser welding is martensite. This numerical result was validated by optical microscope and scanning electron microscopy. This observation was also confirmed by the values of micro-hardness higher in the weld zone *(400 HVN)*. Comparison of numerical and experimental results confirm the consistency and robustness of the simulation. The simulation also allowed us to obtain the values of tensile strength in the base metal, welded and heat affected zones.

Finally, in the last part of the simulation, we have achieved the metallo-thermo-mechanical coupling. The results obtained in the previous section have been implemented in various mechanical models: the classical mechanics model and the mechanical model taking into account the deformation due to the effects of metallurgical expansion. This effect has been built through the coefficient of thermal expansion of ferritic and martensitic and volume fractions obtained from the thermo-metallurgical model. The results showed that the distribution of residual stresses in the fusion zone and the heat affected as a result of the deformation thermo-metallurgical gives higher than those estimated by the classical elastoplastic model values. It seems that the thermo-metallurgical strain has less influence on the elastoplastic model for laser welding.

To validate the robustness of our model, the comparison between experimental and numerical results was performed:

• The temperature profile was validated. The evolution curves of temperature versus time experiment performed using thermocouples are identical to those obtained by the numerical analysis.

• From a geometrical point of view, the size of the melt (width, depth, cross-section) are similar.

• The micrographic metallurgical observations are consistent and the phases present in a particular fraction of martensite prevails in the melting zone.

• The micro-hardness values in both the base metal and in the heat affected zone melting are consistent with those predicted by the numerical analysis.

• The out of plan measured experimentally and numerically obtained displacement have similar shape. However the numerical analysis gives higher amplitudes than those obtained experimentally.

• Finally, the profile of the numerical analysis of residual stress was compared to the experience provided by the literature. The comparison with our numerical results showed trends and values close to those obtained experimentally in the case of assembled in the case of recovery of DP600 steel sheets by other welding processes joints.

In summary, the majority of experimental and numerical results are consistent. A more detailed experimental analysis of residual stresses would be appropriate.

Perspectives for future research

Following this work, many questions arise and that may be guidelines for future work to follow. They can be classified into two categories:

Thermomechanical characterization

The tensile test was performed on the DP600 steel at room temperature in order to characterize the mechanical properties. Thus, a campaign of experimentation at different temperatures *(400°C to 800°C)* should be considered. Indeed, dependent mechanical properties of the phases due to the inherent heating and rapid cooling laser welding must be taken into account in the numerical analysis.

Numerical analysis of laser welding Nd: YAG

Implement the transformation induced plasticity (TRIP) for the mechanical model. Under the influence of this parameter, the residual stresses predicted weld is lower than the model without TRIP effect. This requires taking into account a set of heavy data on the mechanical properties according to the phases. So a characterization campaign experience is required.

Consider the influence of the shape factor of the FZ in the analysis of the formation of the residual stresses. This idea is based on the effect of stress concentration on geometric discontinuities.

The clamping state must be analyzed to optimize the distortion model without forgetting the effect of different mechanical models and technical mesh.

REFERENCES

[1] J.X. Zhang C. Liu. Numerical simulation of transient welding angular distortion with external restraints. Science and Technology of Welding and Joining, 14(1):26–31, 2009.

[2] K. Dilger V. Michailov C. Schwenk, M. Rethmeier. Schweißsimulation im fahrzeugbau - möglichkeiten, grenzen und herausforderungen. Technical report, DVS Report, Nr. 237, pp. 353, 2005.

[3] Fanrong Kong and Radovan Kovacevic. 3d finite element modeling of the thermally induced residual stress in the hybrid laser/arc welding of lap joint. Journal of Materials Processing Technology, In Press, Accepted Manuscript:–, 2010.

[4] B. Lenz. Finite Elemente-Modellierung des Laserstrahlschweißens für den Einsatz in der Fertigungsplanung. PhD thesis, TU München, 2001.

[5] M. Siddique M. Abid. Numerical simulation of the effect of constraints on welding deformations and residual stresses in a pipe-flange joint. Modelling Simul. Mater. Sci. Eng, 13:919–933, 2005.

[6] M.J. PAiner P.E. Stafford M.A. Wahab, M.S. Alam. Experimental and numerical simulation of restraining forces in gas metal arc welded joints. Welding Journal, 85(2):35–43, 2006.

[7] NI. Measurement strain with strain gages. Tutorial, National Instruments INC, www.ni.com, 28 Sept 2012.

[8] M. Rethmeier S. Roeren, C. Schwenk. Different approaches to model clamping conditions within a weld simulation. In Proceedings of the 8th Conference on Mathematical Modelling of Weld Phenomena, 2006.

[9] T. Schenk, I.M. Richardson, M. Kraska, and S. Ohnimus. Non-isothermal thermomechanical metallurgical model and its application to welding simulations. Science and Technology of welding and joining, 14(2):152–160, 2009.

266

[10]   Tobias Schenk. Modeling welding Distortion Influence of Clamping and Sequencing. PhD thesis, Material Innovation Institute, www.m2i.nl, 2011.

[11]   Muhammad Zain ul abdein. Experimental investigation and numerical simulation of laser beam welding induced residual stresses and distortion in AA6056-T4 Sheets for Aeronautic application. PhD thesis, 2009.

[12]   E. van der Aa. Local Cooling During Welding: Prediction and Control of Residual Stresses and Buckling Distortion. PhD thesis, TU Delft, 2007.

[13]   John A. Goldak. Computational Welding Mechanics. Springer, 2005.

AVIS DU JURY SUR LA REPRODUCTION DE LA THESE SOUTENUE

Titre de la thèse:

Etude expérimentale et numérique des assemblages soudés: Evaluation des contraintes résiduelles appliquée à l'acier DP600 soudé par laser de haute puissance ND:YAG

Nom Prénom de l'auteur : SEANG CHANSOPHEAK

Membres du jury :
- Monsieur BARRALLIER Laurent
- Monsieur MALARD Benoit
- Monsieur CRETTEUR Laurent
- Monsieur RAGNEAU ERIC
- Monsieur GLORIANT Thierry
- Madame KOUADRI-DAVID Afia
- Monsieur BOURY Hubert
- Monsieur PAILLARD Pascal

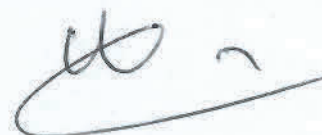Président du jury : *Thierry GLORIANT*

Date de la soutenance : 27 Juin 2013

Reproduction de la these soutenue

☒ Thèse pouvant être reproduite en l'état

☐ Thèse pouvant être reproduite après corrections suggérées

Fait à Rennes, le 27 Juin 2013

Signature du président de jury

Le Directeur,

M'hamed DRISSI

Résumé

Les études sur les procédés de soudage et sur la fiabilité des structures assemblées apparaissent actuellement comme un domaine de recherche actif, ouvert et complexe, car elles nécessitent de combiner de nombreuses connaissances dans différents domaines de la physique, de la mécanique et des procédés. La distribution des contraintes résiduelles joue un rôle important dans la vie des structures en favorisant la rupture par fatigue ou par fissuration. Ainsi, une meilleure compréhension des contraintes résiduelles évite l'utilisation de facteurs de sécurité plus élevés et, par conséquent permet de mieux optimiser le cycle de vie des structures soudées. A travers ce travail de thèse, nous nous sommes intéressés au soudage par laser d'un acier dual phase DP600, soudé en configuration par recouvrement, dont l'application est l'utilisation dans le domaine automobile. Cette thèse présente deux volets : un volet expérimental et un volet numérique.

L'étude expérimentale nous a permis d'une part d'appréhender les conséquences métallurgiques et mécaniques du procédé laser sur l'acier DP600 et d'autre part d'utiliser et de valider les résultats numériques des modèles développés. L'étude numérique a eu pour objectif de prédire l'histoire thermique, métallurgique et l'évolution des caractéristiques mécaniques des tôles soudées par faisceau laser. Nous avons développé, sur un code de calcul par éléments finis Abaqus, trois modèles numériques.
Le modèle thermomécanique, nous a permis de simuler la distribution spatio-temporelle de la température. Dans ce cas, le chargement appliqué est dépendant des paramètres du procédé et des caractéristiques du faisceau laser et est associé à des conditions aux limites. Pour le modèle mécanique, nous avons considéré un comportement élasto-plastique avec un chargement thermique transitoire, résultat du modèle thermique.
Le deuxième modèle thermo-métallurgique nous a permis de simuler les phénomènes d'austénisation pendant la phase de chauffage *(modèle de Waeckel)* et de prendre en compte les fractions volumiques des phases martensitiques générées par les transformations de phases austénite–martensite lors du refroidissement *(modèle de Koistinen-Marburger).*
 Enfin, dans la dernière partie de simulation, nous avons réalisé le couplage thermo-metallo-mécanique. Les résultats obtenus dans la partie précédente, ont été implémentés dans deux modèles mécaniques : le modèle mécanique classique et le modèle mécanique avec prise en compte de la déformation liée aux effets de dilatation métallurgique. Cet effet a été intégré à travers le coefficient de dilatation thermique des phases ferritiques et martensitiques et des fractions volumiques obtenues à partir du modèle thermo-métallurgique. Les résultats ont montré que la répartition des contraintes résiduelles dans la zone de fusion et dans la zone affectée thermiquement sous l'effet de la déformation thermo-métallurgique donne des valeurs supérieures à celles estimées par le modèle élasto-plastique classique.

Mots-Clés: Soudage Laser Nd :YAG, Acier DP600, Caractérisation expérimentale, simulation numérique, contrainte résiduelles.

Abstract

Studies on welding processes and the reliability of assembled structures currently appear as an area of active research, open and complex as they need to combine knowledge in many different fields of physics, mechanics and processes. The distribution of residual stress plays an important role in the life of welded structures by promoting fatigue failure or cracking. Thus, a better understanding of residual stress avoids the use of higher safety factors and therefore helps to optimize the life cycle of welded structures. Through this work, we are interested in laser welding of steel DP600 dual phase welded overlap configuration, the application is the use in the automotive field. This thesis has two components: an experimental and a numerical part.

The experimental study allowed us, firstly to understand the metallurgical and mechanical effects of laser welding on steel DP600 and secondly to use and validate the numerical results of the developed models. The numerical study aimed to predict the thermal history, and metallurgical changes in mechanical properties of laser beam welded sheets. We have developed three numerical models by using a finite element code inside Abaqus.

The thermomechanical model allowed us to simulate the temporal and spatial distribution of temperature. In this case, the applied load is dependent on the processing parameters and characteristics of the laser beam and is associated with boundary conditions. For the mechanical model, we considered an elastoplastic behavior with a transient thermal loading result of the thermal model.

The second thermo-metallurgical model allowed us to simulate the phenomena austenitizing during the heating phase *(Waeckel model)* and take into account the volume fraction of martensitic phase transformations generated by the austenite-martensite transformation during cooling *(Koistinen-Marburger model)*.
Finally, in the last part of simulation, we have achieved the metallo-thermo-mechanical coupling. The results obtained in the previous section have been implemented in two mechanical models: the classical mechanics model and the mechanical model taking into account the deformation due to the effects of metallurgical expansion. This effect has been built through the coefficient of thermal expansion of ferritic and martensitic phases and volume fractions obtained from the thermo-metallurgical model. The results showed that the distribution of residual stresses in the fusion zone and the heat affected as a result of the deformation thermo-metallurgical field gives values higher than those estimated by the classical elastic-plastic model.

Keywords: Nd:YAG Laser Welding, DP600 Steel, Experimental characterization, Numerical simulation, Residual stresses.